Universidade Vigo

Escola Internacional de Doutoramento

Sandra Míguez Lago

TESE DE DOUTORAMENTO

COVALENT ORGANIC HELICAL CAGES: DESIGN, SYNTHESIS, AND APPLICATIONS BASED ON MOLECULAR RECOGNITION

Dirixida pola Prof. Mª Magdalena Cid Fernández e o Dr. José Lorenzo Alonso Gómez

Ano: 2016

"Mención Internacional"

Universidade de Vigo

Escola Internacional de Doutoramento

A Prof. Mª Magdalena Cid Fernández e o Dr. José Lorenzo Alonso Gómez

FAN CONSTAR que o presente traballo, titulado "COVALENT ORGANIC HELICAL CAGES: DESIGN, SYNTHESIS, AND APPLICATIONS BASED ON MOLECULAR RECOGNITION", que presenta Dna. Sandra Míguez Lago para a obtención do título de Doutora, foi elaborado baixo a súa dirección no programa de oficial de doutoramento "RD1393/2007 – Doutoramento en Ciencia e Tecnoloxía Química" da Universidade de Vigo.

En Vigo, a 07 de Novembro de 2016.

Os Directores da tese de doutoramento

Prof. Mª Magdalena Cid Fernández Dr. José Lorenzo Alonso Gómez

Universidade de Vigo

Escola Internacional de Doutoramento

O Prof. Dr. D. Ángel Rodríguez de Lera, Director do Departamento de Química Orgánica da Universidade de Vigo, CERTIFICA QUE:

O traballo descrito na presente memoria, con título "COVALENT ORGANIC HELICAL CAGES: DESIGN, SYNTHESIS, AND APPLICATIONS BASED ON MOLECULAR RECOGNITION", foi realizado nos laboratorios do Departamento de Química Orgánica da Universidade de Vigo, e constitúe a Memoria que presenta Dna. Sandra Míguez Lago, para optar ó Grao de Doutora pola Universidade de Vigo.

Vigo, Novembro 2016

Ado. Prof. Dr. Ángel Rodríguez de Lera

Abbreviations

Å	Ångström
Ac	acetyl, $CH_3C(O)$-
AM1	Austin-Model 1
aq.	aqueous
br.	broad (IR)
B3LYP	Becke, 3-parameter, Lee-Yang-Parr functional
Bu	butyl
°C	degree centigrade (0 °C = 273.15 K)
calcd.	calculated
cat	catalyst
cpl	circularly polarized light
CSP	chiral stationary phase
d	doublet (NMR)
DCM	dichloromethane
DEA	diethynylallene
DFT	density functional theory
DMF	*N,N*-dimethylformamide
ECD	electronic circular dichroism
EI-MS	electron impact mass spectrometry
eq	equivalent
ESI-MS	electrospray ionization mass spectrometry
Et	ethyl
FC	flash chromatography
g	gram
GC	gas chromatography
h	hour
HMBC	heteronuclear multiple bond correlation
HPLC	high performance liquid chromatography
HR	high resolution
HSQC	heteronuclear single quantum correlation
Hz	hertz (s^{-1})

i-	*iso*-
I	intensity
IR	infrared (spectroscopy)
J	coupling constant (NMR)
L	liter
LanL2DZ	Los Alamos National Laboratory Double Zeta basis set
LDA	lithium di*iso*propylamide
LHMDS	lithium hexamethyldisilazide
m	meter
m	multiplet (NMR)
M	molarity [$molL^{-1}$]
Me	methyl
MHz	megahertz
min.	minutes
MS	mass spectrometry
NMR	nuclear magnetic resonance
OR	optical rotation
ORD	optical rotatory dispersion
ppm	parts per million
Pr	propyl
py	pyridine
q	quartet (NMR)
s	singlet (NMR)
sat.	saturated
t	triplet (NMR)
TBAF	tetrabutylammonium fluoride
TFA	trifluoroacetic acid
THF	tetrahydrofuran
TIPS	tri*iso*propylsilyl
TLC	thin layer chromatography
TMEDA	*N*,*N*,*N'*,*N'*-tetramethyl-1,2-ethylenediamine

TMS	trimethylsilyl
UV	ultra-violet
VCD	vibrational circular dichroism
Vis	visible
vs.	versus
α	optical rotation
δ	chemical shift (NMR)
ε	extinction coefficient
λ	wavelength
μ	micro (10^{-6})
ρ	density
ν	frequency

Table of Contents

1. Introduction

1.1. Molecular Cages.

"Molecular Cage" is by far the most used term to designate those molecules whose main characteristic is the presence of a permanent internal void with the appropriate size, shape, and functionalities in order to stablish a complex with one or more guest molecules, with their resulting applications. Conceptually similar to that one, the word "Box" is mainly used in some publications for naming some macromolecules, which resemble more macrocycles than real cages.[1] "Capsule" attempts to express a supramolecular linkage between complementary parts or molecules.[2] Terms "Container" or "Scavenger" make reference to the ability of entrapping smaller molecules reversibly or irreversibly.[3] The origin of the development of the supramolecular chemistry by Pedersen,[4] Cram[3] and Lehn[5] was certainly the starting point for the design and synthesis of molecular cages.

1.1.1. Molecular Cages Classification.

Regarding the nature of the interactions that hold molecular cages together, they can be classified into two main categories, Supramolecular Cages and Covalent Cages, which can be in turn subdivided in two different groups, metallorganic and organic ones (**Figure 1**).

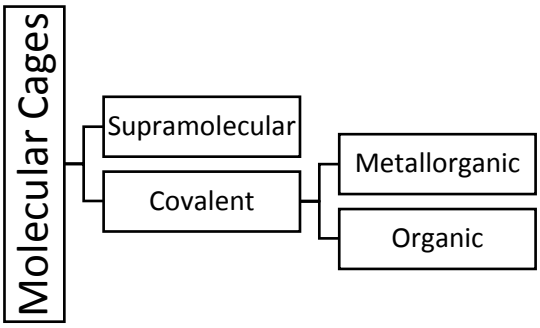

Type of bond / attraction	Range of bond energies (kJ/mol)
Ionic Bonds	700 – 4000
Covalent Triple Bonds	800 – 1000
Covalent Double Bonds	500 – 700
Covalent Single Bonds	200 – 500
Dipole attraction forces	40 – 400
Hydrogen Bonds	10 – 40

Figure 1. Top: Classification of molecular cages attending the interactions holding their structures. Bottom: Typical bond energies range table.

1.1.1.1 Supramolecular Cages.

The initial growth of the supramolecular branch can be attributed *inter alia* to the publications reported by J. Rebek and coworkers dealing with the design and synthesis of several supramolecular capsules hold together mainly by sets of hydrogen bonds.[6] Hydrogen bonds, with their high directionality, specificity and biological relevance, represent just one of the many examples of supramolecular interactions possible in order to form supramolecular cages. Along

with hydrogen bonding, there are other supramolecular interactions such as halogen bonding,[7,8] dipole-dipole interactions, ionic interactions,[9] π-π stacking, and Van der Waals or hydrophobic interactions (**Figure 2**). Despite the fact of being most of them relatively weak interactions in comparison with covalent bonds, the cooperativity or synergy between them gives rise to the needed strength for further applications. Moreover, the weakness of this type of interactions can be in some cases a strategic ally for the easy catch and release of the guest.[10]

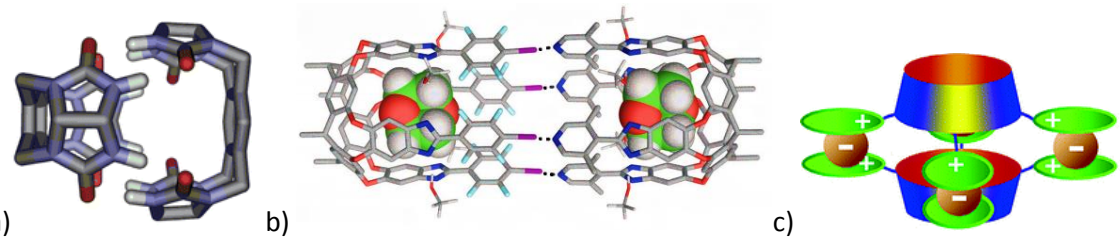

Figure 2. a) Rebek's Tennis-ball hold together by hydrogen bonds.[11] b) Diederich's halogen-bonded capsule.[7] c) Schematic representation of an ionic cage reported by Verboom and coworkers.[9]

1.1.1.2 Covalent Cages.

Covalent Cages can be divided into two main subcategories: The purely Organic Molecular Cages and the Metallorganic Cages. In the first case, the bonds defining their skeletons are solely covalent bonds formed between either non-metallic atoms or a non-metallic atom with a metalloid, such as C−C, C−N, C−O, C−S, S−S and B−O bonds. In the second case, coordinative (or covalent dative) bonds between a transition metal and a non-metallic atom are the key links of the cage structure.

Metallorganic Cages rank among the most famous structures in this field, due to the high directionality and bond strength of the coordinative bond stablished between the metallic centers and the corresponding ligands. This fact makes easier the selection of an appropriate metal center and a ligand in order to get well-defined architectures. On the other hand, the main disadvantage of this type of cages is the lability of the coordinative bond, which promotes the exchange of ligands according to the stability of the formed molecule. This fact constrains the choice of the solvent and the nature of the guest. A renowned example of coordination cages are the ones reported by Fujita and coworkers.[12] Many of these are based on the coordination between a palladium atom and nitrogen compounds giving rise to a whole set of geometries and applications, such as fluorinated compounds complexation,[13] polycyclic aromatic hydrocarbons (PAHs) encapsulation as is the case of corannulene,[14] or Diels-Alder reaction chamber,[15] among others. Other authors have reported the used of metallorganic cages as drug delivery agents,[16] reactors for hydroformylation in presence of a Rh-catalyst,[17] or even encapsulating agents for chemical warfare agent simulants (**Figure 3**).[18]

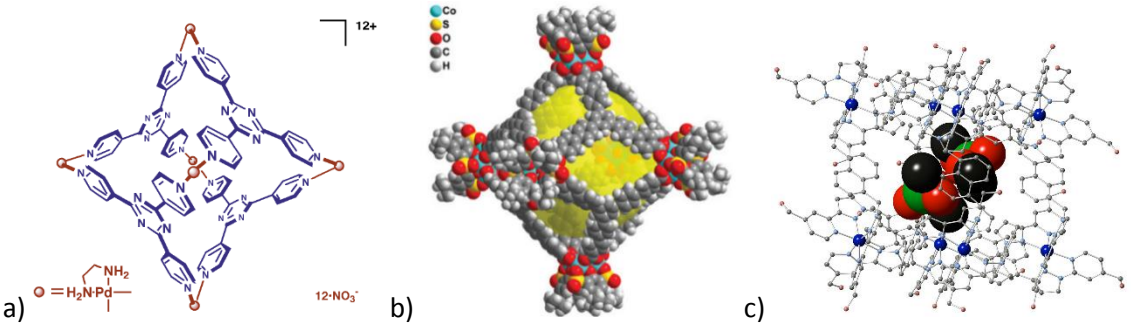

Figure 3. a) Palladium coordinative metallorganic cage,[12] b) ibuprofen encapsulating cage,[16] and c) cage with warfare agent simulant inside.[18]

In general, purely organic cages, in contrast to metallorganic ones, do not present the disadvantage of been labile. In spite of that, a relatively emerging and interesting approach for building covalent organic cages, called Dynamic Covalent Chemistry (DCC or DCvC),[19–21] is based on the formation of reversible covalent bonds in a thermodynamically-controlled assembly process. This has given rise to complex molecular topologies, such as Borromean rings,[22] Solomon knots,[23] or trefoil knots.[24] The fact that such reactions are in equilibrium, favors the self-healing process, leading to the formation of the most thermodynamically favored species. The most common types of reactions within this current are amide bond formation, imine bond formation, boronic acid/ester condensation, alkene or alkyne metathesis, and disulfide bonds among others (**Table 1**).[21,25]

Reaction Type	Chemical Reaction
Amide Formation	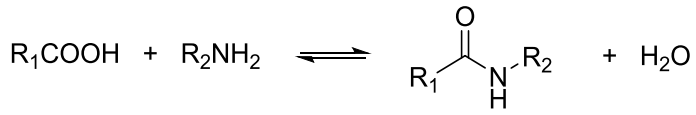
Imine Formation	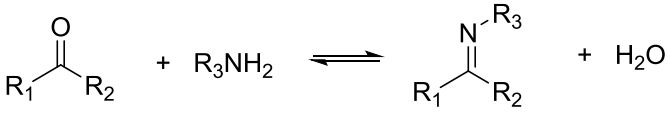
Boronic Acid Condensation	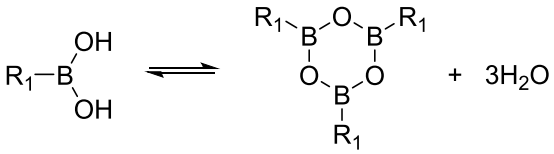
Alkene/Alkyne Metathesis	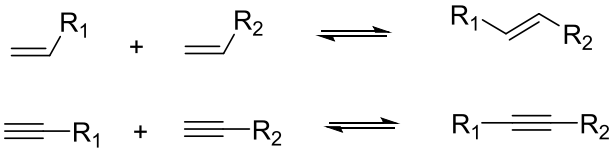
Disulfide Bond Formation	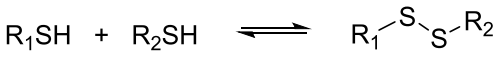

Table 1. Most representative examples of Dynamic Covalent Reactions on the synthesis of organic molecular cages.

With respect to the synthetic method applied, although synthesis in solution is by far the most used technique on the formation of molecular cages, there are some others paving their way in the experimental academic research. Thus we find the environmental-friendly Mechanochemistry,[26] which dispenses with solvent, and the Dynamic Flow Synthesis,[27] which allows the use of high-dilution conditions yielding large scale products.

The large scale synthesis of molecular cages brought along the development of a huge variety of applications.[28] Thus, molecular cages have been employed as trapping of greenhouse gases,[29,30] chiral stationary phases for the separation of racemates in gas chromatography,[31–33] templates for small metallic nanoparticles growth,[34,35] and chiroptical sensors of non-chromophoric molecules (**Figure 4**).[36]

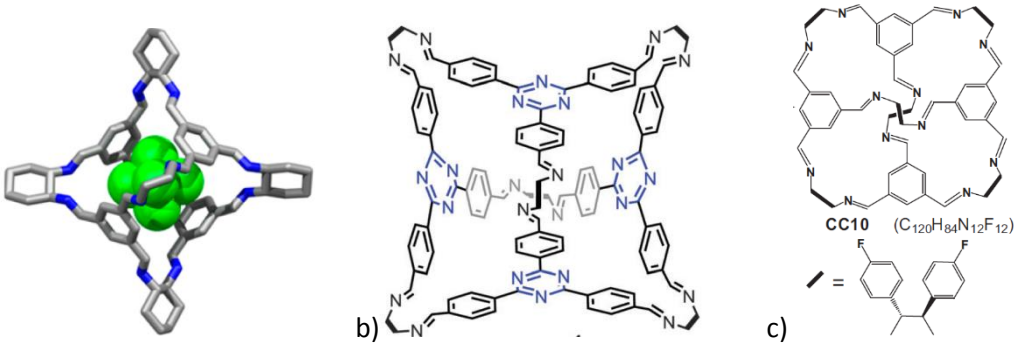

Figure 4. a) Resolved position of SF_6 inside a cage cavity determined from the single crystal structure.[29] b) Structure of a molecular cage presenting selective absorption of CO_2 over N_2.[30] c) Structure of a chiral molecular cage employed as chiral stationary phase in chromatography.[33]

The applicability of a particular molecular cage strongly depends on the dynamics of guest encapsulation and the exchange process (**Figure 5**). For that, it is necessary to know about the timescales involved in molecular recognition phenomena. On the one hand, diffusion-governed complexes where both species are immersed in the same environment (usually a solvent) are found. The duration of the interaction in this case is typically less than a nanosecond, which is the limit for reactivity of two molecules. When molecules react at every single collision, it is said that the process is diffusion-controlled. On the other hand, are found reversible encapsulation processes, whose interaction time ranges from nanoseconds to several orders of magnitude of seconds. This approach of the reactants for a longer time due to its encapsulation inside a molecular cage, often results into an increased reactivity or even into a different reactivity than expected to that in the simple bulk solvent.[15]

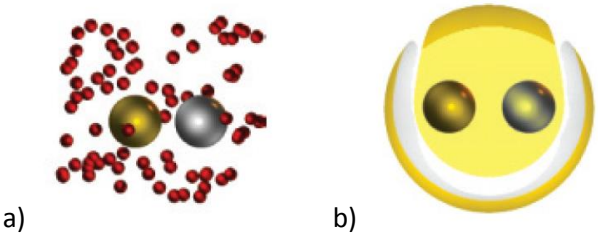

Figure 5. a) Diffusion controlled process, and b) reversible encapsulation schemes.[15]

Despite all the foregoing and the abundance of molecular cages on literature, the chiral ones are still a minority compared to the achiral ones, due to the inherently difficulty of handling molecules containing chiral elements either due to the tedious separation of the stereoisomers

involved,[27] or by the precautions to be considered against racemization processes.[37] Given their scarcity and high applicability, it is convenient to consider the development of molecular chiral boxes as a field of great interest in which there is still much work to do.

1.2. Chirality.

1.2.1. Definition of chirality.

Chirality is defined as a property present on molecules which are non-superimposable with their corresponding mirror images. According to this, it seems an easy task to determine if a molecule is chiral or not (achiral), but actually this determination of chirality gets more difficult as systems increase in size. There are some general rules that can be followed in order to determine if a molecule is chiral or achiral. In general, for a molecule, the presence of a plane of symmetry or a center of symmetry makes a molecule achiral. Thus, with regard to the symmetry elements that molecules possess, they can be classified into different Point Groups. In terms of point groups, all chiral molecules lack an improper axis of rotation (S_n), which means that they cannot contain a center of inversion (i) or a mirror plane (σ). As a result, only molecules belonging to C_1, C_n, D_n, T, O, and I point groups are chiral. A flow chart for determining the point group of a molecule represents a useful tool for determining if a molecule is chiral or not (**Figure 6**).

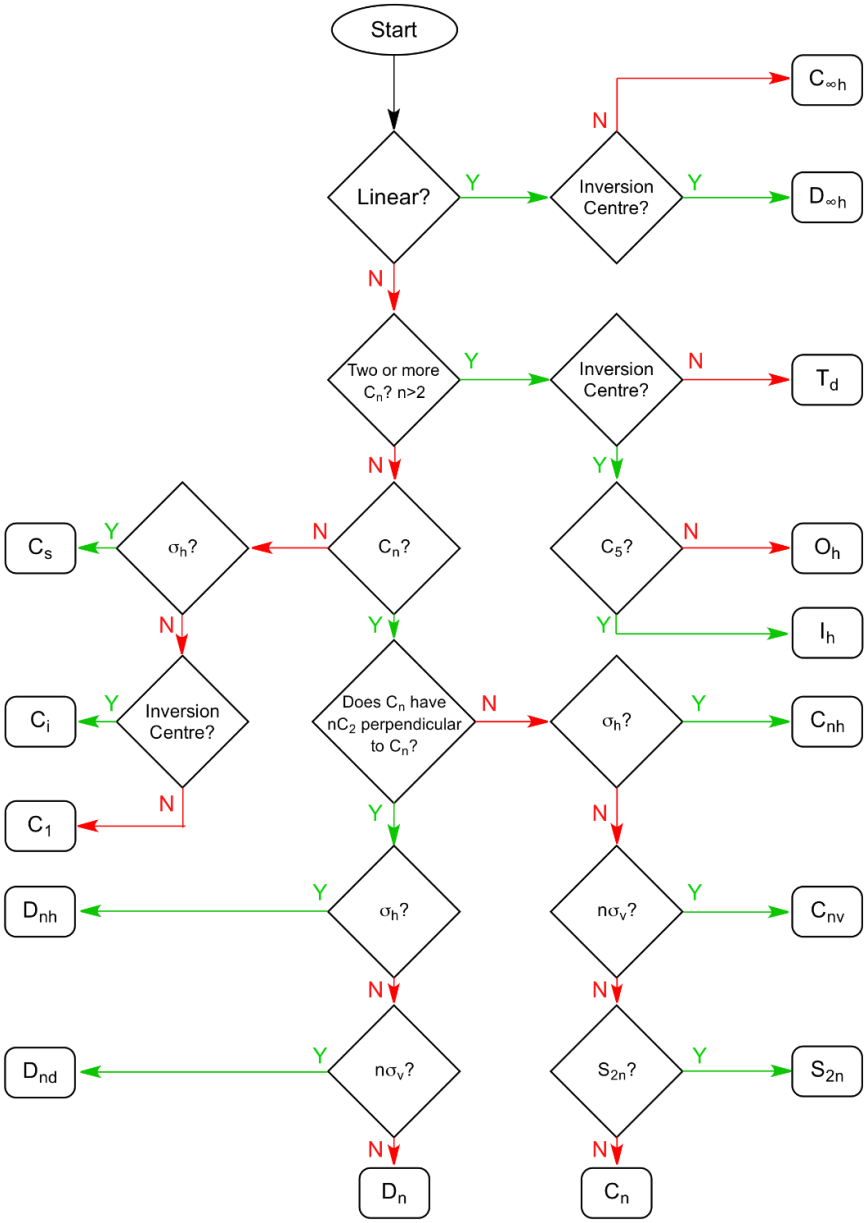

Figure 6. Flow chart for determining the Point Group to which a molecule belongs.[38]

1.2.2. Chirality in Nature.

Nature is full of chiral molecules and chiral supramolecular assemblies. This fact is showed for most of biological systems, which present a prodigious stereo-specificity in synthesis, uptake, sensing, and metabolic processing. Both amino acids, which are all chiral except glycine, and carbohydrates, which are commonly found in the D-configuration, are good examples of homochirality, property of compounds where all the constitutive units are of the same chiral form. A universal example of homochirality is the DNA double helix, which can be dextro- or levo-rotatory.

Often, the two enantiomers of a chiral compound radically differ on their organoleptic properties, because living systems usually interact with them in different ways. A classic example

is the different characteristic piney and lemon odor caused by the biological interactions of (−) and (+)-Limonene at the human nose.[39] Chirality is also found at the macroscopic level in plant and animal kingdoms among others. Examples of that are the coiling direction of climber plants, the coiled shells of gastropods,[40] and the structure of many viruses capsids (**Figure 7**).[41]

a)  b)  c) 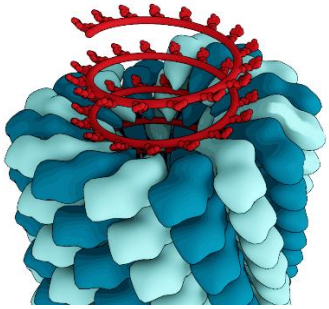

Figure 7. a) Curling trendily of a vine plant.[42] b) Coiled shell of a snail.[43] c) Helical capsid of the tobacco virus.[44]

The origin of homochirality in Nature is to date not entirely understood. It is not clear if this feature has a purpose, but some theories relate it with a way of storing information.[45] Another proposal is based on the fact that the formation of large organized molecules reduces entropy barriers, as it has been experimentally verified with amino acids, which form large aggregates more abundantly from enantiopure substrates than from racemic ones.[46]

1.2.3. Source of chirality.

Existence of chirality in molecules was traditionally attributed to the presence of an asymmetrically substituted atom, this means a tetrahedral atom bearing four different substituents. However, there are other symmetry elements responsible for the presence of chirality in molecules rather than stereogenic centers, such as chiral axes and planes (**Figure 8**). Axial chirality is a kind of dissymmetry due to the presence of a chiral axis, around which the rotation is restricted (atropisomerism phenomenon) or blocked. So is the case of some properly substituted biaryls, spiranes and allenes. The most widely used substituted biaryls are binaphtyls, which have been employed in numerous applications such as sensors, asymmetric catalysis and synthesis of chiral conjugated polymers.[47] On the other hand, spiranes, [48] which are bicyclic compounds linked together by a shared atom, have been also reported as common elements of many natural products.[49]

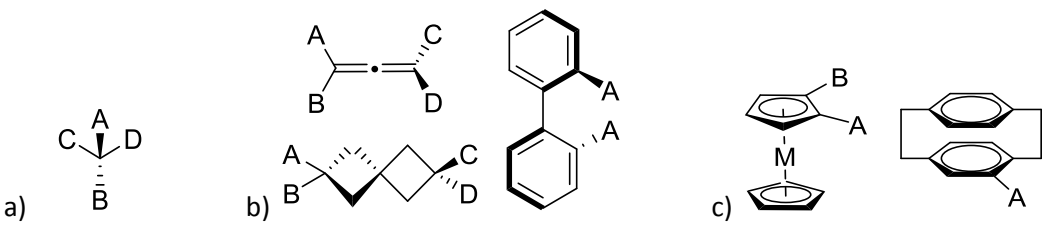

Figure 8. Schematic representation of: a) Chiral center. b) Chiral axes (substituents not all necessarily different). c) Chiral planes.

1.2.3.1. Allenes.

Allenes are the smallest members within the family of cumulenes.[50] Allenes have a general formula $R_2C=C=CR_2$, an ideal 180° C=C=C bond angle, and a *sp* hybridation of the central C atom. Moreover, they possess two orthogonal π bonds when described by the classical model, [51] whilst a more accurate description considers a helical disposition of the orbitals (**Figure 9**).[52] Allenes, as well as its family, composed by cumulenes bearing an odd number of carbons, when properly substituted, present the same chirality as that of an elongated tetrahedron.

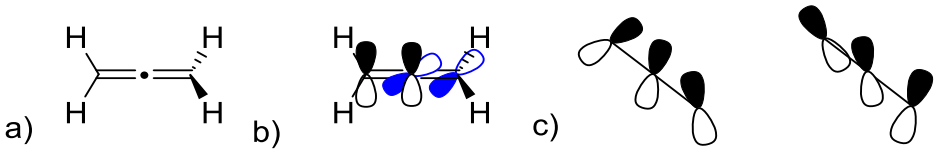

Figure 9. a) Structure of the simplest allene. b) Classical orbital description of the simplest allene. c) More accurate orbital description of the simplest allene: Right-handed HOMO (left) and left-handed HOMO (right).

When dealing with a chiral allene, its chirality can be explained by using two sets of descriptors, (*aR*)/(*aS*) or (*P*)/(*M*), where (*aR*) corresponds with (*M*) and (*aS*) corresponds with (*P*).[53] The most recommended nomenclature for axially chiral compounds employs the *P*/*M* descriptors. For determining them, one should first assign the priorities of the substituents on the frontal carbon and the carbon on the back and then trace the shortest path from the substituent with the highest priority in the front to the one with the highest priority in the back. If the sense is clockwise, then the allene is *plus* or (*P*), and on the contrary, if the sense is counterclockwise, then the allene is *minus* or (*M*) (**Figure 10**).

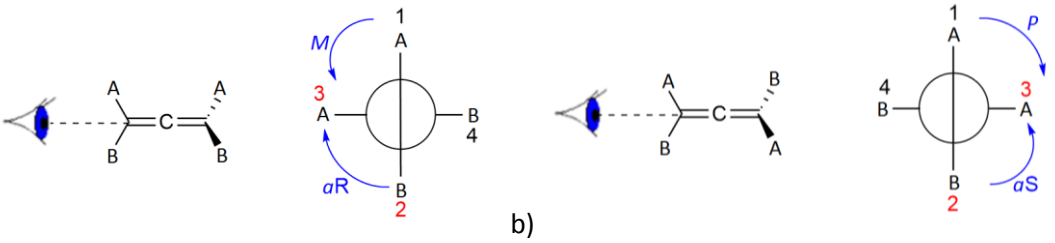

Figure 10. Example of nomenclature of a pair of enantiomers of a chiral allene. a) (*aR*) or (*M*) configuration. b) (*aS*) or (*P*) configuration.

Allenes can be found in the skeleton of many natural products as well as pharmaceuticals, ranging from steroids and prostaglandins to aminoacids and nucleosides (**Figure 11**).[54] This appearance of optically active allenes was first observed by Celmer and Solomons as early as 1952 with the structure of the antibiotic mycomicin.[55] In addition, allenes have been employed as starting material on the synthesis of a huge variety of non-allenic natural products.[56]

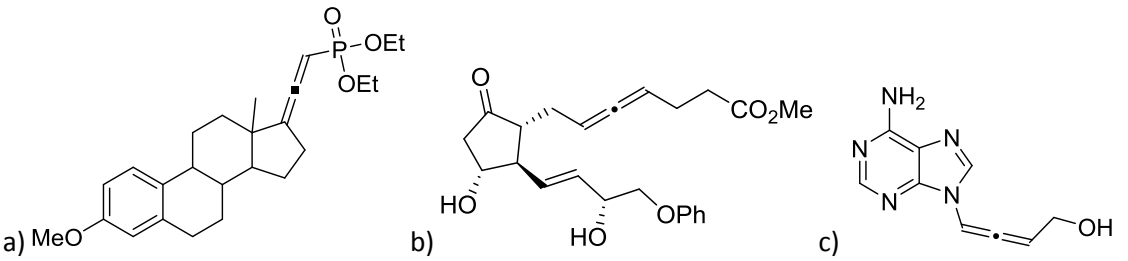

Figure 11. a) Allenic steroid inhibitor of sterol biosynthesis.[54] b) Allenic prostaglandin (Enprostil) which inhibits gastric secretion.[54] c) Allenic nucleoside (Adenallene) which possess cytotoxicity and inhibition of HIV replication.[54]

Moreover, allenes have been used as precursors for the synthesis of acyclic products such as olefins, 1,3-dienes, enynes, and differently substituted allenes, as well as for the synthesis of carbo- and heterocyclic compounds.[52]

The development of the chemistry of allenes had remained dormant for many decades due to the belief that they were highly unstable. However, this belief has proved to be untrue, and the chemistry of allenes has developed greatly in the last four decades.

Due to this now demonstrated broad applicability of allenes, they have become interesting targets. Due to its similarity to olefins, many different olefin-forming procedures where employed for synthesizing them. Elimination reactions, such as metal-mediated dehalogenations,[57] dehydrohalogenations in basic media,[58] and acid- or catalyst-promoted dehydrations[59] are some examples of reactions used on the synthesis of allenes. The main disadvantage of such processes was the use of relatively harsh conditions, which can induce undesired secondary processes such as addition, isomerization and even polymerization. Allenes can also be obtained through Wittig reactions,[60] treatment of olefins with carbenes,[61–64] treatment of vicinal dihalides with zinc,[65] dehydrohalogenation,[66] dehydration of alkyl alcohols or enols,[67,68] and Pd-catalyzed S_N2' substitution of the propargylic compounds (**Scheme 1**).[69–72] This last approach has been widely employed, and possess two different modes for the palladium attack depending on the leaving group present on the substrate. On the *anti* mode the Pd^0 attack takes place opposite to the face where the leaving group is placed, whilst on the *syn* mode there is a coordination between the Pd^0 and the leaving group, favoring the Pd^0 attack over the same face where the leaving group is. Thus, the presence of one or another leaving group strongly affects the transference of stereochemical information from the carbon bearing the leaving group to the newly formed allene.

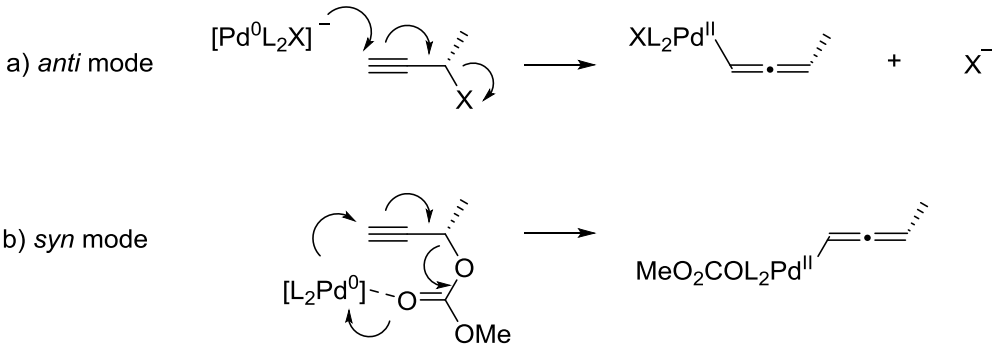

Scheme 1. Oxidative addition mechanism of the Pd^0 catalyst over the propargylic substrate. a) *Anti* mode. b) *Syn* mode.

The use of Pd-catalyzed S_N2' reaction conditions can be also applied to bispropargylic substrates yielding 1,3-diethynylallenes (DEAs),[71] which, through incorporation of bulky side chains to its structure resulted in an increasing of stability, fact that promotes its use as substrate for further applications.[72]

DEAs, both as racemate and as enantiopure molecule, have been included in structures such as allenophanes (in combination with aromatic spacers),[37,73–76] acyclic[77] and cyclic[78] oligomers and recently also in metallorganic molecular cages (**Figure 12**).[36]

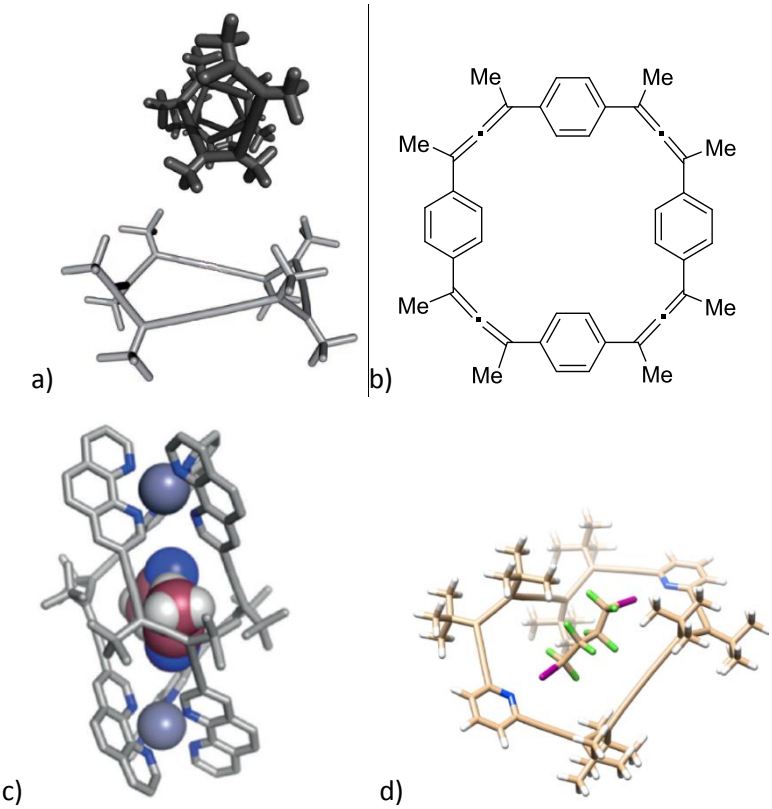

Figure 12. a) Cyclic[78] (bottom) and acyclic[77] (top) allene oligomers. b) First allenophane reported by Krause and coworkers.[73] c) Metallorganic cage reported by Diederich and coworkers.[36] d) Allenophane forming an inclusion complex with a diiodoperfluoroalkane reported by Cid and coworkers.[75]

1.2.4. Chiroptical spectroscopies.

Chiroptical spectroscopic methods have been broadly employed for determining the absolute configuration, studying the conformational space and determining the chiroptical strength of chiral molecules. Electronic circular dichroism (ECD), vibrational circular dichroism (VCD), vibrational Raman optical activity (VROA) and optical rotatory dispersion (ORD) are frequently used chiroptical spectroscopic methods. Normally, these techniques are employed combined in order to evaluate or double-check the results obtained, but they can be also used independently, depending on the pursued goal.

The basis of all chiroptical spectroscopies is the same: the interaction of an incident light with the chiral sample. This incident light can be linearly polarized or circularly polarized respectively.

The linearly polarized light can be achieved as a summation of two circularly polarized electric components to the left and to the right (E_L and E_R) with the same phase and magnitude.[79] If the components are out of phase and/or possess different magnitudes, the resultant light is elliptically polarized light, and in the particular case in which the dephasing is exactly 90° but the magnitude of the components is the same, then the resulting light is circularly polarized (**Figure 13**).

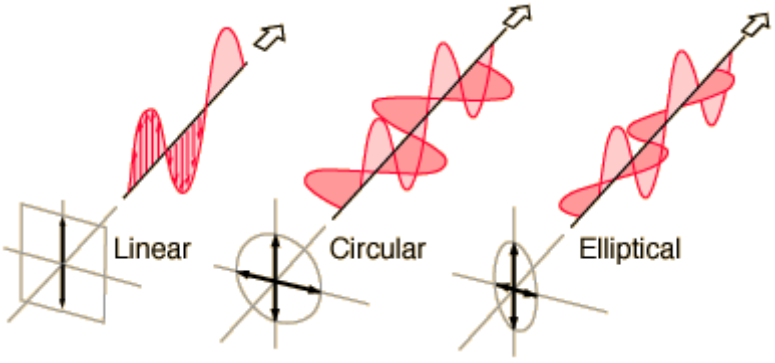

Figure 13. From left to right: Linear, circular and elliptical polarized lights.

A sample is said to be optically active when it differently interacts with both components of polarized light, being able to manifest itself in different ways. On the one hand, the plane of the polarization of the incident light can be rotated by an angle α, phenomenon called Optical Rotation (OR), and whose value is characteristic of every single chiral compound. It depends on the wavelength of the incident light and the external conditions such as solvent and temperature. It can be precisely defined as the angle between the major axis of the ellipse and the plane of polarization of the original linear polarized light. The phenomenon which causes this angle rotation is called birefringence. Birefringence is a consequence of the different speed/refractive index of left and right circularly polarized lights while travelling through the sample. On the other hand, if absorption of both circularly polarized lights to the left and to the right is different, this will result in the difference of the amplitude of the two components in the absorbed light. This resultant light will be then elliptical, and this phenomenon is called Circular Dichroism (CD) (**Figure 14**).[80]

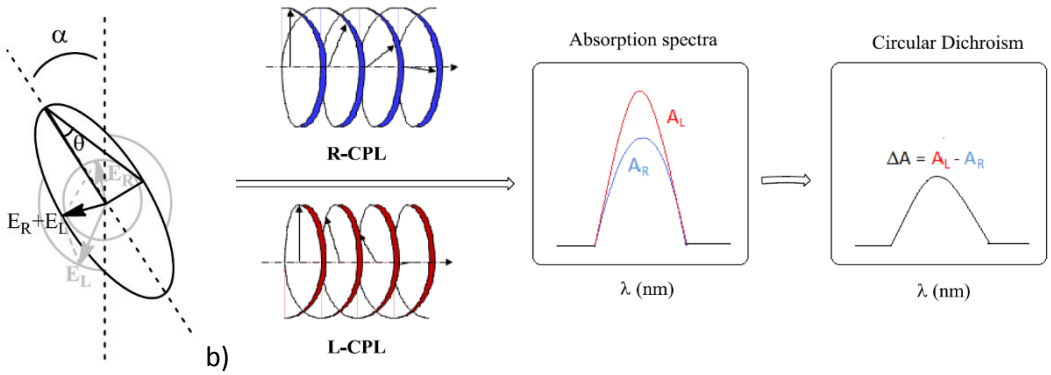

a) b)

Figure 14. a) Optical Rotation scheme. b) Circular Dichroism scheme.

Mathematically, the CD is defined by:

$$CD = A_L - A_R = \Delta A$$

being A_L and A_R the absorptions of the left and right circularly polarized lights respectively.

Normally, the value given by a circular dichroism spectrophotometer is the ellipticity (θ, in *mdeg*), which is related with the CD by the following equation:

$$\theta = 32982 \cdot CD$$

Analogously to the Lambert-Beer Law:

$$\Delta\varepsilon\ (\mathrm{Lmol^{-1}cm^{-1}}) = CD\ /\ (c \cdot l)$$

where *c* is the molar concentration of the sample and *l* is the pathlength of the cuvette in cm.

As the absorption spectrum gives always positive values for absorption, the bands on the CD can be either positive or negative, and are called Cotton effects, in honor of one of its discoverers.[80]

When dealing with a circularly incident light on the UV region of the electromagnetic spectrum, the CD is called Electronic Circular Dichroism (ECD), since the absorptions promote transitions between electronic states. However, when the incident light belongs to the IR region, the CD is called Vibrational Circular Dichroism (VCD).

The chiral efficiency of a system can be measured by the dimensionless *anisotropy* or *dissymmetry* factor, also called *g*-factor at different regions of the spectra, and it is given by the following equation:

$$g\text{-factor} = (\Delta\varepsilon\ /\ \varepsilon) = (\theta\ /\ (A \cdot 32982))$$

where *A* represents the conventional absorbance of non-polarized light.

Values of *g*-factor for organic molecules reported so far fluctuate in the range from thousandths to hundredths, for example, *g*-factor values were reported for polyaromatic compounds (0.05),[81] alleno-acetylenic oligomers and macrocycles (0.01),[77,78] and protein complexes (0.06).[82] *g*-factors for organic molecules in combination with sub-nanometer metallic clusters (0.005),[83] metal nanospheres with surface-plasmon CD (up to 0.001),[84–87] and anisotropic gold nanorods (0.02)[88] are in the same range.

The strength of the chiroptical response is a magnitude strongly dependent on the shape-persistency of the molecule, which avoids partial or total average of the chiroptical signal. Therefore, rigid systems are required in order to get outstanding chiroptical responses, so valuable in the construction of chiroptical sensing devices.

1.3. Sensing

Sensors are small devices capable of measuring a chemical or physical magnitude (input) of a sample by using a recognition element, and transforming it into a magnitude such as an electronic magnitude (output) at a signal transducer. The establishment of a correlation between both allows the detection and even quantification of the input in the sample. The combination of different recognition elements with different signal transducers gives rise to a whole set of sensors, ranging from the electrochemical, gravimetric, and electric to the optical ones.

Nowadays sensors have become indispensable tools, being used for a wide range of clinical, environmental, and industrial applications. Emerging needs of the population are the main cause of the impressive growth of this field, and the multidisciplinarity is the key of success in the development of new sensors. The future sensors point to the early detection of disease biomarkers, minimizing the use of invasive processes, as a major goal to achieve.

Diseases are normally related with a failure on a metabolic or regulatory process, in which the great majority of metabolites as well as therapeutic targets, such as proteins and DNA, and drugs that palliate or cure those illnesses are chiral. It is also noteworthy the importance of chirality in molecules such as pesticides, since different enantiomers can cause completely different effects on the environment. The food industry is also affected by the presence of chiral sensors capable of analyzing edibles and organoleptic molecules, which provide the smell and taste of the food. Therefore, building sensors having chiral recognition elements or even using chiroptical spectroscopies as sensing techniques can be envisaged as an interesting target for the scientific community.

Despite this evidence, and even if there are many examples where the recognition element is chiral, such as cyclodextrins, proteins, antibodies, polysaccharides, Molecular Imprinted Polymers (MIPs), helical polymers, crown ethers, and calixarenes among others, to date no commercial sensor that makes use of chiral spectroscopies such as circular dichroism or optical rotation exists on the market. However, is impressive the number of examples and bibliography that can be found for sensors involving chiral recognition elements in combination with electric, gravimetric and electrochemical techniques.[89]

1.3.3. Sensors with Chiral Recognition Elements.

1.3.3.1. Electrochemical Sensors.

Electrochemical sensors are the most reliable and sensitive ones. They usually consume small sample volumes, being susceptible of miniaturization. On the other hand they have a short life time and require the use of reference electrodes. They can be classified into potentiometric and voltammetric/amperometric. Potentiometric ones measure the difference between two potentials (ΔV). They are based on the Nernst equation, which relates the voltage with the ion activity (or the concentrations) of the species involved on the redox process. The basic parts of the cell are an ion-sensitive membrane and a reference electrode. The chiral receptor can be immobilized on the membrane by physical absorption, covalent binding, and formation of self-assembled monolayers (SAMs). Sensors to differentiate L/D-carnitine with macrocyclic antibiotics[90] or L/D-phenylalanine with polymeric films have been described.[91]

The second type of sensors within the electrochemical ones are the Voltammetric/Amperometric, which are based on measurements of current. These sensors are based on the measurement of developed current when a changing or fixed potential is applied to the sample. Nanowires with a high surface area have been used as a voltammetric sensor.[92] A example of an amperometric sensor is the glucose sensor, based on an immobilized enzyme on the surface of the electrode.[93]

1.3.3.2. Gravimetric Sensors.

Besides the electrochemical techniques, sensors can be also governed by mass changes. This is the case of Gravimetric-Mass Sensors-Resonators, which are capable of measuring sub-nanogram level changes exhibiting long time stability. In this category, the most famous devices are the Quartz-Crystal Microbalances (QCMs), often called Thickness Shear Mode Resonators (TSMRs), and Bulk Acoustic Waves (BAWs) (**Figure 15**). QCMs consist of a resonator/piezoelectric quartz crystal and a sensing film coated on its surface. Shift of the resonance frequency of QCM is proportional to the variations in mass of the sensing layer deposited on the electrode due to adsorption of analyte molecules onto the surface and/or into the bulk material.

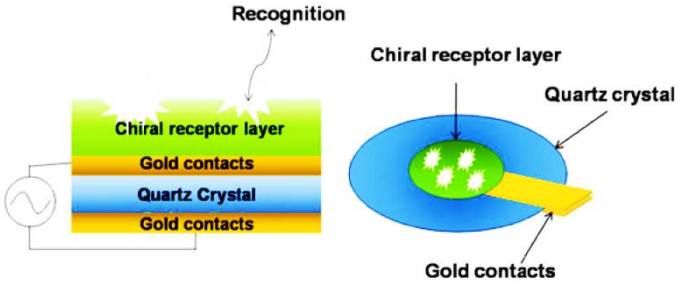

Figure 15. QCM for chiral recognition example.

This kind of sensors have made use of Cyclodextrins, Molecular Imprinted Polymers (MIPs) and biological elements among others. An extraordinary example of QCM sensor is the one reported by Nakanishi and coworkers, able to differentiate between (*S*) and (*R*) enantiomers of the controversial drug Thalidomide.[94]

1.3.3.3. Electrical Sensors.

Electrical Sensors can be defined as the ones which rely on changes of the electric properties of the sensitive material upon interaction with an analyte, whereby no electrochemical phenomenon takes place. Typically, the procedure involves placing a material between conducting electrodes to which a voltage is applied and subsequently measuring the electrical conductivity or capacitance. They can be divided into three subcategories: Chemiresistors, Organic Field Effect Transistors (OFETs), and Chemocapacitors.

Chemiresistors are usually employed for detection of gases and volatile organic compounds. They are based on a chemical modulation of the surface or bulk conductivity of the sensitive layer. Unfortunately, very little work has been reported on enantiomeric sensing employing chemiresistors.

Organic Field Effect Transistors (OFETs) are three terminal transducers consisting of an organic semiconductive layer, a dielectric layer, and three conductive terminals, the source, drain, and gate. The current (I_{DS}) that flows between source and drain through the semiconductor, upon application of a bias (V_{DS}), is modulated by a perpendicular electric field generated by a voltage applied on the gate electrode (V_{GS}). Charge carriers induced in the organic semiconductor at the interface with the gate dielectric are the responsible of the different charge transport regimes (**Figure 16**). The observables measured are normally I_{DS} *vs* V_{DS} or V_G in the presence and absence of the analyte.

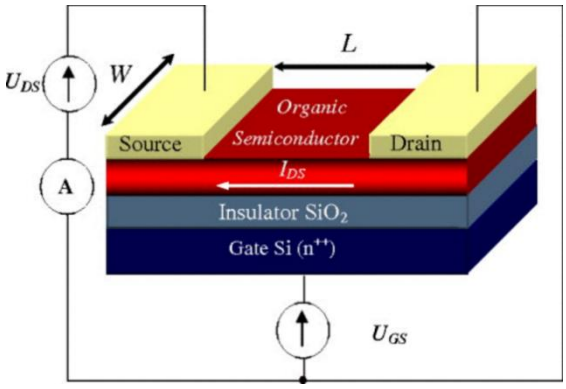

Figure 16. Schematic representation of an OFET structure.

Chemocapacitors are formed by a couple of electrodes with a dielectric material in between and the generated electric field strongly depends on the permittivity of the dielectric sensitive layer and also on the degree of swelling of the polymeric layer.

1.3.3.4. Optical Sensors.

Optical sensors convert a physicochemical interaction into an optical signal, by means of using the interaction between light and matter, generally in the visible, IR, and UV regions. Here, Surface Plasmon Resonance (SPR) sensors and the Reflectometric Interference Spectroscopy-Based Sensors (RIfS) are presented.

On the SPR, surface plasmon waves are generated by irradiating with light the surface of a thin metal film (**Figure 17**). It is a high sensitive and versatile method that is used to measure changes in the refractive index caused on metal surfaces by interactions of the analyte and the sensing layer. Amplified SPR sensing has been achieved by using metallic nanoparticles (NPs), which provide high surface area films and exhibit localized plasmon excitons. Example of that is the work of Katz and coworkers in which Au-NPs plus calixarenes give rise to a sensor based on both SPR and electronic circular dichroism.[95]

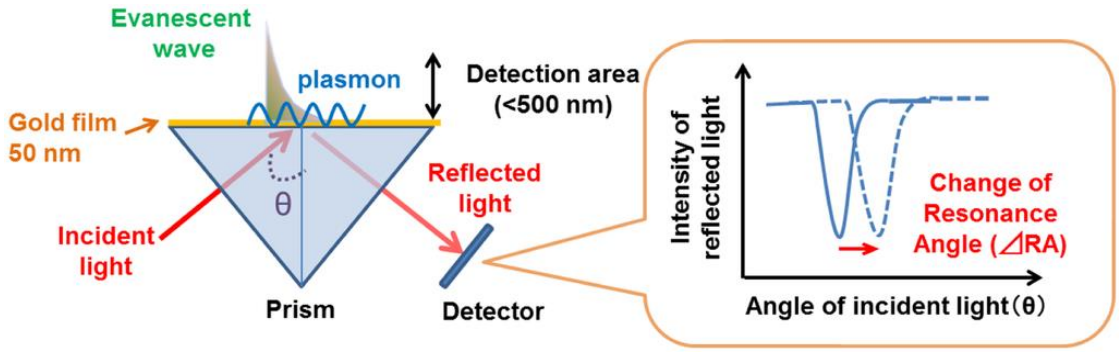

Figure 17. SPR based sensor principle.[96]

RIfS detects the changes in the thickness of a sensitive layer upon sorption/adsorption of the analyte. Upon interaction of the analyte molecules with the sensing layer, the film swells and the interference pattern is changed. These kind of sensors have been employed for the enantioselective detection of chiral inhalation anesthetics among others.[97]

Chiral sensors are a powerful tools which provide on-line analysis so useful in industrial processes control and in enantiomer screening. The employed transducer depends on the application for which it is used. Despite the fact of having in hand a broad combination of recognition elements with the appropriate transducers, the development of sensors based on the use of chiroptical spectroscopies is still a future challenge.

1.4. Outline

Our research group has developed the synthesis of new chiral containers, bearing ditertbutyldietynylallenes (DEAs) and also more recently spiranes as axially chiral motifs and different aromatic spacers, such as anthracene and differently substituted pyridines and bipyridines. The study of the chiroptical properties of these allenophanes has also been accomplished, in order to determine their structure-properties relation. Moreover, they have been employed in applications such as pH sensor and selective host for diiodoperfluoroalkanes. Thus, this thesis arises from the interest of broadening the range of chiral hosts, taking the leap to the next level of structural complexity, with the design of chiral cages (**Scheme 2**).

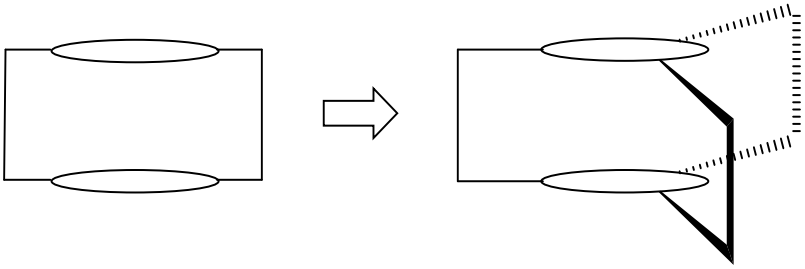

Scheme 2. Evolution from macrocycles to cages. Generic structures where the ellipses are the spacers and the branches connecting them contain the chiral moieties.

The general aims of this investigation are the design and synthesis of novel shape-persistent covalent organic helical cages with outstanding chiroptical properties, based on the coupling of axially chiral building blocks with C_3 symmetric aromatic cores. Besides, an additional goal is the performance of complexation studies both *in silico* as well as experimentally through NMR spectroscopy with a series of selected guests. Finally, the guests showing higher affinities for the covalent organic helical cages proposed will be tested as sensors employing chiroptical spectroscopic techniques in virtue of their outstanding chiroptical properties.

In **Chapter 1** a brief introduction to the world of molecular cages, chirality and sensing is given. Some of the main contents of this **Chapter 1** are the classification, advantages *vs* disadvantages, and some outstanding applications of molecular cages, going a bit more in depth in the case of the chiral purely organic ones. With respect to chirality, an explanation on the basis and types of chiroptical techniques is given, highlighting the most common axially chiral building blocks, and specially allenes. Finally, a broad stroke about the field of sensors is pointed out, emphasizing sensors bearing chiral recognition elements and the bibliography paucity concerning commercially available sensors based on chiroptical transducers.

Chapter 2 offers a discussion about why 1,3-diethynylallene (DEA) was chosen among the possible axially chiral building blocks and also about the final symmetry of the cages proposed and the importance of the shape persistency in order to achieve strong chiroptical responses. In addition, further discussion about the general strategy based on the synthetic sequence Cross

Coupling–Deprotection–Homodimerization (**Scheme 3**) is given together with an analysis of the use of the enantiopure DEA *vs* the use of the racemic mixture followed by separation of the stereoisomers. The second part of this **Chapter 2** deals with a short incursion into the world of Molecular Dynamics, as a result of a 2-month stay at the Technische Universität München (TUM) in Munich (Germany), in order to simulate the stability of several possible complexes between the first proposed molecular cage and diverse aromatic flat guests. This way a selection of the supposed as more appropriate guests was made, in order to test them experimentally on complexation studies.

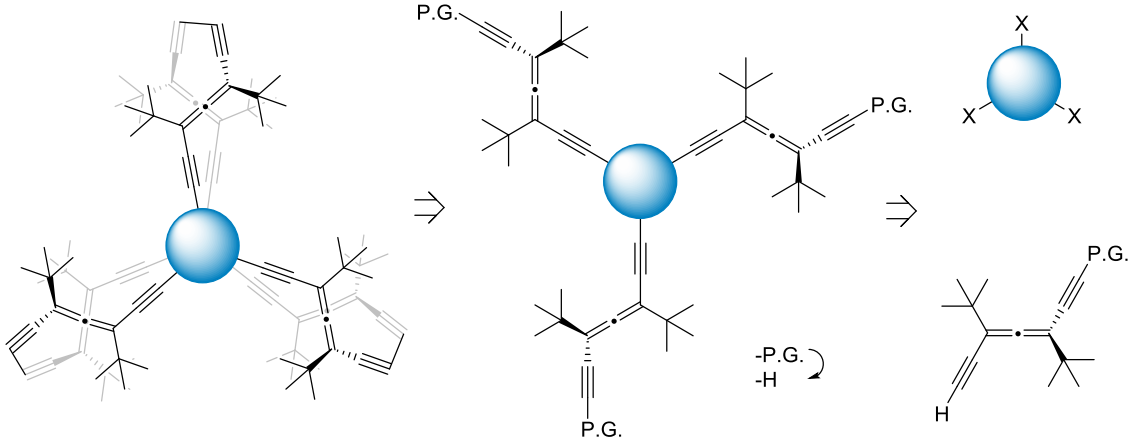

Scheme 3. Schematic retrosynthetic scheme of the molecular cages via triple coupling of the core (blue sphere) with three equivalents of enantiopure allene, followed by deprotection of the protecting groups, and finally homodimerization yielding the corresponding D_3 symmetric molecular cage.

In **Chapter 3** a detailed description and discussion of the experimental procedure on the synthesis and full characterization of the cage bearing a benzene core, $(P,P)_3$-**1H**, is given. As a continuation of the synthesis of this cage, several complexation studies with the guest candidates, chosen as a result of Molecular Dynamics studies performed in **Chapter 2**, were experimentally tested.

The success on the synthesis of the benzenic chiral cage paved the way for the design and synthesis of cages having different electronic character cores in **Chapter 4**. Three were the initial core proposals: a deficient 1,3,5-fluorinated benzenic core in cage $(P,P)_3$-**1F**, a slightly electron rich 1,3,5-methylated benzenic core in cage $(P,P)_3$-**1Me**, and an electron poor triazine core for cage $(P,P)_3$-**1N** (**Figure 18**). For $(P,P)_3$-**1Me** and also $(P,P)_3$-**1H** complexations with the sandwich compounds were probed by means of ^{1}H NMR spectroscopy, electronic circular dichroism (ECD), and mass spectrometry measurements.

In **Chapter 5** two novel cage structures were proposed, as a result of a 45-days stay at the Friedrich-Alexander Universität (FAU) in Erlangen (Germany). Cores here mentioned are based on N-heterotriangulenes, bigger flat aromatic molecules with well-defined redox properties having C_3 symmetry and containing an inner Nitrogen as heteroatom. Specifically, *N*-heterotriangulenes employed contain carbonyl and dimethylmethylene bridges, which would lead to the formation of molecular cages $(M,M)_3$-**1TCO** and $(M,M)_3$-**1TMe** respectively.

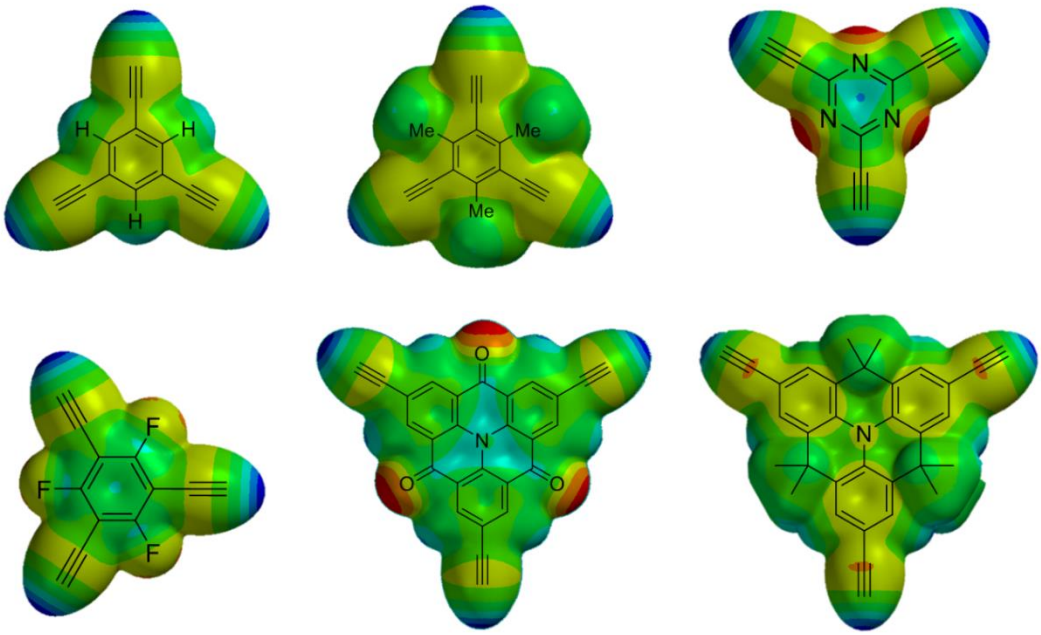

Figure 18. From left to right and from top to bottom: Structure of the cores of the proposed molecular cages coupled with three acetylene moieties superimposed with their corresponding electrostatic potential maps (*Spartan'14* V1.1.2). Benzene, methylated benzene, triazine, fluorinated benzene, carbonyl triangulene and methylated triangulene. Colors towards red indicate electron richness and color towards blue-green indicate electron poor regions.

Finally, **Chapter 6** accounts for all the experimental details of the cage molecules, as well as for the corresponding intermediates and some of the non-commercial guests. Characterizations in general make use of ^{1}H, ^{19}F, ^{13}C and two-dimensional NMR experiments, IR, UV-Vis and ECD spectroscopies, MS, and X-Ray crystallography.

1.5. References

[1] J. C. Barnes, M. Juríček, N. L. Strutt, M. Frasconi, S. Sampath, M. A. Giesener, P. L. McGrier, C. J. Bruns, C. L. Stern, A. A. Sarjeant, et al., *J. Am. Chem. Soc.* **2013**, *135*, 183–192.

[2] M. M. Conn, J. R. Jr., *Chem. Rev.* **1997**, *97*, 1647–1668.

[3] D. J. Cram, *Nature* **1992**, *356*, 29–36.

[4] C. J. Pedersen, *Science (80-.).* **1988**, *241*, 536–540.

[5] J.-M. Lehn, *Chem. Soc. Rev.* **2007**, *36*, 151–160.

[6] J. M. Rivera, T. Martín, J. Rebek, *J. Am. Chem. Soc.* **2001**, *123*, 5213–5220.

[7] O. Dumele, N. Trapp, F. Diederich, *Angew. Chem. Int. Ed.* **2015**, *54*, 12339–12344.

[8] R. Sure, S. Grimme, *Chem. Commun.* **2016**, *85*, 1711–1713.

[9] Gennady V. Oshovsky, David N. Reinhoudt, W. Verboom, *J. Am. Chem. Soc.* **2006**, *128*, 5270–5278.

[10] L. C. Palmer, J. Rebek, Jr., *Org. Biomol. Chem.* **2004**, *2*, 3051–3059.

[11] R. Wyler, J. de Mendoza, J. Rebek, *Angew. Chem. Int. Ed.* **1993**, *32*, 1699–1701.

[12] M. Fujita, K. Umemoto, M. Yoshizawa, N. Fujita, T. Kusukawa, K. Biradha, *Chem. Commun.* **2001**, *96*, 509–518.

[13] H. Takezawa, T. Murase, G. Resnati, P. Metrangolo, M. Fujita, *Angew. Chemie* **2015**, *127*, 8531–8534.

[14] B. M. Schmidt, T. Osuga, T. Sawada, M. Hoshino, M. Fujita, *Angew. Chem. Int. Ed.* **2016**, *55*, 1561–1564.

[15] T. Murase, M. Fujita, *Chem. Rec.* **2010**, *10*, 342–347.

[16] S. Du, T.-Q. Yu, W. Liao, C. Hu, *Dalton Trans.* **2015**, *44*, 14394–402.

[17] C. García-Simón, R. Gramage-Doria, S. Raoufmoghaddam, T. Parella, M. Costas, X. Ribas, J. N. H. Reek, *J. Am. Chem. Soc.* **2015**, *137*, 2680–2687.

[18] C. G. P. Taylor, J. R. Piper, M. D. Ward, *Chem. Commun.* **2016**, *52*, 6225–6228.

[19] N.-N. Liu, S. Song, D.-M. Li, Y.-S. Zheng, L. Pu, G. A. Hembury, V. V. Borovkov, Y. Inoue, A. Zehnacker, M. A. Suhm, et al., *Chem. Commun.* **2012**, *48*, 4908–4910.

[20] Y. Jin, Q. Wang, P. Taynton, W. Zhang, *Acc. Chem. Res.* **2014**, *47*, 1575–1586.

[21] Y. Jin, C. Yu, R. J. Denman, W. Zhang, *Chem. Soc. Rev.* **2013**, *42*, 6634–6654.

[22] K. S. Chichak, S. J. Cantrill, A. R. Pease, S.-H. Chiu, G. W. V Cave, J. L. Atwood, J. F. Stoddart, *Science (80-.).* **2004**, *304*, 1308–1312.

[23] C. D. Pentecost, K. S. Chichak, A. J. Peters, G. W. V. Cave, S. J. Cantrill, J. F. Stoddart, *Angew. Chem. Int. Ed.* **2007**, *46*, 218–222.

[24] N. Ponnuswamy, F. B. L. Cougnon, J. M. Clough, G. D. Pantoş, J. K. M. Sanders, *Science (80-.).* **2012**, *338*, 783–785.

[25] M. Mastalerz, *Angew. Chem. Int. Ed.* **2010**, *49*, 5042–5053.

[26] T. Friščić, *Chem. Soc. Rev.* **2012**, *41*, 3493–3510.

[27] M. E. Briggs, A. G. Slater, N. Lunt, S. Jiang, M. A. Little, R. L. Greenaway, T. Hasell, C. Battilocchio, S. V Ley, A. I. Cooper, *Chem. Commun.* **2015**, *51*, 17390–17393.

[28] S. Lefevre, D. Zhang, E. Godart, M. Jean, N. Vanthuyne, J.-C. Mulatier, J.-P. Dutasta, L. Guy, A. Martinez, *Chemistry* **2016**, *22*, 2068–2074.

[29] T. Hasell, M. Miklitz, A. Stephenson, M. A. Little, S. Y. Chong, R. Clowes, L. Chen, D. Holden, G. A. Tribello, K. E. Jelfs, et al., *J. Am. Chem. Soc.* **2016**, *138*, 1653–1659.

[30] H. Ding, Y. Yang, B. Li, F. Pan, G. Zhu, M. Zeller, D. Yuan, C. Wang, *Chem. Commun.* **2015**, *51*, 1976–1979.

[31] S.-M. Xie, J.-H. Zhang, N. Fu, B.-J. Wang, L. Chen, L.-M. Yuan, *Anal. Chim. Acta* **2016**, *903*, 156–163.

[32] A. Kewley, A. Stephenson, L. Chen, M. E. Briggs, T. Hasell, A. I. Cooper, *Chem. Mater.* **2015**, *27*, 3207–3210.

[33] J.-H. Zhang, S.-M. Xie, B.-J. Wang, P.-G. He, L.-M. Yuan, *J. Chromatogr. A* **2015**, *1426*, 174–182.

[34] J.-K. Sun, W.-W. Zhan, T. Akita, Q. Xu, *J. Am. Chem. Soc.* **2015**, *137*, 7063–7066.

[35] B. Mondal, K. Acharyya, P. Howlader, P. S. Mukherjee, *J. Am. Chem. Soc.* **2016**, *138*, 1709–1716.

[36] O. Gidron, M.-O. Ebert, N. Trapp, F. Diederich, *Angew. Chem Int. Ed.* **2014**, *53*, 13614–13618.

[37] S. Odermatt, J. L. Alonso-Gómez, P. Seiler, M. M. Cid, F. Diederich, *Angew. Chem. Int. Ed.* **2005**, *44*, 5074–5078.

[38] University of Liverpool, "Point Group Flow Chart," can be found under http://www.chemtube3d.com/SymHOME.htm, **n.d.**

[39] T. W. G. Solomons, C. B. Fryhle, S. A. Snyder, in *Org. Chem. (International Student Version)*, Wiley, **2013**.

[40] M. Schilthuizen, A. Davison, *Naturwissenschaften* **2005**, *92*, 504–515.

[41] A. Luque, D. Reguera, *Biophys. J.* **2010**, *98*, 2993–3003.

[42] "Zarcillo - Wikipedia, la enciclopedia libre," can be found under https://es.wikipedia.org/wiki/Zarcillo, **n.d.**

[43] Pinterest, "Snail," can be found under https://es.pinterest.com/pin/511228995172492273/, **n.d.**

[44] W. W. C. (William W. C. Topley, G. S. (Graham S. Wilson, L. H. (Leslie H. Collier, A. Balows, M. Sussman, *Topley and Wilson's Microbiology and Microbial Infections. Volume 1: Virology*, Arnold, **1998**.

[45] J. D. Carroll, *Chirality* **2009**, *21*, 354–358.

[46] Ryan R. Julian, Sunnie Myung, D. E. Clemmer, *J. Phys. Chem. B* **2005**, *109*, 440–444.

[47] A. Shockravi, A. Javadi, E. Abouzari-Lotf, *RSC Adv.* **2013**, *3*, 6717–6746.

[48] W. Ten Hoeve, H. Wynberg, *J. Org. Chem.* **1979**, *44*, 1508–1514.

[49] L. K. Smith, I. R. Baxendale, *Org. Biomol. Chem.* **2015**, *13*, 9907–9933.

[50] G. P. Moss, P. A. S. Smith, D. Tavernier, *Pure Appl. Chem.* **1995**, *67*, 1307–1375.

[51] J. H. Van't Hoff, *Arch. néerlandaises des Sci. exactes Nat.* **1874**, *9*, 445–454.

[52] E. Soriano, I. Fernández, *Chem. Soc. Rev.* **2014**, *43*, 3041–3105.

[53] V. Prelog, G. Helmchen, *Angew. Chem. Int. Ed.* **1982**, *21*, 567–583.

[54] A. Hoffmann-Röder, N. Krause, *Angew. Chem. Int. Ed.* **2004**, *43*, 1196–1216.

[55] W. D. Celmer, I. A. Solomons, *J. Am. Chem. Soc.* **1952**, *74*, 1870–1871.

[56] S. Yu, S. Ma, *Angew. Chem. Int. Ed.* **2012**, *51*, 3074–3112.

[57] M.-H. Lin, W.-S. Tsai, L.-Z. Lin, S.-F. Hung, T.-H. Chuang, Y.-J. Su, *J. Org. Chem.* **2011**, *76*,

8518–8523.

[58] R. Barlet, Y. Vo-Quang, *Bull. Soc. Chim. Fr.* **1969**, 3729–3760.

[59] H. Kurata, M. Monden, T. Kawase, M. Oda, *Tetrahedron Lett.* **1998**, *39*, 7135–7138.

[60] G. Wittig, A. Haag, *Chem. Ber.* **1963**, *96*, 1535–1543.

[61] W. von E. Doering, P. M. LaFlamme, *Tetrahedron* **1958**, *2*, 75–79.

[62] W. R. Moore, H. R. Ward, *J. Organomet. Chem.* **1962**, *25*, 4179–4181.

[63] L. Skatteböl, *Tetrahedron Lett.* **1961**, *2*, 167–172.

[64] C. E. Janßen, N. Krause, *Eur. J. Org. Chem.* **2005**, *2005*, 2322–2329.

[65] Y. M. Slobodin, A. P. Khitrov, *J. Gen. Chem. USSR* **1961**, *31*, 3680–3681.

[66] H. Gilman, R. A. Tomasi, *J. Org. Chem.* **1962**, *27*, 3647–3650.

[67] R. BOLZE, H. EIERDANZ, K. SCHLUETER, W. MASSA, W. GRAHN, A. BERNDT, *Chem. Inform.* **1983**, *14*, DOI 10.1002/chin.198310067.

[68] J. Lorenzo Alonso-Gómez, Yolanda Pazos, Armando Navarro-Vázquez, Johan Lugtenburg, M. Magdalena Cid, *Org. Lett.* **2005**, *7*, 3773–3776.

[69] M. Ogasawara, H. Ikeda, T. Hayashi, *Angew. Chem. Int. Ed.* **2000**, *39*, 1042–1044.

[70] G. A. Molander, E. M. Sommers, S. R. Baker, *J. Org. Chem.* **2006**, *71*, 1563–1568.

[71] A. Christian, A. Jutand, *Acc. Chem. Res* **2000**, *33*, 314–321.

[72] R. Livingston, L. R. Cox, S. Odermatt, F. Diederich, *Helv. Chim. Acta* **2002**, *85*, 3052–3077.

[73] S. Thorand, F. Vögtle, N. Krause, *Angew. Chem. Int. Ed.* **1999**, *38*, 3721–3723.

[74] I. R. Lahoz, A. Navarro-Vázquez, A. L. Llamas-Saiz, J. L. Alonso-Gómez, M. M. Cid, *Chem. - A Eur. J.* **2012**, *18*, 13836–13843.

[75] S. Castro-Fernández, I. R. Lahoz, A. L. Llamas-Saiz, J. L. Alonso-Gómez, M.-M. Cid, A. Navarro-Vázquez, *Org. Lett.* **2014**, *16*, 1136–1139.

[76] I. R. Lahoz, S. Castro-Fernández, A. Navarro-Vázquez, J. L. Alonso-Gómez, M. Magdalena Cid, *Chirality* **2014**, *26*, 563–573.

[77] P. Rivera-Fuentes, J. L. Alonso-Gómez, A. G. Petrovic, F. Santoro, N. Harada, N. Berova, F. Diederich, *Angew. Chem. Int. Ed.* **2010**, *49*, 2247–2250.

[78] J. L. Alonso-Gómez, P. Rivera-Fuentes, N. Harada, N. Berova, F. Diederich, *Angew. Chem. Int. Ed.* **2009**, *48*, 5545–5548.

[79] S. Allenmark, J. Gawronski, *Chirality* **2008**, *20*, 606–608.

[80] K. Nakanishi, N. Berova, P. L. Polavarapu, R. W. Woody, *Comprehensive Chiroptical Spectroscopy, Volume 1, Instrumentation, Methodologies, and Theoretical Simulations*, Wiley-VCH Verlag GmbH & Co. KGaA, Weinheim, Germany, **2013**.

[81] R. S. Walters, C. M. Kraml, N. Byrne, D. M. Ho, Q. Qin, F. J. Coughlin, S. Bernhard, J. Robert A. Pascal, *J. Am. Chem. Soc.* **2008**, *130*, 16435–16441.

[82] R. M. Pearlstein, R. C. Davis, S. L. Ditson, *Proc. Natl. Acad. Sci. U. S. A.* **1982**, *79*, 400–

402.

[83] C. Gautier, T. Bürgi, *ChemPhysChem* **2009**, *10*, 483–492.

[84] Gabriel Shemer, Olga Krichevski, Gil Markovich, Tatiana Molotsky, Irit Lubitz, Alexander B. Kotlyar, *J. Am. Chem. Soc.* **2006**, *128*, 11006–11007.

[85] W. Chen, A. Bian, A. Agarwal, L. Liu, H. Shen, L. Wang, C. Xu, N. A. Kotov, *Nano Lett.* **2009**, *9*, 2153–2159.

[86] I. Lieberman, G. Shemer, T. Fried, E. M. Kosower, G. Markovich, *Angew. Chem. Int. Ed.* **2008**, *47*, 4855–4857.

[87] T. Molotsky, T. Tamarin, A. Ben Moshe, G. Markovich, A. B. Kotlyar, *J. Phys. Chem. C* **2010**, *114*, 15951–15954.

[88] A. Guerrero-Martínez, B. Auguié, J. L. Alonso-Gómez, Z. Džolić, S. Gómez-Graña, M. Žinić, M. M. Cid, L. M. Liz-Marzán, *Angew. Chem. Int. Ed.* **2011**, *50*, 5499–5503.

[89] K. Manoli, M. Magliulo, L. Torsi, Springer International Publishing, **2013**, pp. 133–176.

[90] A. A. Rat'ko, R.-I. Stefan, J. K. F. van Staden, H. Y. Aboul-Enein, *Talanta* **2004**, *63*, 515–519.

[91] Y. Chen, L. Chen, R. Bi, L. Xu, Y. Liu, *Anal. Chim. Acta* **2012**, *754*, 83–90.

[92] J. Huang, Z. Wei, J. Chen, *Sensors Actuators B Chem.* **2008**, *134*, 573–578.

[93] L. C. Clark, C. Lyons, *Ann. NY Acad. Sci.* **1962**, *102*, 29–45.

[94] T. Nakanishi, N. Yamakawa, T. Asahi, N. Shibata, B. Ohtani, T. Osaka, *Chirality* **2004**, *16*, S36–S39.

[95] J.-M. Ha, A. Solovyov, A. Katz, *Langmuir* **2009**, *25*, 153–158.

[96] Y. Yanase, T. Hiragun, K. Ishii, T. Kawaguchi, T. Yanase, M. Kawai, K. Sakamoto, M. Hide, *Sensors* **2014**, *14*, 4948–4959.

[97] Birgit Kieser, Christopher Fietzek, Roswitha Schmidt, Georg Belge, Udo Weimar, Volker Schurig, Günter Gauglitz, *Anal. Chem.* **2002**, *74*, 3005–3012.

2. Design of Covalent Organic Helical Cages from Chiral Axes

The sensitivity of chiroptical responses to conformational changes[1] and supramolecular interactions[2] along with the ability of molecular containers to give rise to molecular recognition processes,[3] entails the need to design chiral cages. In order to be useful for sensing applications, these molecular containers should present strong chiroptical responses. Since conformational freedom may considerably diminish the chiroptical responses through partial cancelation between different conformations,[1] shape-persistency is desired when designing systems to present strong chiroptical responses.[4]

A clear example of structural rigidity are polyhedra (**Figure 1**), composed by flat faces, which define a finite volume. Such structures comply with Euler's law, which postulates that the number of vertices (V) plus the number of faces (F) is equal to the summation of the number of edges (E) plus two (V + F = E + 2).[5]

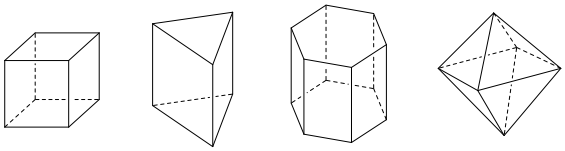

Figure 1. Examples of common polyhedra. From left to right: cube, triangular prism, hexagonal prism, and octahedron.

Polyhedra are not just mere mathematical geometries used in art and architecture, but they are also present in nature. Examples of natural polyhedral structures are the capsids of many viruses,[6] outer shell of carboxysomes,[7] the honeycombs, and the structure of many proteins (**Figure 2**).[8]

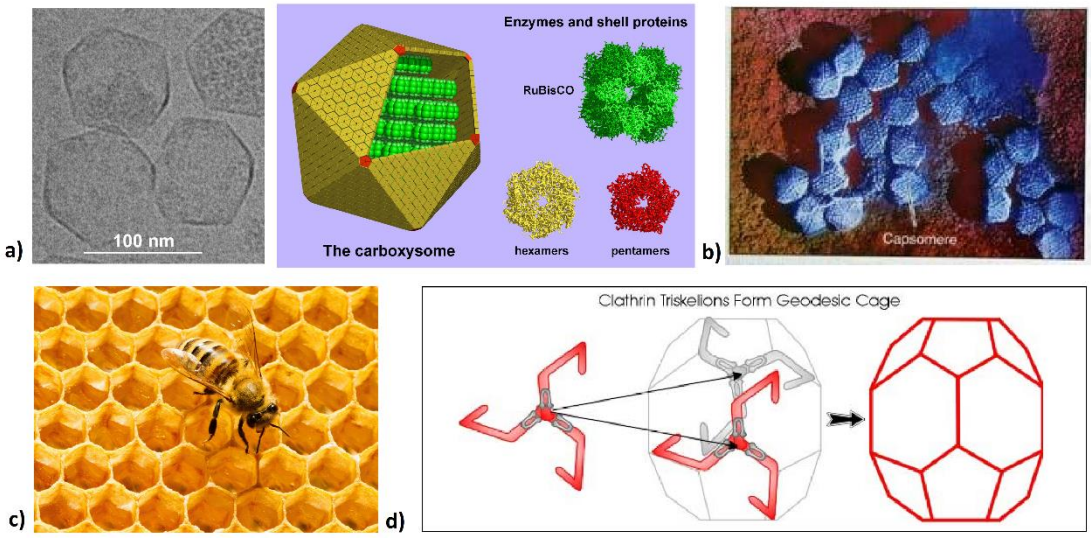

Figure 2. a) Icosahedral carboxysome (bacterial organelle) structure: micrography (left) and schematic representation (right). b) Icosahedral *Mastadenovirus*, responsible of respiratory, intestinal and eye infections in humans, mammals and diverse vertebrates. c) Honeycomb structure composed of laterally fused hexagonal prisms. d) Self-assembled cage of clathrins (proteins involved in the formation of coated vesicles during the endo- and exocytosis) in the soccer-ball configuration (right) and constitutive triskelion monomer model (left).[8]

Scientists, in their investigative zeal, have designed numerous polyhedral molecular cages, mainly for its use in molecular recognition processes, cataloging their structural motifs in terms of their resemblance to Platonic, Archimedean, prismatic, antiprismatic, and irregular solids.

2.1. Design of the Structure of Covalent Organic Helical Cages from chiral axes

Most of the synthetic cages have organometallic nature, due to the high directionality of the metal-ligand bond, which simplifies their mechanism of assembly. Among organometallic polyhedra there is a broad variety of applications related with the presence of a specific metal, and/or just their geometric features, as for example in the case where they act as complements of biological receptors (**Figure 3**).[9–13] Supramolecular assemblies occupy the second position, with the hydrogen bonding as the main supramolecular interaction holding such polyhedral together.[14] Regarding the purely organic molecular cages,[15] they tend to be more flexible than the metallorganic ones, constituting their syntheses in a shape-persistent manner a great challenge.

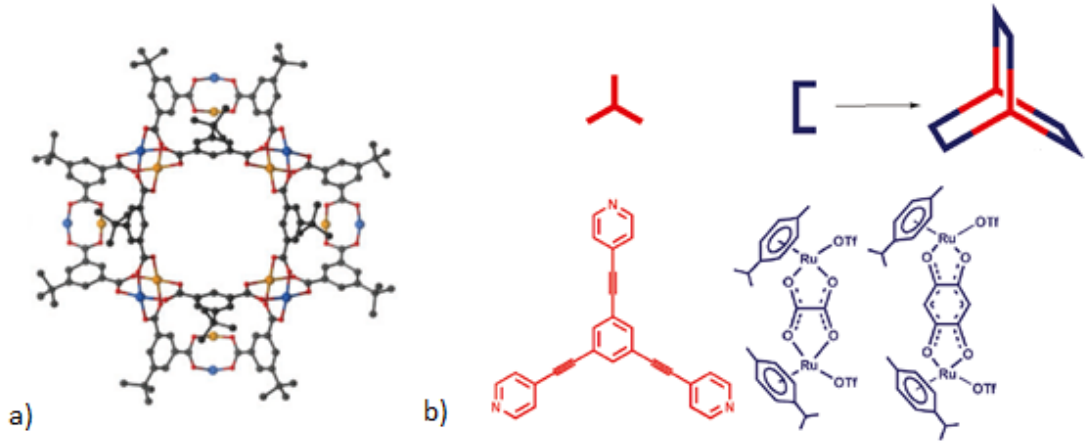

Figure 3. a) Hetero-bimetallic metal–organic polyhedral molecular cage with hydrogen absorption ability.[9] b) Trigonal prism metal–organic cage for fluorescence detection of nitroaromatics.[10]

A particular case of polyhedra are the *n*-prisms, which bear two identical parallel *n*-polygonal faces linked by *n* sides. These bear *n* perpendicular C_2 axes to the main C_n axis, which simplifies their structures, allowing them to be built from a dimerization process of two equal halves. It should be pointed out that all *n*-prisms belong to the achiral point group D_{nh}, therefore, in search of a chirality also at the structural level, the introduction of a twist in such structure around the main axis, rotating both parallel bases in opposite directions, would remove the horizontal plane, belonging, from then on, to the chiral point group D_n (**Scheme 1**).

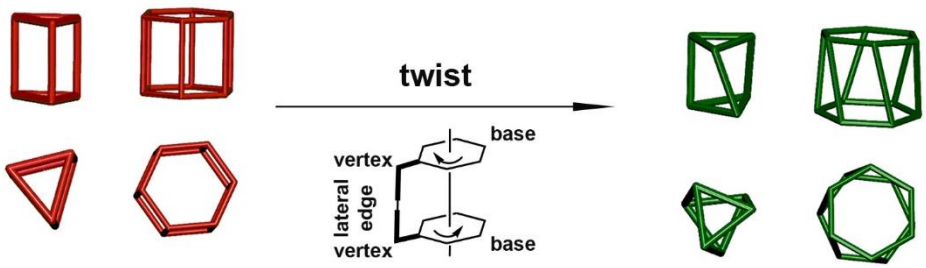

Scheme 1. From left to right: trigonal and hexagonal *n*-prisms, *n* is the number of lateral edges. Red prisms belonging to the point group D_{nh}, and green prisms belonging to the point group D_n. From top to bottom: side and top view of the *n*-prisms.

The simplest twisted *n*-prism is the one with *n* = 3, called twisted trigonal prism. Thus, the design of molecular cages with the shape of twisted trigonal prisms is proposed. As bases of them C_3 symmetric flat cores are proposed. Coupling of these with three equivalents of axially chiral moieties will give rise to tripodal-shaped structures. Such tripodal constructions will lead to the formation of the chiral molecular cages after a homodimerization process, in which the vertices are constituted by the chiral axes (**Scheme 2**).

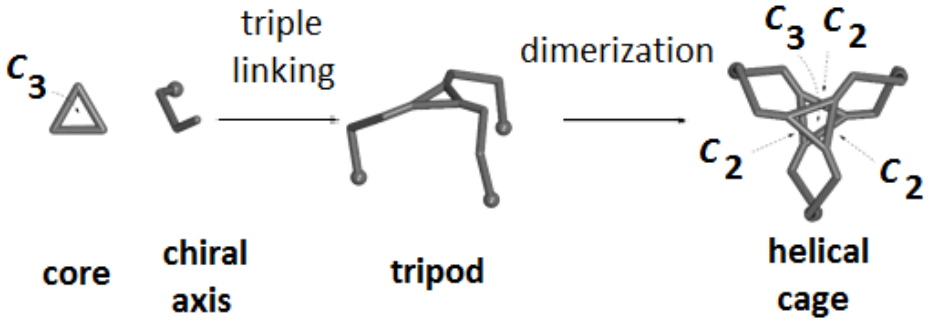

Scheme 2. Schematic representation of the synthetic strategy to build molecular chiral cages.

For the *n*-prism to be twisted, thus bearing a helical structure, coupled chiral axes must present the same chirality, both (*P*), or both (*M*). Homodimers with (*P,P*) or (*M,M*) configuration contain one writhe (W, a structure crosses over itself),[16] with W = 1 and W = –1 respectively, defining a particular torsion angle θ between the two chiral axes. However, formation of (*P,M*) heterodimers leads necessarily, for any torsion angle, to an object with zero writhes, W = 0, which is achiral (**Scheme 3**).

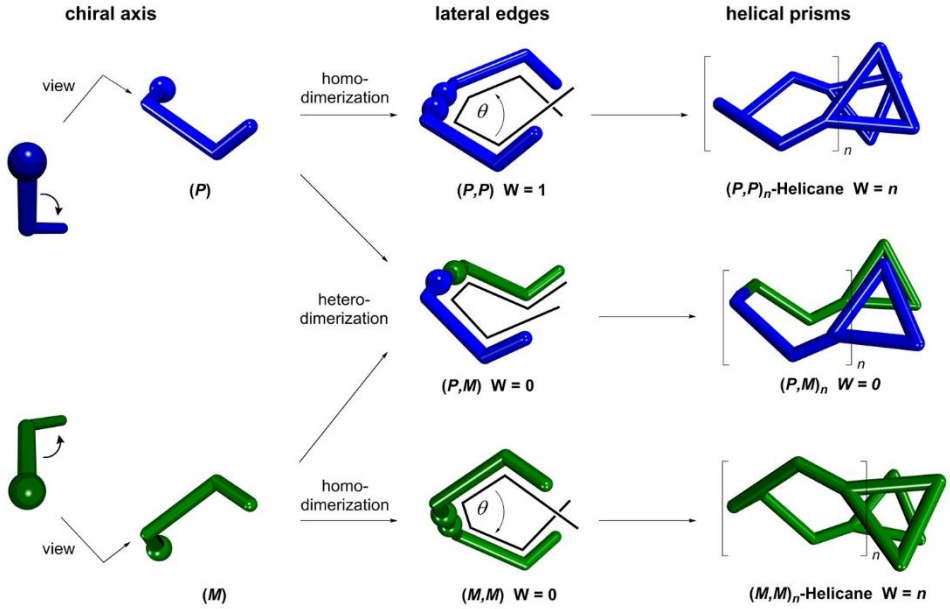

Scheme 3. General strategy to form helical prisms. (*P*) Axially chiral elements depicted in blue and (*M*) axially chiral elements in green. Homodimerization (*P,P*)/(*M,M*) forming a writhe and heterodimerization (*P,M*) forming no white, and thus bearing a plane of symmetry, which will lead to an achiral structure. Triangular structures represent the C_3 symmetric bases of the triangular prism.

A particular set of *n*-polygonal bases and rigid chiral axes will permit the construction of a helical prism with defined height and width. Therefore, following this general design strategy we may gain access to a wide variety of helical cages.

2.2. Synthetic approach: enantiopure vs racemic chiral axes

Many different strategies can be outlined on the synthesis of chiral molecular cages. On the one hand, the most direct and efficient strategy is based on the use of achiral precursors, which react among themselves, giving rise to chiral architectures either spontaneously or in the presence of a chiral reagent or catalyst.[17,18] Despite its efficiency, the control of the stereoselectivity is still nowadays a nontrivial issue to achieve. On the other hand, racemic precursors can be employed for achieving a diastereomeric set of molecular cages, some of them being chiral, some others not. However, such strategy presents the disadvantage of requiring a tedious subsequent separation of diastereoisomers, employing expensive chiral stationary phases and time-consuming trial and error procedures on the search of the separation ideal conditions.[19] A third alternative strategy is based on the use of enantiopure starting material, followed by the molecular cage formation. Such strategy gives rise to the formation of just one chiral enantiomer, as long as the reaction conditions do not result in racemization. In order to illustrate the different results expected by the above second and third explained strategies, it was carried out the distribution of diastereoisomers formed, using a racemic mixture of axially chiral building blocks on the proposed three-step strategy, based on a triple coupling with an C_3 aromatic core, triple deprotection of such tripodal-shaped molecule, and homodimerization of two trisdeprotected tripods.

The first step, based on the triple coupling of a racemic mixture of chiral axes with a C_3-symmetric core, gives rise to 4 different tripodal-shaped molecules with different configurations, having the homochiral ones (configurations bearing just one enantiomer), (*P*,*P*,*P*) and (*M*,*M*,*M*), a 12.5% population, while heterochiral ones (configurations bearing a combination of both enantiomers), (*P*,*P*,*M*) and (*P*,*M*,*M*), have a 37.5% of population, which arise from combining the two enantiomers (*P*)/(*M*) in sets of three with possibility of repetition, not taking into account the order of the elements (**Equation 1**) (**Scheme 4**).[20]

$$\binom{r+n-1}{r} = \frac{(r+n-1)!}{r! \cdot (n-1)!} = \frac{(3+2-1)!}{3! \cdot (2-1)!} = 4$$

Equation 1. Number of combinations of *n* elements in groups of *r* with repetition allowed, where the order does not matter.[20]

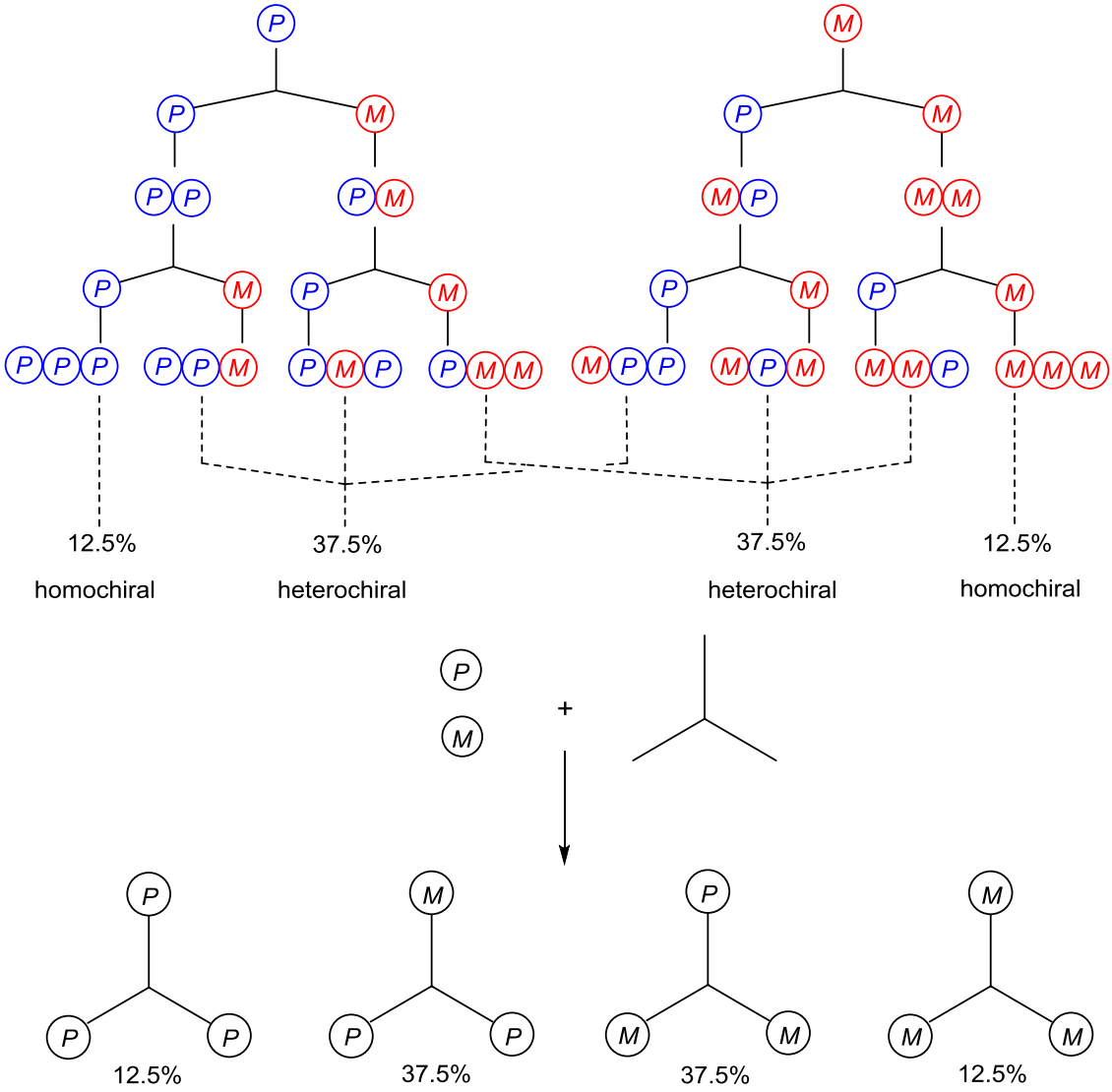

Scheme 4. Combination of two elements, (*P*) and (*M*), in threes (tripods) to give 8 tripods, three and another three of them being equivalent, resulting in 4 different tripods, the homochiral ones (*P,P,P*) and (*M,M,M*) with populations of 12.5% each (100%/8), while the heterochiral ones (*P,P,M*) and (*M,M,P*) have populations of 37.5% each (3 times 12.5%).

On a second step the tripods are combined in pairs between themselves in a dimerization process giving rise to 16 different configurations (**Scheme 5**, **Figure 4**). Each combination of two tripods in which one of them is homochiral, gives rise to a single diastereoisomer (**Scheme 5**, **Figure 4**, **a**-**g**). However, when the combination takes place between two heterochiral tripods, the rotation of one tripod with respect to the other around the C_3 axis of the core gives rise to three different diastereoisomers (**Scheme 5**, **Figure 4**, **h**-**p**).

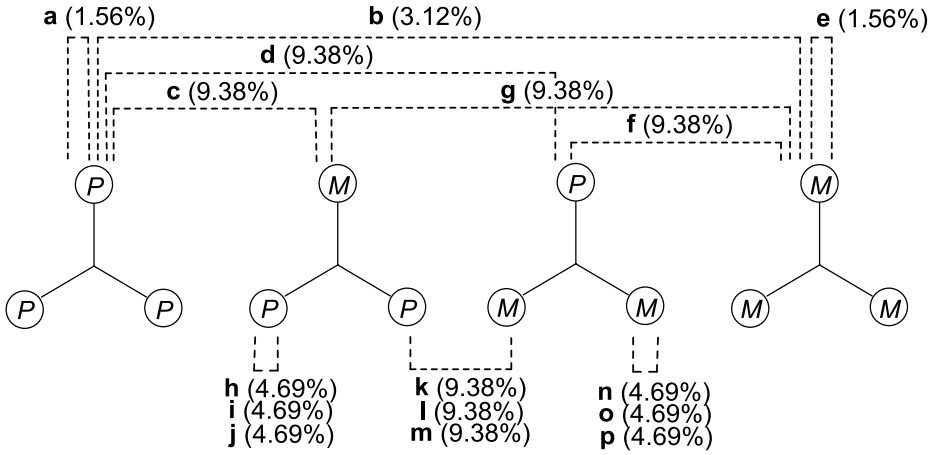

$P_c = P_{(P,P,P)+(P,P,M)} + P_{(P,P,M)+(P,P,P)} =$
$=12.5\% \cdot 37.5\% + 37.5\% \cdot 12.5\% =$
$= 4.69\% + 4.69\% = 9.38\%$

$P_k = (P_{(P,P,M)+(M,M,P)} + P_{(M,M,P)+(P,P,M)})/3 =$
$= (37.5\% \cdot 37.5\% + 37.5\% \cdot 37.5\%)/3 =$
$= (14.06\% + 14.06\%)/3 = 9.38\%$

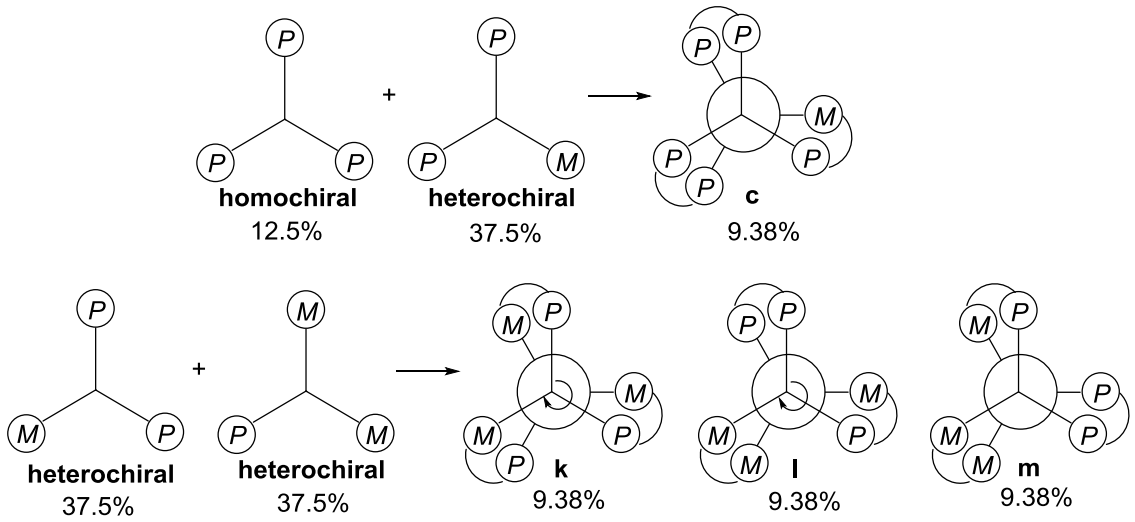

Scheme 5. Combination of tripods in pairs. Top: All possible tripod combinations with statistical probability of each configuration. Bottom: Example of combination of a homochiral with a heterochiral tripod affording **c** *vs* combination of two heterochiral tripods affording **k**, **l**, and **m**, along with examples of probability calculation for configurations **c** and **k**. Curved arrows (bottom) indicate a clockwise rotation of the tripod in the back, originating the next configuration.

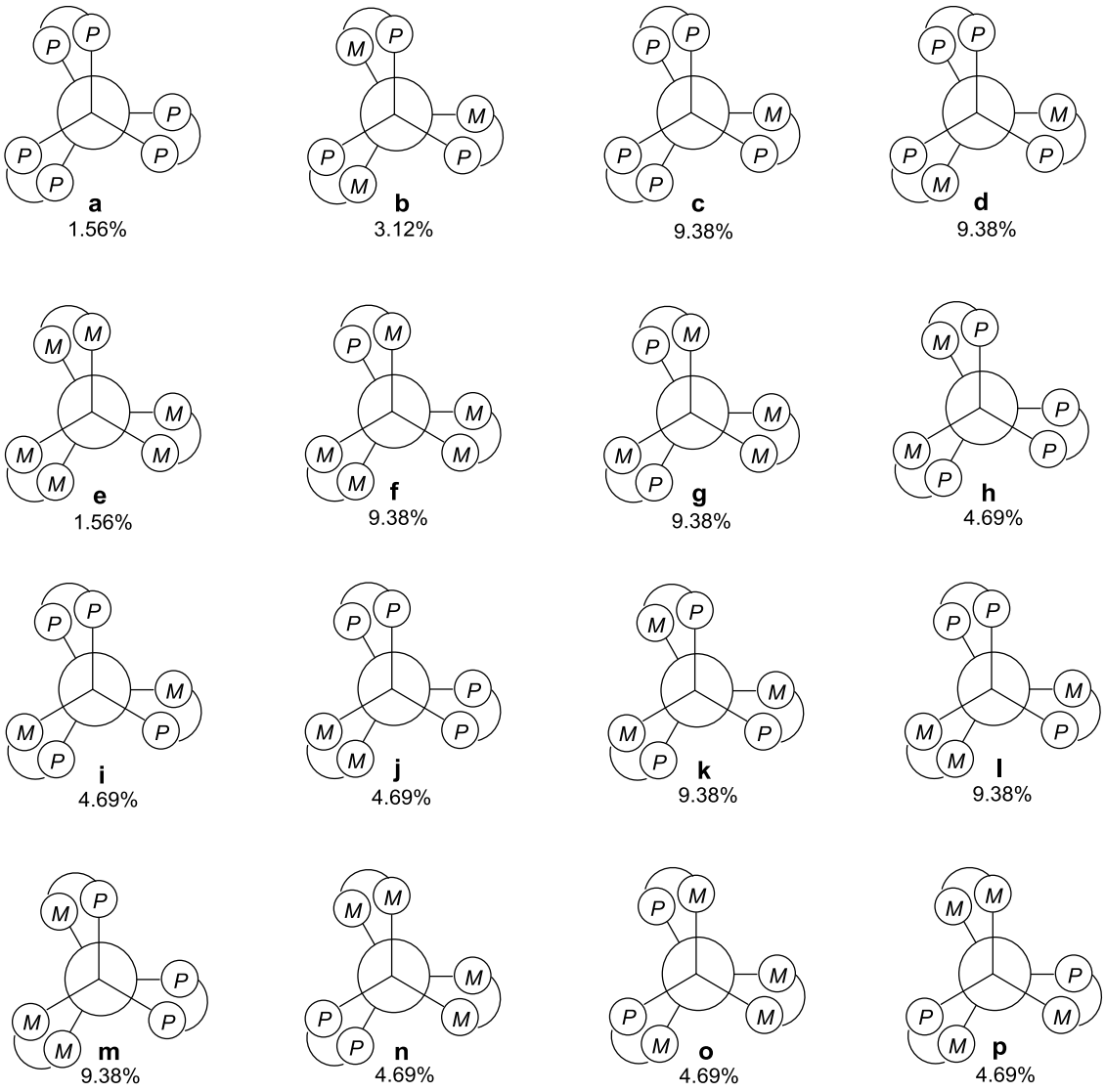

Figure 4. Representation of the 16 diastereoisomers formed from the combination of the 4 tripods in pairs.

In particular, to illustrate the synthesis of covalent organic helical cage (*P,P,P*)$_2$-**1H** along with the analysis of its corresponding diastereoisomers, ditertbutyldiethynylallenes (**DEAs**) as chiral axes and a 1,3,5-trihalosubstituted benzene as the core are used. (*P*)-**DEA-OH** has been chosen due to its chemical stability, chiral properties, and shape-persistency, whilst the aromatic core presents the required C_3 symmetry for the tripodal-shaped molecules. On a first step a coupling between 3 equivalents of (*P*)-**DEA-OH** and the trihalosubstituted core takes place yielding the tricoupled product (*P,P,P*)-**2H**, which after deprotection gives the trisdeprotected molecule (*P,P,P*)-**3H**. Homocoupling of 2 units of (*P,P,P*)-**3H** gives rise to the desired final molecular cage (*P,P,P*)$_2$-**1H**, which can be also labeled by linguistic economy as (*P,P*)$_3$-**1H**, referring to the three homochiral branches linking both aromatic cores (**Scheme 6**).

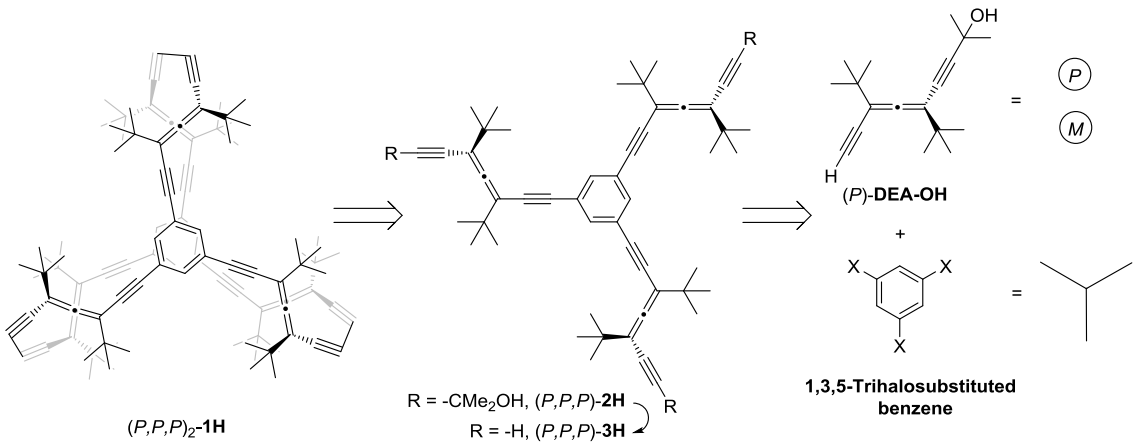

Scheme 6. Retrosynthetic scheme of $(P,P,P)_2$-**1H**.

Thus, following the general process of tripods combination in order to achieve molecular cage **1H** starting from the racemic (±)-**DEA-OH**, gave rise to 16 different configurations, as the general ones presented in **Figure 4** (**Figure 5**). Besides that, all the possible configurations were classified in terms of stereochemistry into chiral or achiral, providing the point group which they belong to, along with the statistical population for each stereoisomer, and its electronic energy at the AM1 level of theory. It was found that 2 of the 16 configurations, **b** and **m**, presenting C_{3h} and C_s symmetries respectively, resulted to be achiral.

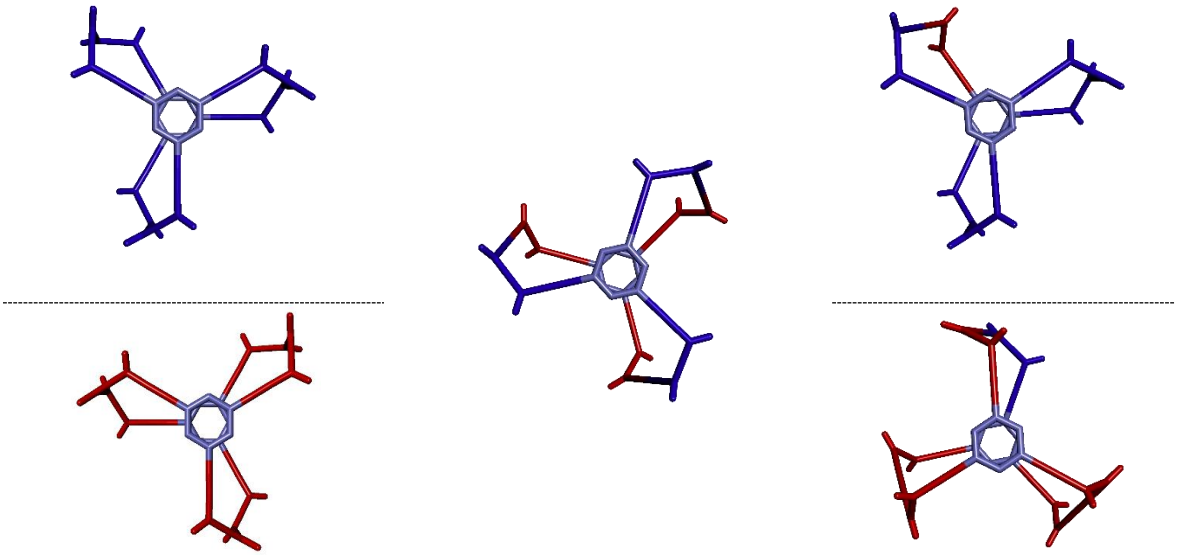

a: $(P,P,P)_2$-**1H** (1.56%) // **e**: $(M,M,M)_2$-**1H** (1.56%) D_3 chiral	**b**: $(P,P,P{-}M,M,M)$-**1H** (3.12%) C_{3h} achiral	**c**: $(P,P,P{-}P,P,M)$-**1H** (9.38%) // **f**: $(M,M,M{-}M,M,P)$-**1H** (9.38%) C_1 chiral

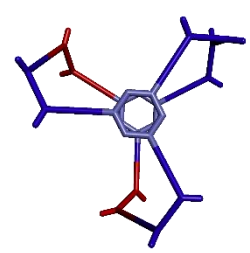

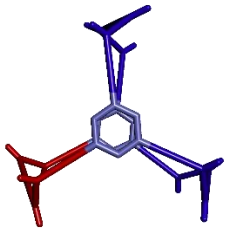

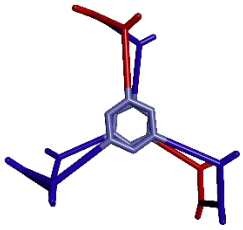

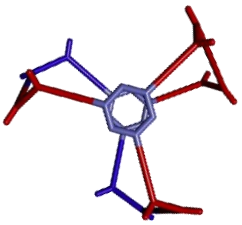

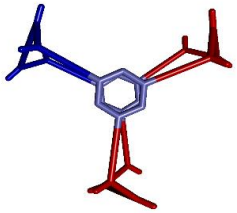

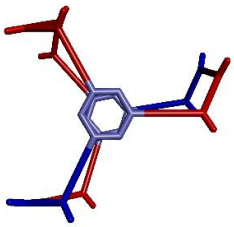

d: (*P,P,P*–*M,M,P*)-**1H** (9.38%) //
g: (*M,M,M*–*P,P,M*)-**1H** (9.38%)
C_1 chiral

h:(*P,P,M*–*P,P,M*)-**1H** (4.69%) //
n: (*M,M,P*–*M,M,P*)-**1H** (4.69%)
C_2 chiral

i: (*P,P,M*–*M,P,P*)-**1H** (4.69%)
// **o**: (*M,M,P*–*P,M,M*)-**1H**
(4.69%)
C_2 chiral

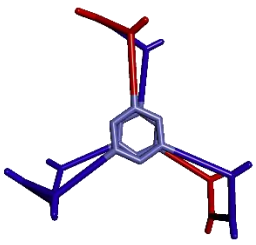

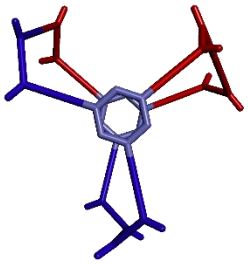

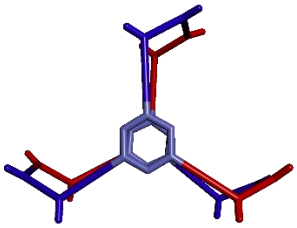

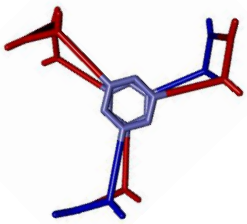

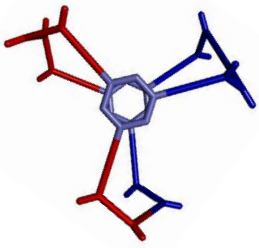

j: (*P,P,M*–*P,M,P*)-**1H** (4.69%) //
p: (*M,M,P*–*M,P,M*)-**1H** (4.69%)
C_2 Chiral

k: (*P,P,M*–*P,M,M*)-**1H** (9.38%) //
l: (*M,M,P*–*M,P,P*)-**1H** (9.38%)
C_1 Chiral

m: (*P,P,M*–*M,M,P*)-**1H**
(9.38%)
C_s achiral

Figure 5. Top views of the 16 possible configurations along with point groups. Benzene cores (gray), (*P*)-**DEA** (blue), (*M*)-**DEA** (red). Labels: correlate with representation in Figure 4. Hydrogens omitted and ^{t}Bu groups replaced by Me for clarity.

All structures were optimized al the AM1 level of theory presenting electronic energy differences below 1 kcal/mol, therefore no differences between the experimental and statistical diastereoisomeric distribution are expected.

The expected very low amount of the desired pair of enantiomers (*P,P,P*)$_2$-**1H** / (*M,M,M*)$_2$-**1H** when using the racemic allene, reinforced the idea of using enantiopure allenes as starting material, therefore, resolving the (±)-**DEA-OH** racemate by means of HPLC with a semipreparative Chiralpak IA chiral column, and then proceeding to couple them to the 1,3,5-trisubstituted benzene. The subsequent homodimerization of homochiral tripods will give rise to just one homochiral enantiomer, which needs no further chiral resolution.

2.3. Molecular Dynamics (MD) assisted host and guest design tailored to the application

The proposed COHC (*P,P*)$_3$-**1H** is envisaged as chiral agent in two different applications. The first one is as recognition element for host–guest applications in solution as an individual system. The second one is based on the formation of organized chiral 2D networks, which can be accomplished by following two different strategies. On the one hand, the direct interaction between (*P,P*)$_3$-**1H** derivatives bearing moieties capable of interacting between themselves through supramolecular interactions. An example of that is the functionalization, either laterally or on the lids of the cage, with groups such as alcohols or carboxylic acids that would form hydrogen bonded dimers (**Figure 6a**). On the other hand we propose the formation of a host–guest complex, followed by either the interaction between encapsulated guests or the interaction of encapsulated guests with a linker (**Figure 6b**).

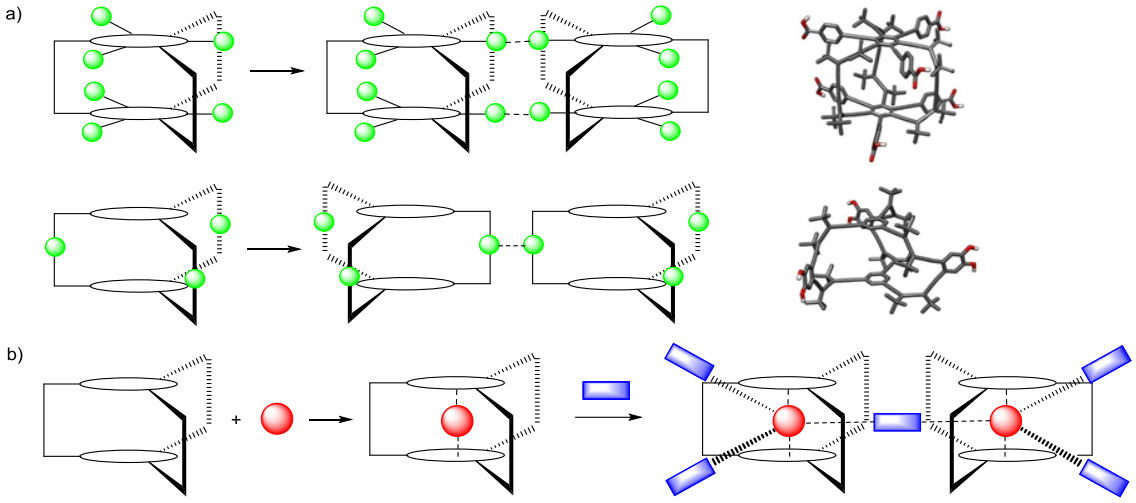

Figure 6. 2D networks formation. a) Derivatization of the cage. Green spheres indicate the derivatization location. Example of carboxylic acid (top) and catechol (bottom). b) Formation of host–guest complex (guest = red spheres) followed by interaction between complexes through linkers (blue rectangles).

Owing to its lower synthetic cost, the strategy based on the complex formation followed by interaction through linkers is chosen. In order to first check the viability of both applications, both host–guest in solution and 2D network formation, the use of Molecular Dynamics (MD)

simulations is postulated as a time− and source−saver tool. Thus, MD simulations were employed on the determination of the most suitable guests for both applications.

To this regard, Molecular Dynamics (MD) simulations have been broadly applied on the host−guest field. MD has accomplished such diverse functions as assisting the interpretation of thermodynamic parameters obtained experimentally,[21] investigating host−guest complex structures in solution,[22–24] estimating the binding free energy of the studied complexes,[25] sampling the energetically favored conformations of the hosts,[26] identifying binding/release mechanisms,[27] finding/predicting appropriate guests for a potential hosts,[28] and studying reorientational dynamics of guests inside the host[29] among others.

MD is a computer-assisted simulation method through which to obtain the physical properties of a model, which tries to imitate as much as possible a real system, by calculating and further analyzing the trajectories of their atoms or constituent molecules.[30] These atoms or molecules are allowed to interact for a defined period of time, giving rise to the evolution of the system. Forces between the particles and their potential energies are calculated using interatomic potentials or molecular mechanics force fields and the positions are obtained by numerically solving differential equations of motion, connecting positions over time.

The method was originally conceived within theoretical physics in the late 1950s and early 1960s[31] but is applied today mostly in materials science and the modeling of biomolecules by using numerical methods. First MD simulation of a biological process, which was published in Nature in 1976,[32] set a precedent on the use of MD for understanding essential protein motion.

The first objective of a MD simulation is to generate molecular trajectories over a finite period of time. Trajectories includes not only positions but also molecular momenta, which also change after interaction with another atoms. Thus, time-dependent momentum vectors $\mathbf{p}_i(t)$ are also achieved. Trajectories must be non-recurrent, lacking a region through which they pass periodically, since one of the conditions for a MD time period to be reliable is that, during the simulation, particles should sample a representative portion of the available space. Thus the motion cannot be periodic. If the simulation is started from an arbitrary set of initial conditions, the system should evolve to an equilibrium state.

There are some rules to take into account in MD concerning time and energy. One of them is that sampling time must be equal to several multiples of the relaxation time for the property to determine. On the other hand, for identifying the equilibrium situation, one must be on the constant-energy surface and, moreover, the entropy of the system must be a maximum.

MD typically deal with systems containing from hundred to thousand atoms. Such small systems are dominated by surface effects, interactions of the atoms with the container walls. In simulations in which these surface effects are not of interest, they are removed by using periodic boundary conditions (pbc).

When using pbc in a simulation of N atoms confined to a volume *V*, such volume *V* is considered to be only a small portion of the bulk material, called *primary cell.* It is representative of the bulk material to the extent that the bulk material is assumed to be composed of the primary cell surrounded by exact replicas of itself. These replicas are called *image cells*, and are the same size and shape as the primary cell and each contain N atoms, which are images of the atoms in the primary cell. Thus the primary cell is periodically replicated in all directions to form a macroscopic sample. This periodicity extends to the positions and momenta of the images in image cells. Cells are separated by open boundaries, so atoms and images can freely enter or

leave any cell. Therefore, the number of atoms in each cell is the constant N because when an atom *i* leaves the primary cell, an image atom simultaneously enters the primary cell through an opposite face. For this to work properly, the shapes of the cells must be space filling, leaving no gaps in the 3D network. During a simulation, only the positions of the N atoms in the primary cell are stored, since positions of images can be computed when needed (**Figure 7**).

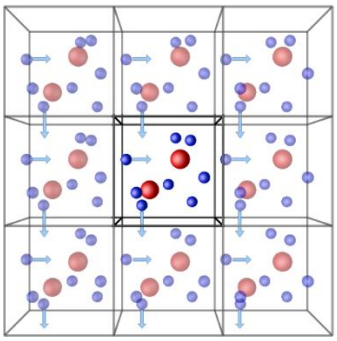

Figure 7. Schematic representation of a primary cell (center) surrounded by 8 identical image cells, all bearing exactly the same number of molecules following the same trajectories.[33]

The number of image cells needed depends on the range of intermolecular forces. Formally, each atom in the primary cell interacts with the N-1 remaining atoms and all their images. When forces are sufficiently short ranged, then only those image cells adjoining the primary cell are needed. For example, for squares in two dimensions, there are eight adjacent image cells, while for cubes in three dimensions, the number of adjacent images is equal to 26. Different shapes have been used as cells, but the squared is among the most used ones. Repeating runs with increasing number of atoms tests the effect of the pbc and the size of the system.[34]

There are at least several tens of software packages able to run MD simulations. However, the most popular ones are by far AMBER (Assisted Model Building with Energy Refinement),[35] GROMACS (GROningen MAchine for Chemical Simulations),[36] and CHARMm.

On the one hand, the software package selected for running the screening of guests in complexation with the initial proposed molecular cage, due to its high versatility was CHARMM[37] (Chemistry at HARvard Macromolecular Mechanics). More specifically it was *c36b1* (version 36 beta release revision 1), which is a FORTRAN 77/95-written program operating in Unix-like systems. This name encompasses a molecular dynamics simulation and analysis package as well as the set of molecular force fields employed on the MD simulations. It was initially developed by Martin Karplus and collaborators and it has suffered numerous further improvements.

On the other hand, the chosen force field, referring to the functional form and parameter sets used to calculate the potential energy of a system, was the classical Merck Molecular Force Field (MMFF), which constitutes a family of force fields developed by Merck Research Laboratories based on the molecular mechanics MM3 force field.[38] This force field is not specific for the simulation of a type of molecules, but performs well for a wide range of organic molecules. Parameters employed by this molecular force field are only computational.

Thus, all necessary parameters to perform molecular dynamics on these systems are set.

2.3.1. Selection of guest candidates for forthcoming complexation studies in solution

MD simulations of flexible molecules such as alkanes and proteins are more complex and time consuming than simulations of rigid systems, since the higher the internal degrees of freedom are, the more complicate the equations of motion become. Moreover, vibrations and rotations, more abundant on flexible systems, tend to relax on time scales very different from those of molecular collisions, making MD longer. For that reason, a feature deserving of evaluation is the shape-persistency of molecular cage (*P,P,P*)$_2$-**1H**. Thus, preliminary MD simulations of the cage were made in vacuum at 500 K. Considerable shape-persistency was observed for the cage in terms of shape and size, which remains in its original form, not breaking itself, and keeping exactly the same chirality during the process (**Figure 8**).

a) 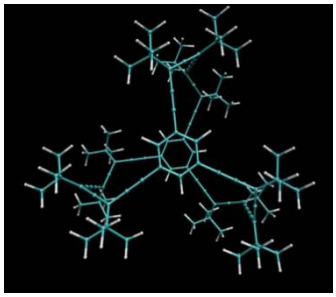 b) 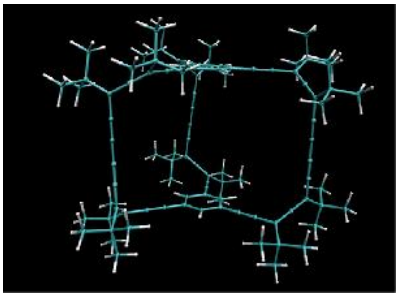

Figure 8. a) Top view, and b) Lateral view of (*P,P,P*)$_2$-**1H** during the simulation. Carbon skeleton depicted in blue and hydrogens represented in white.

The next step was rationally choosing a set of guests to be tested in the complexation with (*P,P,P*)$_2$-**1H**. Considering the D_3 symmetry of the cage, and the available space inside it (*ca.* 9 Å of intercentroid distance between benzene moieties, and *ca.* 10 Å between butadiyne branches) a set of guests bearing C_3 axes was purposed. This selection includes 1,3,5-likewise-substituted/2,4,6-likewise-substituted benzene (labelled as Bz), triazine derivatives (labelled as Tz), cyclohexane derivatives (Cy); substituted trindenes (Td); substituted indacenes (Ic), triphenylenes (TP) and polyamides (PA, the only one lacking C_3 symmetry) (**Figure 9**). For all the guest tested on the complexation studies, it was determined if they form a complex with (*P,P,P*)$_2$-**1H** or not, and in some cases that will be further discussed the time that the complex takes to be formed (**Table 1**).

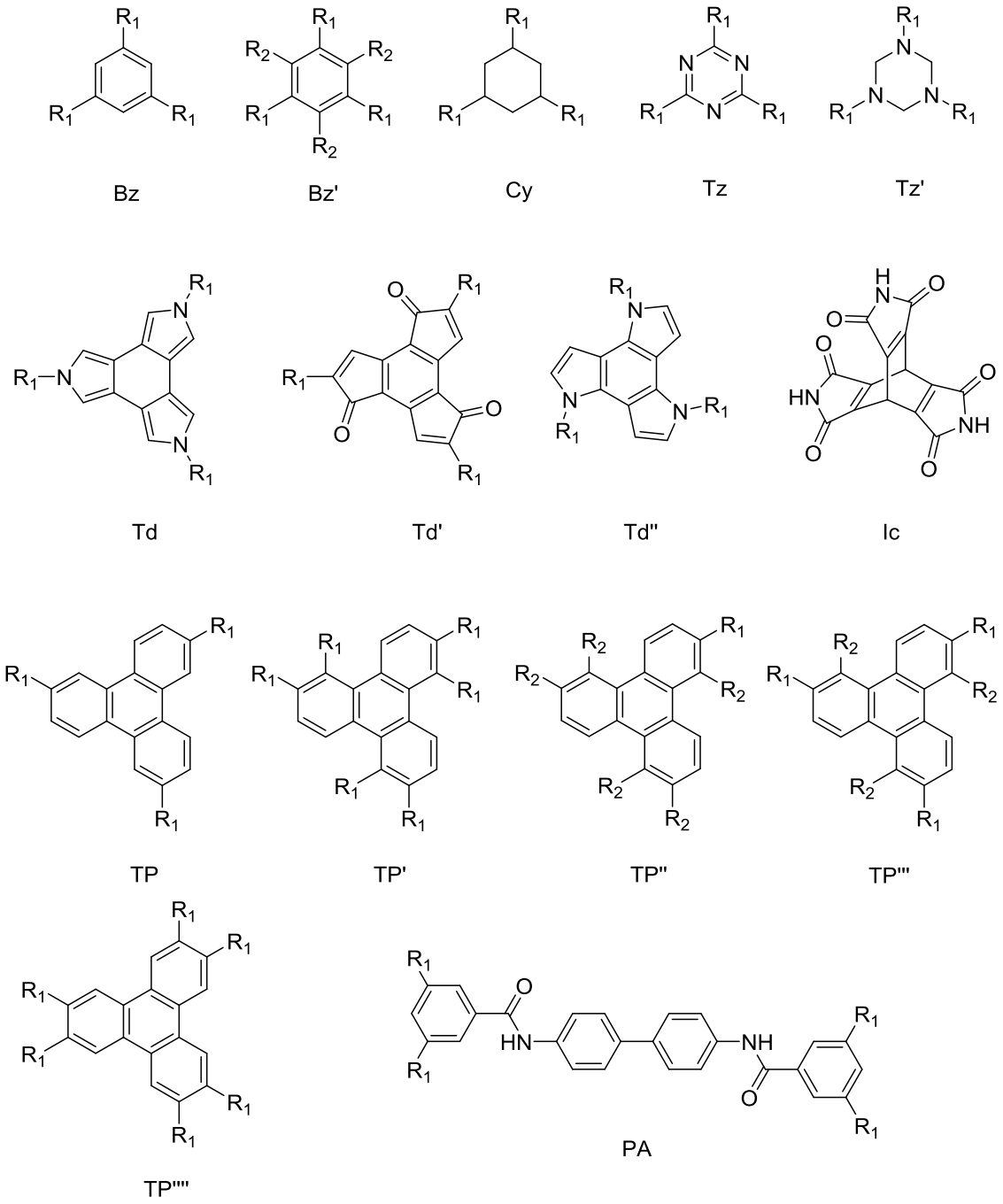

Figure 9. Structure of the guests tested on the MD simulations of the complex formation with their generic abbreviations.

Entry	Core	Substituents	Complex Formation	Observations
1	Bz	R_1 = -COOH	Y	
2	Bz	R_1 = -$(CH_2)_2$COOH	N	
3	Bz	R_1 = -$(CH_2)_3$COOH	N	
4	Bz	R_1 = -$(CH_2)_4$COOH	N	
5	Bz	R_1 = -$(CH)_2$COOH	N	
6	Bz	R_1 = -(CΞC)COOH	N	
7	Bz	R_1 = 	Y	

8	Bz	R_1 = -COCl	N	It stacks on the outer side of the benzene of the cage and stays there
9	Bz	R_1 = -NH_2	Y	
10	Bz	R_1 = -CH=CH_2	Y	The process takes 100000 ftsec
11	Bz	R_1 = -CΞCH	Y	The process takes 10000 ftsec
12	Bz	R_1 = -N_3	Y	The process takes 50000 ftsec
13	Bz	R_1 = -SH	Y	
14	Bz	R_1 = -CH_2SH	Y	The process takes 200000 ftsec
15	Bz'	R_1 = -$(CH_2)_2$COOH	N	
16	Cy	R_1 = -COOH	N	
17	Tz	R_1 = -$(CH)_2$COOH	N	
18	Tz	R_1 = -N=NCOOH	N	
19	Tz	R_1 = -$OCH_2CH=CH_2$	N	Even after 200000 ftsec
20	Tz'	R_1 = -(C=O)CH=CH_2	N	
21	Td	R_1 = -COOH	N	
22	Td'	R_1 = -NH_2	Y	
23	Td''	R_1 = -COOH	Y	The process takes a long time
24	Td''	R_1 = - CH_2COOH	N	
25	Ic		N	
26	TP	R_1 = -COOH	N	
27	TP	R_1 = -CH_2COOH	N	
28	TP	R_1 = -$(CH_2)_2$COOH	N	
29	TP'	R_1 = -NH_2	Y	The process takes 300000 ftsec (allene dihedral constant = 1, CUTNB = 30); and 60000 ftsec (allene dihedral constant = 10, CUTNB = 25)
30	TP'	R_1 = -NH_3^+	Y	The complex is formed immediately
31	TP''	R_1 = -NH_3^+ R_2 = -NH_2	Y	The complex is formed immediately
32	TP'''	R_1 = -NH_3^+ R_2 = -NH_2	Y	The complex is formed immediately
33	TP''''	R_1 = -OH	Y	The process takes 100000 ftsec
34	PA	R_1 = -COCl	N	It stacks on the outer side of the benzene of the cage at 450 K for 300000 ftsec
35	PA	R_1 = -COOH	Y	

Table 1. List of candidate guests and results taken from the simulation output files of the complexation process between (*P,P,P*)$_2$-**1H** and the corresponding guest. Y = complex formation achieved. N = no complex formation achieved.

According to the analysis of the results achieved, the following conclusions about the complexation process between the guest candidates and (*P,P,P*)$_2$-**1H** are drawn:

- The largest dimension of the guest should not exceed 10 Å for it to go into the cage.
- Allowed dimensions of the guest strongly depend on the dihedral angle constraint of the allene moieties, which is directly related with the force needed to deform the dihedral angle of the allenes. In general, the higher the constraint of those is, the smaller the dimension of the guest is allowed for the complexation to take place, since the cage is not so easily deformed. High constraints permit only small-sized guest (7−8 Å), while when the constraint is reduced, large-sized guests are permitted (9−0 Å) (see **Entry 29**, in this case, the time for the complex formation gets reduced due to the reduction of the CUTNB).

- Flexibility of the lateral chains attached to the core of the guests disfavors complex formation (see **Entries 1** to **4** or **Entry 23** vs **24**).
- Flexibility of the central core of the guest also disfavors complex formation (see **Entries 1** and **16** or **Entry 21** vs **Entries 22** and **23**).
- A deficient electronic character of the central core or the guests favors the complexation. This is reasonable, since the benzene rings of the cage are neutral to slightly electron-rich (see **Entries 29** and **30** where the inclusion of a positive charge on the guest accelerates its entry on the cage cavity). Acyl chlorides, considered as electron withdrawing groups, also make the guest core electron deficient, favoring the complexation. Nevertheless, the initial stacking of guests containing acyl chlorides takes place on the outer side of the cage (see **Entries 8** and **34**).

Consequently, it is deduced that shape-persistent guest molecules bearing electron deficient or even positively charged flat aromatic cores and having as largest dimension 10 Å are more prone to enter into the host cavity.

2.3.2. 2D Network formation by guests encapsulation followed by through-linkers interaction

Previous MD simulations of the complexation process between (*P,P,P*)$_2$-**1H** and the possible guests were performed by simply setting both randomly oriented on the phase-space. However, when this simulation was extended to a higher number of hosts and guests, a surface was included on the system in order to facilitate the pre-organization of the molecules above it. The employed surface was a rectangular graphene surface of 88 x 88 Å dimensions built as a set of planar molecules containing N, O and H atoms put together in the same plane. This is an artefact used in order to avoid the occurrence of a CHARMM error, which works only with real molecules.[37] These atoms were *a posteriori* replaced by sp^2 hybridation carbon atoms into the script employed (**Figure 10**).

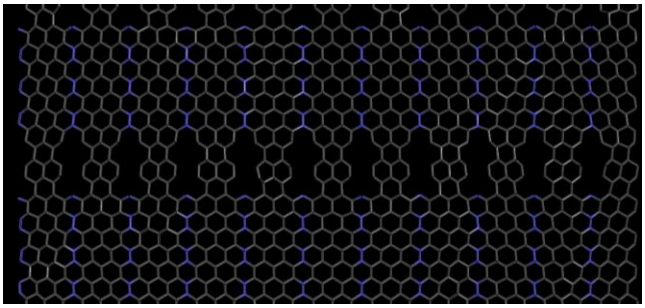

Figure 10. Image of the artificial rectangular graphene surface before modifying the identity of the heteroatoms and their hybridations to sp^2. Gray depict carbon, blue nitrogen and white hydrogen atoms.

It is known that the deposition of chiral molecules as racemic mixtures can arise surfaces with an organized distribution of chiral domains with opposite chirality. However, after having observed the behavior over the surface of a ternary complex between two cage units of opposite chirality and the polyamide present on **Table 1** (**Entry 35**), where two identical homochiral complexes present more tendency to lay parallel to the surface, and therefore more appropriate

for the formation of 2D networks, we decided to use the same homochiral configuration in all the cages instead of the racemate (**Figure 11**).

a) 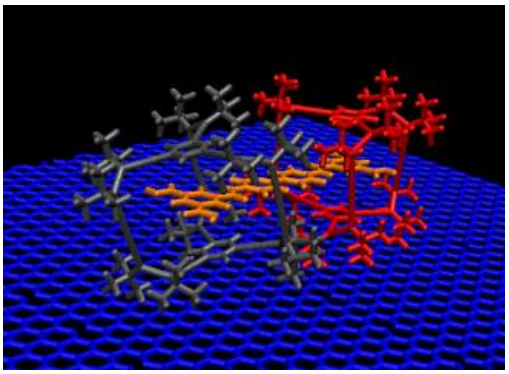 b) 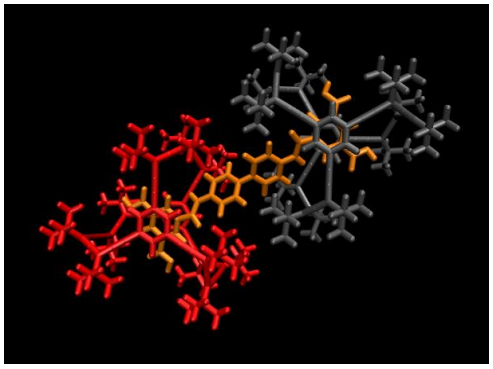

Figure 11. (*P,P,P*)$_2$-**1H** (red)−Polyamide (orange)− (*M,M,M*)$_2$-**1H** (gray) assembly rotating over graphene surface (blue). a) Side view. b) Top view (omitting the surface for clarity).

Next step was to extend the results all over the surface, including a larger amount of cages, guests and linkers. The first guest proposed on the supramolecular approach was benzene-1,3,5-tricarboxylic acid (**Table 1 - Entry 1**)**.** The simulation of several units of (*P,P,P*)$_2$-**1H** complexed with the abovementioned guest resulted into a free motion of them all over the graphene surface. This fact was probably due to the small size of the guests, which were not able to establish interactions between themselves from the interior of (*P,P,P*)$_2$-**1H**. Therefore, the use of a third species as linker between guests was included on the MD simulations in order to act as bridges between cage units. Terephthalic acid, which bears two linearly arranged carboxylic acids pointing in opposite directions, was the linker of choice. Still, exit of the guests out of (*P,P,P*)$_2$-**1H**, and formation of dimers and even trimers of terephthalic acid was observed (**Figure 12**).

a) 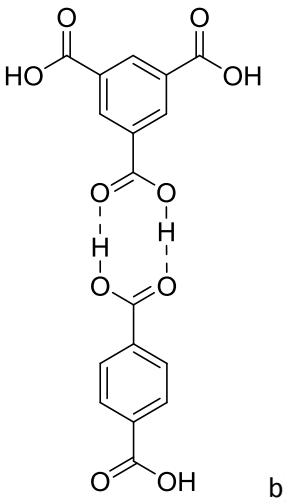 b) 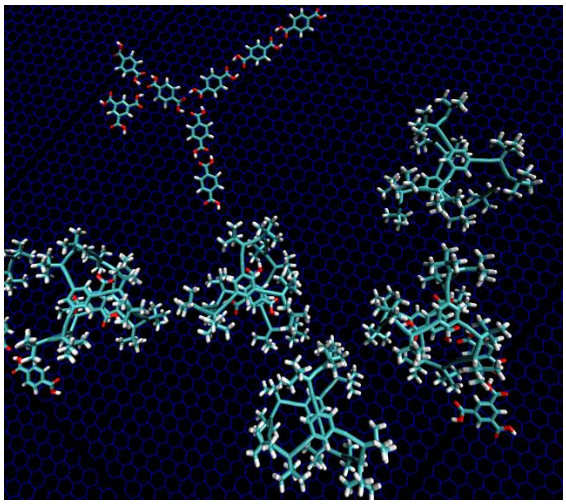

Figure 12. a) Supramolecular interaction between the guest (top) and linker (terephthalic acid, bottom). b) Snapshot of the MD simulation showing the problems of aggregation of linkers (terephthalic acid) and exit of the guests (benzene-1,3,5-tricarboxylic acid) out of the cages. Carbon atoms depicted in clear blue, oxygen atoms in red and hydrogens in white.

The first strategy to tackle the aforementioned problem was based on artificially changing the interactions between the molecules, increasing the interaction coefficients between linkers and guests and reducing these between molecules of the same nature (linkers with themselves and

guests with themselves). After the negative result of such strategy, a different one was proposed. Therefore, a tricationic larger guest, the 1,5,9-triaminotriphenylene-2,6,10-triaminium (**Table 1**, **Entry 32**), was employed with the purpose of maximizing host–guest interactions, and terephthalate linkers were used in order to compensate the charge of the guests. During the MD simulation it was observed an extremely strong interaction between these opposite charged molecules, and in some cases even the decomplexation of the guest out of the host or the entry of the linker inside (*P,P,P*)$_2$-**1H** (**Figure 13**).

a) 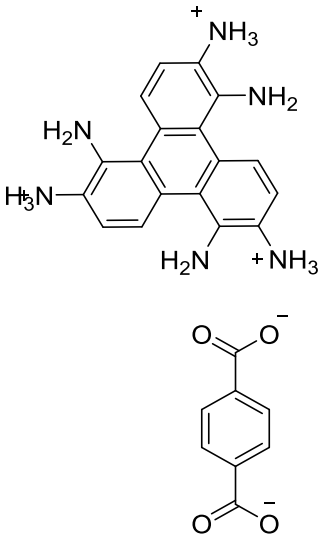

b) 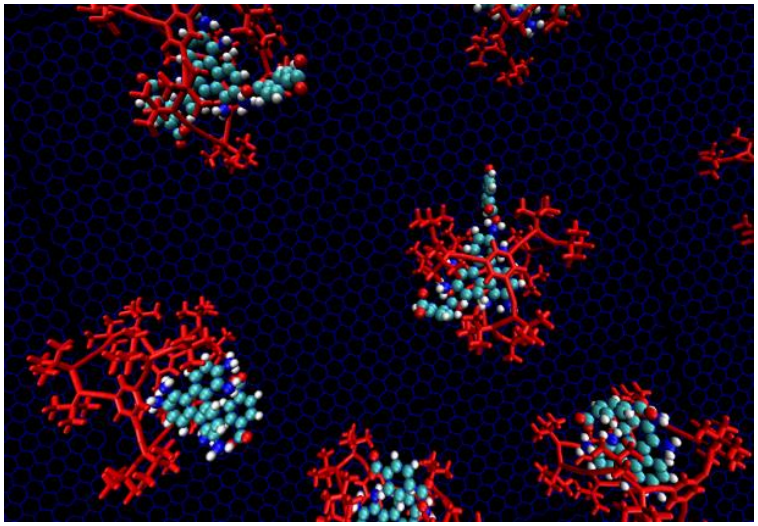

Figure 13. a) Structures of opposite charge guest (top) and linker (bottom). b) Snapshot during the MD simulation. (*P,P,P*)$_2$-**1H** skeleton in red (stick representation). Guests and linkers: Carbon atoms in light blue, nitrogen atoms in dark blue, oxygen atoms in red and hydrogen atoms in white.

Therefore, a different counterion acting as linker was proposed. Sulfate anion (SO_4^{-2}) resulted to be better linker, since it did not stack onto the graphene surface as easily as the terephthalate, but still the interaction with the guest was too strong, making them to go out of the cages. In the light of the results, sulfate was changed by sulfite (SO_3^{-2}), which yielded the formation of several aggregates composed by two complexes and two SO_3^{-2} (**Figure 14**).

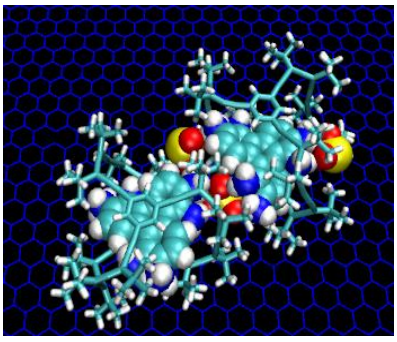

Figure 14. Snapshots of the MD simulation with the 1,5,9-triaminotriphenylene-2,6,10-triaminium inside the cage and SO_3^{-2} anions acting as a linkers. Sulfur atoms in yellow.

Although anion hexafluorophosphate (PF_6^-) could be a good choice, since it has a lower net charge, and, experimentally is soluble in both aqueous and organic solvents, CHARMm *c36b1* fails to recognize molecules in which an atom shares more than four bonds. Nevertheless, chloride (Cl^-) meets this requirement without exceeding the number of bonds. Therefore,

chloride anions were placed artificially on the *.mrk* file close to the positively charged guests in order to compensate their charges and avoid the repulsion between them. A fast aggregation process of all the cages belonging to the system was observed, suggesting a possible hexagonal pattern formation (**Figure 15**). The process takes place with low reversibility, remaining the cages in the same place once linked to each other.

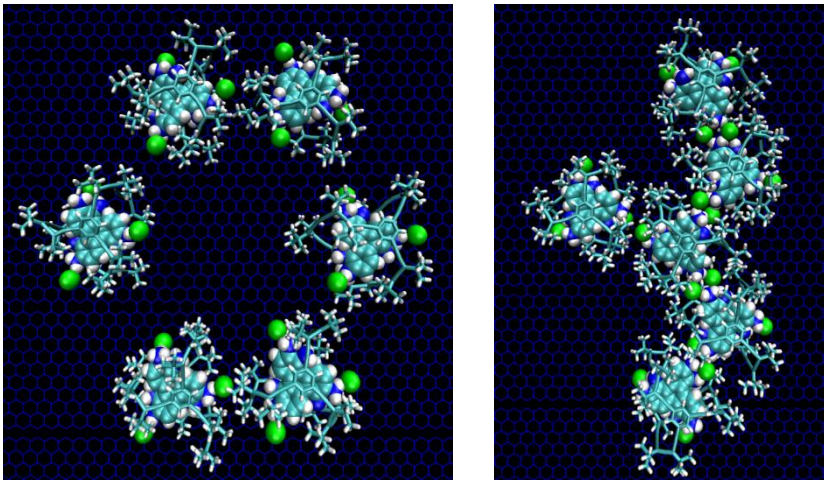

Figure 15. Snapshots before and after the MD simulation employing Cl^- atoms (in green) acting as linkers.

Thereafter, this promising system was tuned in order to mimic conditions found in solution. For that, vacuum was replaced by a Polarizable Continuum Model (PCM) media with a dielectric constant equal to 1.7. The criteria for selecting such value was gradually changing this parameter from 1 to 10 and observing whether the degree of reversibility during the MD simulation was appropriate or not. Such dielectric constant matches well the one for hexane (1.88) (**Table 2**).

Solvent	Dielectric Constant
Hexane	1.88
Cyclohexane	2.02
Benzene	2.3
Toluene	2.38
Chloroform	4.81
Diethyl ether	4.30
Ethyl acetate	6.02
Tetrahydrofurane	7.5
Dichloromethane	9.1
Acetone	21

Table 2. Relation of commonly used solvents with their respective dielectric constants.

A 32-complexes system was also tested yielding the formation of some five- and six-member aggregates on *ca.* 1.5 nanoseconds with high reversibility. The aggregates are arranged such that two chloride atoms lie in the same plane as the guests, compensating the total charge of the system, and acting as a kind of bridge between amino and ammonium groups at distances ranging from 2.3 to 2.9 Å (**Figure 16**). However, before running longer MD simulations, a couple of important parameters were further improved.

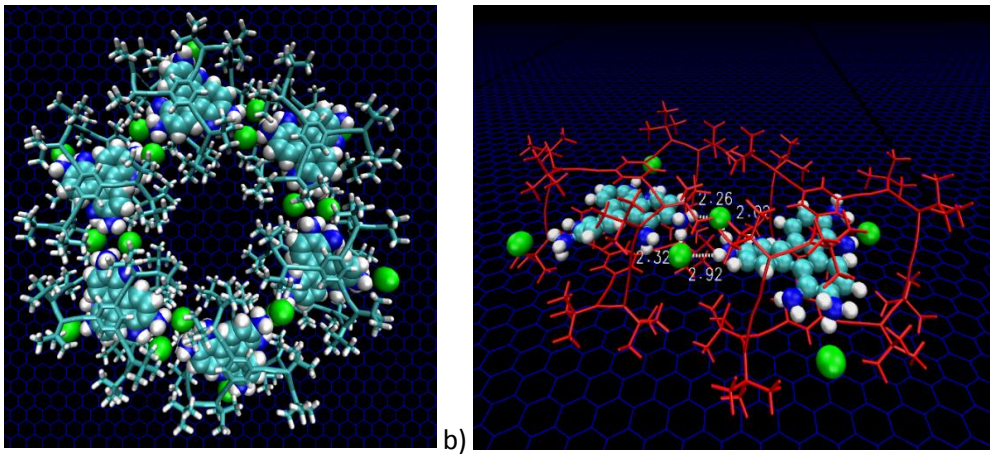

Figure 16. a) Final hexagonal structure of six complex assembly for a dielectric constant of 2.1 after MD simulation. b) Two-complex aggregate with distances between amino/ammonium H atoms and Cl^- atoms in Å.

The first improved parameter was the allene constraint constant. A value of 10 was found to be more appropriate than the one of 20 used so far. This value selection was made by calculating the potential energy for different constraint constants and plotting it *vs* the dihedral angles formed by the *tert*butyl groups of the allene. The curve matching the best the potential energy curve calculated at a B3LYP/6-31G (d) level of theory determined the selected value (**Figure 17**).

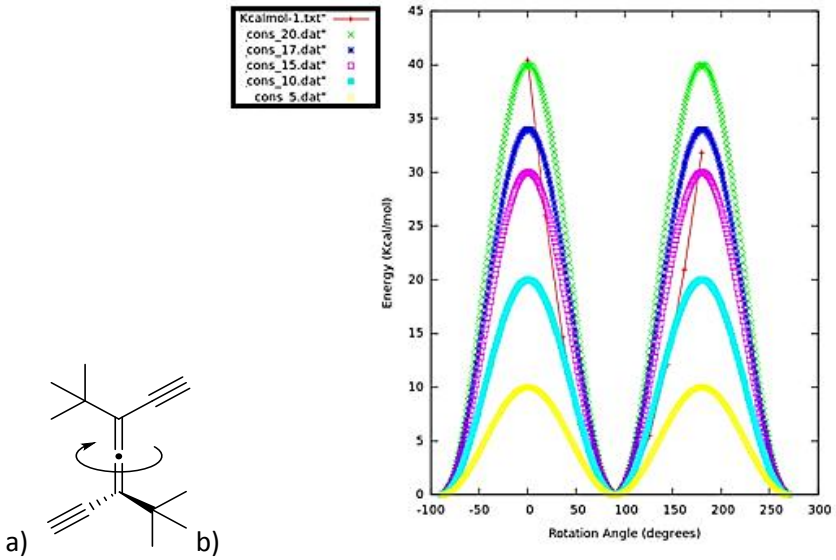

Figure 17. a) Scheme of the rotation of the dihedral angle between *tert*-butyl groups of the diethynylditertbutylallenes. b) Plot of potential energy *vs.* dihedral angle of the diethynylditertbutylallene for different values of constraints constants (5-yellow, 10-light blue, 15-pink, 17-dark blue, 20-green), and plot of the potential energy *vs.* dihedral angle of the diethynylditertbutylallene at the B3LYP/6-31G (d) level of theory (red).

The second parameter improved was the set of cutoff values employed as periodic boundary conditions. To compute the interaction of N atoms with each other, one needs in principle NxN steps. Bonded interactions involve only next neighbors, so they are cheap in terms of computer time. However, for the non-bonded energy calculation (Lennard-Jones potential is commonly employed, describing Van der Waals or dispersion forces) it is customary to introduce a cut-off

distance of the interatomic potential beyond which interactions are ignored.[37] Here are defined the four different cutoff distances employed on the MD simulation (**Figure 18**):

CUTIM = Cutoff for including image atoms.
CUTNB = Distance cutoff for neighbor list.
CTOFFNB = Maximum distance for a pair to consider in energy.
CTONNB = Distance at which smoothing function reduces pair's contribution.

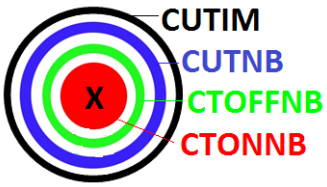

Figure 18. Example of CUTIM (black), CUTNB (blue), CTOFNB (green), and CTONNB (red) regions for a molecule X placed on the center of the cell.

The larger these cutoff values are, the slower the calculation is, so that a compromise between accurate and fast calculation must be adopted. Therefore, the parameter to take into account in order to decide the optimal cutoff set was the time of the calculation for a system composed by 32 cages with their corresponding guests and linkers **(Table 3)**. It is noteworthy that the cutoff radius is always chosen so that an atom can interact with only one image of any given atom. This means that R_{cut} cannot be greater than half the width of the cell (**Figure 19**). It must be considered that non bonded cutoff values should not be smaller than 12 Å.[37] However, increasing the CUTNB implies decreasing the frequency of non-bond list updates at the expense of a higher memory requirement for the non-bond list. It was observed an exponential growth of the consumed calculation time with the increasing of the cutoff values, considering values on **Entry 2** the most acceptable ones.

Entry	CUTNB (Å)	CTOFFNB (Å)	CTONNB (Å)	CUTIM (Å)	CPU time (h)
1	30	29	28	31	4.00
2	25	24	23	26	3.06
3	20	19	18	21	2.27
4	15	14	13	16	1.66
5	10	9	8	11	1.21
6	5	4	3	6	N/A

Table 3. Sets of CUTNB, CUTOFFNB, CUTONNB and CUTIM and the corresponding time consumed for each calculation. N/A = result not available due to an "energy exceeded tolerance" error.

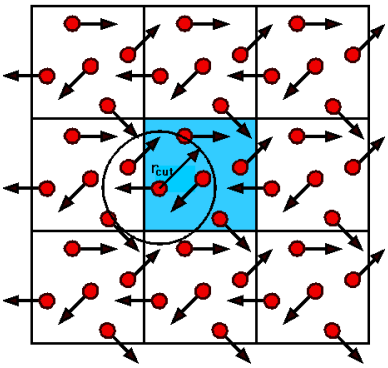

Figure 19. Diagram showing a system formed by 9 unit cells with an r_{cut} smaller than one half of the unit cell length, in order to avoid self−interaction.[39]

Although total energy *E* is constant, the kinetic energy E_k and potential energy *U* fluctuate, but these fluctuations preserve the value of *E*, whose values also fluctuate on a time scale less than 1 psec about an average value.

$$E = E_k(\boldsymbol{p}^N) + \mathcal{U}(\boldsymbol{r}^N) = constant$$

where *N* is the total number of atoms, ***p*** are the momentum vectors, and ***r*** the positions.

Thus, it was confirmed that the total energy of the system presents a normal behavior for CUTNB values ranging from 10 to 30 Å for MD simulations of 1500 fs. Total energy initially increases with the number of steps, and reaches then a *plateau*, due to the transformation of translational energy into vibrational energy (**Figure 20**).

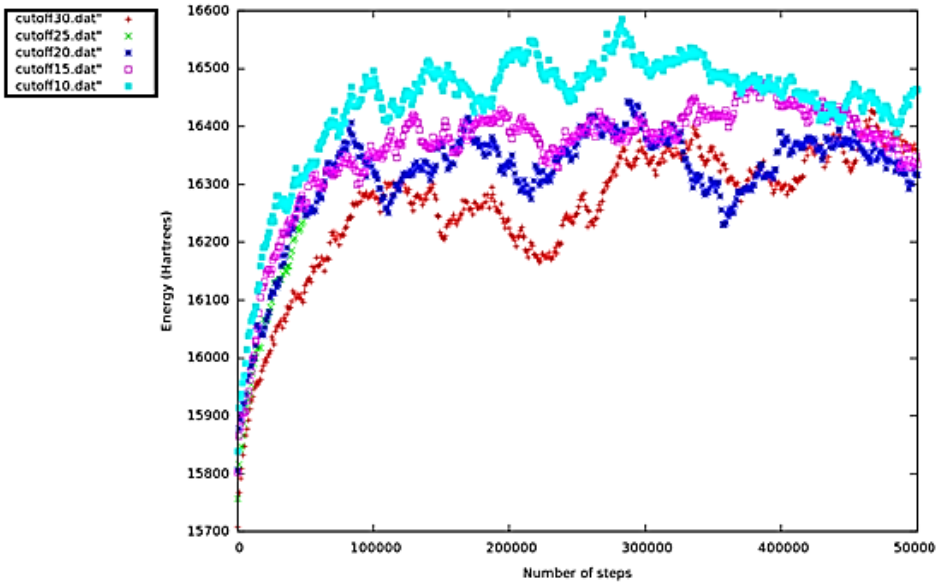

Figure 20. Total energy (in Hartrees) *vs* Number of MD simulation steps for CUTNB values of 10 (light blue), 15 (pink), 20 (dark blue), 25 (green) and 30 Å (red). Total time of calculation = 1500 fs (0.003 fs/step).

Finally, once optimized the required constraints, cutoff values, and checked the correct behavior of the total energy, the MD simulation of the system composed by 32 complexes was again run, yielding the formation of different linked five, six and even seven member fused structures. Such system presented an appropriate reversibility, necessary for the organized growth of the network, through which the number of hexagonal forms rapidly increased with time (**Figure 21**, **22**).

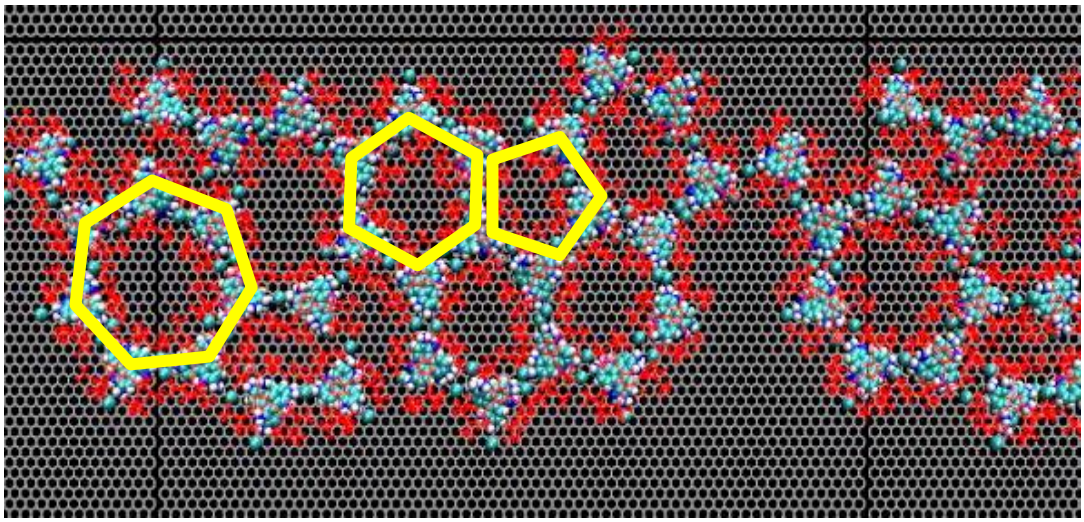

Figure 21. Snapshot of the MD simulation with five, six and seven member aggregates highlighted in yellow. $(P,P,P)_2$-**1H** skeletons in red. Guests and linkers: C atoms in light blue, N atoms in dark blue, H atoms in white, and Cl atoms in green.

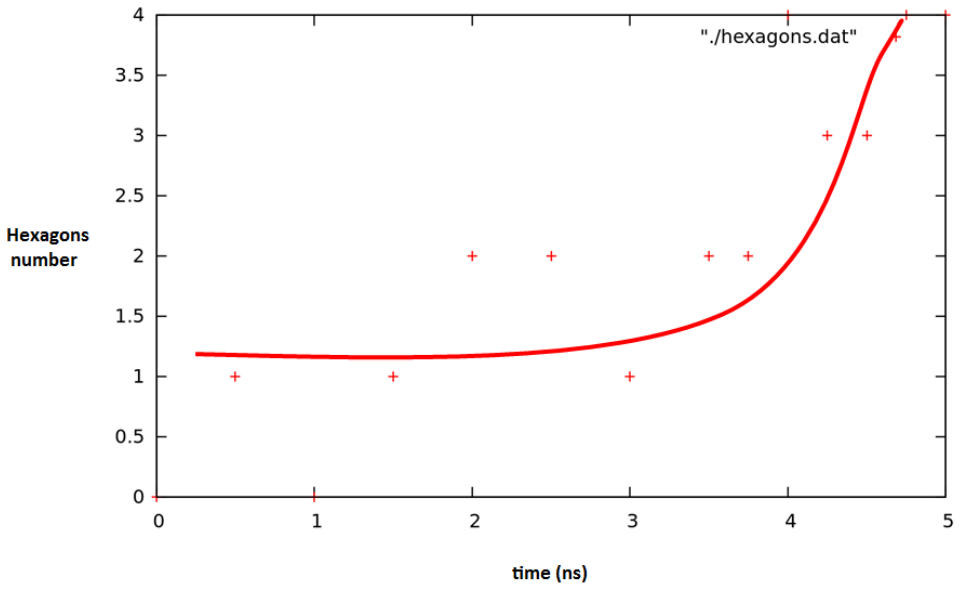

Figure 22. Number of hexagonal aggregates formed *vs* total time of the simulation (in ns).

Finally, it can be concluded that, at least *in silico*, formation of chiral bidimensional networks sorted from the proposed chiral molecular cage $(P,P,P)_2$-**1H**, forming 1:1 complexes with positively charged guests bearing a C_3 axis and negatively charged linkers, is plausible.

2.4. References

[1] J. L. Alonso-Gómez, A. G. Petrovic, N. Harada, P. Rivera-Fuentes, N. Berova, F. Diederich, *Chem. Eur. J.* **2009**, *15*, 8396–8400.

[2] O. Gidron, M.-O. Ebert, N. Trapp, F. Diederich, *Angew. Chem Int. Ed.* **2014**, *53*, 13614–13618.

[3] P. Ballester, M. Fujita, J. Rebek, *Chem. Soc. Rev.* **2015**, *44*, 392–393.

[4] S. Castro-Fernández, I. R. Lahoz, A. L. Llamas-Saiz, J. L. Alonso-Gómez, M.-M. Cid, A. Navarro-Vázquez, *Org. Lett.* **2014**, *16*, 1136–1139.

[5] A. T. Balaban, *J. Chem. Inf. Comput. Sci.* **1997**, *37*, 645–650.

[6] W. Chiu, F. J. Rixon, *Virus Res.* **2002**, *82*, 9–17.

[7] B. D. Rae, B. M. Long, M. R. Badger, G. D. Price, *Microbiol. Mol. Biol. Rev.* **2013**, *77*, 357–379.

[8] I. M. Ilie, W. K. den Otter, W. J. Briels, *J. Chem. Phys.* **2014**, *141*, 65101.

[9] J. M. Teo, C. J. Coghlan, J. D. Evans, E. Tsivion, M. Head-Gordon, C. J. Sumby, C. J. Doonan, *Chem. Commun.* **2016**, *52*, 276–279.

[10] M. Wang, V. Vajpayee, S. Shanmugaraju, Y.-R. Zheng, Z. Zhao, H. Kim, P. S. Mukherjee, K.-W. Chi, P. J. Stang, *Inorg. Chem.* **2011**, *50*, 1506–1512.

[11] G. F. Swiegers, T. J. Malefetse, *Chem. Eur. J.* **2001**, *7*, 3636–3643.

[12] Y. Z. Voloshin, V. V. Novikov, Y. V. Nelyubina, *RSC Adv.* **2015**, *5*, 72621–72637.

[13] J. Bunzen, J. Iwasa, P. Bonakdarzadeh, E. Numata, K. Rissanen, S. Sato, M. Fujita, *Angew. Chem. Int. Ed.* **2012**, *51*, 3161–3163.

[14] S. Pasquale, S. Sattin, E. C. Escudero-Adán, M. Martínez-Belmonte, J. de Mendoza, *Nat. Commun.* **2012**, *3*, 785.

[15] K. Acharyya, P. S. Mukherjee, *Chem. Commun.* **2015**, *51*, 4241–4.

[16] G. R. Schaller, F. Topić, K. Rissanen, Y. Okamoto, J. Shen, R. Herges, *Nat. Chem.* **2014**, *6*, 608–613.

[17] L. Caswell, M. A. Garcia-Garibay, J. R. Scheffer, J. Trotter, *J. Chem. Educ.* **1993**, *70*, 785–787.

[18] D. N. Reinhoudt, L. J. Prins, F. De Jong, P. Timmerman, *Nature* **2000**, *408*, 181–184.

[19] M. E. Briggs, A. G. Slater, N. Lunt, S. Jiang, M. A. Little, R. L. Greenaway, T. Hasell, C. Battilocchio, S. V Ley, A. I. Cooper, *Chem. Commun.* **2015**, *51*, 17390–17393.

[20] R. A. Brualdi, *Introductory Combinatorics*, Pearson, **2009**.

[21] C. Schönbeck, P. Westh, R. Holm, *J. Phys. Chem. B* **2014**, *118*, 10120–10129.

[22] J. Požar, G. Horvat, M. Čalogović, N. Galić, L. Frkanec, V. Tomišić, *Croat. Chem. Acta* **2012**, *85*, 541–552.

[23] R. Choudhury, A. Barman, R. Prabhakar, V. Ramamurthy, *J. Phys. Chem. B* **2013**, *117*,

398–407.

[24] F. Broda, M. O. Vysotsky, V. Böhmer, I. Thondorf, *Org. Biomol. Chem.* **2006**, *4*, 2424–2432.

[25] A. M. M. Rawashdeh, M. I. El-Barghouthi, K. I. Assaf, S. I. Al-Gharabli, *J. Incl. Phenom. Macrocycl. Chem.* **2009**, *64*, 357–365.

[26] J. Y. Ko, S. W. Heo, J. H. Lee, H. Bin Oh, H. Kim, H. I. Kim, *J. Phys. Chem. A* **2011**, *115*, 14215–14220.

[27] A. M. Abramyan, Z. Liu, V. Pophristic, *Phys. Chem. Chem. Phys.* **2014**, *16*, 20406–20410.

[28] I. Thondorf, F. Broda, M. O. Vysotsky, S. E. Matthews, O. Mogck, V. Böhmer, *J. Struct. Chem.* **2005**, *46*, S39–S45.

[29] A. R. Albunia, C. Gaeta, P. Neri, A. Grassi, G. Milano, *J. Phys. Chem. B* **2006**, *110*, 19207–19214.

[30] J. M. Haile, *Molecular Dynamics Simulation : Elementary Methods*, Wiley, **1997**.

[31] B. J. Alder, T. E. Wainwright, *J. Chem. Phys.* **1959**, *31*, 459–466.

[32] A. Warshel, *Nature* **1976**, *260*, 679–683.

[33] Central Michigan University, "Periodic Boundary Conditions," can be found under http://isaacs.sourceforge.net/phys/pbc.html, **n.d.**

[34] L. R. Pratt, S. W. Haan, *J. Chem. Phys.* **1981**, *74*, 1864–1872.

[35] W. D. Cornell, P. Cieplak, C. I. Bayly, I. R. Gould, K. M. Merz, D. M. Ferguson, D. C. Spellmeyer, T. Fox, J. W. Caldwell, P. A. Kollman, *J. Am. Chem. Soc.* **1995**, *117*, 5179–5197.

[36] D. Van Der Spoel, E. Lindahl, B. Hess, G. Groenhof, A. E. Mark, H. J. C. Berendsen, *J. Comput. Chem.* **2005**, *26*, 1701–1718.

[37] B. R. Brooks, C. L. Brooks, A. D. Mackerell, L. Nilsson, R. J. Petrella, B. Roux, Y. Won, G. Archontis, C. Bartels, S. Boresch, et al., *J. Comput. Chem.* **2009**, *30*, 1545–1614.

[38] T. A. Halgren, *J. Comput. Chem.* **1996**, *17*, 490–519.

[39] "Democritus: Periodic Boundary Condition," can be found under http://www.compsoc.man.ac.uk/~lucky/Democritus/Theory/pbc-mi.html, **n.d.**

3. A Covalent Organic Helical Cage with Remarkable Chiroptical Amplification

3.1. Proof of principle

In order to validate the proposed methodology for the synthesis of COHCs, synthesis, characterization and complexation study with the guests chosen by Molecular Dynamics of (*P,P*)$_3$-**1H** and (*M,M*)$_3$-**1H** were performed. The synthetic pathway involves a triple Sonogashira cross−coupling reaction between enantiopure (*P*)-**DEA-OH** with a 1,3,5-trihalobenzene to give the enantiopure tricoupled product (*P,P,P*)-**2H**. Subsequent deprotection under basic conditions will give rise to the tripodal shaped molecule (*P,P,P*)-**3H**. Finally, Cu-catalyzed homodimerization of two units of (*P,P,P*)-**3H** will give rise to the chiral covalent organic molecular cage (*P,P*)$_3$-**1H** (**Scheme 1**). The more significant details regarding the characterization of the final product as well as the intermediates are highlighted. After that, guests inferred from the Molecular Dynamics studies were synthesized and experimentally tested for their complexation with molecular cage (*P,P*)$_3$-**1H**.

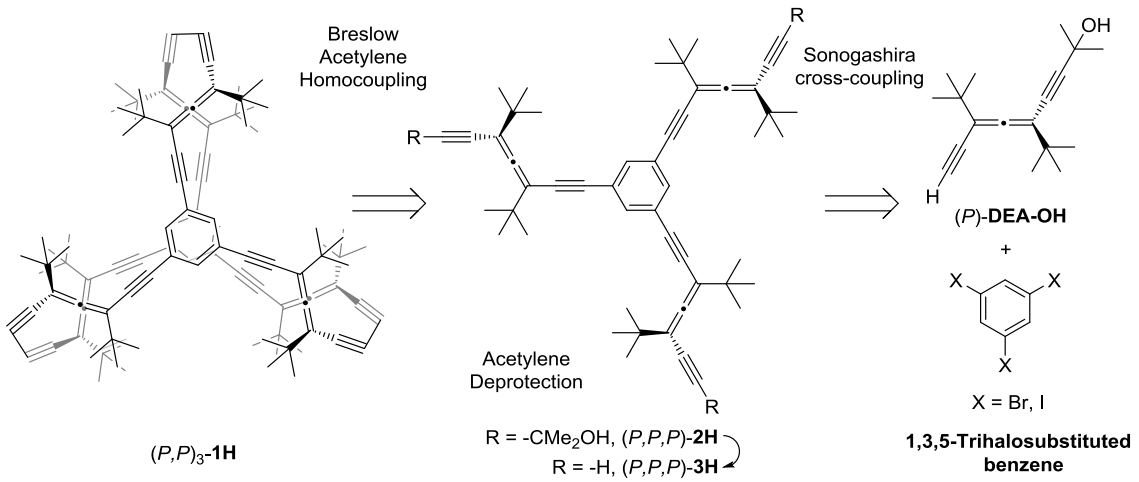

Scheme 1. Retrosynthetic scheme of the molecular cage (*P,P*)$_3$-**1H**.

3.1.1. Sonogashira cross−coupling reactions

A cross−coupling reaction of aryl or vinyl halides with terminal acetylenes employing a palladium catalyst was firstly described by Heck and Cassar in 1975,[1,2] but the use of a Pd(0) catalyst in combination with a Cu(I) salt as a cocatalyst and an amine playing simultaneously the role of base and solvent at room temperature was in the same year introduced by Hagihara and Sonogashira (**Scheme 2**).[3] Benefits of Sonogashira reaction are the use of mild reaction conditions and the high tolerance to a broad variety of functional groups.[4–6] Sonogashira cross-coupling reaction has been employed into a huge variety of applications, such as the synthesis of natural products,[7] the construction of non-natural advanced functional materials, employed on nonlinear optics, polarizers for liquid crystal displays, light-emitting diodes, field effect transistors, photovoltaics, and sensors.[5]

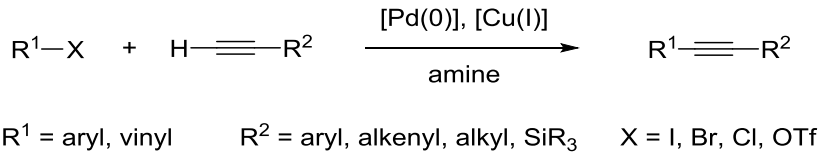

Scheme 2. Sonogashira cross−coupling between aryl or vinyl halides and terminal alkynes.

Original reaction conditions have been modified by changing either catalyst, cocatalyst, amine or additives, in order to improve the yield of the coupling and to avoid the formation of the homocoupling side product. Surprisingly, Sonogashira cross–coupling reaction mechanism is still nowadays not completely clear, due to the inherent difficulty of analyzing the action of both metallic catalysts.[8] Nevertheless, there is an accepted reaction mechanism based on the combination of two cycles, one for Palladium and the other for Copper, being the first one common to other C–C cross-coupling reactions (**Scheme 3**).

On a first step, considered to be the rate determining step of the process, the active $Pd(0)L_2$ species (***a***) undergoes oxidative addition of the aryl or vinyl halide to provide a [Pd(II)] complex (***b***). In that step, $[Pd(0)L_2]$ complex (***a***) is stabilized by ligands which can include the base/solvent molecules.[9] The most widely employed Pd catalyst is $[Pd(PPh_3)_2]$, being $[Pd(PPh_3)_4]$ and $[Pd(PPh_3)_2Cl_2]$ complexes the most common precursors.[10] Different experiments postulate the species $[Pd(0)L_2X]^-$, whose X comes from Ar–X, as the one with the initial activity.[11] $[Pd(0)(L)_2]$ species can be also generated by reductive elimination from the initially generated $[Pd(II)(L)_2(C\equiv CR)_2]$ leading to the undesired diyne. This side product can even be the major product, depending on the amount of oxidant, usually oxygen, in the reaction media. This can be avoided or diminished by exhaustively purging the system.[12]

Electron deficient organohalides are in general more reactive to cross–coupling than electron-rich organohalides, since carbon atom susceptible of being attacked by the Pd catalyst, is therefore a better electrophile.[13] Moreover, general reactivity of the sp^2 species in the oxidative addition step decreases in the following direction: vinyl iodide ≥ vinyl triflate > vinyl bromide > vinyl chloride > aryl iodide > aryl triflate ≥ aryl bromide >> aryl chloride.[5] Next step undergoes through a Pd(II) complex transmetallation with the Cu acetylide to give a complex (***c***), that, after reductive elimination and regeneration of the active catalyst gives the cross–coupled product (**Scheme 3**).

Regarding the Copper cycle, it has not been as clarified as the one for Palladium. It is known that the initial generation of a Cu–alkyne π–complex makes the terminal alkyne more acidic, thus facilitating the copper acetylide formation promoted by the base. Nevertheless, recent studies suggested other processes to play a significant role, such as pre-stabilization of CuI with multidentate ligands.[14] The use of Cu implies a drawback with respect to the necessity of avoid oxygen in order to prevent the undesired alkyne homocoupling in a Hay–Glaser reaction.[15] For this reason, several attempts to avoid the use of Cu have been tested, even when the transmetallation process is not as favored.[16]

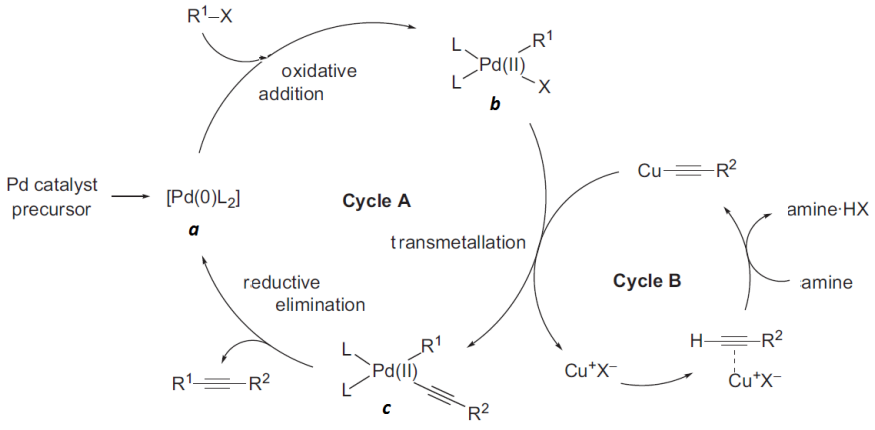

Scheme 3. Sonogashira cross-coupling reaction catalytic cycles.

Despite been Palladium the most widely used metal catalyst on the Sonogashira cross−coupling reaction, many other metals such as Ag,[17] Au,[18] Co,[19] Cu,[20] Fe,[21] In,[22] Ni,[23] Rh,[24] and Ru [25] complexes/nanoparticles have been probed to act as efficient catalysts that follow the same general mechanism as for Pd.

Efficiency of the reaction depends on the set of conditions employed, including the Pd catalyst and its ligands, the Cu salt, solvent, amine, and additives, as well as the electronic and steric characteristics of the electrophile and the alkyne. Concerning the Pd catalysts, $[Pd(PPh_3)_4]$ is unstable in contact with air at temperatures above 0 °C,[26] therefore its freshly prepared use is advised. However, it presents a clear advantage with respect to $[Pd(PPh_3)_2Cl_2]$, since it avoids or limits the formation of homocoupling side products. On the other hand, $[Pd(PPh_3)_2Cl_2]$ presents both air and temperature stability. The general high cost of these and others more specialized Pd catalysts have led researchers to search for a way of recovering them after the reaction takes place. A convenient way of doing so is based on linking the catalyst to a solid or polymeric matrix, susceptible of being recovered by filtration[27] such as palladium on activated charcoal (Pd/C).[28] However, Pd/C recycling leads to a decreasing of the catalytic activity with its use, which makes the process not so efficient.[29]

Regarding the amine base, Et_3N, Et_2NH, and $^{i}Pr_2NH$ are the most widely used, either as base or even as solvent. They are relatively polyvalent, but its efficiency depends on the substrate. Several studies established that stronger bases, such as piperidine and pyrrolidine, increase both yields and reaction rates in the absence of cocatalyst.[30] There are exceptions to such rule, evidenced by many studies in which, for example Hünig's base, $^{i}Pr_2NEt$, has also produced excellent results.[31–33] Besides abstraction of the alkyne proton, and final H−X molecules neutralization, amines can also act as ligands in [aryl−Pd(II)] complexes, which may significantly influence reaction rates.[34]

As already mentioned before, amines have been widely employed not only as bases but also as solvents in the Sonogashira reaction. Notwithstanding, yield improvements have been demonstrated when using a different solvent in combination with the amine. Examples of the most employed ones are tetrahydrofuran (THF),[35] *N*-methylpyrrolidinone (NMP),[36] *N,N*-dimethylformamide (DMF),[32,37] benzene,[38] and toluene.[39]

Another way of improving Sonogashira yields is based on the use of additives, such as ammonium and silver salts,[40] or tetrabutylammonium iodide (TBAI), which act as phase transfer agent in low-temperature reactions (−20 ^{O}C).[32]

Thus, Sonogashira cross-coupling reactions are postulated as versatile tools in the synthesis of unsaturated compounds from a wide variety of substrates.

3.1.2. Homocoupling reaction of terminal alkynes

Oxidative coupling reactions are usually the method of choice for the construction of macrocyclic oligoacetylenes containing buta-1,3-diynyl fragments.[41–43] All of them are based on different variations of the original Glaser reaction that uses CuCl in a solution of ammonia and ethanol in the presence of oxygen to give the homocoupling of two phenylacetylene molecules. Conditions reported by Hay (CuCl, TMEDA, O_2, CH_2Cl_2),[44,45] Eglinton ($CuSO_4$, or $Cu(OAc)_2$, pyridine)[46] and Breslow (CuCl, $CuCl_2$, oxygen-free pyridine)[47] are the most commonly employed. More recently, the use of Pd(II) as cocatalyst in the presence of Cu(I) and O_2, or an external oxidant such as chloroacetone or I_2, has emerged as an alternative for the traditional

Cu(I)/Cu(II) homocoupling-based methods.[48] There are no real agreements as how to predict which homocoupling protocol may be the most suitable for a particular target, although reagent solubility, for example, has been shown to dictate the success of one method over another.[49]

The first acetylenic coupling was reported in 1869 by Carl Glaser.[50] The publications demonstrated the formation of a 1,3-butadiyne species from the oxidative homocoupling reaction of phenylacetylene using copper(I) chloride in a solution of ammonia and ethanol in the presence of oxygen (**Scheme 4**).[50,51] The aforementioned method did not become systematically applied until it was probed that the *in situ* synthesis of the copper (I) derivative was possible, thus avoiding the risk of storing it given its tendency to explode.

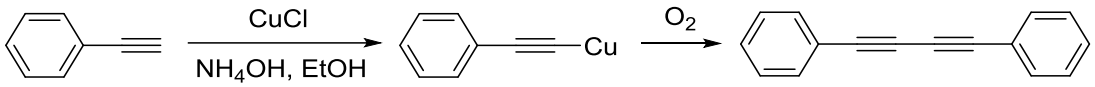

Scheme 4. First acetylenic coupling described by Glaser.

In 1956 Eglinton and Galbraith went a step forward in the development of the oxidative acetylenic coupling, introducing the use of a copper(II) salt, which would further undergo a reduction to Cu(I) in methanol/pyridine (**Scheme 5**).[46]

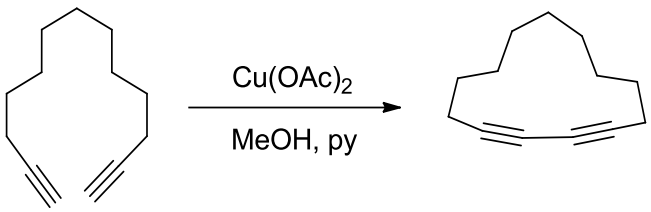

Scheme 5. Acetylenic coupling describe by Eglinton and Galbraith.

Another important modification, which constitutes still nowadays one of the most used methods, was reported in 1960 by Hay. In those studies the oxidative acetylenic couplings were performed with oxygen in the presence of copper(I) chloride and catalytic amounts of the bidentate ligand *N,N,N′,N′*-tetramethylethylenediamine (TMEDA) (**Scheme 6**).[44,45]

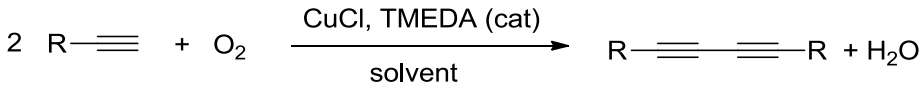

Scheme 6. Hay coupling method.

The proposal of Glaser and related methods for unsymmetrical couplings leads normally to the homocloupling as a major product, rather than to the heterocoupling. Such a problem was solved with the method proposed by Cadiot and Chodkiewicz in 1955, involving a terminal alkyne and 1-bromoacetylene in the presence of an amine and catalytic amounts of copper(I) salt (**Scheme 7**).[52,53] A tremendous variety of diacetylenic compounds has been synthesized through this method.[54–56]

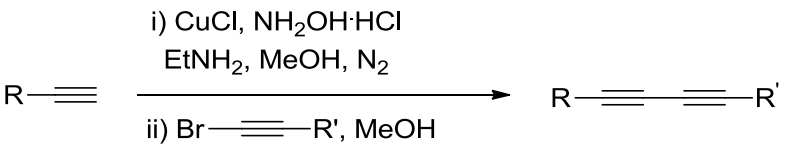

Scheme 7. Cadiot-Chodkiewicz heterocoupling conditions.

The mechanism of Glaser coupling and related methods seems to be rather complex, and so it is not fully understood yet. Studies revealed that the mechanism highly depends on the experimental conditions employed. The first proposed mechanism, which suggested the presence of radical intermediates, was thereafter rejected. Since then, the widely accepted mechanism involves the formation of a dimeric copper(II) acetylide complex, which undergoes coupling of the alkynyl fragments, affording the diyne product (**Scheme 8**).[57–59]

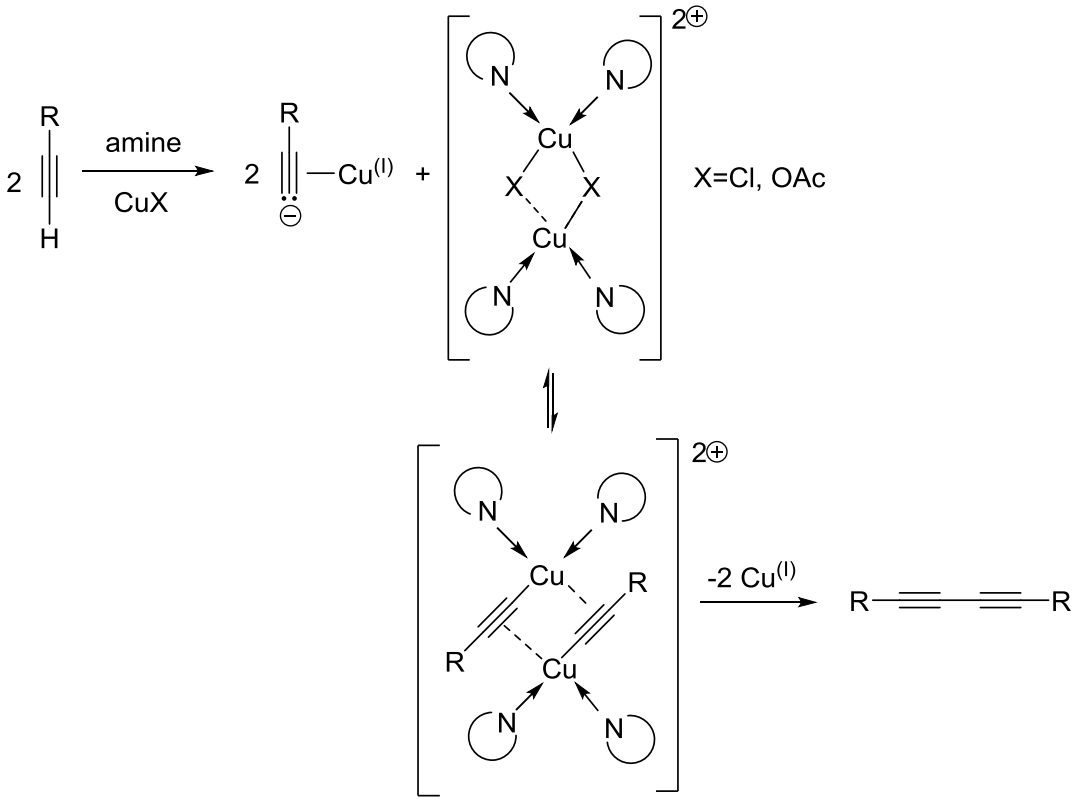

Scheme 8. Proposed mechanism for Glaser homocoupling and related methods.

When dealing with substrates bearing two or more different terminal acetylenes, one may face the problematic of oligomer or polymer formation. A possible solution to this problem is based on employing high-dilution conditions to increase the yield of cyclic products over linear oligomers, method that was firstly formulated and applied by Ruggli in 1912.[60] Ruggli´s method stated that a cyclization is an intramolecular reaction occurring between the two ends of a precursor, which depends on the probability of them finding each other, and is in competition with an intermolecular reaction which gives linear oligomers. The intramolecular ring closure is a first order reaction, thus its rate is proportional to the concentration of the precursor. The intermolecular process is a second order reaction, therefore its rate is proportional to the square of the concentration. Consequently, high dilution should favor the intramolecular ring closure reaction. In conclusion, there is no way of completely suppressing the linear growth, but to palliate it. Experimentally, high-dilution conditions require a large amount of solvent (*ca.* 1 mM concentration). To avoid the use of this large amounts of solvent, it is common to use pseudohigh-dilution (influxion) conditions, in which the reactants are slowly added for hours or even days over the reaction starting materials. An example of application of the method of Ruggli, also known as Ruggli-Ziegler-Dilution-Method (RZDM), Schwarz and coworkers published the synthesis of four different polyamides through a polycondensation methodology (**Figure 1**).[61]

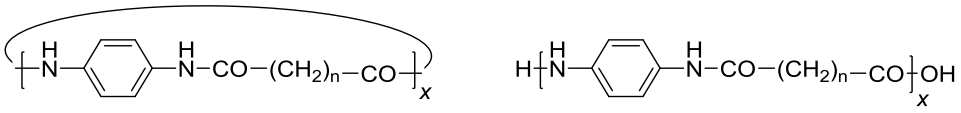

Figure 1. Cyclic polyamide *vs* oligomeric polyamide formation.

As a conclusion, a broad variety of methodologies for the coupling of acetylenes, all based on variations of the initial procedure described by Glaser, are available. High-dilution conditions are typically employed to avoid polymer formation.

3.2. Synthesis of (*P*,*P*)$_3$-1H and (*M*,*M*)$_3$-1H

In virtue of their versatility we decided to use Sonogashira cross−coupling and homocoupling reactions as the key for the synthesis of (*P*,*P*)$_3$-**1H**, whose synthetic pathway involves a triple Sonogashira reaction between three equivalents of enantiopure (*P*)-**DEA-OH** with a 1,3,5-trihalobenzene affording the tricoupled product (*P,P,P*)-**2H**, followed by deprotection which yields tripodal molecule (*P,P,P*)-**3H**, followed by its subsequent homodimerization (**Scheme 9**).

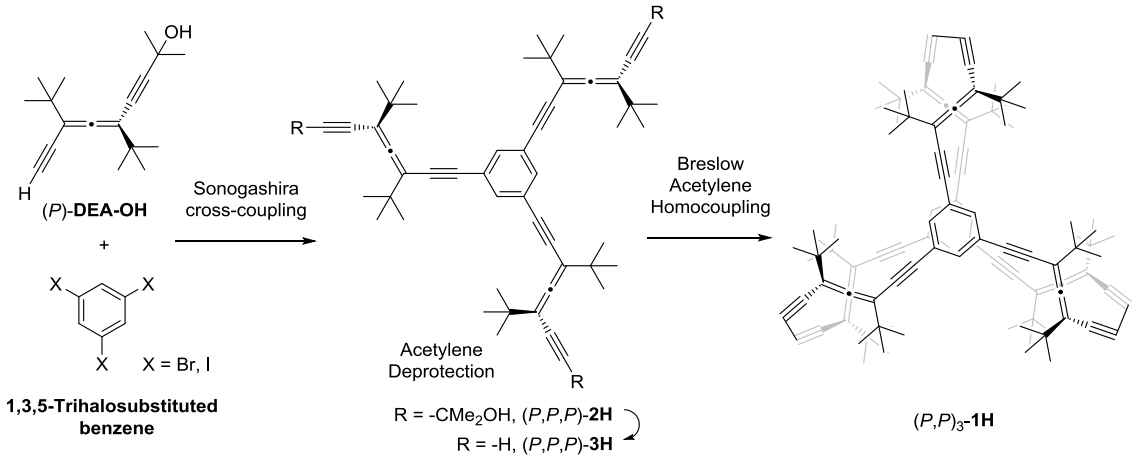

Scheme 9. Synthetic scheme of (*P*,*P*)$_3$-**1H**.

Protecting groups are employed in order to avoid undesired polymerization processes between tripods under Sonogashira conditions in the early stages.

3.2.1. Sonogashira reaction for the synthesis of (*P*,*P*,*P*)-2H and (*M*,*M*,*M*)-2H

Ditertbutyldiethynylallene (**DEA-OH**) was prepared following a previously reported procedure consisting on a 5-step-pathway involving several nucleophilic attacks over carbonyl group containing molecules, alcohol esterification, and a Pd-mediated S_N2' reaction with a racemate precursor (**Scheme 10**). After TIPS deprotection, the resultant racemic mixture was separated using a chiral stationary phase HPLC to give the pure enantiomers (*P*)-**DEA-OH** and (*M*)-**DEA-OH**.[62]

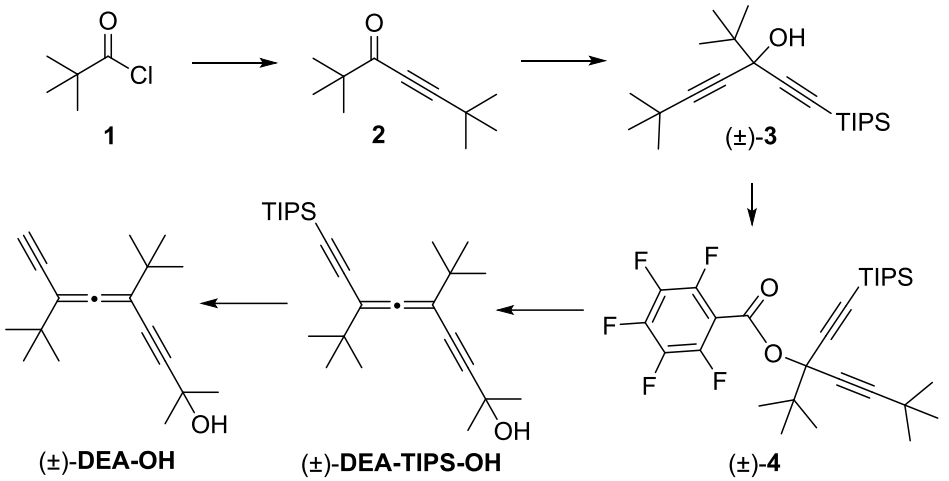

Scheme 10. Synthetic route to 1,3-ditertbutyldiethynyl allene (±)-**DEA-OH**.

Tricoupled product (*P,P,P*)-**2H** was proposed to be synthesized through a Sonogashira cross-coupling reaction between a 1,3,5-trihalosubstituted benzene and (*P*)-**DEA-OH** (**Scheme 11**).

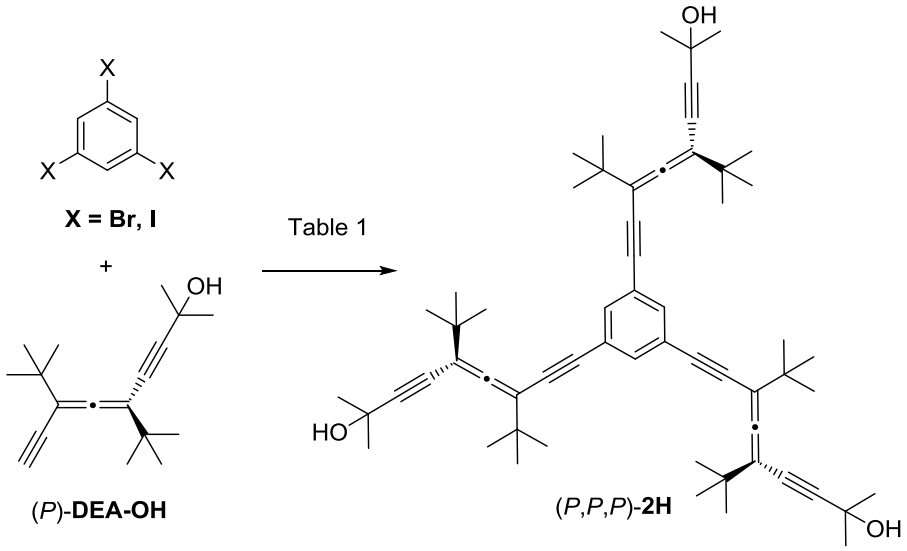

Scheme 11. Sonogashira cross-coupling reaction on the formation of (*P,P,P*)-**2H**.

The search of appropriate conditions (see **Table 1**) was performed, in order to improve the yield of this reaction and avoid the formation of the side products due to mono- and di- substitution processes shown in **Figure 2**.

Initially, the Sonogashira cross-coupling reaction was performed between the commercially available product 1,3,5-tribromobenzene and 3.3 eq of (*P*)-**DEA-OH**. Reaction conditions employed in this case (**Entry 1**, **Table 1**) made use of the classical reagents as $[PdCl_2(PPh_3)_2]$ (20 mol%), [CuI] (10 mol%) and Et_3N acting simultaneously as base and solvent. (*P,P,P*)-**2H** was obtained in a 23% yield after 46 h of reaction at 90 °C, along with side products (*P*)-**MC-2H-Br** in a 15% yield, (*P,P*)-**DC-2H-Br** in a 35% yield, and (*P,P*)-**DEA-OH$_2$** in a 16% yield (**Figure 2**).

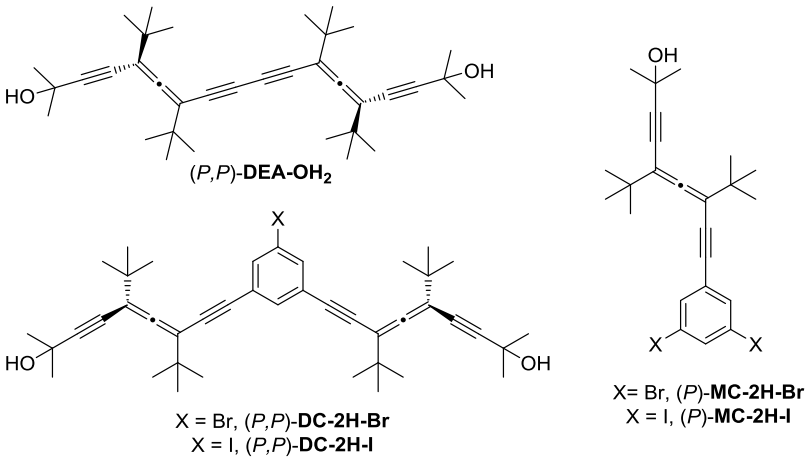

Figure 2. Side products on the formation of (*P,P,P*)-**2H**.

Given the abundance of mono- and dicoupled side products, it was thought that the major problem on the reaction conditions was the low reactivity of the 1,3,5-tribromobenzene starting material. Therefore, the more reactive 1,3,5-triiodobenzene was used instead. 1,3,5-triiodobenzene was synthesized in a 72% yield from 1,3,5-tribromobenzene by treatment with [CuI], and KI in distilled *N,N*-dimethylimidazolidinone under Ar at 200 °C for 17 h.[63]

A significant improvement of the yield on the Sonogashira reaction was observed, and (*P,P,P*)-**2H** was obtained in a 47% yield after 27 h of reaction at 90 °C (**Table 1**, **Entry 2**), along with a mixture of (*P,P*)-**DC-2H-I** and (*P,P*)-**DEA-OH$_2$**. Next, new conditions employing a more active [Pd] catalyst, bearing more hindered phosphines, as well as the addition of additives were tested. Following the conditions described by Li *et al* for 1,3,5-triethynylbenzene (**Table 1**, **Entry 3**), based on the use of [$Pd_2(dba)_3{\cdot}CHCl_3$] (7,5 mol%) as Pd catalyst, CuI (60 mol%), tetrabutylammonium iodide (TBAI) (6 eq) as a phase transfer agent, tri(o-tolyl)phosphine (60 mol%), refluxed DIPEA (10 eq) and freshly distilled DMF as solvent,[64] (*P,P,P*)-**2H** was obtained in a 64% yield after 22 h of reaction at r.t. This result shows the importance of the steric hindrance of the phosphine on the activity of the Pd catalyst. Thus, the use of a more hindered phosphine, trimesitylphosphine (**Table 1, Entry 4**), was tested yielding (*P,P,P*)-**2H** in an 80% yield, with no effect over the formation of the (*P,P*)-**DEA-OH$_2$**.

Entry	X	Conditions	t (h)	T(°C)	(*P,P,P*)-**2H**	(*P*)-**MC-2H-X**	(*P,P*)-**DC-2H-X**	(*P,P*)-**DEA-OH$_2$**
1	Br	$PdCl_2(PPh_3)_2$, CuI, Et_3N	46	90	15%	35%	23%	16%
2	I	$PdCl_2(PPh_3)_2$, CuI, Et_3N	27	90	47%	-	-	-
3	I	$Pd_2(dba)_3{\cdot}CHCl_3$, (o-tolyl)- phosphine, CuI, TBAI, DIPEA, DMF	22	−20 to r.t.	64%	-	-	16%
4	I	$Pd_2(dba)_3{\cdot}CHCl_3$, trimesitylphosphine, CuI, TBAI, DIPEA, DMF	21	−20 to r.t.	80%	-	-	16%

Table 1. Summary of Sonogashira cross−coupling reaction conditions tested.

Obtained results definitely evidence the higher reactivity of iodinated compared to brominated aryls, the importance of the catalyst activity, as well as the role of the phosphine bulkiness (**Figure 3**), which result in shorter reactions times, the possibility of employing lower reaction temperatures, and the favoring of multiple couplings *vs* single couplings over the same substrate.

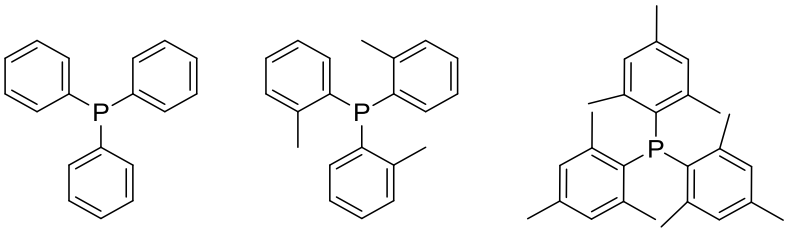

Figure 3. Phosphines employed on the Sonogashira cross-coupling reaction conditions tested. From left to right triphenylphosphine, tri-*o*-tolylphosphine, and trimesitylphosphine.

(*P,P,P*)-**2H**, (*P,P*)-**DC-2H-Br**, and (*P*)-**MC-2H-Br** were fully characterized by means of ^{1}H and ^{13}C NMR spectroscopies, IR, UV-Vis and electronic circular dichroism (ECD), and HR-EI/ESI-MS spectrometry. ^{1}H NMR of (*P*)-**MC-2H-Br** shows a triplet at 7.59 ppm and a doublet at 7.51 ppm, whilst (*P,P*)-**DC-2H-Br** shows the same pattern but exchanging positions, bearing a doublet at 7.50 ppm and a triplet at 7.43 ppm. However, spectrum of (*P,P,P*)-**2H** shows just one singlet at 7.44 ppm for the aromatic protons (**Figure 4**).

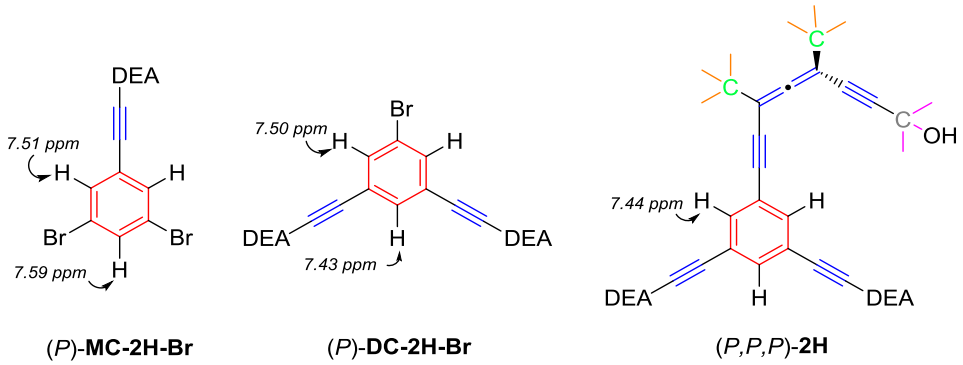

Figure 4. (*P*)-**MC-2H-Br**, (*P*)-**DC-2H-Br**, and (*P,P,P*)-**2H** indicating ^{1}H NMR chemical shifts of the aromatic hydrogens.

Regarding the ^{13}C NMR spectra of (*P*)-**MC-2H**, (*P,P*)-**DC-2H-Br**, and (*P,P,P*)-**2H**, diagnostic signals are the one at *ca.* 212 ppm from the cumulenic carbon (depicted in black on **Figure 4**), the region of the aromatic carbon atoms from 140 to 120 ppm (in red), the region from 105 to 75 ppm presenting alkynes and sp^2 allene carbon atoms (in blue), the one at *ca.* 75 ppm from the quaternary 2-hydroxypropyl protective group (in gray), the signals at *ca.* 35 ppm from the quaternary carbons of the ^{t}Bu groups (in green), the methyl at *ca.* 31 ppm from the protective groups (in pink), and the methyl of the ^{t}Bu groups at *ca.* 29 ppm (in orange).

A characteristic band on the IR spectra of (*P*)-**MC-2H-Br**, (*P,P*)-**DC-2H-Br**, and (*P,P,P*)-**2H**, is the allene C=C stretching at *ca.*1900 cm^{-1}.

Thus, the same procedure was accomplished to give the opposite enantiomer (*M,M,M*)-**2H**. Therefore once confirmed the identity of (*P,P,P*)-**2H** and its enantiomer (*M,M,M*)-**2H**, we continue with the next step of the synthesis of (*P,P*)$_3$-**1H** and (*M,M*)$_3$-**1H**.

3.2.2. Acetonide deprotection to (*P*,*P*,*P*)-3H and (*M*,*M*,*M*)-3H

Next step consists in the 2-hydroxypropyl group (-CMe_2OH, acetonide) deprotection of the alkynes. For that purpose we used a modification of the traditional treatment with NaOH in refluxing benzene.[65–68] Benzene was replaced by the less toxic solvent toluene. Two important factors should be considered in order to get satisfactory results in these reaction. On the one hand, the usage of anhydrous conditions, which prevent the hydrolysis of the base. For that, a procedure based on flaming the powdered NaOH under vacuum, and replacing the moist air by an inert gas such as nitrogen or argon is used. On the other hand, the use of an atmospheric pressure reflux helps the reaction to eliminate acetone, shifting the equilibrium to the products (**Scheme 12**).

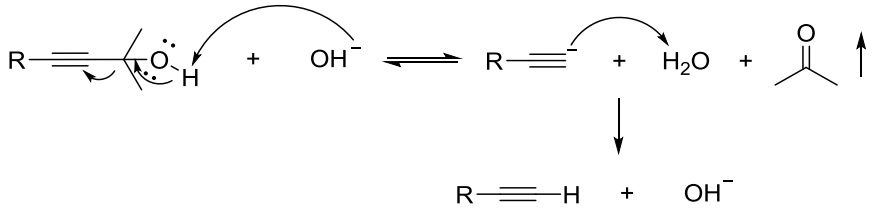

Scheme 12. Reaction mechanism of the 2-hydroxypropyl group deprotection of the alkyne.

Thus, compound (*P,P,P*)-**2H** was treated with powdered flamed NaOH (300 eq) in refluxing toluene under inert atmosphere[69] for 18 h, yielding (*P,P,P*)-**3H** in a 90% yield (**Scheme 13**).

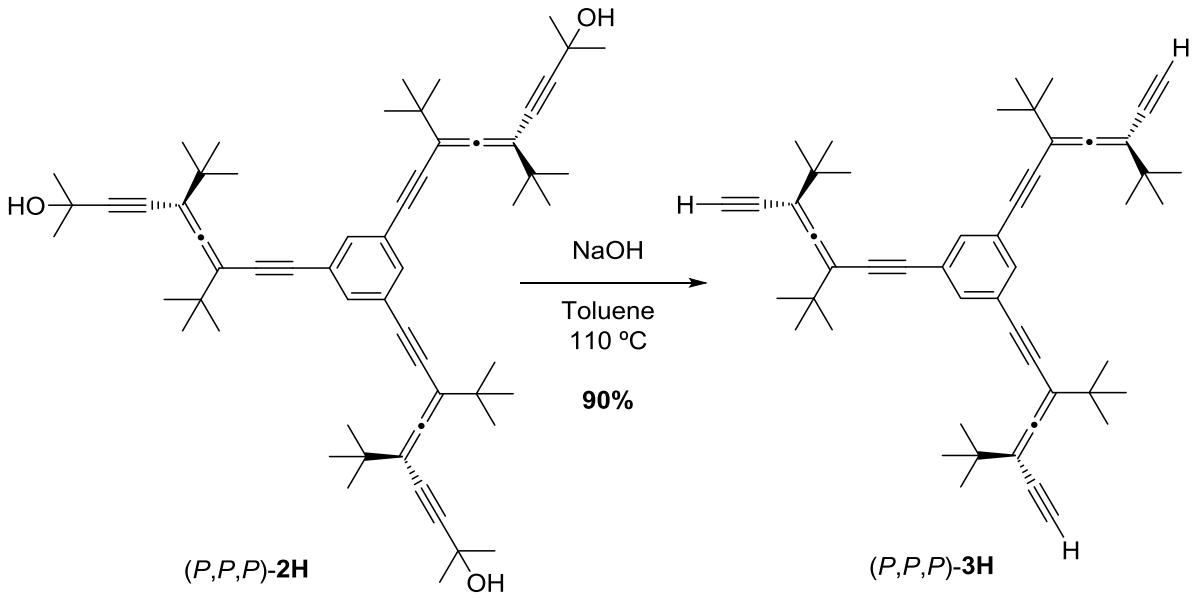

Scheme 13. Synthesis of (*P,P,P*)-**3H** through a deprotection reaction.

^{1}H NMR spectrum of (*P,P,P*)-**3H** shows a characteristic terminal alkyne signal at *ca.* 3 ppm. Regarding the IR spectrum, (*P,P,P*)-**3H** shows, besides the above cited bands for (*P,P,P*)-**2H**, a characteristic sharp band from the C_{alkyne}–H stretching at *ca.* 3300 cm^{-1}, which replaces the previous of the acetonide O–H stretching.

Once having in hand the tripodal shaped molecule (*P,P,P*)-**3H** and having it properly characterized, next step will be the synthesis of molecular cage $(P,P)_3$-**1H**.

3.2.3. Homodimerization for the synthesis of (*P*,*P*)$_3$-1H and (*M*,*M*)$_3$-1H

The synthesis of the molecular cage (*P*,*P*)$_3$-**1H** was proposed through Cu-catalyzed intermolecular homodimerization of the tripodal-shaped molecule (*P,P,P*)-**3H** (**Scheme 14**). The majority of tested conditions on the synthesis of (*P*,*P*)$_3$-**1H** were variants of Breslow's conditions, due to the awareness of the good results previously achieved in our group for different allenic substrates. Moreover, conditions employing relatively small Cu nanoparticles, following the works reported by F. Alonso *et al*, were also tested.[70,71] All conditions tested are summarized on **Table 2**. The first attempt (**Entry 1**) made use of a big excess of CuCl (75 eq) and $CuCl_2$ (11 eq) in dry pyridine at r.t. and inert atmosphere. Pseudo-high-dilution using an addition flow rate of 0.2 mL·h^{-1}, gave traces up to an 8% of (*P,P,P*)-**1H**, along with traces of the side product (*P,P,P*)-**6**, on the light of the ^{1}H NMR spectra results (**Figure 5**).

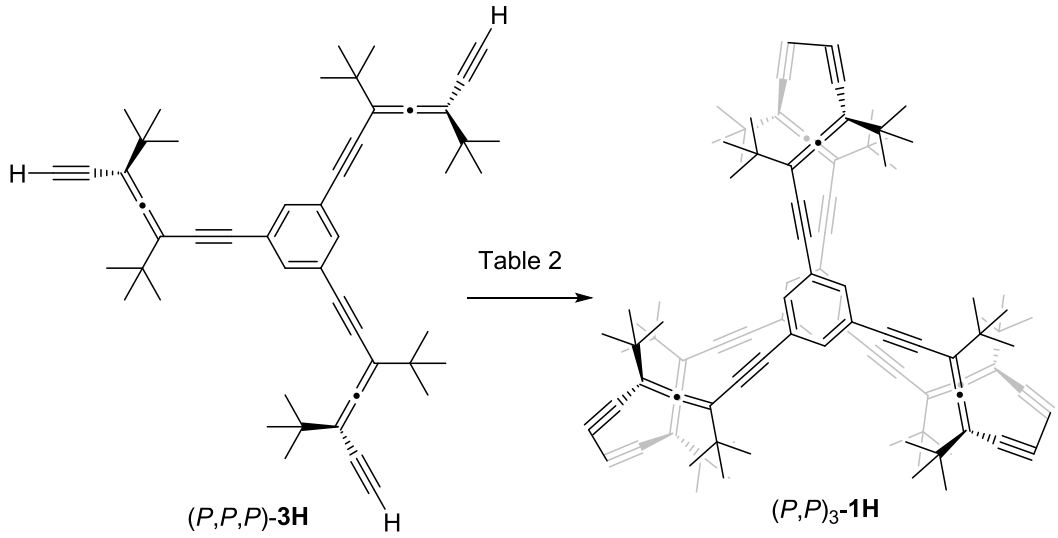

Scheme 14. Synthesis of (*P,P*)$_3$-**1** through a Cu-catalyzed homodimerization reaction.

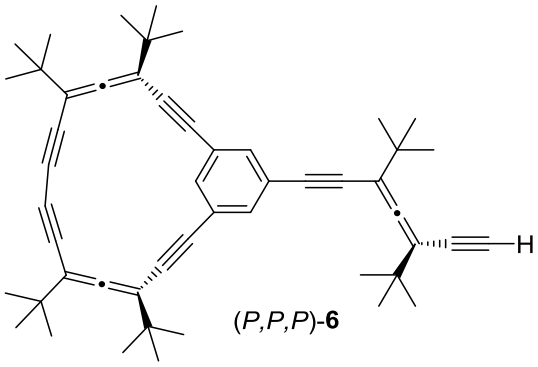

Figure 5. Structure of the side product (*P,P,P*)-**6**.

Conditions employed on **Entry 2**, the same as the previous but with a higher addition flow rate (0.5 mL·h^{-1}), and bubbling with Argon both solutions for 1 h, yielded (*P,P*)$_3$-**1H** in a 10% yield. Next attempt, **Entry 3**, made use of ultrafine novel TiO_2-supported Cu Nanoparticles,[70] in the presence of pyridine as the base in THF and air atmosphere, giving rise to the recovery of the starting material (*P,P,P*)-**3H**. **Entry 4** made use of Breslow conditions but increasing the addition flow rate to 1mL h^{-1}, and performing the workup right after the end of the slow addition,

resulting in a 17% yield of $(P,P)_3$-**1H**, whereas allowing the reaction to evolve for three days before the workup, $(P,P)_3$-**1H** was obtained in a 55% yield (**Entry 5**).

Entry	Conditions	$(P,P)_3$-**1H**	(P,P,P)-**6**	(P,P,P)-**3H**
1	CuCl (75 eq), $CuCl_2$ (11 eq), Py, r.t., Argon (bubbling 15 min), 3 days, ϕ = 0.2 mL·h^{-1}	Traces-8%	Traces	-
2	CuCl (75 eq), $CuCl_2$ (11 eq), Py, r.t., Argon (bubbling 1 h), 3 days, ϕ = 0.5 mL·h^{-1}	10%	-	-
3	Cu-NPs/TiO_2 1 ± 0.4 nm (5% mol eq), Py (1 eq), Dry THF, r.t., Air, 3 days, ϕ = 0.8 mL·h^{-1}	-	-	100%
4	CuCl (75 eq), $CuCl_2$ (11 eq), Py, r.t., Argon (bubbling 30 min), 24 h, ϕ = 1 mL·h^{-1}	17%	-	-
5	CuCl (75 eq), $CuCl_2$ (11 eq), Py, r.t., Argon (bubbling 30 min), 3 days, ϕ = 1 mL·h^{-1}	55%	-	-

Table 2. Homodimerization reaction conditions tested. Labels $(P,P)_3$-**1H**, (P,P,P)-**3H**, and (P,P,P)-**6** make reference to the cage product, starting material, and by-product respectively. ϕ = addition flow rate.

Compound $(P,P)_3$-**1H** was fully characterized by means of ^{1}H, ^{13}C and bidimensional NMR experiments, IR, UV-Vis and ECD spectroscopies, as well as by HR-MALDI-MS and X-ray crystallography. Despite the presence of a high number (112) of H atoms in $(P,P)_3$-**1H**, its ^{1}H NMR spectrum shows just three non-equivalent Hs due to its high symmetry (D_3) (**Figure 6**). Specifically, an aromatic non-equivalent H at 7.38 ppm and two aliphatic Hs at 1.19 an 1.18 ppm from the ^{t}Bu groups, using CD_2Cl_2 as the solvent. ^{13}C NMR spectrum shows a total of 13 signals: a cumulenic at 215 ppm, two aromatic at 133 and 124 ppm, two allenic sp^2 at *ca.* 104 and 103 ppm, four signals for the alkynes between 92 and 76 ppm, two quaternary carbons of the ^{t}Bu groups at *ca.*36 and 35 ppm, and two signals at *ca.* 29 ppm from the methyls of the ^{t}Bu groups (**Figure 6)**. The assignation of all the signals on the spectra with their respective H and C atoms was made through the interpretation of the two-dimensional NMR spectra (**Figure 6**).

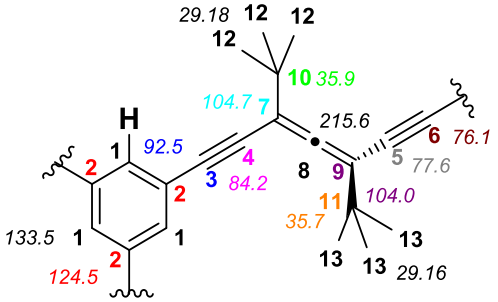

Figure 6. Reduced schematic representation of the $(P,P)_3$-**1H** showing the labels used for the different C and H atoms in the molecule and their respective ^{13}C NMR chemical shifts.

H^1 and C^1 showed a direct coupling on the HSQC (Heteronuclear Single Quantum Correlation) spectrum. C^2 corresponds to the quaternary carbon on the aromatic. Heteronuclear Multiple

Bond Correlation spectrum (HMBC) (**Figure 7**) helped to assigned all the other carbons. Thus, C^3 and C^4 were assigned by proximity to the H^1 with which they couple at three and four bonds of distance respectively. It can also be seen the coupling between H^{12} with C^{10} and C^7, as well as the coupling of H^{13} with C^{11} and C^9. Cumulenic C^8 was assigned due to its characteristic chemical shift.

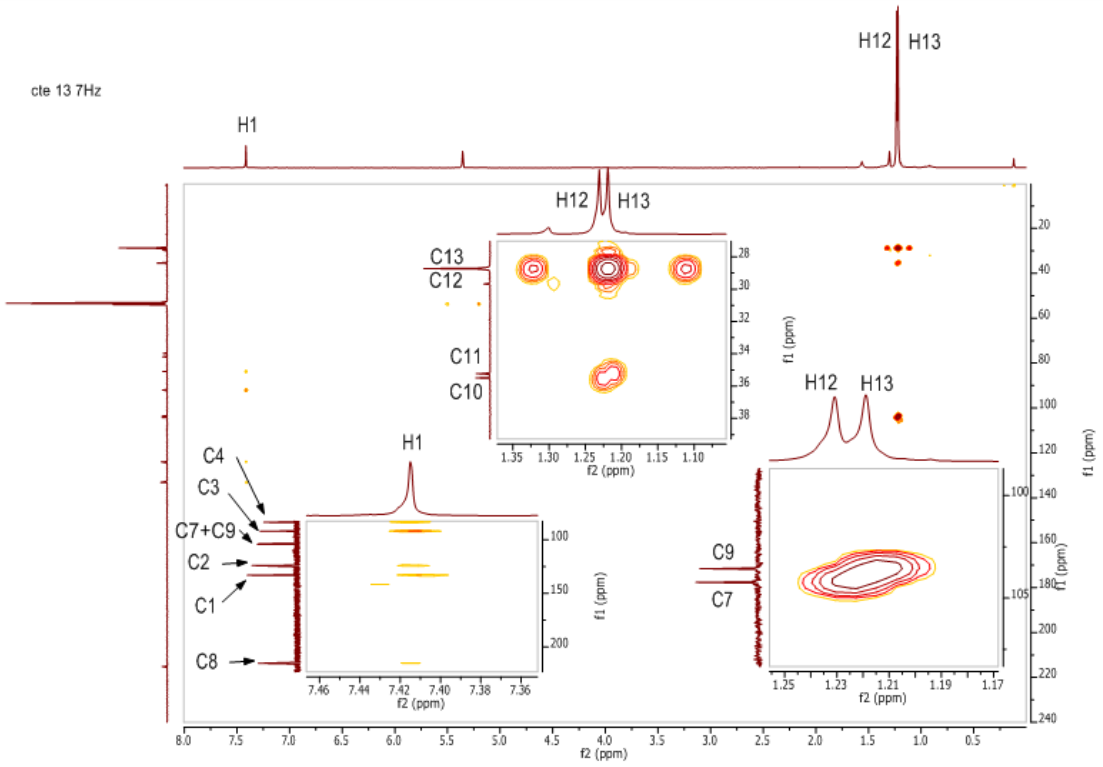

Figure 7. HMBC NMR spectrum of $(P,P)_3$-**1H**.

HR-MALDI-MS analysis of $(P,P)_3$-**1H** showed the presence of the molecular ion $[M]^+$ at *m/z* 1340.90379. It is noteworthy that the molecular mass was not detected with ESI ionization technique, suggesting the need of a milder ionization for large organic molecules. Surprisingly, peaks for different fullerenes, C_{60}, C_{110}, C_{112}, and C_{114} with a similar intensity as the molecular ion of $(P,P)_3$-**1H** were found on the MALDI-MS analysis (**Figure 8**). A possible explanation for this would be the transformation of one or several $(P,P)_3$-**1H** molecules ($C_{102}H_{114}$) or even fragmentations of those into the abovementioned fullerenes through a process of coalescence and annealing, whose energy source is provided by the MALDI laser.[72]

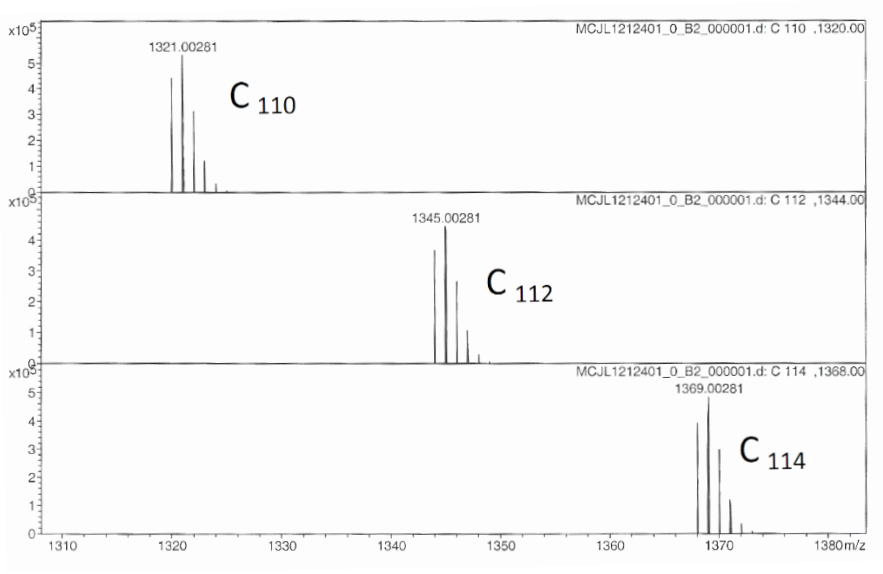

Figure 8. Cutout of HR-MALDI-MS of (*P,P*)$_3$-**1H** showing C_{110}, C_{112} and C_{114} fullerenes formation.

Taking into account the small number of signals obtained on the ^{1}H NMR spectra due to the strongly unsaturated character and symmetry of the molecule, X-Ray Diffraction studies provided a complete picture of the 3D structure of cage (*P,P*)$_3$-**1H**.

Crystallization attempts involved the use of one solvent or a binary mixture of solvents. Moreover, different containers were employed, which involve different volumes of solvent and a different exposition surface with the atmosphere, as well as different temperatures, which imply different evaporation rates. The variety of solvents used went from apolar hexane and pentane, to medium polar chloroform and dichloromethane, to the more polar ones such as acetone and alcohols. (*M*,*M*)$_3$-**1H** was crystallized from a mixture diethylether:methanol. The analysis of the crystalline network showed a unit cell with two independent (*M*,*M*)$_3$-**1H** molecules with different conformations. One of the molecules is more twisted and has a *tert*butyl pointing inwards the other cage within the unit cell. This leads to the intercentroid distances 8.0 Å and 8.6 Å respectively. The inner cavities of both cages are full of disordered solvent molecules and there are no channels or pores all along the network (**Figure 9**). The presence of two different conformations in the unit cell of (*M*,*M*)$_3$-**1H** indicates a certain degree of flexibility in the molecule, whose allenic dihedral angles are slightly prone to be deformed.

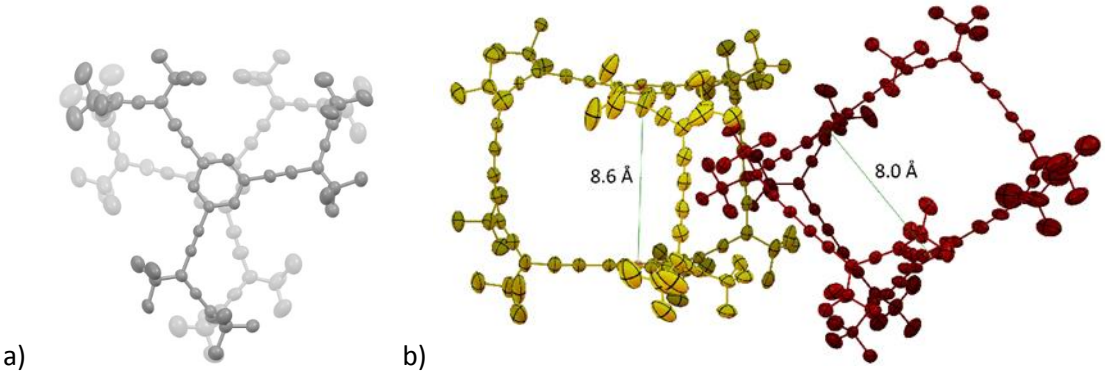

Figure 9. a) Ellipsoidal representation of one of the two conformers presented in the unit cell of the crystalline structure of (*M,M*)$_3$-**1H**. b) Ellipsoidal representation of the unit cell. CCDC 1062729.

The ECD spectrum of helical cage (*P*,*P*)$_3$-**1H** features a very intense positive band at 247 nm ($\Delta\varepsilon$ = 613 L·mol^{-1}·cm^{-1}) and four negative bands at 260, 280, 300, and 315 nm (**Figure 10**). The spacing between them of *ca.* 2200 cm^{-1} is in good agreement with the presence of a vibronic progression. ECD spectrum of (*M*,*M*)$_3$-**1H** was also recorded displaying a mirror image with its enantiomer. Compared to the ECD intensity of six units of (*M*)-**DEA**,[73] (*M*,*M*)$_3$-**1H** and (*P*,*P*)$_3$-**1H** present a 10-fold chiroptical amplification (**Figure 11**). As mentioned above, conformational stability is important to reach strong chiroptical responses since different conformations of the same species typically feature very distinct chiroptical responses that may at least partially cancel out.[74] Thus, the intense chiroptical response achieved for (*M*,*M*)$_3$-**1H** gives us an idea of its high shape-persistency.

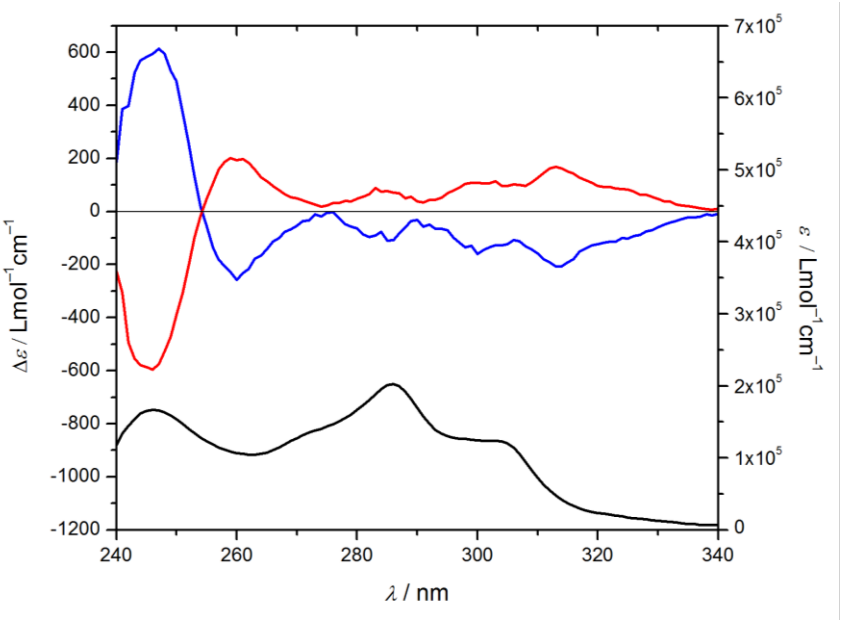

Figure 10. Absorbance spectrum (lower, black) and ECD (upper) of (*P*,*P*)$_3$-**1H** (blue) and (*M*,*M*)$_3$-**1H** (red) in $CHCl_3$ at *ca.* 10^{-5} M.

By comparing (*M*,*M*)$_3$-**1H** presenting a single conformation with its precursor (*M*,*M*,*M*)-**3H**, featuring high conformational freedom, the ECD intensities of the synthesized chiral cage are considerably enhanced (**Figure 11**). The anisotropy or dissymmetry *g*-factor is the ratio between the ECD and the absorption, $\Delta\varepsilon/\varepsilon$, and measures the efficiency of the sample to differentiate between left and right circularly polarized light.[75] In isotropic solutions of organic molecules, systems featuring strong chiral *g*-factors include polyaromatics[76] as well as alleno-acetylenic macrocycles[77] and oligomers,[78] with absolute values between 10^{-2} and 10^{-3}. The maximum *g*-factor of (*P*,*P*)$_3$-**1H** and (*M*,*M*)$_3$-**1H** in chloroform, with a value of $6\cdot10^{-3}$, is among the most intense for organic molecules and outstanding for purely organic covalent cages.[79–81]

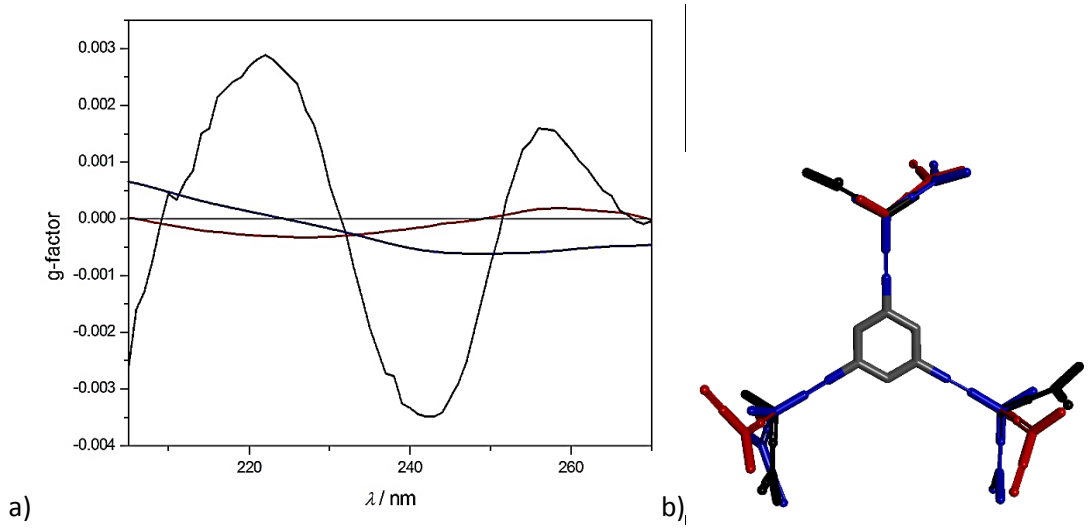

Figure 11. a) Comparison of *g*-factor for (*M,M*)$_3$-**1H** (black), (*M,M,M*)-**3H** (blue) and (*M*)-**DEA-OH** (red) in hexane. b) Rotation of the (*P*)-**DEA-OH** moieties about the single bonds connecting it to the aromatic core in (*P,P,P*)-**3H**.

In summary, we have efficiently synthesized the two enantiomers of a helical prism-like cage. The helicity of (*M,M*)$_3$-**1H** with D_3 symmetry was unambiguously confirmed by X-ray crystallography. (*P,P*)$_3$-**1H** and its enantiomer (*M,M*)$_3$-**1H** feature outstanding chiroptical responses among covalent organic cages. The chiroptical enhancement of this organic helical cage compared to other allenophanic analogues[82] stems from its shape-persistence.

Now we have in hand a cavity prompt for inclusion complex formation, such feature will be addressed in the following section.

3.3. Complexation studies: [(*P,P*)$_3$-1H@Guests]

Molecular Dynamics studies presented on Chapter 2 pointed out a series of appropriate guests to reach stable complexes with molecular cage (*P,P*)$_3$-**1H**. Among them, the best results were obtained for triphenylene derivatives bearing three positively-charged functional groups, as for example the triply charged **HATP-Asym** (**Figure 12**). However, the difficulty of generating such molecules led us to try with the neutral ones, and subsequently protonate them. Besides triphenylene derivatives, benzene derivatives were also tested (**Figure 12**).

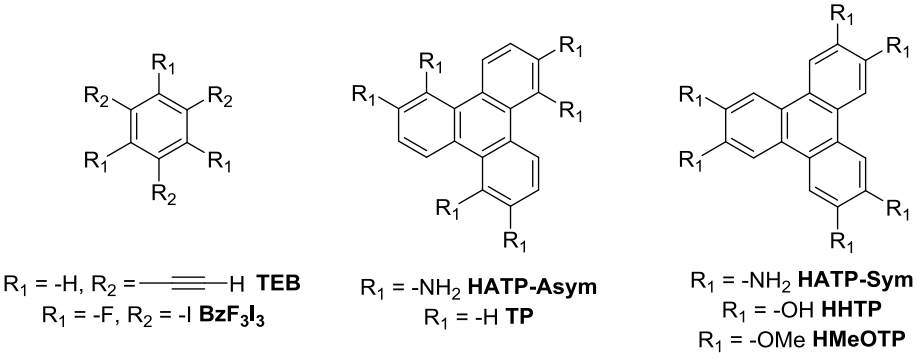

Figure 12. Aromatic guests selected for complexation tests with cage (*P,P*)$_3$-**1H**.

Complexation tests were made by performing ^{1}H NMR titrations in which small portions of the guest were added, either solid or in solution, to a solution of known concentration of (*P,P*)$_3$-**1H**. Such additions were done in the NMR tube. The measured observable in all cases was the chemical shift of aromatic Hs as well as those from *t*Bu groups of the cage. Data was analyzed by plotting the variation of the chemical shift (Δ*δ*) *vs* the number of equivalents of guest added. The plot of 1/Δ*δ* *vs* 1/[guest], known as Benesi-Hildebrand data treatment,[83] was done for those that present a significant chemical shift change of the ^{1}H NMR signal and show a clear saturation curve, in order to determine association constant (K_a) for the complexes [(*P,P*)$_3$-**1H**@guest].

Attempts to synthetize **HATP-Asym** following the known procedure[84] were unsuccessful, therefore this compound could not be tested. Hexaaminotriphenylene **HATP-Sym** and **HMeOTP** were prepared in a 94% and 80% yield, respectively, through an oxidative trimerization of *o*-phenylenediamine or *o*-dimethoxybenzene, using a previously reported procedure for similar substrates (**Scheme 15**).[85] The complexation of both **HATP-Sym** and **HMeOTP** with (*P,P*)$_3$-**1H** could not be established, due to the low solubility of both guests in CD_2Cl_2 and $CDCl_3$.

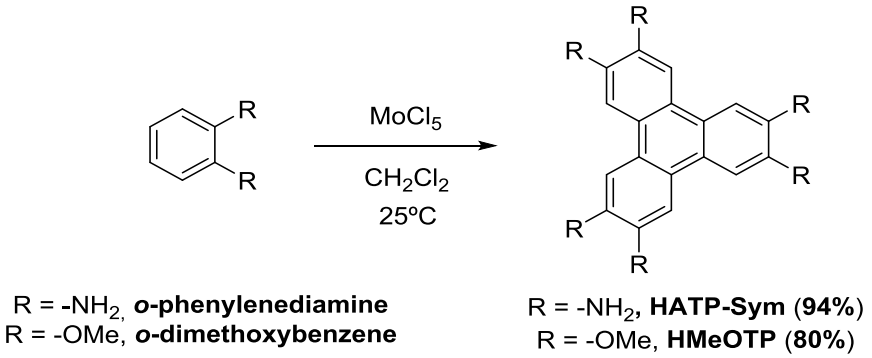

Scheme 15. Synthesis of **HATP-Sym** and **HMeOTP**.

Next complexation attempt was made with the commercially available hexahydroxytriphenylene (**HHTP**) in THF-d_6. Despite the good solubility of **HHTP** in such solvent, the chemical shift of the aromatic H of (*P,P*)$_3$-**1H** in the presence of a big excess of **HHTP** was of *ca.* 0.006 ppm, which is on the order of the ^{1}H NMR error. Thus, no association constant could be determined. On the other hand, although an analyzable Δ*δ* of the aromatic Hs of **1H** was obtained with triphenylene (**TP**) in deuterated benzene or deuterated dichloromethane, the saturation point was not reached.

1,3,5-triethynylbenzene (**TEB**) was prepared following the procedure depicted in **Scheme 16** .[86] Its complexation with **1H** was then tested in C_6D_6 at r.t. The shift of the aromatic signal of **1H** moved randomly upfield and downfield, but on the order of the NMR error, indicating no complex formation.

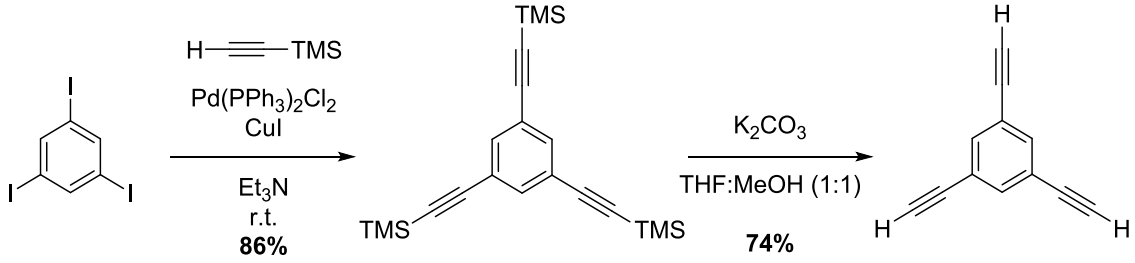

Scheme 16. Synthesis of **TEB**.

1,3,5-Trifluoro-2,4,6-triiodobenzene (**BzF_3I_3**), presenting a more electron deficient character, more appropriate for the complexation with (*P,P*)$_3$-**1H** was also tested. The maximum $\Delta\delta$ observed was *ca.* 0.1 ppm, slightly reaching the saturation point, and the Benesi−Hildebrand plot (**Figure 13**, right side) showing a good linearity, through which a small association constant of *ca.* 9 M^{-1} was determined (**Equation 1**).

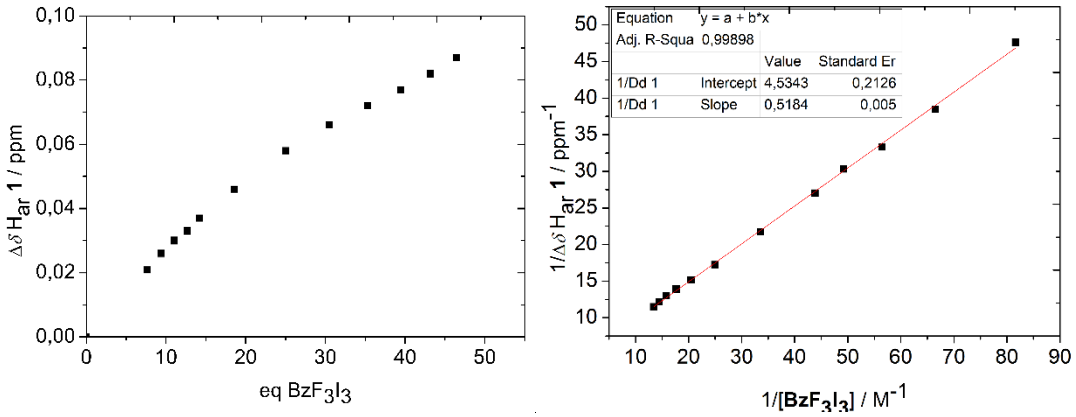

Figure 13. Saturation curve (left) and Benesi-Hildebrand representation (right) for (*P,P*)$_3$-**1H@BzF_3I_3**.

$$y = a + b \cdot x \qquad\qquad K_a = \frac{a}{b}$$

Equation 1. General equation of a linear regression line, being *a* the intercept and *b* the slope (left) and Benesi-Hildebrand determination of the association constant (K_a) through such parameters (right).

The achieved results were analyzed in terms of accomplishment of the ideal 55% packing coefficient rule enunciated by Mecozzi and Rebek.[87] Since cavity of (*P,P*)$_3$-**1H** is laterally open, we approximated it to that of a cylinder, considering a radius R = 4.3 Å, and a height h = 8.3 Å, whose values were taken from the reported crystalline structure of (*M,M*)$_3$-**1H**. Thus, the cylinder volume, calculated as $\pi \cdot R^2 \cdot h$, is 482 Å^3. Guest volumes, as well as packing coefficients with respect to the calculated cylinder volume, are given in **Figure 14**, showing that, if only steric effects were considered, the most appropriate guests would be **TP**, and **HHTP**. However, the complex formation with those has not been detected.

GUEST	V (Å^3)[A]	P. C. (%)[B]
TEB	186.7	39
BzF_3I_3	189.7	39
TP	259.0	54
HHTP	294.1	61
HATP-Asym	312.5	64.8
HATP-Sym	314.6	65.3
HMeOTP	415.1	86

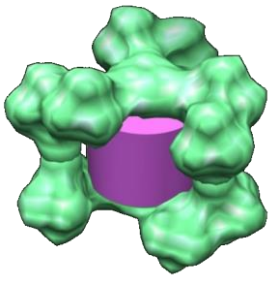

Figure 14. Left: Guest volumes and respective packing coefficients with respect to the average cylindrical cavity size. [a] Guest volumes were calculated using *Spartan'14* V1.1.2 considering a summation of atoms with van der Waals radii of a CPK model of a molecule with a defined optimized geometry. [b] Packing Coefficients (P.C.) were calculated as the ratio between the guest volume and the approximated cylindrical cavity volume. Right: Space-filling model of (*P,P*)$_3$-**1H** (green) with cylinder inside its cavity (pink).

In order to achieve a better understanding of the poor results achieved on the complexations of the abovementioned flat aromatic guests with (*P,P*)$_3$-**1H**, the electrostatic potential of both guests and the core of (*P,P*)$_3$-**1H** were calculated and mapped over the electron density surface, using *Gaussian 09* at the B3LYP/6-31G(d) level of theory, except for **BzF$_3$I$_3$** for which B3LYP/LanL2DZ level of theory was employed (**Figure 15**).[88] The core of (*P,P*)$_3$-**1H** shows a neutral to slightly rich electronic character, so, it is conceivable that it will stablish complexations with those guests bearing electron poor character. Both triphenylene and their derivatives have electronic characters ranging from the neutrality (as in the case of **HHTP** in green) to the electronic richness (as the rest in orange-red). The only proposed flat guest having poor electronic character, due to the presence of the six halogens on the benzenic ring, is **BzF$_3$I$_3$**, which is in fact the only guest showing positive results towards complexation with molecular cage (*P,P*)$_3$-**1H**.

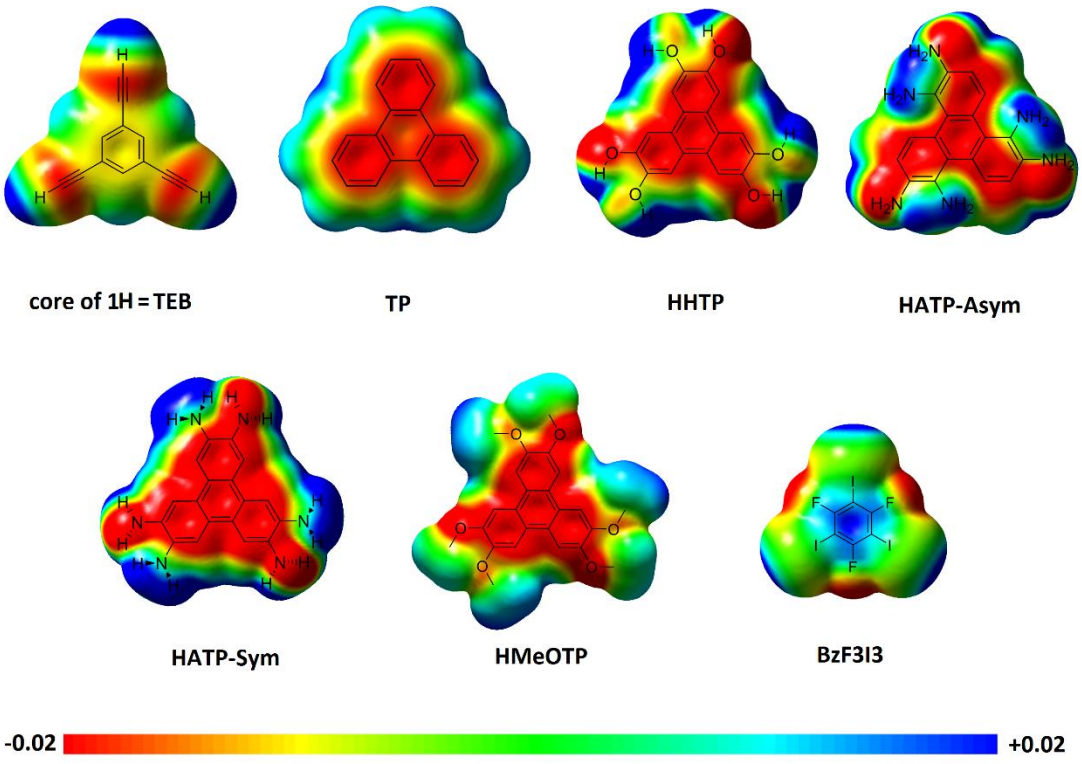

Figure 15. Representation of the electrostatic potential mapped over the electronic density surface of the aromatic core of (*P,P*)$_3$-**1H** and the tested guests with *Gaussian 09* at the B3LYP/6-31G(d) level of theory, except for **BzF$_3$I$_3$** using B3LYP/LanL2DZ level of theory (isovalue = 0.020, density = 0.00040). Color scale: red indicating electron rich and blue electron poor regions.

These results show the prevalence of the electronic character of the guest over the steric effects. Moreover, the main supramolecular interaction that our system can stablish with the proposed guest is π–π stacking, and given the large height of (*P,P*)$_3$-**1H** (*ca.* 8.3 Å of intercentroid distance) compared to the VdW diameter of the carbon atom in the benzene molecule, 3.4 Å, such interaction would take place with just one of the lids of (*P,P*)$_3$-**1H**. Therefore, guests with the capability of interacting with both lids are desired.

3.4. References

[1] L. Cassar, *J. Organomet. Chem.* **1975**, *93*, 253–257.

[2] H. A. Dieck, and F. R. Heck, *J. Organomet. Chem.* **1975**, *93*, 259–263.

[3] K. Sonogashira, Y. Tohda, and N. Hagihara, *Tetrahedron Lett.* **1975**, *16*, 4467–4470.

[4] R. Chinchilla, and C. Nájera, *Chem. Rev.* **2007**, *107*, 874–922.

[5] R. Chinchilla, and C. Nájera, *Chem. Soc. Rev.* **2011**, *40*, 5084–5121.

[6] X.-F. Wu, P. Anbarasan, H. Neumann, and M. Beller, *Angew. Chem. Int. Ed.* **2010**, *49*, 9047–9050.

[7] K. C. Nicolaou, P. G. Bulger, and D. Sarlah, *Angew. Chem. Int. Ed.* **2005**, *44*, 4442–4489.

[8] K. Sonogashira, *J. Organomet. Chem.* **2002**, *653*, 46–49.

[9] L. Xue, and Z. Lin, *Chem. Soc. Rev.* **2010**, *39*, 1692–1705.

[10] K. L. Vikse, M. A. Henderson, A. G. Oliver, and J. S. McIndoe, *Chem. Commun.* **2010**, *46*, 7412–7414.

[11] Vincent Grosshenny, Francisco M. Romero, and R. Ziessel, *J. Org. Chem.* **1997**, *62*, 1491–1500.

[12] G. P. McGlacken, and I. J. S. Fairlamb, *European J. Org. Chem.* **2009**, *2009*, 4011–4029.

[13] W. B. Austin, N. Bilow, W. J. Kelleghan, and K. S. Y. Lau, *J. Org. Chem.* **1981**, *46*, 2280–2286.

[14] M. Beaupérin, A. Job, H. Cattey, S. Royer, P. Meunier, and J.-C. Hierso, *Organometallics* **2010**, *29*, 2815–2822.

[15] G. Evano, N. Blanchard, and M. Toumi, *Chem. Rev.* **2008**, *108*, 3054–3131.

[16] H. Plenio, *Angew. Chem. Int. Ed.* **2008**, *47*, 6954–6956.

[17] P. Li, and L. Wang, *Synlett* **2006**, *2006*, 2261–2265.

[18] V. K. Kanuru, G. Kyriakou, S. K. Beaumont, A. C. Papageorgiou, D. J. Watson, and R. M. Lambert, *J. Am. Chem. Soc.* **2010**, *132*, 8081–8086.

[19] L. Feng, F. Liu, P. Sun, and J. Bao, *Synlett* **2008**, *2008*, 1415–1417.

[20] J.-H. Li, J.-L. Li, D.-P. Wang, S.-F. Pi, Y.-X. Xie, M.-B. Zhang, and X.-C. Hu, *J. Org. Chem.* **2007**, *72*, 2053–2057.

[21] M. Carril, A. Correa, and C. Bolm, *Angew. Chem. Int. Ed.* **2008**, *47*, 4862–4865.

[22] H. N. Borah, D. Prajapati, and R. C. Boruah, *Synlett* **2005**, *2005*, 2823–2825.

[23] L. Wang, P. Li, and Y. Zhang, *Chem. Commun.* **2004**, *95*, 514–515.

[24] V. K. Kanuru, S. M. Humphrey, J. M. W. Kyffin, D. A. Jefferson, J. W. Burton, M. Armbrüster, and R. M. Lambert, *Dalt. Trans.* **2009**, *107*, 7602–7605.

[25] S. Park, M. Kim, D. H. Koo, and S. Chang, *Adv. Synth. Catal.* **2004**, *346*, 1638–1640.

[26] D. R. Coulson, L. C. Satek, and S. O. Grim, *Inorg. Synth.* **1972**, *13*, 121–124.

[27] N. Kann, and Nina, *Molecules* **2010**, *15*, 6306–6331.

[28] Y. Lunxiang, and J. Liebscher, *Chem. Rev.* **2007**, *107*, 133–173.

[29] Z. Novák, A. Szabó, J. Répási, and A. Kotschy, *J. Org. Chem.* **2003**, *68*, 3327–3329.

[30] M. Alami, F. Ferri, and G. Linstrumelle, *Tetrahedron Lett.* **1993**, *34*, 6403–6406.

[31] A. V. Nyuchev, E. A. Sharonova, N. A. Lenshina, A. S. Shavyrin, M. A. Lopatin, I. V. Balalaeva, I. P. Beletskaya, and A. Y. Fedorov, *Synthesis of Fluorescent Coumarin Triazolylglycosides*, **2011**.

[32] K. Nakamura, H. Okubo, and M. Yamaguchi, *Synlett* **1999**, *1999*, 549–550.

[33] A. J. Boydston, M. M. Haley, R. Vaughan Williams, and J. R. Armantrout, *J. Org. Chem.* **2002**, *76*, 8812–8819.

[34] A. Tougerti, S. Negri, and A. Jutand, *Chem. Eur. J.* **2007**, *13*, 666–676.

[35] S. Thorand, and K. Norbert, *J. Org. Chem.* **1998**, *63*, 8551–8553.

[36] M. Kivala, C. Boudon, J.-P. Gisselbrecht, P. Seiler, M. Gross, and F. Diederich, *Angew. Chem. Int. Ed.* **2007**, *46*, 6357–6360.

[37] C. R. Hopkins, and N. Collar, *6-Substituted-5H-pyrrolo[2,3-B]pyrazines via Palladium-Catalyzed Heteroannulation from N-(3-Chloropyrazin-2-Yl)-Methanesulfonamide and Alkynes*, **2004**.

[38] J. Uenishi, K. Matsui, and H. Ohmiya, *J. Organomet. Chem.* **2002**, *653*, 141–149.

[39] B. Dhudshia, and A. N. Thadani, *Chem. Commun.* **2006**, *11*, 668–670.

[40] A. Mori, J. Kawashima, T. Shimada, M. Suguro, K. Hirabayashi, and Y. Nishihara, *Org. Lett.* **2000**, *2*, 2935–2937.

[41] S. Höger, *J. Polym. Sci. Part A Polym. Chem.* **1999**, *37*, 2685–2698.

[42] P. Siemsen, R. C. Livingston, and F. Diederich, *Angew. Chem. Int. Ed.* **2000**, *39*, 2632–2657.

[43] H. a. Stefani, A. S. Guarezemini, and R. Cella, *Tetrahedron* **2010**, *66*, 7871–7918.

[44] A. Hay, *J. Org. Chem.* **1960**, *25*, 1275–1276.

[45] A. S. Hay, *J. Org. Chem.* **1962**, *27*, 3320–3321.

[46] G. Eglinton, and A. R. Galbraith, *Chem. Ind.* **1956**, 737–738.

[47] D. O'Krongly, S. R. Denmeade, M. Y. Chiang, and R. Breslow, *J. Am. Chem.Soc.* **1985**, *107*, 5544–5545.

[48] R. Rossi, A. Carpita, and C. Bigelli, *Tetrahedron Lett.* **1985**, *26*, 523–526.

[49] F. Diederich, P. J. Stang, and R. R. Tykwinski, *Modern Supramolecular Chemistry : Strategies for Macrocycle Synthesis*, Wiley-VCH, Weinheim, **2008**.

[50] C. Glaser, *Ber. Dtsch. Chem. Ges.* **1869**, *2*, 422–424.

[51] C. Glaser, *Ann. Chem. Pharm.* **1870**, *154*, 137–171.

[52] W. Chodkiewicz, and P. Cadiot, *C. R. Hebd. Seances Acad. Sci.* **1955**, *241*, 1055–1057.

[53] W. Chodkiewicz, *Ann. Chim.* **1957**, *2*, 819–869.

[54] G. Eglinton, and W. McRae, *Adv. Org. Chem.* **1963**, *4*, 225–328.

[55] T. F. Rutledge, in *Acetylenic Compd.*, Reinhold, New York, **1968**, p. 245.

[56] P. Cadiot, and W. Chodkiewicz, Viehe, H. G, Eds., Dekker, New York, **1969**, p. 597.

[57] L. Fomina, B. Vazquez, E. Tkatchouk, and S. Fomine, *Tetrahedron* **2002**, *58*, 6741–6747.

[58] L. Kurti, and B. Czako, *Strategic Applications of Named Reactions in Organic Synthesis : Background and Detailed Mechanisms.*, Elsevier Science, Burlington, M.A., **2005**.

[59] A. E. Wendlandt, A. M. Suess, and S. S. Stahl, *Angew. Chem. Int. Ed.* **2011**, *50*, 11062–11087.

[60] P. Ruggli, *Justus Liebig's Ann. der Chemie* **1912**, *392*, 92–100.

[61] Hans R. Kricheldorf, and S. Böhme, and G. Schwarz, *Macromolecules* **2001**, *34*, 8879–8885.

[62] J. L. Alonso-Gómez, P. Schanen, P. Rivera-Fuentes, P. Seiler, and F. Diederich, *Chemistry* **2008**, *14*, 10564–10568.

[63] K.-I. Yamashita, M. Tsuboi, M. S. Asano, and K.-I. Sugiura, *Synth. Commun.* **2012**, *42*, 170–175.

[64] J. Li, and P. Huang, *Res. Chem. Intermed.* **2011**, *38*, 403–411.

[65] C. S. Swindell, W. Fan, and P. G. Klimko, *Tetrahedron Lett.* **1994**, *35*, 4959–4962.

[66] S. J. Harris, and D. R. M. Walton, *Tetrahedron* **1978**, *34*, 1037–1042.

[67] J. G. Rodríguez, R. Martín-Villamil, F. H. Cano, and I. Fonseca, *J. Chem. Soc. Perkin Trans. 1* **1997**, *113*, 709–714.

[68] P. G. M. Wuts, and T. W. Greene, *Greene's Protective Groups in Organic Synthesis*, John Wiley & Sons, Inc., Hoboken, NJ, USA, **2006**.

[69] C. Sicre, Regioselectividad En Acoplamientos Cruzados Catalizados Por Paladio de 2,4-Dibromopiridina. Síntesis Estereoselectiva Del Pigmento Ocular A2E., Universidade de Vigo, **2006**.

[70] F. Alonso, T. Melkonian, Y. Moglie, and M. Yus, *European J. Org. Chem.* **2011**, 2524–2530.

[71] F. Alonso, and M. Yus, *ACS Catal.* **2012**, *2*, 1441–1451.

[72] S. W. McElvany, M. M. Ross, N. S. Goroff, and F. Diederich, *Science (80-.).* **1993**, *259*, 1594–1596.

[73] J. L. Alonso-Gómez, P. Schanen, P. Rivera-Fuentes, P. Seiler, and F. Diederich, *Chem. Eur. J.* **2008**, *14*, 10564–10568.

[74] G. Pescitelli, L. Di Bari, and N. Berova, *Chem. Soc. Rev.* **2011**, *40*, 4603–4625.

[75] W. Kuhn, *Trans. Faraday Soc.* **1930**, *26*, 293–308.

[76] R. S. Walters, C. M. Kraml, N. Byrne, D. M. Ho, Q. Qin, F. J. Coughlin, S. Bernhard, and J.

Robert A. Pascal, *J. Am. Chem. Soc.* **2008**, *130*, 16435–16441.

[77] J. L. Alonso-Gómez, P. Rivera-Fuentes, N. Harada, N. Berova, and F. Diederich, *Angew. Chem. Int. Ed.* **2009**, *48*, 5545–5548.

[78] P. Rivera-Fuentes, J. L. Alonso-Gómez, A. G. Petrovic, F. Santoro, N. Harada, N. Berova, and F. Diederich, *Angew. Chem. Int. Ed.* **2010**, *49*, 2247–2250.

[79] R. Shomura, S. Higashibayashi, H. Sakurai, Y. Matsushita, A. Sato, and M. Higuchi, *Tetrahedron Lett.* **2012**, *53*, 783–785.

[80] A. Bouchet, T. Brotin, M. Linares, H. Ågren, D. Cavagnat, and T. Buffeteau, *J. Org. Chem.* **2011**, *76*, 4178–4181.

[81] R. Yamakado, K. Mikami, K. Takagi, I. Azumaya, S. Sugimoto, S. Matsuoka, M. Suzuki, K. Katagiri, M. Uchiyama, and A. Muranaka, *Chem. Eur. J.* **2013**, *19*, 11853–11857.

[82] J. L. Alonso-Gómez, A. Navarro-Vázquez, and M. M. Cid, *Chem. Eur. J.* **2009**, *15*, 6495–6503.

[83] H. A. Benesi, and J. H. Hildebrand, *J. Am. Chem. Soc.* **1949**, *71*, 2703–2707.

[84] Y. Zhu, J. Li, Z. Liu, G. Cheng, S. Dong, and E. Wang, *J. Mol. Catal. B Enzym.* **1998**, *4*, 33–39.

[85] S. Kumar, and M. Manickam, *Chem. Commun.* **1997**, *14*, 1615–1666.

[86] G. Hennrich, V. M. Lynch, and E. V. Anslyn, *Chem. Eur. J.* **2002**, *8*, 2274–2278.

[87] S. Mecozzi, and J. Rebek, Jr., *Chem. Eur. J.* **1998**, *4*, 1016–1022.

[88] S. E. Wheeler, and K. N. Houk, *J. Chem. Theory Comp.* **2009**, *5*, 2301–2312.

4. Covalent Organic Helical Cages as Sandwich Compound Containers

4.1. Introduction

Substitution is known as a useful tool in order to change the electronic character of molecules, therefore affecting host–guest affinities. Examples of such modifications are reported in the host–guest studies involving macrocyclic polyethers,[1,2] cyclodextrins,[3] and small aromatic molecules.[4] Methylation[5,6] is a common modification, not only in terms of electronics (making hosts more electron rich) but also sterics (making them more hindered) and solubility (improving it in organic solvents). Another derivatization which acts in the opposite sense is fluorination, making in general hosts more electron deficient.[7] However, there are many examples in which fluorination promotes complexation with cationic species, due to the electronegative character of fluorine.[8,9] Moreover, fluorine atoms over a host have been described as fingerprints in sensors for neutral organic compounds,[10] as well as promoters of the fluorophobic effect on the complexation of fluorinated cyclodextrins with fluorinated organic molecules.[11]

In light of the utility of host substitution effect, **Chapter 4** presents the synthesis/synthetic approach, characterization, and in some cases complexation studies of molecular cages bearing structures similar to the benzenic one (*P,P*)$_3$-**1H**, but presenting different electronic characters. Among them, a more electron rich methylated core in cage (*P,P*)$_3$-**1Me**, a more electron deficient fluorinated core in cage (*P,P*)$_3$-**1F**, and triazine core in cage (*P,P*)$_3$-**1N** were proposed (**Figure 1**). Their syntheses are based on the same three-step strategy as the one described for (*P,P*)$_3$-**1H**. The first step deals with a triple cross-coupling reaction (Sonogashira conditions in the case of (*P,P*)$_3$-**1Me** and (*P,P*)$_3$-**1F**, and Negishi conditions in the case of (*P,P*)$_3$-**1N**) between ditertbutyldiethynylallenes (-CMe$_2$OH-protected (*P*)-**DEA-OH** or the TIPS-protected (±)-**DEA-TIPS**) and the proposed core, followed by a deprotection reaction, and a subsequent Cu-catalyzed homocoupling reaction of two tripods.

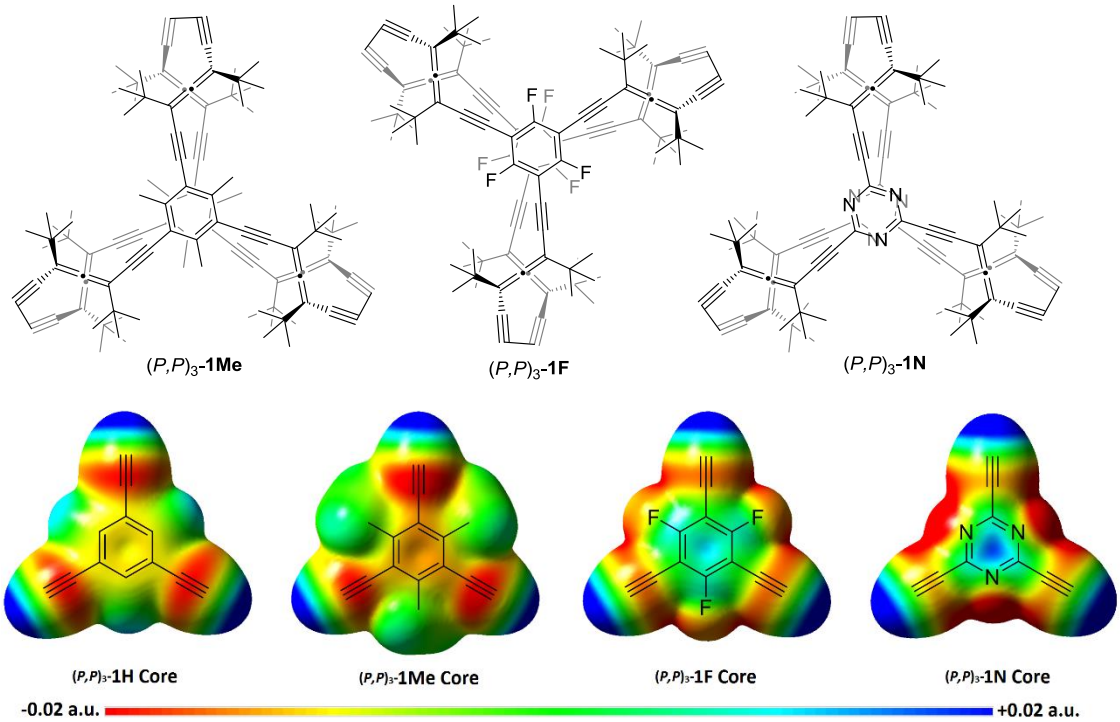

Figure 1. Top: Structure of molecular cages (*P,P*)$_3$-**1Me**, (*P,P*)$_3$-**1F**, and (*P,P*)$_3$-**1N**. Bottom: Molecular Electrostatic Potential (MEP) maps of the cores of (*P,P*)$_3$-**1H**, (*P,P*)$_3$-**1Me**, (*P,P*)$_3$-**1F**, and (*P,P*)$_3$-**1N**, calculated with *Gaussian09* at the B3LYP76-31Gd level of theory. Colors close to red indicate electron rich regions and colors towards blue indicate electron deficient regions.

Besides, a comparative complexation study with (*P,P*)$_3$-**1H** and (*P,P*)$_3$-**1Me** was done, employing sandwich compounds as guests, one of which was detected by ECD spectroscopy besides by ^{1}H NMR. Sandwich compounds (SCs) perfectly meet the requirement proposed at the end of the previous section, based on the establishment of two π–π interactions with the proposed molecular cages.

Metal Sandwich Compounds (SCs) have been exploited in the synthesis of inorganic nanoparticles,[12] the design of ionic liquids,[13] bioconjugates with antibiotic[14] and anticancer activity,[15] electric-stimulus-responsive multilayer films,[16] and catalytic species.[17] In addition, their redox properties make SCs attractive guests to be detected.[18–24] On the other hand, cyclophanes[25] are compounds that bear aromatic units connected by aliphatic chains. Particularly, paracyclophanes, the same as the aforementioned sandwich compounds, may present two parallel aromatic rings suitable for undergoing π–π interactions with the lids of the covalent organic helical cages (*P,P*)$_3$-**1H** and (*P,P*)$_3$-**1Me**. Therefore, a series of new guests was proposed in order to obtain complexes with (*P,P*)$_3$-**1H** and (*P,P*)$_3$-**1Me** (**Figure 2**).

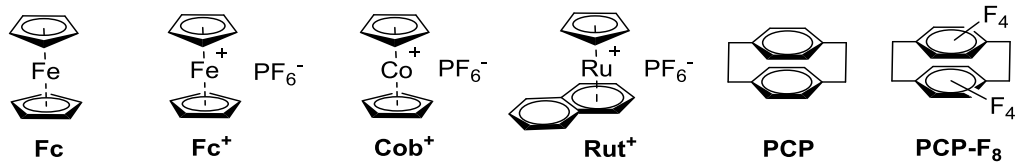

Figure 2. Structure of guests tested on complexation with molecular cages (*P,P*)$_3$-**1H** and (*P,P*)$_3$-**1Me**.

4.2. Synthesis of (*P,P*)$_3$-1Me

Synthesis of (*P,P*)$_3$-**1Me** was formulated analogously to the one of (*P,P*)$_3$-**1H**, according to **Scheme 1**, but starting from 1,3,5-triiodo-2,4,6-trimethylbenzene as aromatic core instead of the previous 1,3,5-triiodobenzene.

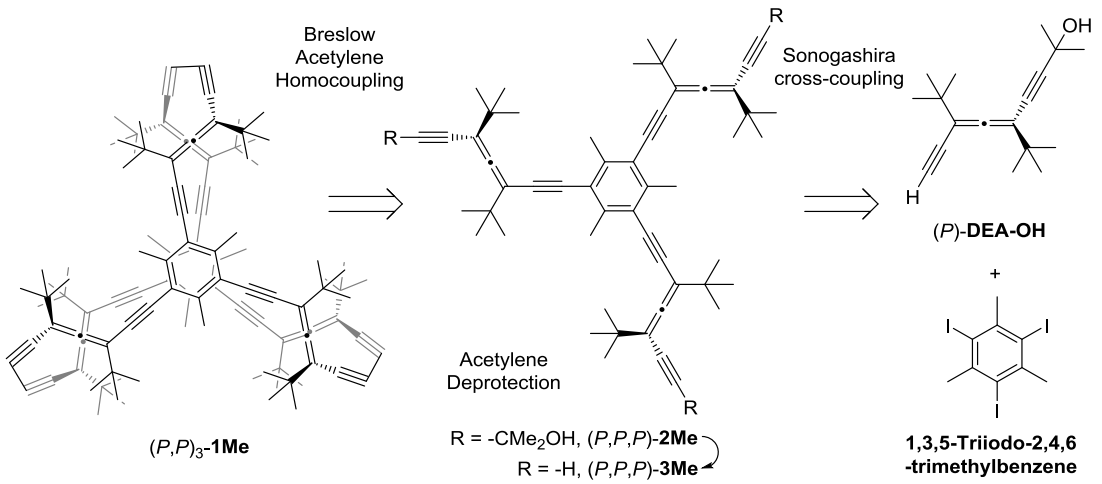

Scheme 1. Retrosynthesis of molecular cage (*P,P*)$_3$-**1Me**.

4.2.1. Synthesis of (*P,P,P*)-2Me

Proposed general synthetic pathway to (*P,P,P*)-**2Me**, depicted in **Scheme 2**, consists of a Sonogashira cross−coupling reaction, followed by an acetylene deprotection, and ending on a Cu-catalyzed homocoupling reaction under Breslow conditions.

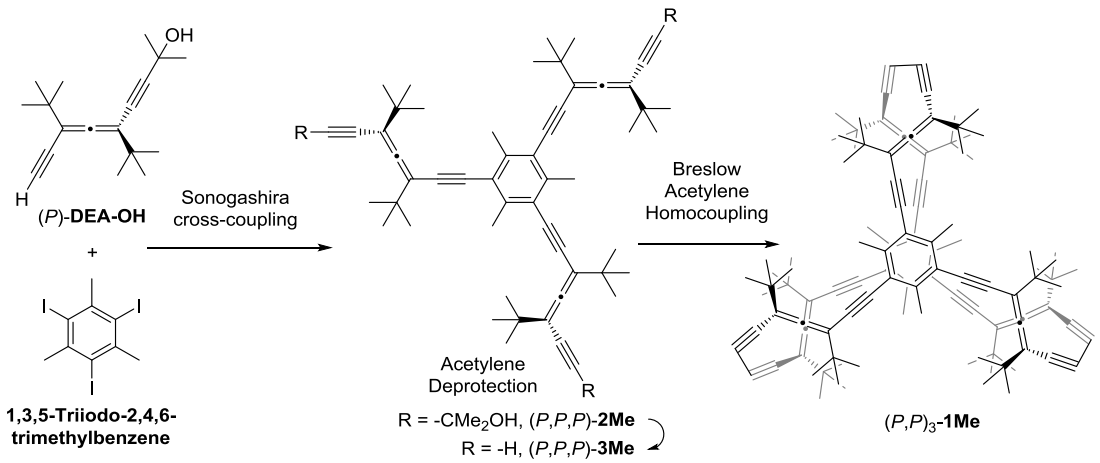

Scheme 2. Synthetic pathway to $(P,P)_3$-**1Me**.

First, 1,3,5-triiodo-2,4,6-trimethylbenzene or 1,3,5-triiodomesitylene was synthesized in a 72% yield following a previously reported procedure based on the treatment of mesitylene with molecular iodine, periodic acid and sulfuric acid in acetic acid at 100 °C for 7 days (**Scheme 3**).[26]

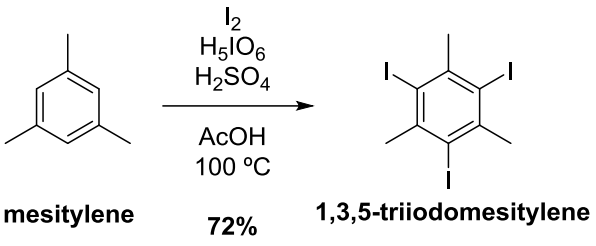

Scheme 3. Synthesis of 1,3,5-triiodomesitylene.

Next, tricoupled product (*P,P,P*)-**2Me** was synthesized through the Sonogashira cross-coupling methodology, between three equivalents of the enantiopure (*P*)-**DEA-OH** and the aromatic core 1,3,5-triiodomesitylene (**Scheme 4**).

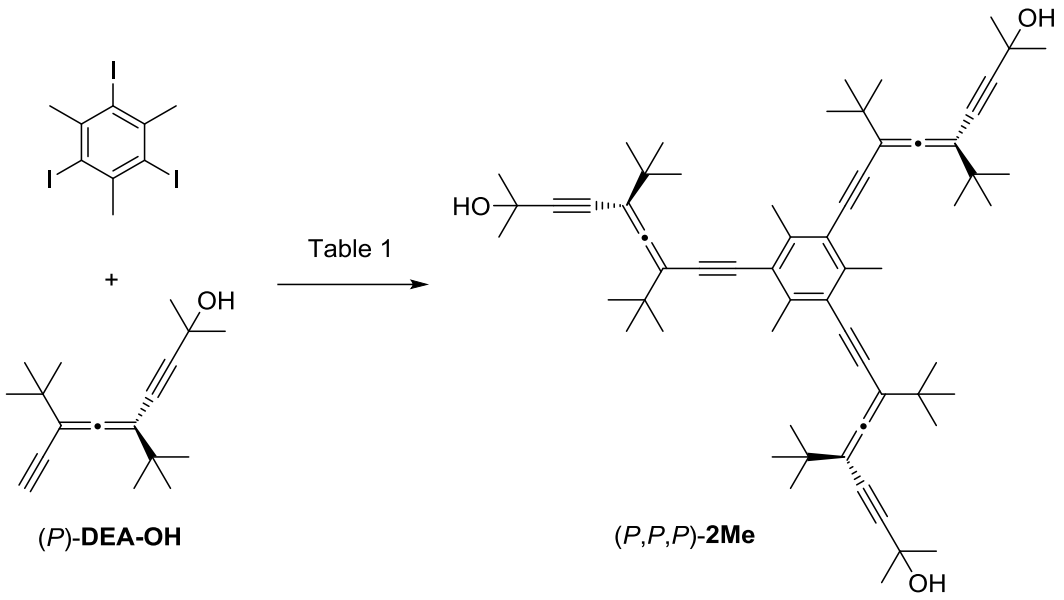

Scheme 4. Synthetic scheme to (*P,P,P*)-**2Me**.

When a mixture of (*P*)-**DEA-OH** and triiodomesitylene was treated under classical reaction conditions with $PdCl_2(PPh_3)_2$ and CuI in Et_3N (**Table 1**, **Entry 1**),[26] several side products such as monocoupled and dicoupled product ((*P*)-**MC-2Me** (43%) and (*P,P*)-**DC-2Me** (24%) respectively), as well as the allene homodimer (*P,P*)-**DEA-OH$_2$** (8%) (**Figure 3**) were obtained. Although more than 3 equivalents of (*P*)-**DEA-OH** were employed, the conversion was not complete. To avoid side products formation a search of improved Sonogashira conditions was done. A summary of tested conditions is shown in **Table 1**.

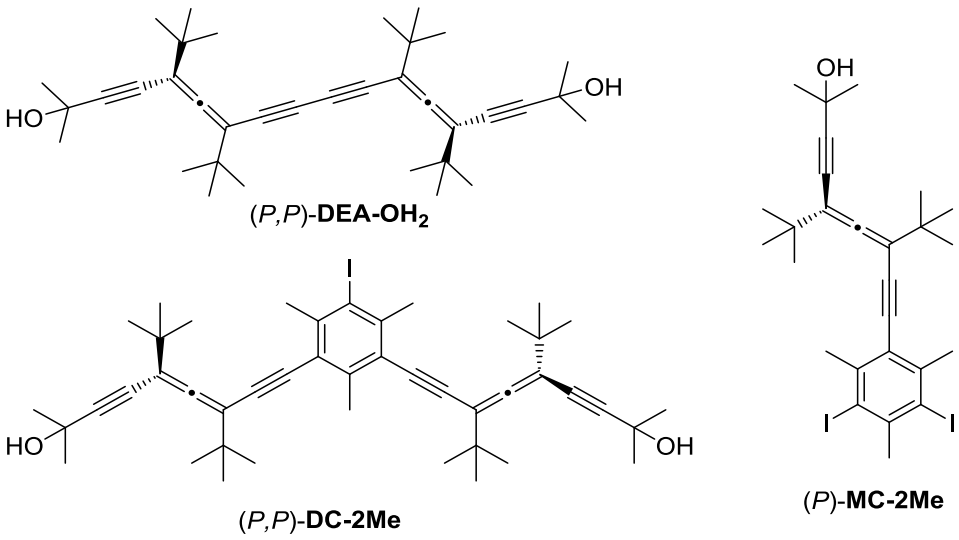

Figure 3. By-products on the synthesis of (*P,P,P*)-**2Me**.

More reactive conditions, **Table 1**, **Entry 2**, employing $Pd_2(dba)_3$, higher amount of CuI, additives such as tetrabutylammonium iodide (TBAI), Hünig's base *N,N*-diisopropylethylamine (DIPEA) in DMF, did not improve the outcome .

Changing the phosphine by a bulkier one and the Pd catalyst by another more reactive, along with the addition of larger amounts of all the reagents distributed in two times, **Table 1**, **Entry 3**, resulted in a 56% yield of tricoupled product (*P,P,P*)-**2Me**, along with a 19% of (*P,P*)-**DEA-OH$_2$**.

Entry	Conditions	t (h)	T(°C)	(*P,P,P*)-**2Me**	(*P*)-**MC-2Me**	(*P,P*)-**DC-2Me**	(*P,P*)-**DEA-OH$_2$**	**PhMe$_3$I$_3$**
1	$PdCl_2(PPh_3)_2$ (7 mol%), CuI (5 mol%), Et_3N, N_2	21	r.t.	21%	43%	24%	8%	25% rec
2	$Pd_2(dba)_3$ (8 mol%), CuI (60 mol%), TBAI (6 eq), DIPEA (10 eq), tri-o-tolylphosphine (60 mol%), DMF, N_2	15	r.t.	22%	43%	23%	8%	33% rec
3	$Pd_2(dba)_3{\cdot}CHCl_3$ (12 mol%), CuI (90 mol%), TBAI (9 eq), DIPEA (15 eq), trimesitylphosphine (90 mol%), DMF, N_2	21	r.t.	56%	-	-	19%	11% rec

Table 1. Summary of Sonogashira cross-coupling reaction conditions tested. Labels (*P,P,P*)-**2Me**, (*P*)-**MC-2Me**, (*P,P*)-**DC-2Me**, and (*P,P*)-**DEA-OH$_2$** make reference to the tricoupled product, monocoupled product, dicoupled product and the homodimer of the ditertbutyldiethynylallene respectively.

The presence of the three methyl groups on the benzene ring of (*P,P,P*)-**2Me** makes, as expected, the oxidative addition between the Pd catalyst and the aryl iodide in the first step of the Sonogashira cross−coupling reaction less efficient when compared to the analogous step for the synthesis of (*P,P,P*)-**2H**.

Tricoupled product (*P,P,P*)-**2Me**, as well as side products (*P*)-**MC-2Me** and (*P,P*)-**DC-2Me** were fully characterized by means of ^{1}H and ^{13}C NMR, IR, UV-Vis and electronic circular dichroism (ECD) spectroscopies, and HR-EI/ESI-MS spectrometry. ^{1}H NMR of (*P,P,P*)-**2Me** shows a characteristic singlet at 2.57 ppm diagnostic of the equivalent methyl groups on the aromatic core, whilst (*P*)-**MC-2Me** shows for such methyl groups a couple of singlets at 2.96 ppm (1 methyl group) and 2.68 ppm (2 equivalent methyl groups), and (*P,P*)-**DC-2Me** presents also a couple of singlets at 2.69 and 2.54 ppm, integrating for 2 and 1 methyl groups respectively. On the ^{13}C NMR spectra of (*P,P,P*)-**2Me**, (*P,P*)-**DC-2Me**, and (*P*)-**MC-2Me**, the aromatic methyl groups appear at 20.4 ppm, 29.4 and 20.3 ppm, and 39.0 and 29.7 ppm respectively.

4.2.2. Synthesis of (*P,P,P*)-3Me

Deprotection of 2-hydroxypropyl group of (*P,P,P*)-**2Me** to give the terminal acetylene in (*P,P,P*)-**3Me** (**Scheme 5**) was tested under different basic conditions in order to maximize the product yield. The results are shown in **Table 2**.

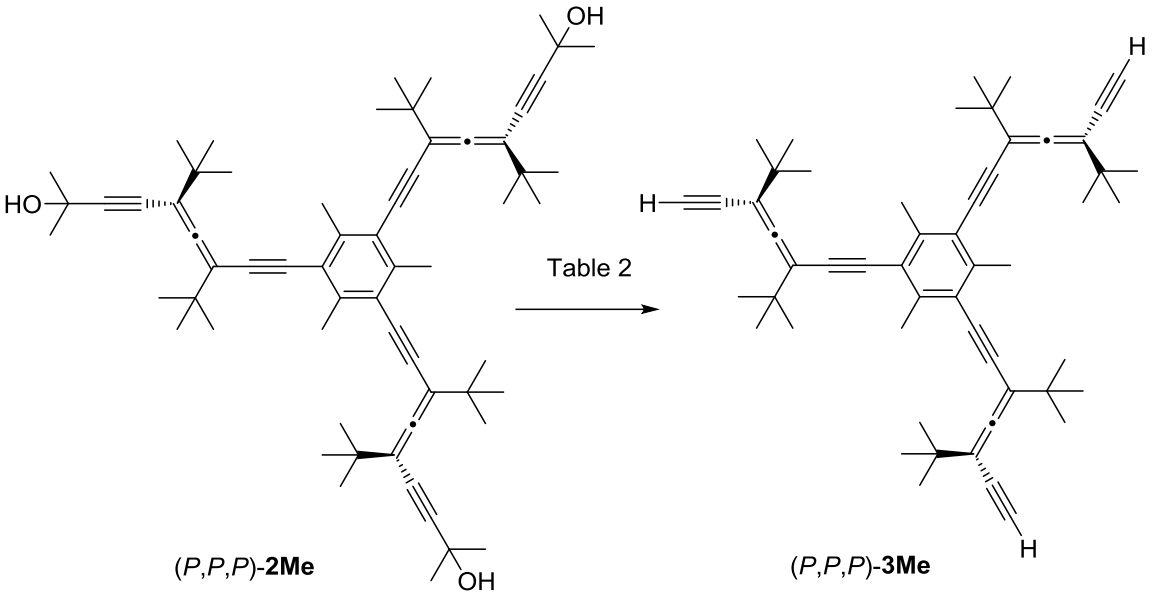

Scheme 5. Synthesis of (*P,P,P*)-**3Me**.

Entry	Conditions	t (h)	T(°C)	(*P,P,P*)-**3Me**
1	K^{t}BuO (3−38eq), Toluene	24	65−95	-
2	NaOH (300 eq), Toluene	3	110	23%
3	KOH (6−114 eq), Toluene	24	80−90	34%

Table 2. Deprotection conditions employed on the synthesis of (*P,P,P*)-**3Me**.

As shown in **Table 2**, **Entry 1**, when using a stoichiometric ratio up to an excess (38 eq) of K^{t}BuO in toluene at 65 °C, in order to minimize polymer and other possible side products formation, starting material was recovered. Traditional conditions, **Table 2**, **Entry 2**, employing an excess of powdered flamed NaOH in refluxing toluene achieved a modest 23% yield of (*P,P,P*)-**3Me**. Finally, the spaced addition of small amounts of powdered flamed KOH up to 114 equivalents during a period of 24 h in toluene at 90 °C (**Table 2**, **Entry 3**), procedure which makes use of conditions similar to those previously reported by Li et al,[27] improved the yield of (*P,P,P*)-**3Me** up to a 34% yield.

With respect to the characterization of (*P,P,P*)-**3Me**, the only significant details are, as in the case of (*P,P,P*)-**3H**, the occurrence of the characteristic terminal alkyne signal on the ^{1}H NMR at 3.01 ppm, along with the disappearance of the signals corresponding to the carbon atoms of the protective group on the ^{13}C NMR.

4.2.3. Synthesis of (*P,P*)$_3$-1Me

In the light of the good results reported in **Chapter 2** for the Cu-catalyzed homodimerization of (*P,P,P*)-**3H** to give (*P,P*)$_3$-**1H** under Breslow conditions, (*P,P,P*)-**3Me** was analogously treated (**Scheme 6**), affording molecular cage (*P,P*)$_3$-**1Me** in a 32% yield, along with traces of side product (*P*)$_6$-**7** (**Figure 4**).

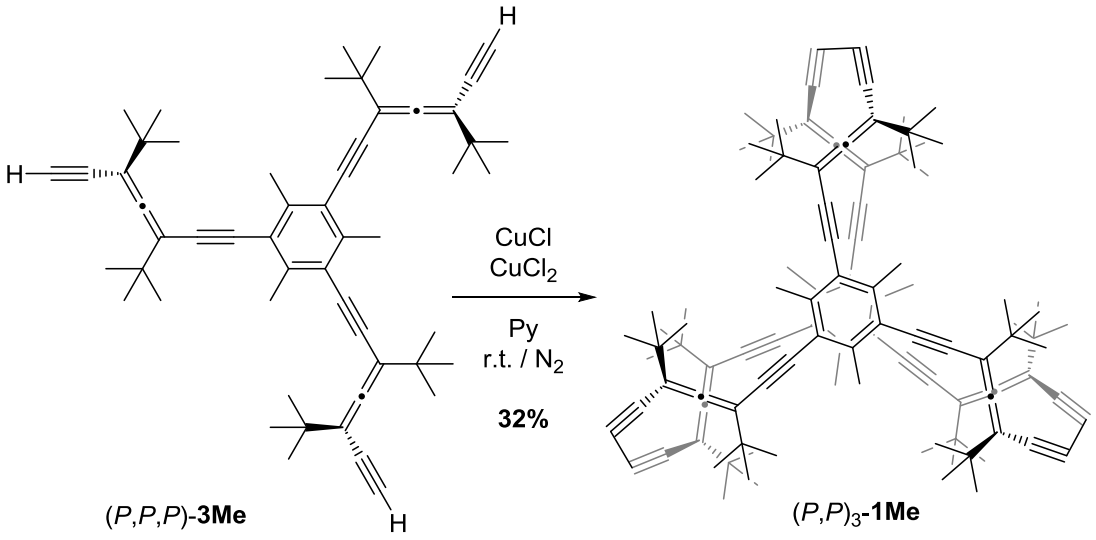

Scheme 6. Synthesis of (*P,P*)$_3$-**1Me**.

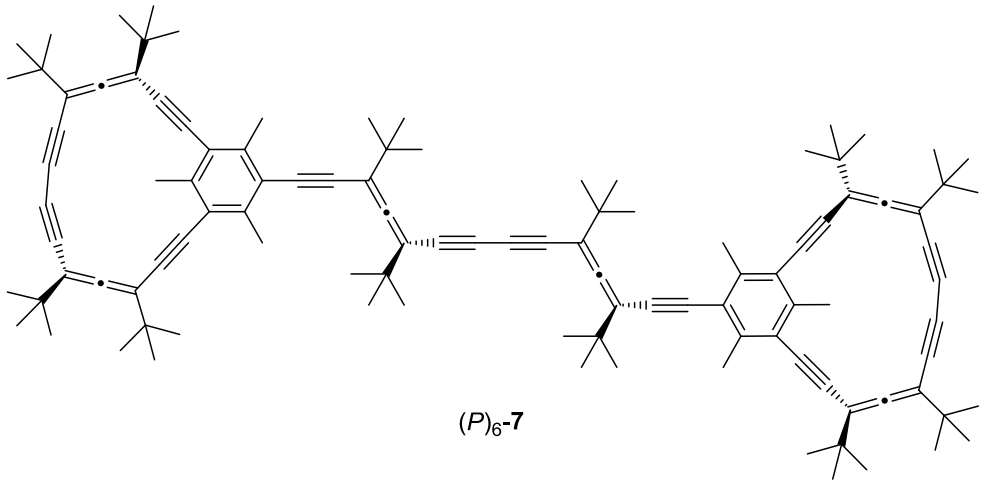

Figure 4. Side product on the synthesis of (*P,P*)$_3$-**1Me**.

Molecular cage (*P,P*)$_3$-**1Me** was fully characterized by means of ^{1}H and ^{13}C NMR, HR-MALDI-MS, IR, UV-Vis and ECD spectroscopies. The electronic circular dichroism (ECD) spectrum of (*P*,*P*)$_3$-**1Me** is composed of an intense positive band at 246 nm and four negative weaker bands at 263, 291, 306, and 327 nm, presenting (*M*,*M*)$_3$-**1Me** a mirror image spectrum compared to the one of (*P*,*P*)$_3$-**1Me**. Such a band profile gives rise to a spacing between the four negative bands of *ca.* 2000 cm^{-1}, which is in good agreement with the typical vibronic progression in 1,3-butadiynes.[28] It is noteworthy that, with respect to the summation of six allenic units, the ECD intensity in (*P*,*P*)$_3$-**1Me** presents *ca.* 16-fold chiroptical amplification.[29] This results on a dissymmetry factor (*g*-factor) calculated by $\Delta\varepsilon/\varepsilon$ with a maximum value of 0.004 in chloroform, which is in the order of the maximum values found for purely organic molecules reported so far.[30,31] Moreover, the absorption spectrum of (*P*,*P*)$_3$-**1Me** is *ca.* 5 nm redshifted with respect to that of (*P*,*P*)$_3$-**1H**, a fact that correlates with the calculated HOMO−LUMO gap decrease ((*P*,*P*)$_3$-**1H**: HOMO–LUMO gap = 4.3 eV; (*P*,*P*)$_3$-**1Me**: HOMO–LUMO gap = 4.2 eV; B3LYP/6-31G(d) (**Figure 5**).

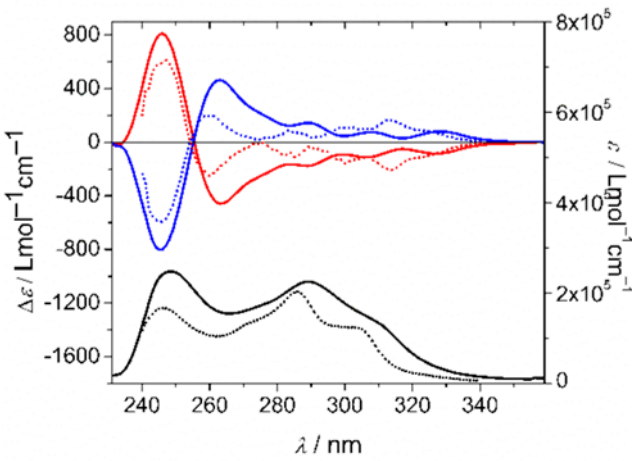

Figure 5. Absorbance spectra (lower panel) of (*P,P*)$_3$-**1Me** (solid black line) and (*P,P*)$_3$-**1H** (dotted black line), and ECD spectra (upper panel) of (*P,P*)$_3$-**1Me** (solid red line), (*P,P*)$_3$-**1H** (dotted red line), (*M,M*)$_3$-**1Me** (solid blue line), and (*M,M*)$_3$-**1H** (dotted blue line) in $CHCl_3$ at *ca.* 10^{-5} M.

Absorbance spectra of (*P,P*)$_3$-**1H** and (*P,P*)$_3$-**1Me** were measured in solvents with different polarities. The results show a redshift of the main bands of the spectra with the increase of the polarity of the solvent (**Figure 6**). This fact highlights the presence of higher polarity excited states of both molecular cages in comparison with their respective ground states.

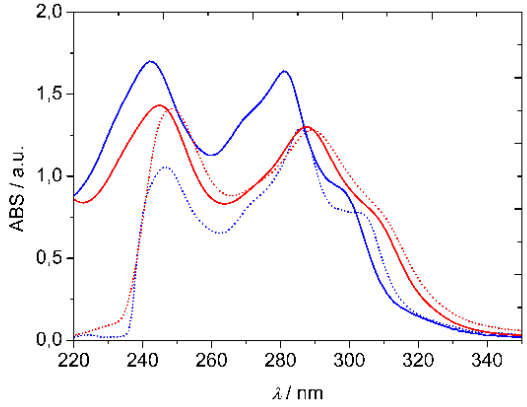

Figure 6. Absorbance spectra of (*P,P*)$_3$-**1H** (in hexane, solid blue line; in $CHCl_3$, dotted blue line) and (*P,P*)$_3$-**1Me** (in hexane, solid red line; in $CHCl_3$, dotted red line) at ca. 10^{-5} M.

4.3. Molecular cages (*P,P*)$_3$-1H and (*P,P*)$_3$-1Me as sandwich compounds containers: Chiroptical detection.

In **Chapter 3**, the unsuccessful attempts to form stable complexes between (*P,P*)$_3$-**1H** and different C_3-symmetric flat guests, led us to think on trying guests which could stablish π–π interactions with both lids of the cage. Thus, both Sandwich Compounds (SCs) and paracyclophanes (PCPs) meet such requirements. To evaluate the capability of Covalent Organic Helical Cages (COHCs) (*P,P*)$_3$-**1H** and (*P,P*)$_3$-**1Me** as sandwich compound containers,

complexation tests with several SCs were carried out through ^{1}H NMR titrations, adding small amounts of a known weight of the guest to a solution of known concentration of the host. PF_6^- was the counterion of all cationic SCs to eliminate counterion effects.[12] The measured observables were the chemical shifts of the aromatic hydrogens in (*P,P*)$_3$-**1H** and hydrogens of the methyl groups on the aromatic ring in (*P,P*)$_3$-**1Me**. Association constants were initially determined through the classic Benesi–Hildebrand data treatment an further refined through a more accurate iterative numeric method (**Table 3**).[32,33] First SC tested was ferrocene (**Fc**) with cage (*P,P*)$_3$-**1H** in acetone, which resulted in no complex formation. However, its charged analogue, ferrocenium (**Fc$^+$**) showed the formation of an inclusion complex with an association constant K_a = 22 M^{-1} (**Figure 6**, **Figure 7**).[34]

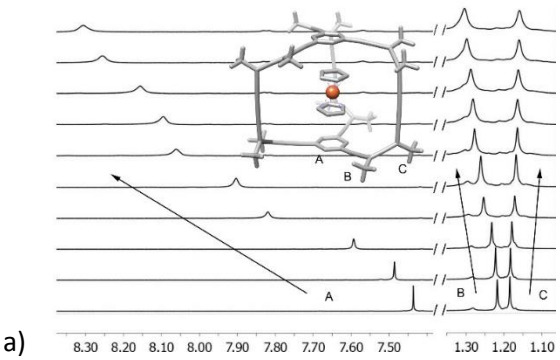

Figure 6. a) Cutout of a series of ^{1}H NMR spectra from the addition of **Fc$^+$** (from 0 up to 11 equivalents) over a solution in acetone-d_6 of (*P,P*)$_3$-**1H**. Aromatic H of (*P,P*)$_3$-**1H** (A) is downfield shifted, while ^{t}Bu groups (B and C) shift in opposite directions.

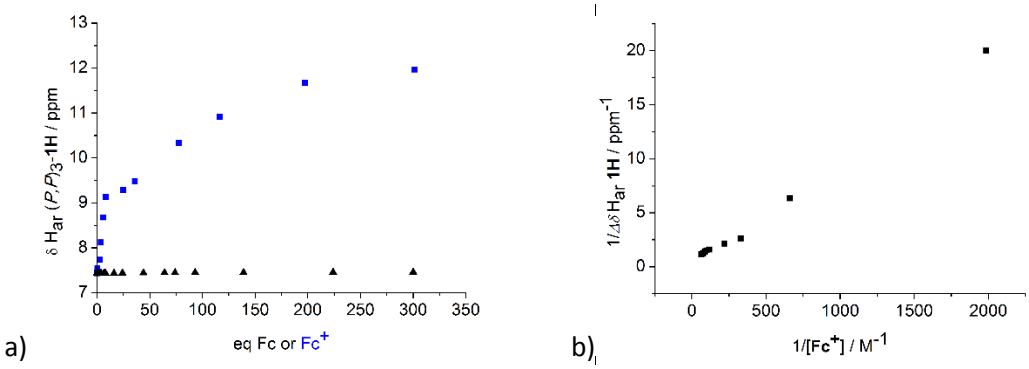

Figure 7. a) Saturation curves for Fc (black) and Fc$^+$ (blue) with molecular cage (*P,P*)$_3$-**1H**. b) Benesi-Hildebrand plot of [(*P,P*)$_3$-**1H**@**Fc$^+$**].

Due to the paramagnetic character and instability of Fc$^+$, which has an intercentroid distance of 3.38 Å,[35] we widened the study to the more stable cobaltocenium (**Cob$^+$**) with a similar intercentroid distance (3.26 Å),[36] and found practically the same affinity with (*P,P*)$_3$-**1H** in acetone (K_a = 16 M^{-1}) (**Figure 8**).

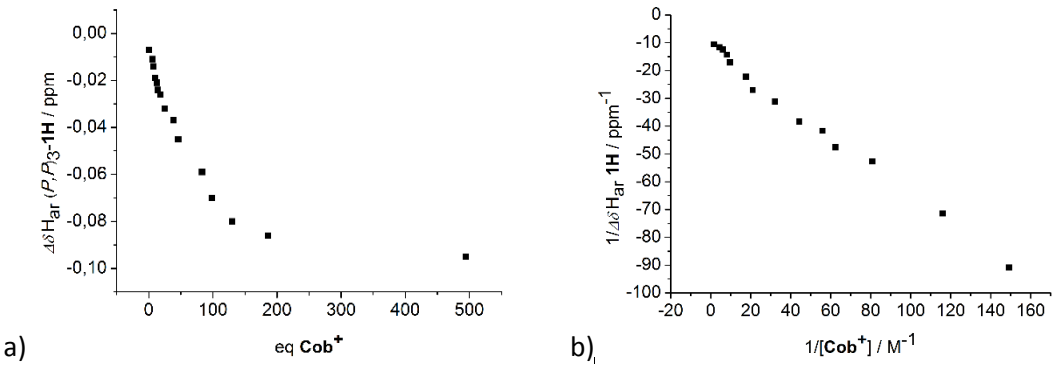

Figure 8. a) Saturation curve and b) Benesi-Hildebrand plot for [(P,P)$_3$-**1H**@**Cob**$^+$] in acetone-d_6.

η^5-Cyclopentadienyl-η^6-naphthaleneruthenium (III) (**Rut**$^+$) showed a slightly higher affinity (K_a = 29 M^{-1}) as compared to **Cob**$^+$, indicating an improvement that could be due to the larger area of interaction and/or larger intercentroid distance (3.53 Å)[37,38] (**Table 3**) (**Figure 9**).

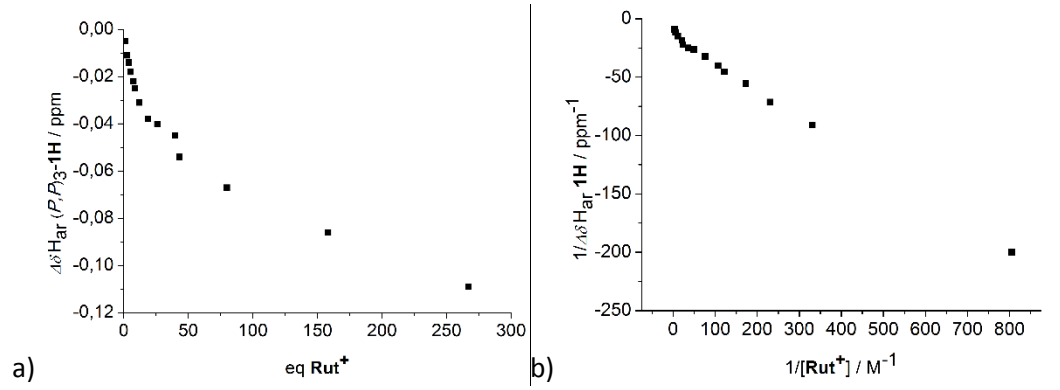

Figure 9. a) Saturation curve and b) Benesi-Hildebrand plot for [(P,P)$_3$-**1H**@**Rut**$^+$] in acetone-d_6.

To study the influence of the solvent in this molecular recognition process,[39] we changed from acetone to dichloromethane (DCM) that shows a lower polarity, resulting in an enhancement of the binding affinity of **Rut**$^+$ with (P,P)$_3$-**1H** to K_a = 50 M^{-1} (**Figure 10**, **Figure 11a**).

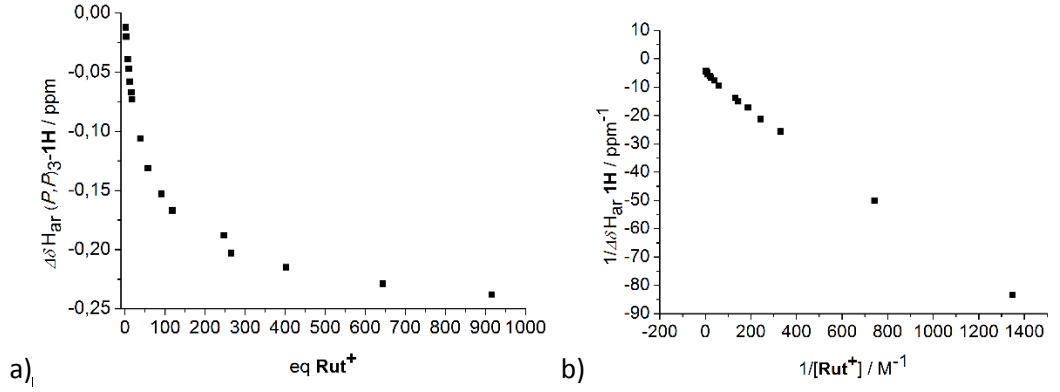

Figure 10. a) Saturation curve and b) Benesi-Hildebrand plot for [(P,P)$_3$-**1H**@**Rut**$^+$] in CD_2Cl_2.

On the other hand, molecular cage (P,P)$_3$-**1Me**, thought to be a better encapsulating agent of electron poor guests, due to its richer electronic character, showed an association constant for **Rut**$^+$ in DCM of 905 M^{-1}, 18-fold larger than that of unmethylated (P,P)$_3$-**1H** (**Figure 11b**, **Figure 12**).

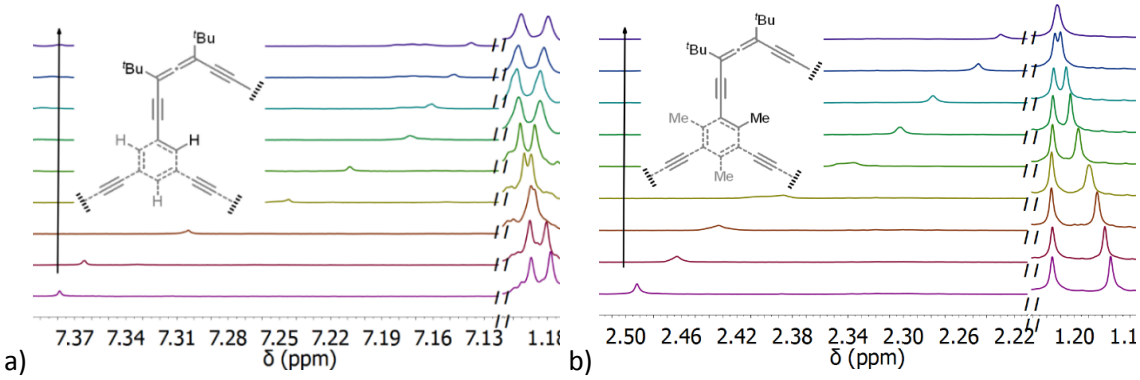

Figure 11 a) Cutout of a series of ^{1}H NMR spectra from the addition of **Rut**$^+$ (0 eq → 900 eq **Rut**$^+$) to a solution in CD_2Cl_2 of $(P,P)_3$-**1H**. Aromatic H of $(P,P)_3$-**1H** is upfield shifted, while ^{t}Bu groups shift in opposite directions, tending to cross themselves. b) Cutout of a series of ^{1}H NMR spectra from the addition of **Rut**$^+$ over a solution of $(P,P)_3$-**1Me** (0 eq → 75 eq **Rut**$^+$) in CD_2Cl_2 at r.t. A pronounced downfield shift of the Me groups on the phenyl rings of $(P,P)_3$-**1Me** was observed. The two nonequivalent ^{t}Bu groups of $(P,P)_3$-**1Me** shifted in opposite directions till they merge. $(P,P)_3$-**1Me** scheme highlight the above-mentioned NMR-active nuclei. Arrows indicate increasing concentration of **Rut**$^+$. Chemical shifts in ppm.

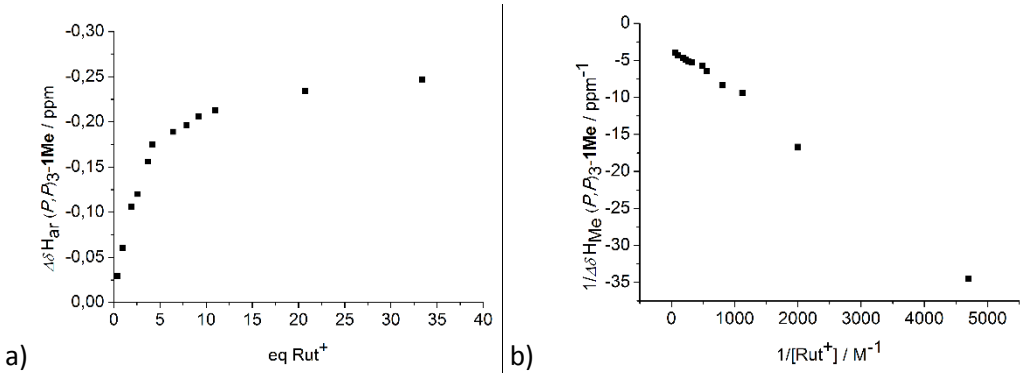

Figure 12. a) Saturation curve and b) Benesi-Hildebrand plot for [$(P,P)_3$-**1Me**@**Rut**$^+$] in CD_2Cl_2.

Sandwich compound **Cob**$^+$, as for the case of unmethylated $(P,P)_3$-**1H**, presents a lower binding affinity with respect to **Rut**$^+$ in DCM (K_a = 296 M^{-1}) (**Figure 13**).

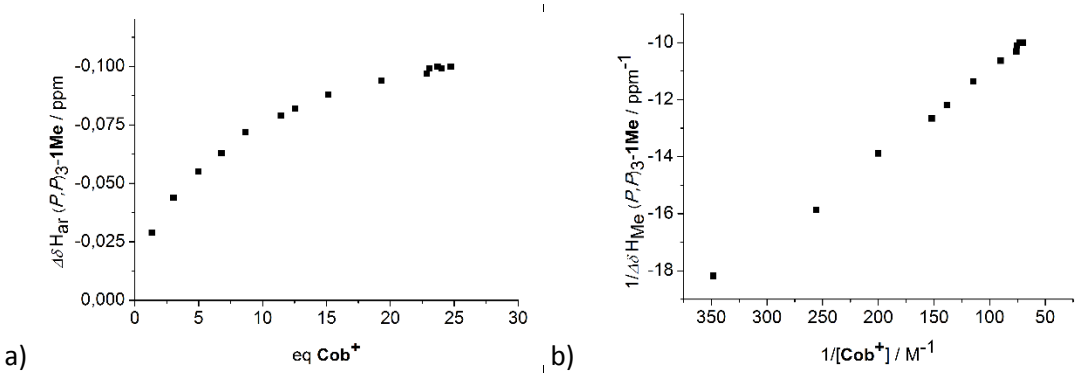

Figure 13 a) Saturation curve and b) Benesi-Hildebrand plot for [$(P,P)_3$-**1Me**@**Cob**$^+$] in CD_2Cl_2.

Paracyclophanes[25] which are compounds that bear aromatic units connected by aliphatic chains, present two parallel aromatic rings suitable for undergoing π–π interactions with the COHC lids, similarly to sandwich compounds. In order to explore this possibility, [2.2]paracyclophane (**PCP**) and 4,5,7,8,12,13,15,16-octafluoro [2.2]paracyclophane (**PCP-F$_8$**) were also tested. While no complexation between (*P*,*P*)$_3$-**1H** and **PCP** was observed, the inclusion complex [(*P*,*P*)$_3$-**1Me**@**PCP-F$_8$**] in DCM presents a K_a = 43 M^{-1} (**Figure 14**). Complex formation could be favored by the more electron-deficient character of the fluorinated aromatic rings of the paracyclophane guest. The formation of all complexes was further supported by HR-ESI-MS or HR-MALDI-MS, certifying the 1:1 stoichiometry.

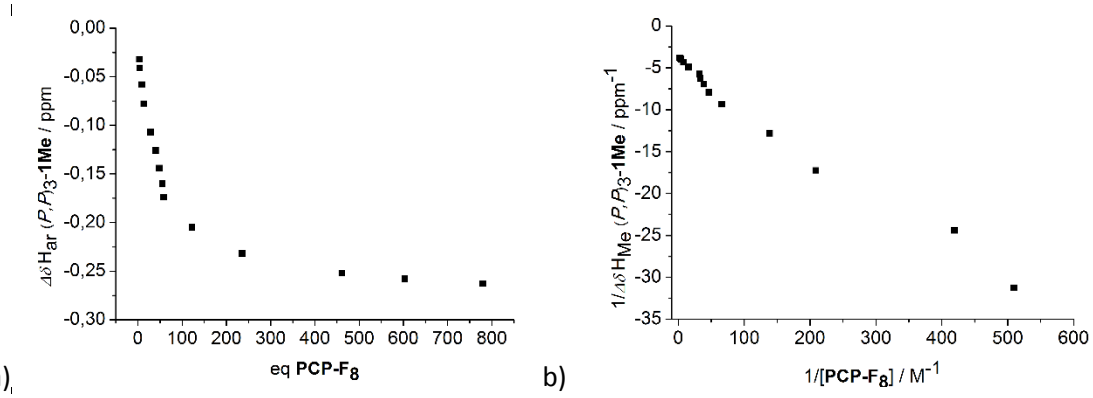

Figure 14. a) Saturation curve and b) Benesi-Hildebrand plot for [(*P*,*P*)$_3$-**1Me**@**PCP-F$_8$**] in CD_2Cl_2.

	Fc	Fc$^+$	Cob$^+$	Rut$^+$	PCP	PCP-F$_8$
(*P*,*P*)$_3$-**1H**	n/c[c,d]	22[c]	16[c]	29,[c] 50[d]	n/c[c]	n/a
(*P*,*P*)$_3$-**1Me**	n/a	n/a	296[d]	905[d]	n/a	43[d]

Table 3. Association constants (K_a) and structure of tested guests in the complexation studies. Ferrocene (**Fc**), ferrocenium hexafluorophosphate (**Fc$^+$**), cobaltocenium hexafluorophosphate (**Cob$^+$**), η^5-cyclopentadienyl-η^6-naphthaleneruthenium (III) hexafluorophosphate (**Rut$^+$**), [2.2]paracyclophane (**PCP**), and 4,5,7,8,12,13,15,16-octafluoro [2.2]paracyclophane (**PCP-F$_8$**). K_a (M^{-1}) table is shown for both [(*P*,*P*)$_3$-**1H**@guest] and [(*P*,*P*)$_3$-**1Me**@guest]. [c] Solvent = acetone-d_6. [d] Solvent = dichloromethane-d_2. n/c = no complex formation observed. n/a = data not available.

The achieved results were analyzed in terms of accomplishment of the ideal 55% packing coefficient rule enunciated by Mecozzi and Rebek.[40] Since cavities of both (*P*,*P*)$_3$-**1H** and (*P*,*P*)$_3$-**1Me** are laterally open, we approximated the resulting cavity to that of a cylinder, considering a radius R = 4.3 Å, and a height h = 8.3 Å, whose values were taken from the reported crystalline structure of (*P*,*P*)$_3$-**1H**. Thus, the cylinder volume, calculated as $\pi \cdot R^2 \cdot h$, is 482.1 Å^3. Guest volumes, as well as packing coefficients with respect to the calculated cylinder volume, are given in **Table 4**, showing that, if only steric effects were considered, the most appropriate guests

would be **PCP**, **Rut$^+$**, and **PCP-F$_8$**. However, the complex formation with **PCP** has not been detected.

	Cob$^+$	**Fc**	**Fc$^+$**	**PCP**	**Rut$^+$**	**PCP-F$_8$**
V (Å^3)[a]	168.1	171.8	172.3	236.8	240.2	282.9
P.C. (%)[b]	35	36	36	49	50	59

Table 4. Guest volumes and respective packing coefficients with respect to the average cylindrical cavity size. [a] Guest volumes were calculated using *Spartan'14* V1.1.2 considering a summation of van der Waals radii of defined optimized geometries. [b] Packing Coefficients (P.C.) were calculated as the ratio between the guest volume and the approximated cylindrical cavity volume.

In addition, in order to further explain the consistency of the K_a values achieved, the electrostatic potential maps of both molecular cage cores and the different guests were computed (**Figure 15**). Calculations were made using *Gaussian09* at the B3LYP/6-31G(d) level of theory for both cores as well as for all guests except for **Rut$^+$**, which requires the use of a higher calculation basis set such as the LanL2DZ. On the one hand, a slightly different electronic character of both cores is observed, being the aromatic ring of (*P,P*)$_3$-**1H**, less electron rich than that of (*P,P*)$_3$-**1Me** (**Figure 15a, b**). The results are in good agreement with those already reported in the literature.[41–43] On the other hand, guests showing electron rich areas (red), such as **PCP** and **Fc** (**Figure 15c, e**), would be less prone to undergo a complexation process with either cage, (*P,P*)$_3$-**1H** or (*P,P*)$_3$-**1Me**, whilst guests bearing electron deficient areas (blue), such as **PCP-F$_8$**, **Fc$^+$**, **Cob$^+$**, and **Rut$^+$** (**Figure 15d, f, g, h**) would. Only two of the six proposed guests, **Rut$^+$** and **PCP-F$_8$**, meet both steric and electronic requirements. Whereas **Cob$^+$** does not meet steric requirements it does bind (*P,P*)$_3$-**1Me** with K_a of 296 M^{-1}. As expected for an open cavity, these results suggest that the electronic effect plays a greater role than the steric one.

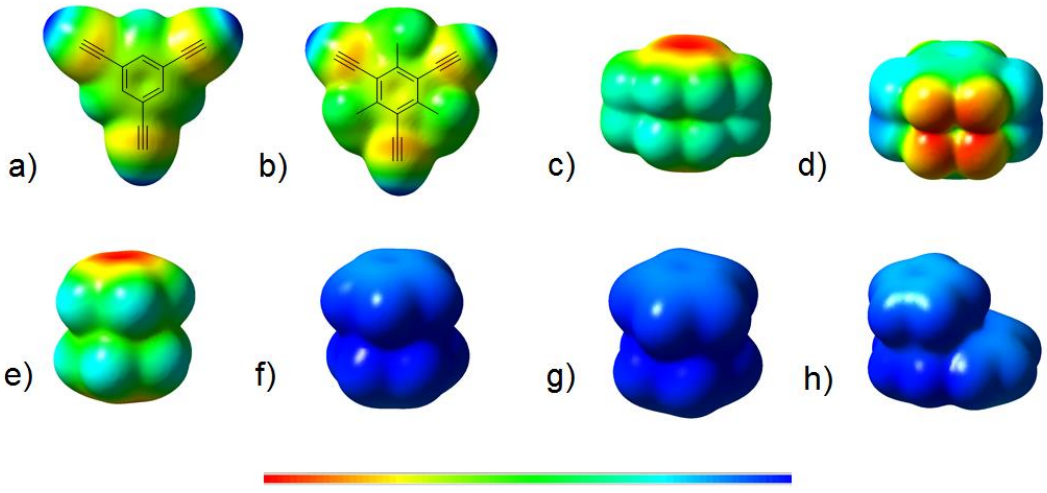

Figure 15. Electrostatic potential map of: a) (*P,P*)$_3$-**1H** core; b) (*P,P*)$_3$-**1Me** core; c) **PCP**; d) **PCP-F$_8$**; e) **Fc**; f) **Fc$^+$**; g) **Cob$^+$**; h) **Rut$^+$**. Color scale: red indicating electron rich and blue electron poor regions. *GaussView 5.0.8* (Isovalue = 0.0100, density = 0.00400).

Sandwich organometallic compounds may present reversible redox processes with low potentials what enables them as to be used in electrochemical sensing.[44] On the other hand,

the interest on continuous detection methods requires the development of new sensing methodologies.[45] Moreover, the sensitivity of chiroptical responses to conformational changes[46] and intermolecular interactions invites to explore chiroptical sensing applications. In this field, organometallic chiral containers have been used to detect nonchromophoric guests.[47] Therefore, in order to go a step further in the development of redox chiroptical sensors, a titration of $(P,P)_3$-**1Me** with **Rut**$^+$ in 1,2-dichloroethane was studied by ECD. The observed changes in the ECD responses enabled the detection of the ruthenium sandwich organometallic compound **Rut**$^+$ in solution (**Figure 16**).

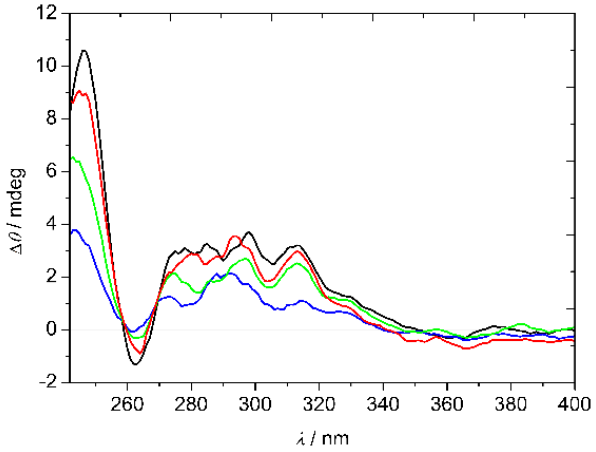

Figure 16. Induced ECD for the complexation of [$(P,P)_3$-**1Me**@**Rut**$^+$] with 30 eq (black line), 25 eq (red), 17 eq (green) and 8 eq (blue) of **Rut**$^+$ in DCE, obtained from the subtraction of the ECD of [$(P,P)_3$-**1Me**@**Rut**$^+$] to that of $(P,P)_3$-**1Me**. This difference is attributed to the formation of the [$(P,P)_3$-**1Me**@**Rut**$^+$] inclusion complex.

In summary, the evaluation of inclusion complex formation of COHCs $(P,P)_3$-**1H** and $(P,P)_3$-**1Me**, with **Fc**, **Fc**$^+$, **Cob**$^+$, **Rut**$^+$, **PCP**, and **PCP-F$_8$** was performed. As predicted, the presence of methyl groups in the phenyl rings of the COHCs induced a large enhancement in the binding affinities. Particularly, the magnitude of the association constant for [$(P,P)_3$-**1Me**@**Rut**$^+$] along with the intense chiroptical responses of $(P,P)_3$-**1Me** enabled the detection of the entrapped organometallic sandwich compound by electronic circular dichroism.

4.4. Synthesis of $(P,P)_3$-1F

The second derivatization of the initially proposed benzenic molecular cage includes six fluorine atoms replacing the previous aromatic hydrogen atoms, namely, molecular cage $(P,P)_3$-**1F**, which would bear an electronic deficient character. The synthetic scheme to be followed was the same as the one used for $(P,P)_3$-**1H** and $(P,P)_3$-**1Me** (**Scheme 7**) in which the electrophile in the Sonogashira cross−coupling reaction would be 1,3,5-triiodo-2,4,6-trifluorobenzene and two different allenic alkynes were considered: 2-hydroxypropyl-protected (*P*)-**DEA-OH** (route a) and TIPS-protected (±)-**DEA-TIPS** (route b). The latter was quantitatively obtained by treating the bisprotected **DEA-TIPS-OH** with K^{t}BuO (1 eq) in dry toluene at 60 °C for 1 h (**Scheme 8**). Unfortunately, (±)-**DEA-TIPS** was not able to be resolved by employing chiral HPLC (Chiralpack IA) using different mobile phases.

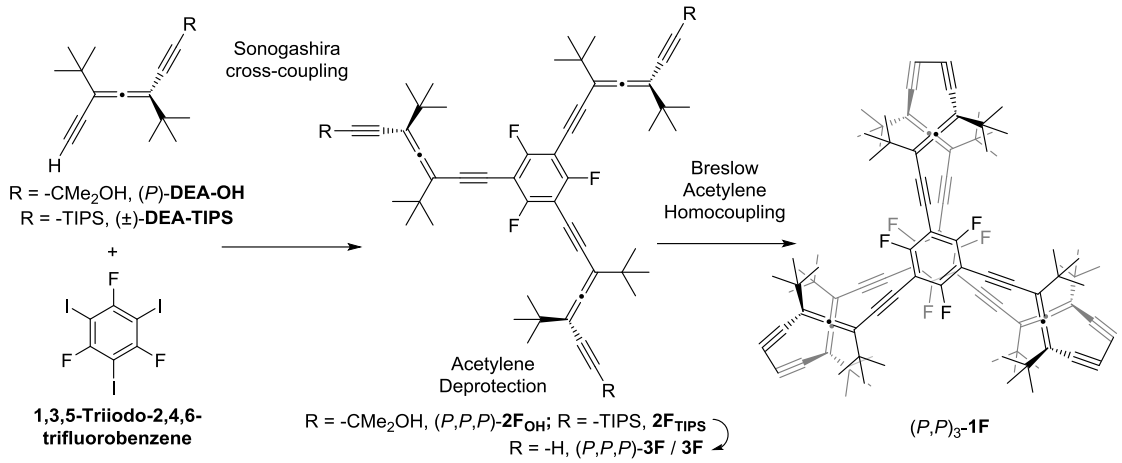

Scheme 7. Synthetic scheme of $(P,P)_3$-**1F**.

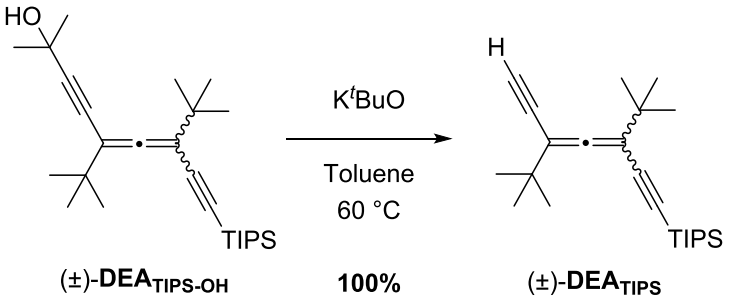

Scheme 8. Bisprotected (±)-**DEA-TIPS-OH** selective deprotection to give (±)-**DEA-TIPS**.

4.4.1. Synthesis of (*P,P,P*)-$2F_{OH}$ and $2F_{TIPS}$

Before using enantiopure (*P*)-**DEA-OH** or (±)-**DEA-TIPS** as starting materials in the Sonogashira triple cross-coupling reaction, since they are expensive in terms of synthetic effort and chiral separation, 2-hydroxypropyl-protected and TMS-protected acetylenes were employed instead. The tricoupled, dicoupled, monocoupled and homodimer products are labelled as **2F'**, **DC-2F'**, **MC-2F'**, and **HD'** respectively (**Scheme 9**).

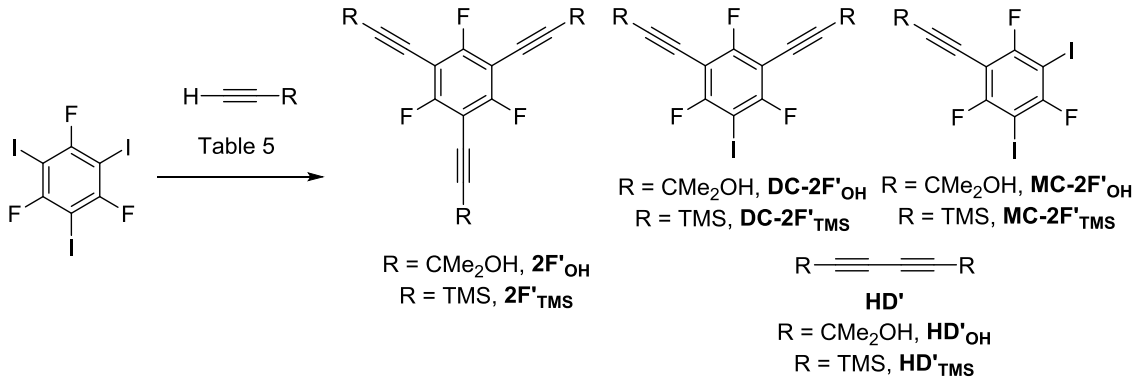

Scheme 9. Synthetic trials for the Sonogashira coupling between the trifluorinated core and 2-hydroxypropyl-protected and TMS-protected acetylenes.

The set of conditions tested made use of classical Sonogashira conditions, employing $Pd(PPh_3)_2Cl_2$, CuI, and a base under inert atmosphere, as well as the more reactive Pd catalyst with bulkier phosphines previously tested (**Table 5**). As a conclusion, in the case of the coupling with the TMS-acetylene, classical conditions previously reported employing *N,N,N*-triethylamine (Et_3N) gave the best result, achieving a 56% yield of **2F'$_{TMS}$** (**Entry 2**).[48] On the other hand, for acetonide-protected acetylene, also classical conditions but with *N,N*-diisopropylamine (DIPA) provided the best results, yielding **2F'$_{OH}$** in a 84% yield (**Entry 6**).

Entry	R	Conditions	t (h)	T (°C)	2F'	HD'	MC-2F'	DC-2F'	PhF_3I_3
1	TMS	$Pd(PPh_3)_2Cl_2$ (20 mol%), CuI (10 mol%), DIPA	20	r.t.	35%	-	-	-	-
2	TMS	$Pd(PPh_3)_2Cl_2$ (20 mol%), CuI (10 mol%), Et_3N	22	r.t.	56%	-	-	-	-
3	CMe_2OH	$Pd(PPh_3)_2Cl_2$ (20 mol%), CuI (10 mol%), Et_3N	15	r.t.	-	60%	-	-	35% rec.
4	CMe_2OH	$Pd(PPh_3)_2Cl_2$ (20 mol%), CuI (10 mol%), Et_3N, freeze-pump-thaw (3 cycles)	14	r.t.	-	58%	-	-	39% rec.
5	CMe_2OH	$Pd(PPh_3)_2Cl_2$ (20 mol%), CuI (10 mol%), Et_3N (3.3 eq), freeze-pump-thaw (x3), DCM	14	r.t.	-	60%	trace	trace	50% rec.
6	CMe_2OH	$Pd(PPh_3)_2Cl_2$ (6 mol%), CuI (6 mol%), DIPA	22	70	84%	-	-	-	-
7	CMe_2OH	$Pd_2(dba)_3{\cdot}CHCl_3$ (7.5 mol%), CuI (60 mol%), trimesitylphosphine (60 mol%), TBAI (6 eq), DIPEA (10 eq), DMF	24	−6 to r.t.	-	57%	-	-	-

Table 5. Sonogashira cross-coupling conditions tested for the coupling of the trifluorinated core and 2-hydroxypropyl/TMS-protected acetylene. All reactions were performed under N_2.

Once having the optimal conditions for the 2-hydroxypropyl and TMS protected acetylenes on hand, next, (*P*)-**DEA-OH** and (±)-**DEA-TIPS** were used to prepare (*P,P,P*)-**2F$_{OH}$** and **2F$_{TIPS}$,** respectively. Side products of these reactions are depicted in **Figure 17**.

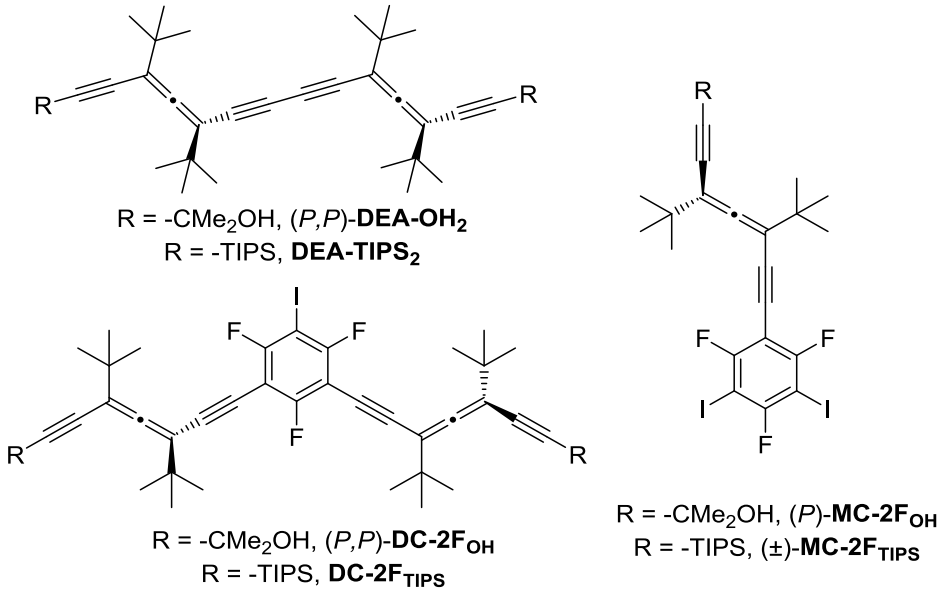

Figure 17. Side products of the synthesis of (*P,P,P*)-**2F$_{OH}$** and **2F$_{TIPS}$**. Dicoupled, monocoupled and homodimer of allene labelled as (*P,P*)-**DC-2F$_{OH}$**, (*P*)-**MC-2F$_{OH}$**, and (*P,P*)-**DEA-OH$_2$** respectively.

A summary of conditions tested on the synthesis of (*P,P,P*)-**2F$_{OH}$** and **2F$_{TIPS}$** is presented on **Table 6**. conditions which resulted more reactive in the case of the benzenic and methylated cores,[49] **Entry 1**, were tested for the coupling of (*P*)-**DEA-OH** and the trifluorinated aromatic core, affording a 26% of monocoupled product (*P*)-**MC-2F$_{OH}$** along with a 45% yield of (*P,P*)-**DEA$_2$**. The conditions employed in the previous tests with 2-hydroxypropyl-acetylene (**Entry 2**) which make use of $Pd_2(PPh_3)_2$ (6 mol%), CuI (6 mol%), and DIPA, afforded (*P,P,P*)-**2F$_{OH}$** in a 90% yield. Regarding the coupling of the trifluorinated core with racemic allene (±)-**DEA-TIPS** (**Entry 3**) afforded **2F$_{TIPS}$** in a 23% yield.

Entry	DEA	Conditions	T(°C)	(*P,P,P*)-**2F$_{OH}$** / **2F$_{TIPS}$**	(*P*)-**MC-2F$_{OH}$** / **MC-2F$_{TIPS}$**	(*P,P*)-**DC-2F$_{OH}$** / **DC-2F$_{TIPS}$**	(*P,P*)-**DEA-OH$_2$** / **DEA-TIPS$_2$**
1	(*P*)-**DEA-OH**	$Pd_2(dba)_3{\cdot}CHCl_3$ (7.5 mol%), CuI (60 mol%), TBAI (6 eq), trimesitylphosphine (60 mol%), DIPEA (10 eq), DMF	−6 to r.t.	-	26%	-	45%
2	(*P*)-**DEA-OH**	$Pd_2(PPh_3)_2$ (6 mol%), CuI (6 mol%), DIPA	70	90%	-	-	10%
3	(±)-**DEA-TIPS**	$Pd_2(PPh_3)_2$ (6 mol%), CuI (6 mol%), DIPA	75	23%	23%	20%	32%

Table 6. Sonogashira cross-coupling reaction conditions tested on the synthesis of (*P,P,P*)-**2F$_{OH}$** and **2F$_{TIPS}$**. Reaction time was 20 h for all Entries. **2F$_{TIPS}$**, **MC-2F$_{TIPS}$**, **DC-2F$_{TIPS}$**, and **DEA-TIPS$_2$** were obtained as diastereoisomeric mixtures.

Significant signals of the characterization of (*P,P,P*)-**2F$_{OH}$** and **2F$_{TIPS}$** are the ^{19}F NMR singlet at −101 ppm, and the ^{13}C NMR aromatic carbon attached to the F, showing a doublet of triplets at 161 ppm with C−F coupling constants ^{1}J and ^{3}J of 260 and 8 Hz respectively.

4.4.2. Synthesis of (*P,P,P*)-3F

As in the case of the triple Sonogashira coupling, different conditions were initially tested with the tricoupled product **2F'$_{OH}$** in order to achieve trisdeprotected product **3F'** and save the trisallenic derivative (*P,P,P*)-**2F$_{OH}$** (**Scheme 10**).

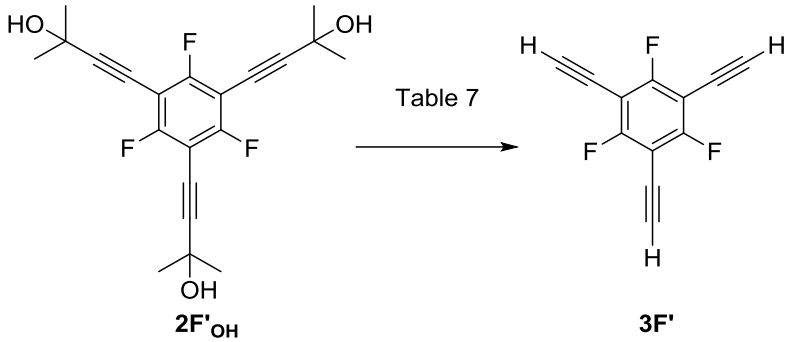

Scheme 10. Synthesis of **3F'** from **2F'$_{OH}$**.

Among all conditions tested, presented on **Table 7**, the best results (**Entry 2**) were obtained using powdered flamed NaOH (4.5 eq) in refluxing dry toluene under N_2 atmosphere for 26 h, that afforded **3F'** in a 33% yield.

Entry	Conditions	t (h)	T (°C)	3F'	Other
1	Powdered flamed NaOH (18 eq), Toluene, N_2	15	110	11%	-
2	Powdered flamed NaOH (4.5 eq), Toluene, N_2	26	110	33%	-
3	K^{t}BuO (2 eq), Toluene, N_2	4.5	110	Traces	-
4	K^{t}BuO (5 eq), Toluene, N_2	45	r.t. to 80	-	Insoluble unknown product
5	NBu_4OH (1M in MeOH) (30 mol% → 90 mol%), Toluene, N_2	23	55 to 75	-	Product from exchange of 1 or 2 -F atoms by -OMe
6	K^{t}BuO (4 eq), Toluene, N_2 flow	8	60	Traces	Traces of Mono- and Bisdeprotected
7	K^{t}BuO (4 eq), Toluene, N_2, distillation setup	4.5	60	14%	-

Table 7. Deprotection conditions tested on the synthesis of **3F'**.

Thereon, the treatment of (*P,P,P*)-**2F$_{OH}$** with flamed powdered NaOH (84 eq, excess employed in order to have an easy to handle amount of NaOH) in refluxing toluene for 15 h, afforded (*P,P,P*)-**3F** in a 62% yield (**Scheme 11**). On the other hand, in the case of the TIPS-protected tricoupled

product **2F$_{TIPS}$**, the classic reagent for deprotection of silanes, tetrabutylammonium fluoride (TBAF) in tetrahydrofuran (THF) at r.t., was used, affording **3F** in a 75% yield after 15 min.

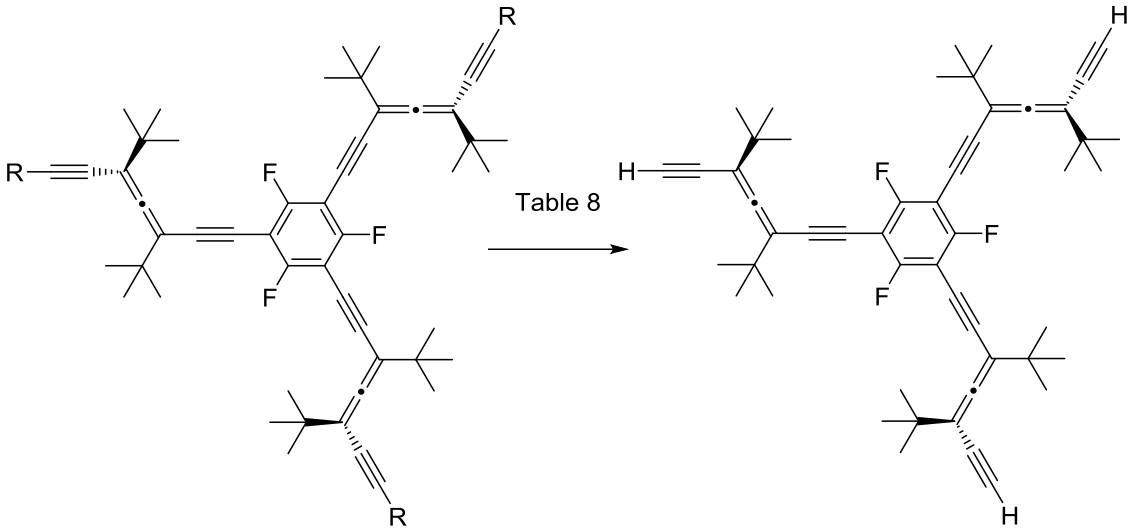

Scheme 11. Synthesis of (*P,P,P*)-**3F** and **3F**. **2F$_{TIPS}$** and **3F** are diastereisomeric mixtures.

Entry	DEA	Conditions	t (h)	T(°C)	(*P,P,P*)-**3F** / **3F**
1	(*P*)-**DEA-OH**	NaOH (84 eq), Toluene	15	110	62%
2	(±)-**DEA-TIPS**	TBAF (3 eq, 1M in THF), THF	0.25	r.t.	75%

Table 8. Summary of conditions employed on the deprotection reaction to give (*P,P,P*)-**3F** or **3F**. **3F** as a diastereisomeric mixture.

If we consider both triple coupling and triple deprotection reactions for both *Route a* (2-hydroxypropyl-protected (*P*)-**DEA-OH**) and *b* ((±)-**DEA-TIPS**), the overall yield is 56% for *Route a* and 17% for *Route b*, concluding that the pathway involving the 2-hydroxypropyl protecting group is globally more efficient.

Regarding the characterization of (*P,P,P*)-**3F**, it is noteworthy to mention the appearance of a characteristic band at *ca.*1460 cm^{-1} from the C–F stretching on its IR spectrum.

4.4.3. Synthesis of (*P,P*)$_3$-1F

Synthesis of fluorinated molecular cage (*P,P*)$_3$-**1F** was achieved through a Cu-catalyzed homodimerization of two units of trisdeprotected product (*P,P,P*)-**3F** (**Scheme 12** and **Table 9**). The first attempt (**Entry 1**) was done under pseudohighdilution Breslow conditions, in the presence of excess of CuCl and $CuCl_2$ in dry pyridine at r.t., affording side product (*P*)$_6$-**8** in a 3% yield (**Figure 18**). The same conditions but at 40 °C (**Entry 2**) were tested rendering traces of the side product (*P*)$_6$-**9** instead.

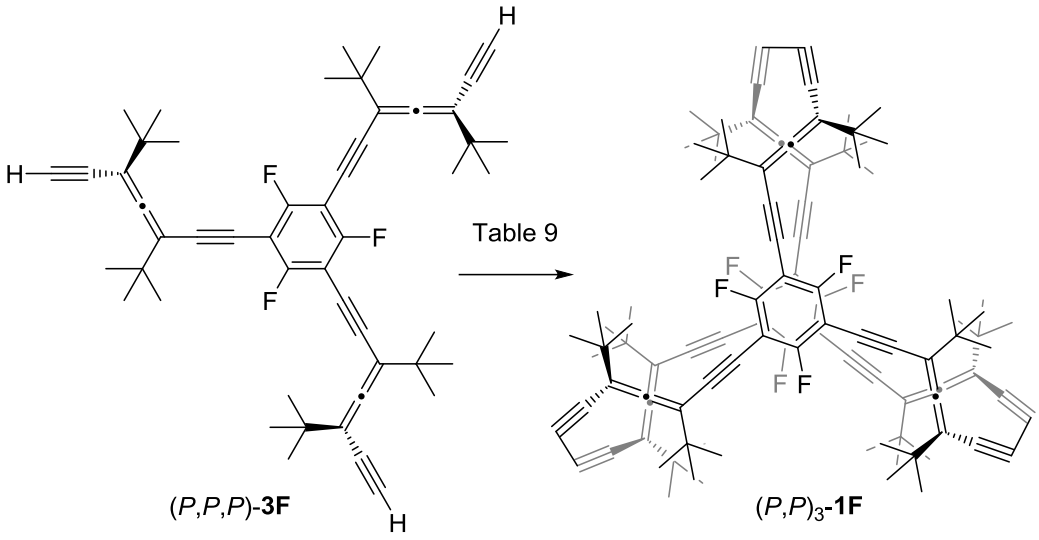

Scheme 12. Synthesis of $(P,P)_3$-**1F**.

Entry	Conditions	$(P,P)_3$-**1F**	$(P)_6$-**9**	$(P)_6$-**8**
1	CuCl (75 eq), $CuCl_2$ (11 eq), Py, r.t., N_2 (1 h bubbling), 3 days, ϕ = 1 mL·h^{-1}	-	-	3%
2	CuCl (75 eq), $CuCl_2$ (11 eq), Py, 40 °C, N_2 (1 h bubbling), 3 days, ϕ = 1 mL·h^{-1}	-	traces	-

Table 9. Summary of conditions tested on the synthesis of $(P,P)_3$-**1F**.

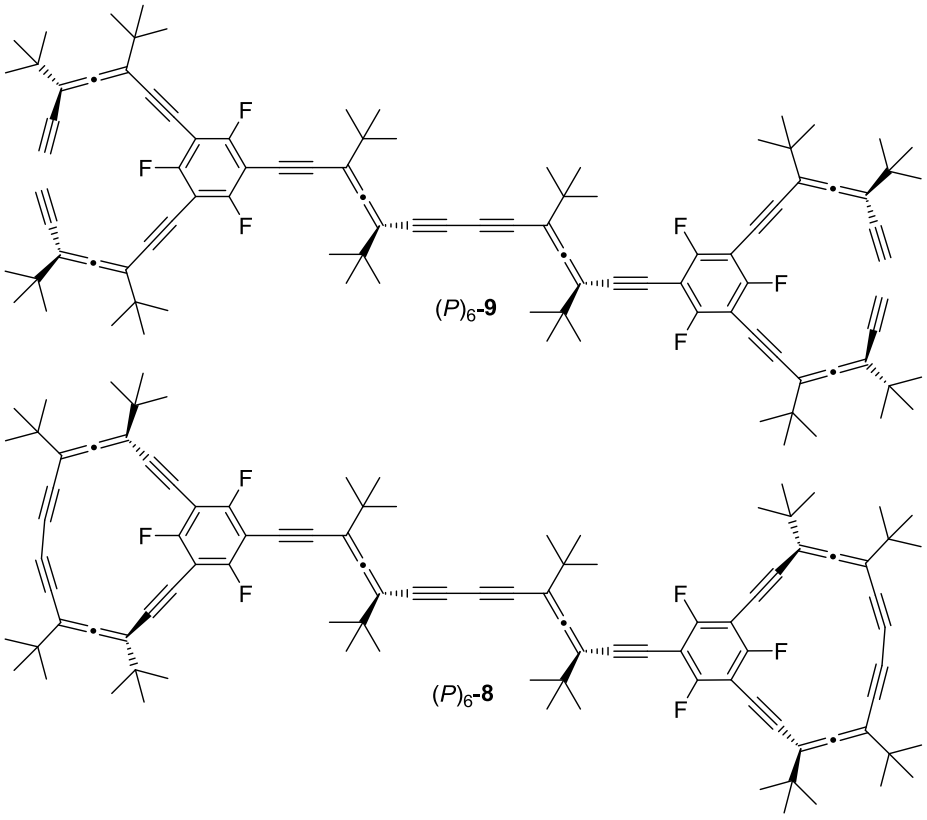

Figure 18. Side products obtained towards $(P,P)_3$-**1F**.

In conclusion, molecular cage (*P,P*)$_3$-**1F** could not be synthesized through Breslow homocoupling conditions, but the traces of (*P*)$_6$-**9** found in experiment present on **Table 9**, **Entry 2**, reveal that we reached a point close to the final product, that could be somehow improved. We postulate a possible solution using a templating agent for the two fluorinated electron deficient cores to approach.

4.5. Synthetic approach to (*P,P*)$_3$-1N

One interest in the research group is the use of nitrogen containing heterocycles due to the potential applicability of the electron pair over the nitrogen atom and the electronic character of the aromatic ring. Thus, molecular cage (*P,P*)$_3$-**1N** (**Figure 19**), which besides having an electron deficient core, bears six nitrogen atoms, was proposed. Initially, synthetic proposed strategy for (*P,P*)$_3$-**1N** was based in the same basic steps as for the previously reported cages, starting with a triple cross−coupling between the core and the corresponding (*P*)-**DEA-OH**, followed by subsequent deprotection and homodimerization reactions. The main difference here lies on the use of Negishi reaction conditions instead of Sonogashira conditions for the coupling between the cyanuric chloride (2,4,6-trichloro-1,3,5-triazine) and TIPS-protected (±)-**DEA-TIPS** for the initial attempts. This change of allene was made due to the incompatibility of the cyanuric chloride with alcohols in the presence of bases, present on 2-hydroxypropyl-protected (*P*)-**DEA-OH.**[50] Cyanuric chloride is also incompatible with amines (usually employed as base and/or solvent in Sonogashira reaction),[51–54] and with DMF (affording Gold's reagent).[55–57] As in the case of (*P,P*)$_3$-**1F**, some preliminary reactivity tests between cyanuric chloride and 2-hydroxypropyl-/TMS-protected acetylene under Negishi conditions were also performed (**Scheme 13**).

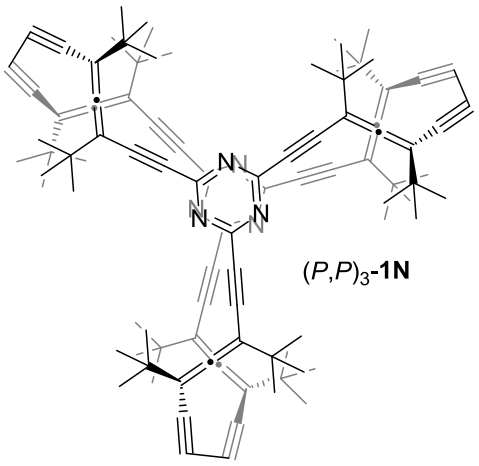

Figure 19. Structure of molecular cage (*P,P*)$_3$-**1N**.

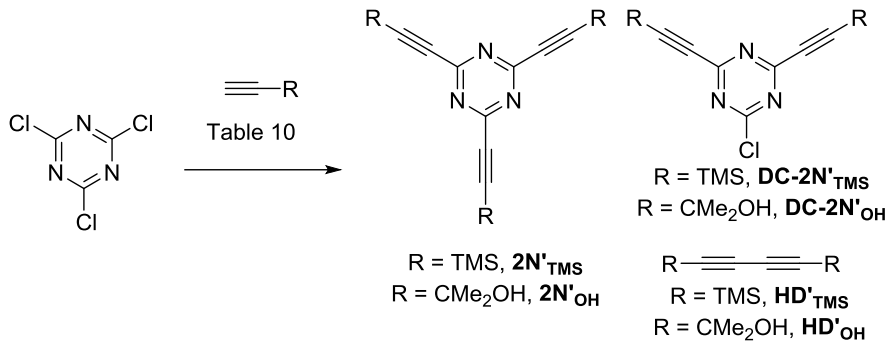

Scheme 13. Coupling between cyanuric chloride and differently protected acetylenes.

As done in the case of (*P,P*)$_3$-**1F**, model system was initially studied. First conditions tested, (**Entry 1**, **Table 10**), were a replica of previously reported conditions,[58,59] based on the formation of the TMS-acetylene organolithium, followed by transmetallation with a Zn salt to form the zincate, which undergoes a Negishi coupling with the cyanuric chloride in presence of Pd(PPh$_3$)$_4$. **2N'$_{TMS}$** was obtained in a 41%, along with a 31% of dicoupled product **DC-2N'$_{TMS}$**, and a 4% of homodimer of TMS-acetylene **HD'$_{TMS}$**. The outcome of the reaction did not improve when the zincate solution was filtered in order to avoid the presence of Zn salts, and allowed the second step to react for longer but at 0 °C (**Entry 2**, **Table 10**). Next, since the presence of moisture on the $ZnCl_2$ may be the cause for the low yield achieved, $ZnCl_2$ was overnight dried at 130 °C under vacuum and the SiO_2 employed on the F.C. purification was partially H_2O-deactivated. These modifications resulted in a quantitative yield of **2N'$_{TMS}$ (Entry 3**, **Table 10)**. Despite the presumable incompatibility of cyanuric chloride with Sonogashira conditions reported by Li et al,[49] a test with 2-hydroxypropyl-protected acetylene was done and, as expected, acetylene homodimer **HD'** was obtained in an 80% yield (**Entry 4**, **Table 10**).

Entry	R	Conditions	2N'	DC-2N'	HD'
1	TMS	**1)** TMS-acetylene (5 eq) + *n*BuLi (5 eq, −78 °C addition; r.t. 5 min); **2)** $ZnCl_2$ (5 eq) (r.t., 30 min); **3)** $C_3N_3Cl_3$ (1 eq) + [Pd(PPh$_3$)$_4$] (5 mol%) (30 °C, 17 h).	41%	31%	4%
2	TMS	**1)** TMS-acetylene (8 eq) + *n*BuLi (8 eq, −78 °C addition; −78 °C 1 h); **2)** $ZnCl_2$ (8 eq) (0 °C, 1.5 h); **3)** $C_3N_3Cl_3$ (1 eq) + [Pd(PPh$_3$)$_4$] (20 mol%) (r.t., 24 h) over filtrated zincate.	13%	8%	5%
3	TMS	**1)** TMS-acetylene (8 eq) + *n*BuLi (8 eq, −78 °C addition; −78 °C, 1 h); **2)** $ZnCl_2$ (8 eq, dried overnight 130 °C in vacuum) (0 °C, 3 h); **3)** $C_3N_3Cl_3$ (1 eq) + [Pd(PPh$_3$)$_4$] (20 mol%) (0 °C addition; r.t., 64 h) over filtrated zincate. FC (SiO_2 6% wt/wt H_2O deactivated)	100%	-	-
4	CMe_2OH	$C_3N_3Cl_3$, $Pd_2(dba)_3{\cdot}CHCl_3$ (7.5 mol%), CuI (60 mol%), TBAI (6 eq), DIPEA (10 eq), DMF (distilled over $MgSO_4$), N_2, −20 °C → 0 °C, 4.5 h	-	-	80%

Table 10. Negishi cross−coupling conditions tested between cyanuric chloride and 2-hydroxypropyl-/TMS-protected acetylenes.

So, the same and other conditions were tested for (±)-**DEA-TIPS** (**Scheme 14**) drying the $ZnCl_2$ using different methodologies and temperatures. Mostly, the recovery of the starting material ((±)-**DEA-TIPS**) (from 11 to 100%) was the main product.

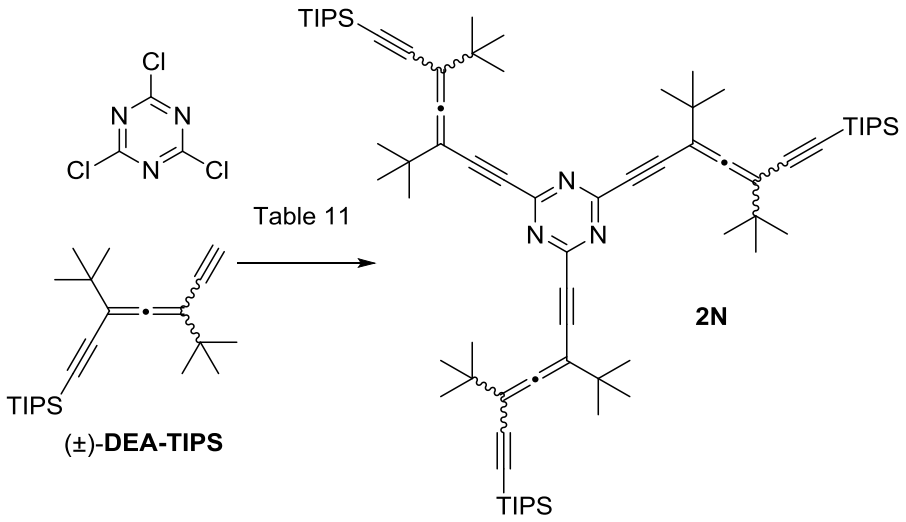

Scheme 14. Coupling between cyanuric chloride and racemic (±)-**DEA-TIPS** to give **2N**.

Entry	Conditions	(±)-**DEA-TIPS**
1	(±)-**DEA-TIPS** (5 eq) in THF + **1)** *n*BuLi (5 eq, −78 °C addition; r.t. 30 min); **2)** $ZnCl_2$ (5 eq, dried overnight 160 °C in vacuum glass oven) (r.t., 30 min); **3)** $C_3N_3Cl_3$ (1 eq) + $[Pd(PPh_3)_4]$ (5 mol%) (r.t. addition; 30 °C, 15 h) over DEA_b-zincate. FC (SiO_2, Hexane)	62% rec.
2	(±)-**DEA-TIPS** (5 eq) in THF + **1)** *n*BuLi (5 eq, −78 °C addition, r.t. 30 min); **2)** $ZnCl_2$ (5 eq, dried overnight 130 °C in vacuum glass oven + 20 eq commercial) (r.t., 30 min); **3)** $C_3N_3Cl_3$ (1 eq) + $[Pd(PPh_3)_4]$ (5 mol%) (r.t. addition; 30 °C, 15 h) over DEA-zincate. FC (SiO_2, Hexane)	87% rec.
3	(±)-**DEA-TIPS** (5 eq) in THF + **1)** *n*BuLi (5 eq, −78 °C addition; r.t. 30 min); **2)** $ZnCl_2$ (5 eq, under vacuum melted, redissolved under N_2) (r.t., 30 min); **3)** $C_3N_3Cl_3$ (1 eq → 8 eq) + $[Pd(PPh_3)_4]$ (5 mol%) (r.t. addition; 30 °C → 50 °C, 46 h) over DEA-zincate. FC (SiO_2, Hexane)	50% rec.
4	(±)-**DEA-TIPS** (3.1 eq) in THF + **1)** *n*BuLi (3.1 eq, −78 °C addition; r.t. 30 min); **2)** $ZnCl_2$ (3.1 eq, dried in the oven at 114 °C, cooled under N_2) (r.t., 30 min); **3)** $C_3N_3Cl_3$ (1 eq) + $[Pd(PPh_3)_4]$ (20 mol%) (r.t. addition; 30 °C → 35 °C, 40 h) over DEA-zincate. FC (SiO_2 Hexane:DCM 4%)	11% rec.+ Unknown Product
5	(±)-**DEA-TIPS** (3.1 eq) in THF + **1)** *n*BuLi (3.1 eq, −78 °C addition; r.t. 1 h); **2)** $ZnCl_2$ (3.1 eq, dried under vacuum at 130 °C, cooled under N_2) (0 °C, 4 h); **3)** $C_3N_3Cl_3$ (1 eq) + $[Pd(PPh_3)_4]$ (10 mol%, freshly synthesized) (r.t., 48 h) over DEA-zincate. FC (SiO_2, Hexane)	58% rec.

6	(±)-**DEA-TIPS** (3.1 eq) in THF + **1)** *n*BuLi (3.1 eq, −78 °C addition; −78 °C 1 h); **2)** $C_3N_3Cl_3$ (1 eq) (r.t. → 30 °C, 3 days) over DEA-zincate. FC (SiO_2, Hexane)	100% rec.
7	(±)-**DEA-TIPS** (3.1 eq) in THF + **1)** *n*BuLi (3.1 eq, −78 °C addition, r.t. 1 h); **2)** $ZnCl_2$ (3.1 eq, dried under vacuum at 130 °C, cooled under N_2) (0 °C, 4 h); **3)** $C_3N_3Cl_3$ (1 eq) + [$Pd(PPh_3)_4$] (10 mol%, freshly synthesized) (r.t. → 70 °C, 3 days) over DEA-zincate. FC (SiO_2, Hexane)	97% rec.

Table 11. Conditions tested on the coupling between cyanuric chloride and (±)-**DEA-TIPS**.

In light of the negative results achieved through the use of Negishi conditions for the coupling between cyanuric chloride and both (*P*)-**DEA-OH** and (±)-**DEA-TIPS**, an alternative potential synthesis of tricoupled product (*P,P,P*)-**2N** or **2N** is proposed by means of using previously reported Stille cross-coupling conditions for alkynylstannanes with cyanuric chloride.[60]

In summary, in this **Chapter 4** we have synthesized and fully characterized the helical cage compound (*P,P*)$_3$-**1Me**. Moreover, a comparative complexation study of it and cage (*P,P*)$_3$-**1H** with different sandwich compounds as well as paracyclophanes was performed, showing the improvement on the complexation ability of (*P,P*)$_3$-**1Me** induced by the presence of the six methyl groups on the aromatic lids. Particularly, complex (*P,P*)$_3$-**1Me@Rut$^+$** was chiroptically detected by means of electronic circular dichroism. On the other hand, molecular cages (*P,P*)$_3$-**1F** and (*P,P*)$_3$-**1N** were not able to be synthesized, however, alternative futurible syntheses are proposed for each of them.

4.6. References

[1] S. S. Moore, T. L. Tarnowski, M. Newcomb, and D. J. Cram, *J. Am. Chem. Soc.* **1977**, *99*, 6398–6405.

[2] K. Hirose, K. Ogasahara, K. Nishioka, Y. Tobe, and K. Naemura, *J. Chem. Soc. Perkin Trans. 2* **2000**, *89*, 1984–1993.

[3] Y. Liu, C.-C. You, T. Wada, and Y. Inoue, *J. Chem. Res.* **2000**, *2000*, 90–92.

[4] C. A. Hunter, C. M. R. Low, C. Rotger, J. G. Vinter, and C. Zonta, *Proc. Natl. Acad. Sci. U. S. A.* **2002**, *99*, 4873–4876.

[5] L. Trollope, D. L. Cruickshank, T. Noonan, S. A. Bourne, M. Sorrenti, L. Catenacci, and M. R. Caira, *Beilstein J. Org. Chem.* **2014**, *10*, 3136–3151.

[6] G. Wenz, *Beilstein J. Org. Chem.* **2012**, *8*, 1890–1895.

[7] M. Etzkorn, J. C. Timmerman, M. D. Brooker, X. Yu, and M. Gerken, *Beilstein J. Org. Chem.* **2010**, *6*, DOI 10.3762/bjoc.6.39.

[8] H. Takemura, H. Kariyazono, M. Yasutake, N. Kon, K. Tani, K. Sako, T. Shinmyozu, and T. Inazu, *Eur. J. Org. Chem.* **2000**, *2000*, 141–148.

[9] H. Takemura, S. Nakashima, N. Kon, M. Yasutake, T. Shinmyozu, and T. Inazu, *J. Am. Chem. Soc.* **2001**, *123*, 9293–9298.

[10] Y. Zhao, G. Markopoulos, and T. M. Swager, *J. Am. Chem. Soc.* **2014**, *136*, 10683–10690.

[11] M. M. Becker, and B. J. Ravoo, *Chem. Commun.* **2010**, *46*, 4369–4371.

[12] L. Ren, J. Zhang, C. G. Hardy, S. Ma, and C. Tang, *Macromol. Rapid Commun.* **2012**, *33*, 510–516.

[13] T. Inagaki, T. Mochida, M. Takahashi, C. Kanadani, T. Saito, and D. Kuwahara, *Chem. Eur. J.* **2012**, *18*, 6795–804.

[14] J. Zhang, Y. P. Chen, K. P. Miller, M. S. Ganewatta, M. Bam, Y. Yan, M. Nagarkatti, A. W. Decho, and C. Tang, *J. Am. Chem. Soc.* **2014**, *136*, 4873–4876.

[15] S. Vanicek, H. Kopacka, K. Wurst, S. Vergeiner, L. Oehninger, I. Ott, and B. Bildstein, *Zeitschrift für Anorg. und Allg. Chemie* **2015**, *641*, 1282–1292.

[16] J. Wei, L. Ren, C. Tang, and Z. Su, *Polym. Chem.* **2014**, *5*, 6480–6488.

[17] L. Hintermann, L. Xiao, A. Labonne, and U. Englert, *Organometallics* **2009**, *28*, 5739–5748.

[18] R. Mohammad, M. Ahmad, and L. Y. Heng, *Sensors* **2013**, *13*, 10014–10026.

[19] J. Yu, S. Liu, and H. Ju, *Biosens. Bioelectron.* **2003**, *19*, 401–409.

[20] N. Kobayashi, and T. Osa, *Chem. Lett.* **1986**, 421–424.

[21] T. Matsue, D. H. Evans, T. Osa, and N. Kobayashi, *J. Am. Chem. Soc.* **1985**, *107*, 3411–3417.

[22] A. Ueno, F. Moriwaki, T. Osa, F. Hamada, and K. Murai, *Tetrahedron Lett.* **1985**, *26*, 899–

902.

[23] D. P. Buck, P. M. Abeysinghe, C. Cullinane, A. I. Day, J. G. Collins, and M. M. Harding, *Dalt. Trans.* **2008**, *7*, 2328–2334.

[24] Ivy Philip, and A. E. Kaifer, *J. Org. Chem.* **2005**, *70*, 1558–1564.

[25] S. Kotha, M. E. Shirbhate, and G. T. Waghule, *Beilstein J. Org. Chem* **2015**, *11*, 1274–1331.

[26] D. Trawny, V. Kunz, and H.-U. Reissig, *Eur. J. Org. Chem.* **2014**, 6295–6302.

[27] Y. Li, L. Xu, S. L.-F. Chan, Y. Li, R. Jiang, H. Liu, and C.-M. Che, *Chem. Asian J.* **2014**, *9*, 2842–2849.

[28] D. Padula, I. R. Lahoz, C. Díaz, F. E. Hernández, L. Di Bari, A. Rizzo, F. Santoro, and M. M. Cid, *Chem. - A Eur. J.* **2015**, *21*, 12136–12147.

[29] S. Míguez Lago, M. M. Cid Fernández, and J. L. Alonso Gómez, *Eur. J. Org. Chem.* **2016**, DOI 10.1002/ejoc.201600997.

[30] P. Rivera-Fuentes, J. L. Alonso-Gómez, A. G. Petrovic, F. Santoro, N. Harada, N. Berova, and F. Diederich, *Angew. Chem. Int. Ed.* **2010**, *49*, 2247–2250.

[31] P. Rivera-Fuentes, J. L. Alonso-Gómez, A. G. Petrovic, F. Santoro, N. Harada, N. Berova, and F. Diederich, *Angew. Chemie* **2010**, *122*, 2296–2300.

[32] P. Thordarson, *Chem. Soc. Rev.* **2011**, *40*, 1305–1323.

[33] J. Fernández-Rosas, M. Pessêgo, M. Cepeda-Plaza, N. Basilio, M. Parajó, P. Rodríguez-Dafonte, and L. García-Río, *Org. Biomol. Chem.* **2015**, *13*, 1213–1224.

[34] S. Míguez-Lago, A. L. Llamas-Saiz, M. Magdalena Cid, and J. L. Alonso-Gómez, *Chem. Eur. J.* **2015**, *21*, 18085–18088.

[35] R. Martinez, and A. Tiripicchio, *Acta Crystallogr. Sect. C Cryst. Struct. Commun.* **1990**, *46*, 202–205.

[36] F. A. Cotton, L. M. Daniels, and C. C. Wilkinson, *Acta Crystallogr. Sect. E Struct. Reports Online* **2001**, *57*, 529–530.

[37] J. M. Lynam, L. M. Milner, N. S. Mistry, J. M. Slattery, S. R. Warrington, and A. C. Whitwood, *Dalt. Trans.* **2014**, *43*, 4565–4572.

[38] E. E. Karslyan, D. S. Perekalin, P. V. Petrovskii, K. A. Lyssenko, and A. R. Kudinov, *Russ. Chem. Bull.* **2009**, *57*, 2201–2203.

[39] J. P. Gallivan, and D. A. Dougherty, *J. Am. Chem. Soc.* **2000**, *122*, 870–874.

[40] S. Mecozzi, and J. Rebek, Jr., *Chem. Eur. J.* **1998**, *4*, 1016–1022.

[41] Y. Yang, and L. Yu, *Phys. Chem. Chem. Phys.* **2013**, *15*, 2669–2683.

[42] J. Rodríguez-Otero, E. M. Cabaleiro-Lago, Á. Peña-Gallego, and M. Merced Montero-Campillo, *Tetrahedron* **2009**, *65*, 2368–2371.

[43] A. Vargas-Caamal, S. Pan, F. Ortiz-Chi, J. L. Cabellos, R. A. Boto, J. Contreras-Garcia, A. Restrepo, P. K. Chattaraj, and G. Merino, *Phys. Chem. Chem. Phys.* **2016**, *550*, 550–556.

[44] C. T. Li, Q. Y. Cao, J. J. Li, Z. W. Wang, and B. N. Dai, *Inorg. Chim. Acta* **2016**, *449*, 31–37.

[45] S. Vaddiraju, D. J. Burgess, I. Tomazos, F. C. Jain, and F. Papadimitrakopoulos, *J. Diabetes Sci. Technol. J Diabetes Sci Technol* **2010**, *44*, 1540–1562.

[46] J. L. Alonso-Gómez, A. G. Petrovic, N. Harada, P. Rivera-Fuentes, N. Berova, and F. Diederich, *Chem. Eur. J.* **2009**, *15*, 8396–8400.

[47] O. Gidron, M.-O. Ebert, N. Trapp, and F. Diederich, *Angew. Chem Int. Ed.* **2014**, *53*, 13614–13618.

[48] G. Hennrich, and A. M. Echavarren, *Tetrahedron Lett.* **2004**, *45*, 1147–1149.

[49] J. Li, and P. Huang, *Res. Chem. Intermed.* **2011**, *38*, 403–411.

[50] S. Ito, Y. Ueta, T. T. T. Ngo, M. Kobayashi, D. Hashizume, J. Nishida, Y. Yamashita, and K. Mikami, *J. Am. Chem. Soc.* **2013**, *135*, 17610–17616.

[51] W. Huang, W. Zheng, D. J. Urban, J. Inglese, E. Sidransky, C. P. Austin, and C. J. Thomas, *Bioorg. Med. Chem. Lett.* **2007**, *17*, 5783–5789.

[52] C. A. M. Afonso, N. M. T. Lourenco, and A. de A. Rosatella, *Molecules* **2006**, *11*, 81–102.

[53] P. Rushton, and M. F. G. Stevens, *J. Chem. Soc. Perkin Trans. 1* **1985**, 1533–1539.

[54] B. Kolesinska, and Z. J. Kaminski, *Tetrahedron* **2009**, *65*, 3573–3576.

[55] S. A. Jadhav, and R. K. Pardeshi, *Heterocycl. Lett.* **2016**, *6*, 99–104.

[56] H. Gold, *Angew. Chem.* **1960**, *72*, 956–959.

[57] J. T. Gupton, C. Colon, C. R. Harrison, M. J. Lizzi, and D. E. Polk, *J. Org. Chem.* **1980**, *45*, 4522–4524.

[58] M. Sonoda, A. Inaba, K. Itahashi, and Y. Tobe, *Org. Lett.* **2001**, *3*, 2419–2421.

[59] A. O. King, E. Negishi, F. J. Villani, and A. Silveira, *J. Org. Chem.* **1978**, *43*, 358–360.

[60] R. Faust, and B. Göbelt, *Tetrahedron Lett.* **1997**, *38*, 8017–8020.

5. Triangulene-based Molecular Cages

5.1. Introduction

Exploration of different cores in pursuing chiral organic molecular cages has been proved to be a valuable tool in order to tune their complexation capabilities. As an example, we have demonstrated the improvement in the complexation of organometallic sandwich compounds by molecular cages by just adding methyl groups to the aromatic lids, as shown for the electron-rich cage (*P,P*)$_3$-**1Me** in **Chapter 4**. By virtue of the increasing on the association constant (K_a) achieved on the [(*P,P*)$_3$-**1Me**@**Rut**$^+$] complex formation in comparison to that formed with the non-methylated cage (*P,P*)$_3$-**1H**, the first one was detected by means of electronic circular dichroism (ECD). Given the redox properties of the previously proposed organometallic sandwich compounds, in **Chapter 5** the design and synthesis of chiral organic molecular cages bearing redox-active cores is proposed. This fact would allow the combination of chirality detection modulated by the application of a current to the solution in which both host and guest were dissolved (**Scheme 1**).

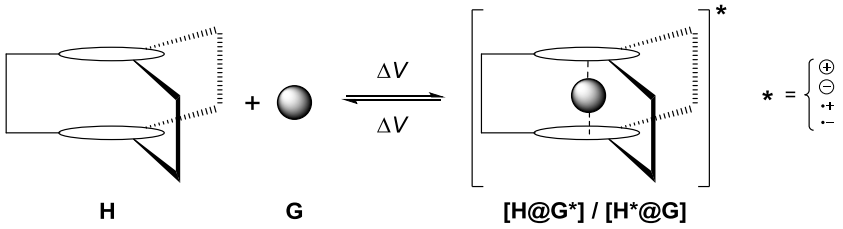

Scheme 1. Host–Guest complex formation modulated by the application of a voltage (ΔV), which induces a charge over the H or G, favoring/disfavoring the complex formation.

Triangulenes, which are highly conjugated triangular-shaped molecules formed by the fusion of six benzenoid rings, have been demonstrated to be highly redox-active species. Specifically, those bearing a nitrogen atom as the inner heteroatom, known as *N*-heterotriangulenes have been broadly investigated (**Figure 1a**). Many *N*-heterotriangulenes get reversibly oxidized to give the radical cation species,[1] which are more stable than their non-bridged analogous bearing no *para* substitution. The only non *para*-substituted heterotriangulene radical cation that could be isolated and whose structure could be unambiguously determined was until 2013 the compound known as *N*-trioxatriangulenium (N-TOTA$^{\cdot+}$) shown in **Figure 1b**.[1] Before that, but in strongly acidic solution, radical cation of (4,4,8,8,12,12-hexamethyl-4*H*,8*H*,12*H*-benzo [1,9] quinolizino [3,4,5,6,7-*defg*]acridine) was also reported.[2] Decades after that, the latter compound mentioned was achieved and detected by means of electric paramagnetic resonance (EPR) spectroscopy after treatment with tris(pentafluorophenyl)borane ($B(C_6F_5)_3$). Such radical cation crystal was also obtained by treatment with the silver salt $Ag(Al(OC(CF_3)_3)_4)$, absorbing in the visible region at *ca.* 600 nm, and evolving to a dicationic species with diradical character (**Figure 1b**).[3]

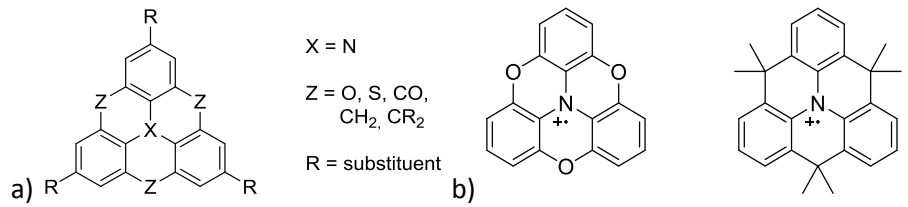

Figure 1. a) Schematic representation of an *N*-heterotriangulene, with the different substituents and bridges reported on literature so far. b) Radical cation *N*-trioxatriangulenium (N-TOTA$^{\cdot+}$) (left), and its dimethylmethylene-bridged analogous (right).

Synthesis and stability studies concerning triangulenes were already accomplished in 1953 by Clar et al.[4] A famous example of this class of compounds within the family of triangulenes are planarized triphenylmethane dyes, molecules which gained much attention due to their absorption-emission properties.[5,6] Two decades later, Hellwinkel et al. reported the synthesis of diverse heterotriangulenes incorporating nitrogen as inner heteroatom and dimethylmethylene or carbonyl bridges.[2,7] Such compounds can be defined as planarized relatives of triphenylamine, known for being a good hole-transporting moiety.[8–10] Thus, planarized analogous overcome triphenylamines drawbacks,[11] showing a better electronic communication between aromatic rings across the central nitrogen atom.[12] For that reason, and despite the emergence on literature of differently substituted heterotriangulenes, such as those having phosphorous/arsenic[13] and boron[14] as inner heteroatoms, the ones with nitrogen have been the most widely developed.

Since then, many have been the applications in which these *N*-heterotriangulene derivatives have been tested (**Figure 2**), such as, dye sensitized solar cells (DSSCs),[15–19] that show in general lower cost and an easier fabrication methodology than the traditional solar cells; organic light emitting diodes (OLEDs),[20,21] as well as organic field effect transistors (OFETs).[22] Besides, *N*-heterotriangulenes have been integrated into higher-order molecular structures such as 1D fibers,[23] postulated to show better charge transport than thin films; and also into 2D covalent networks formed over metallic surfaces, imitating pristine graphene but N-doped.[24,25] Finally, incorporation of *N*-heterotriangulenes into macrocycles is postulated as useful structure employed as molecular switches, due to a change in shape favored by a redox process.[26]

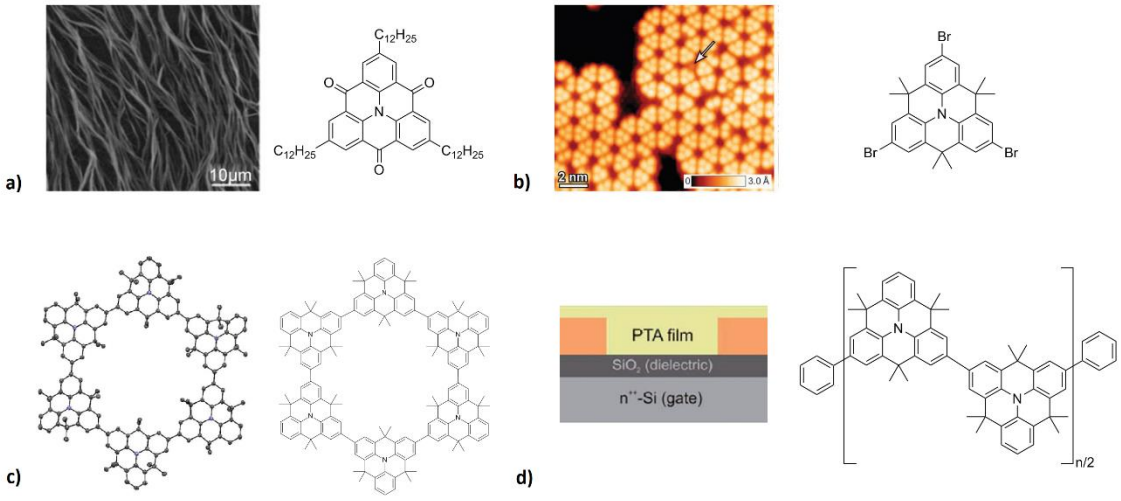

Figure 2. a) Tapping-mode AFM image of the aligned fibers of an alkynylated carbonyl-bridged *N*-heterotriangulene.[23] b) STM topograph (−2 V, 100 pA) of a covalent polymer formed from a methylated N-heterotriangulene at 300 °C. The arrow points to a molecule which misses all CH_3 groups.[24] c) Top view of the X-ray crystal structure of macrocycle composed by 6 *N*-heterotriangulene units (nitrogen atoms in blue, carbon atoms in gray, hydrogens omitted for clarity).[26] d) Chemical structure of the PTA polymer and schematic representation of bottom-gate/bottom-contact (BG/BC) OFETs (salmon part made of Au).[22]

Numerous derivatives of the *N*-heterotriangulenes have been achieved from the halogenated analogous with a broad variety of substituents (aryl, vinyl, alkenyl, alkynyl) through transition-metal−catalyzed cross−coupling reactions such as Heck, Stille, Sonogashira, and Suzuki-Miyaura

methodologies.[11] Thus, such methodologies can be applied on the synthesis of covalent organic helical cages, when combined with enantiopure diethynylallenes (**DEAs**).

In order to broaden the scope of covalent organic chiral cages, the synthesis of two new helical cages (*M,M*)$_3$-**1TCO** (CO-bridged *N*-heterotriangulene as core) and (*M,M*)$_3$-**1TMe** (dimethylmethylene-bridged *N*-heterotriangulene as core) were proposed, according to the retrosynthetic pathway depicted on **Scheme 2**.

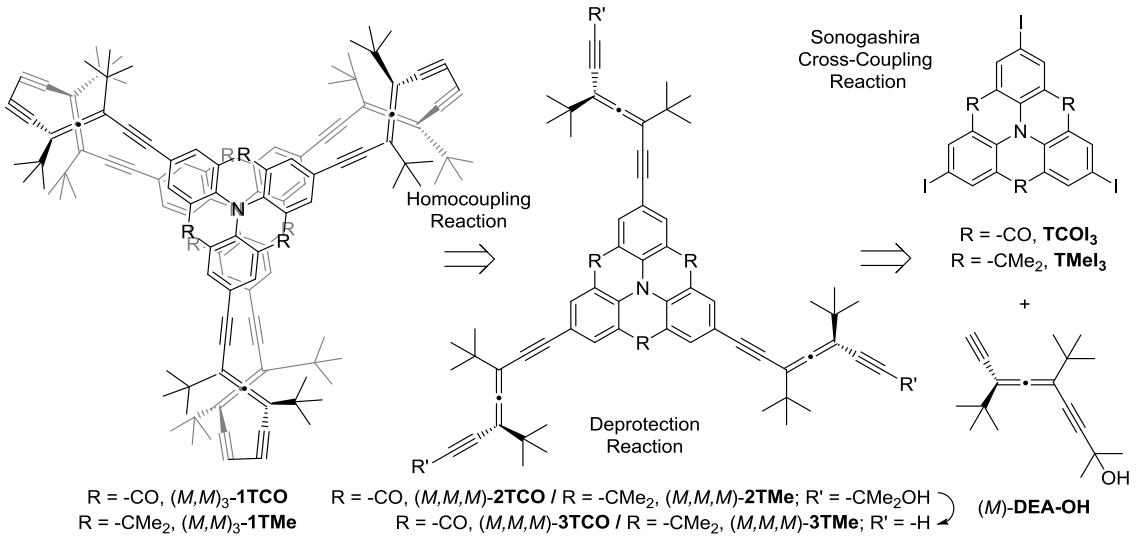

Scheme 2. Retrosynthetic scheme of covalent organic helical cages (*M,M*)$_3$-**1TCO** and (*M,M*)$_3$-**1TMe**, based on a cross–coupling reaction between (*M*)-**DEA-OH** and triangulenic cores, followed by (*M*)-**DEA-OH** deprotection, and Cu-catalyzed homocoupling of two tripodal shaped molecules.

These two heterotriangulenic cores will have totally different electronic characters, being the carbonyl-bridged one electron deficient, whilst the dimethymethylene-bridged one is slightly electron rich as shown by the corresponding electrostatic potential surfaces depicted in **Figure 3**.

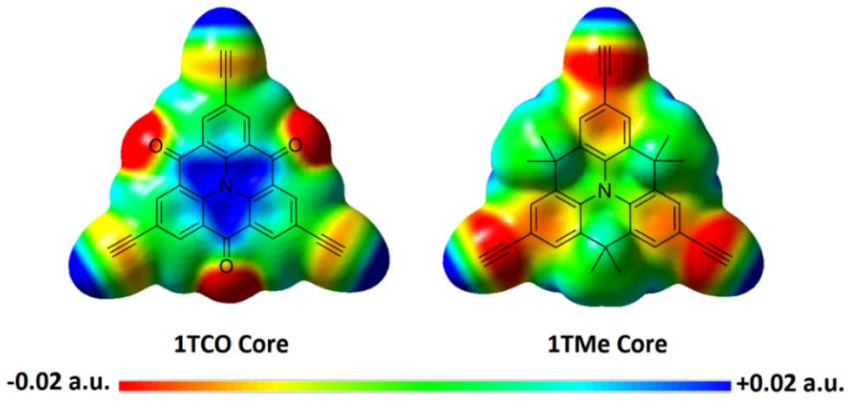

Figure 3. Electrostatic potential map (MEP) mapped over the electronic density surface for the triangulenic cores of **1TCO** and **1TMe** bearing three acetylenes each at the B3LYP/6-31G(d) level of theory. Colors towards red indicate electronic richness and colors towards dark blue indicate electronic deficiency.

Such a difference on the electronic character of the two triangulenic cages (*M,M*)$_3$-**1TCO** and (*M,M*)$_3$-**1TMe** offers, moreover, the possibility of complexing guests ranging from the electron rich to the electron deficient ones.

5.2. Synthetic approach to (*M,M*)$_3$-1TCO

The synthesis of (*M,M*)$_3$-**1TCO** begins with a triple Sonogashira cross−coupling reaction between three equivalents of enantiopure ditertbutyldiethynylallene (*M*)-**DEA-OH** with triiodotriangulene **TCOI$_3$** to afford the tricoupled product (*M,M,M*)-**2TCO**, which after deprotection and homodimerization should yield the covalent organic molecular cage (*M,M*)$_3$-**1TCO** (**Scheme 3**).

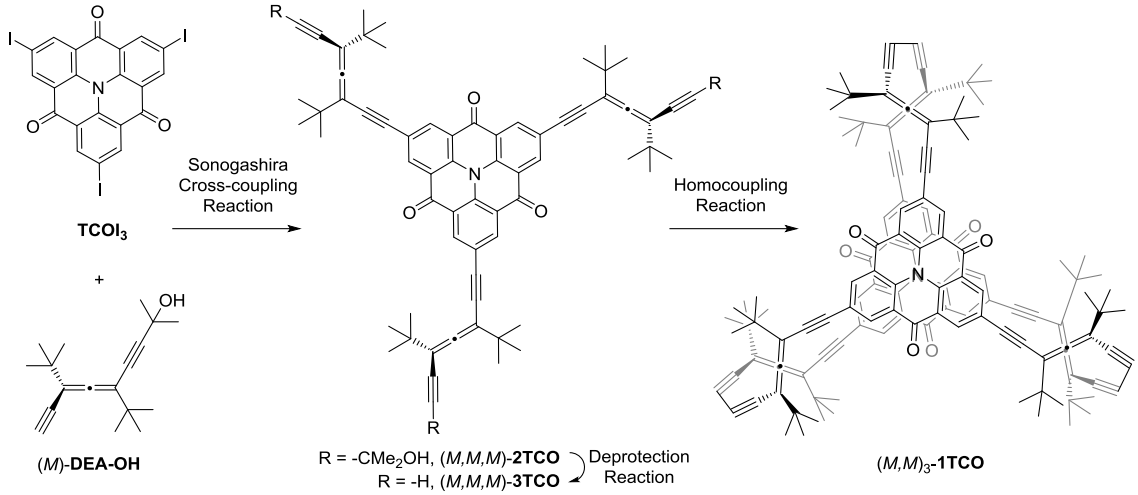

Scheme 3. Synthetic scheme to (*M,M*)$_3$-**1TCO**.

5.2.1. Synthesis and characterization of (*M,M*)$_3$-2TCO

N-heterotriangulene **TCOI$_3$**, proposed core for the synthesis of the cage (*M,M*)$_3$-**1TCO**, was generously provided by the group of Prof. Milan Kivala at the Friedrich-Alexander-Universität (F.A.U.), Erlangen−Nürnberg, Germany.[27] The starting material **T-4** was synthesized in a 60% yield from methyl-2-aminobenzoate and methyl-2-iodobenzoate according to a previously reported procedure (**Scheme 4**).[20] An aromatic electrophilic substitution to introduce the iodine atom, followed by base-driven hydrolysis of the ester moieties and a Friedel-Crafts acylation rendered compound **T-5** in a 48% yield.[28–30]

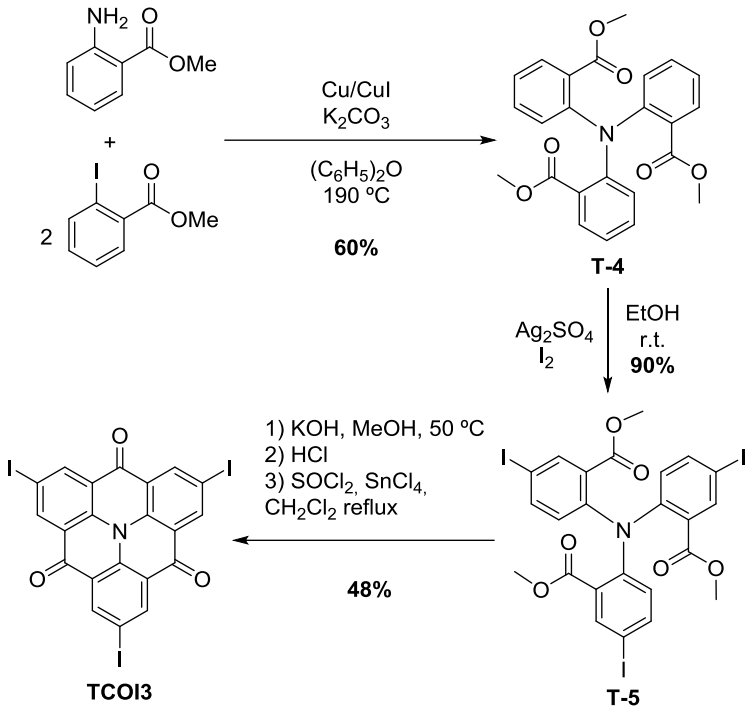

Scheme 4. Synthetic route to carbonyl-N-heterotriangulene core **TCOI$_3$**.

The Sonogashira cross-coupling reaction between the electron deficient core **TCOI$_3$**[31] with 3.5 equivalents of enantiopure (*M*)-**DEA-OH** in the presence of $PdCl_2(PPh_3)_2$ (5 mol%), CuI (10 mol%), using *N,N*-diisopropylamine (DIPA) as base and cosolvent (170 eq) in dry toluene under Argon at 60 °C for 15 h, afforded tricoupled product (*M,M,M*)-**2TCO** in a 70% yield along with a 8% of a mixture of (*M*)-**MC-2TCO** and (*M,M*)-**DC-TCO**, and a 2% of (*M,M*)-**DEA-OH$_2$** (**Scheme 5**, **Figure 4**).

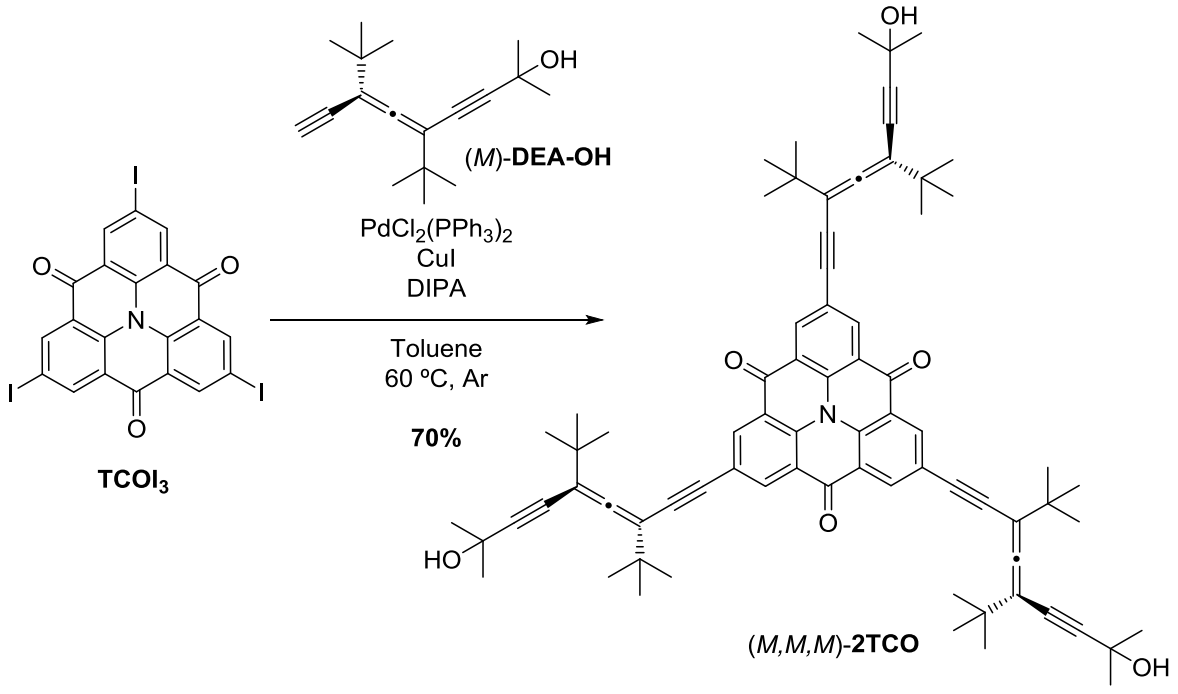

Scheme 5. Synthesis of (*M,M,M*)-**2TCO**.

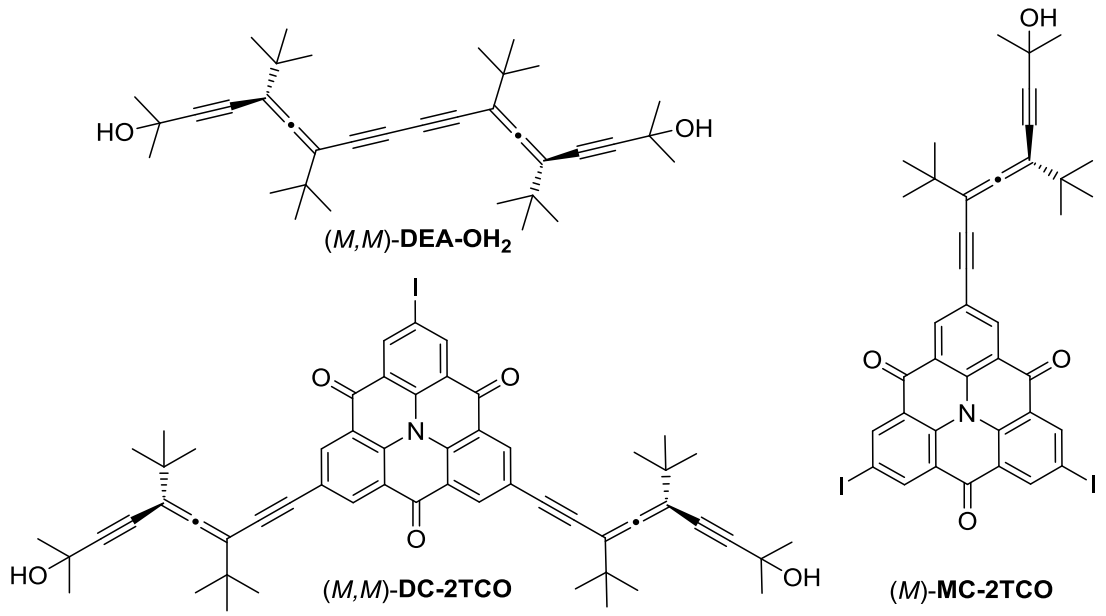

Figure 4. Side products on the synthesis of (*M,M,M*)-**2TCO**. **DC** means dicoupled and **MC** means monocoupled.

(*M,M,M*)-**2TCO** was fully characterized by means of ^{1}H, ^{13}C, HSQC, and HMBC NMR experiments, HR-ESI mass spectrometry, IR, UV-Vis and ECD spectroscopies, as well as cyclic voltammetry (CV).

On the one hand, ^{1}H NMR of (*M,M,M*)-**2TCO** shows a singlet from the aromatic hydrogens of the triangulene at 8.93 ppm, another singlet from methyl groups of the (*M*)-**DEA-OH** acetonide at 1.57 ppm, and the *t*Bu groups of (*M*)-**DEA-OH** 1.28 and 1.21 ppm respectively. On the other hand, ^{13}C NMR shows, besides the typical signals of the allene, the characteristic signal for the C=O group at 175.3 ppm, along with four aromatic carbon signals at 137.0 (C−H, assigned by HSQC), 136.8, 123.8 and 122.3 ppm. However, interpretation of HSQC and HMBC NMR spectra did not totally clarified the identity of every single signal on the ^{13}C NMR spectrum.

The IR spectrum shows two strong and sharp diagnostic signals at 1662 and 1466 cm^{-1} corresponding to the C=O and C−N stretching respectively. Moreover, CV measured in dichloromethane *vs* Fc^{+}/Fc couple shows two quasi-reversible reduction potentials at −1.45 and −1.52 V respectively, very similar to those of TIPS-ethynyl-substituted carbonyl-bridged triangulene previously reported.[31]

Finally, the most relevant issue from the characterization of (*M,M,M*)-**2TCO** is that the compound presents a flat ECD spectrum in $CHCl_3$ measured for several solutions of concentration ranging from $8\cdot10^{-5}$ M to $2\cdot10^{-5}$ M, fact which suggests that the carbonyl-bridged triangulene core could have racemized the enantiopure allenes, maybe through formation of radical cation species.

In order to test appropriate experimental conditions for the dimerization reaction, diastereomeric mixture of **2TCO** was deprotected affording **3TCO** in a 12% yield following standard conditions, but, unfortunately, different attempts of coupling two **3TCO** units did not render molecular cage **1TCO**.

5.3. Synthesis and characterization of (*M,M*)$_3$-1TMe

In the light of the obtained results so far, a cage based on dimethylmethylene-bridged *N*-heterotriangulene, (*M,M*)$_3$-**1TMe**, was proposed. As most of the previously reported molecular cages, its synthesis is based on the triple Sonogashira cross−coupling, deprotection, and homodimerization strategy depicted on **Scheme 6**.

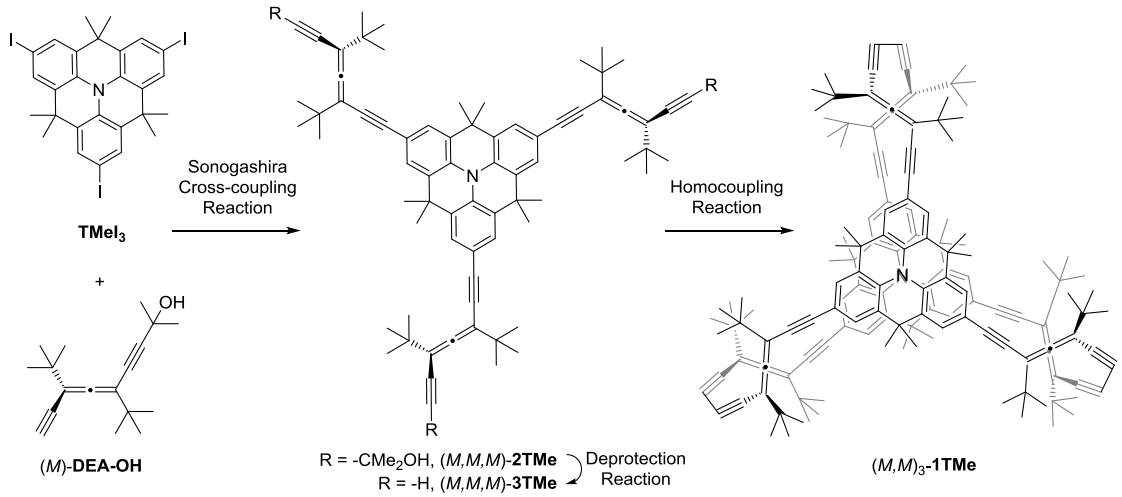

Scheme 6. Retrosynthetic scheme of helical molecular cage (*M,M*)$_3$-**1TMe**.

5.3.1. Synthesis and characterization of (*M,M,M*)-3TMe.

Following the proposed methodology, a key intermediate in the synthesis of (*M,M*)$_3$-**1TMe** is (*M,M,M*)-**3TMe** which in turn come from (*M,M,M*)-**2TMe**. The precursor of (*M,M,M*)-**2TMe**, *N*-heterotriangulene **TMe**, was prepared by the group of Prof. Milan Kivala at the FAU, Erlangen-Nürnberg, Germany combining an Ullman coupling to give the trimethylester **T-4**, that after a Grignard reaction followed by a dehydration reaction affords **TMe** in a 12% overall yield **(Scheme 7)**.[20,32] Next, **TMe** was treated with 3 equiv of *N*-iodosuccinimide (NIS) in dry chloroform under N_2 atmosphere for 2 days affording **TMeI$_3$** in a 41% yield.[32]

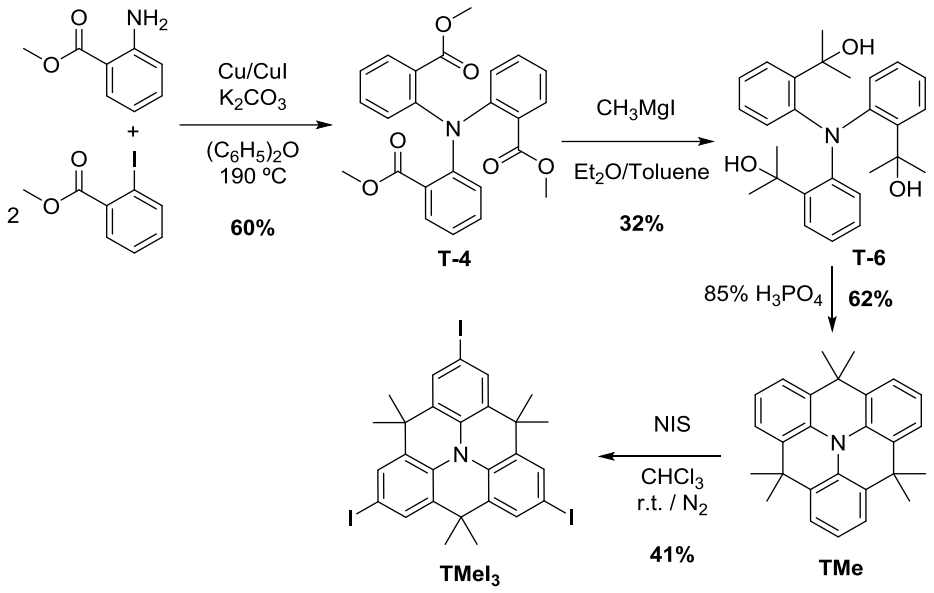

Scheme 7. Synthetic route to dimethylmethylene-bridged *N*-heterotriangulene **TMeI$_3$**.

The cross−coupling reaction of **TMeI$_3$** with 3.3 equivalents of the enantiopure allene (*M*)-**DEA-OH** employing Sonogashira conditions, 16 mol% $PdCl_2(PPh_3)_2$, 16 mol% CuI, in dry *N,N*-diisopropylamine (DIPA), at 75 °C under N_2, afforded (*M,M,M*)-**2TMe** in a 46% yield along with a 46% yield of the allene homodimer (*M,M*)-**DEA-OH$_2$** (**Scheme 8**).[33]

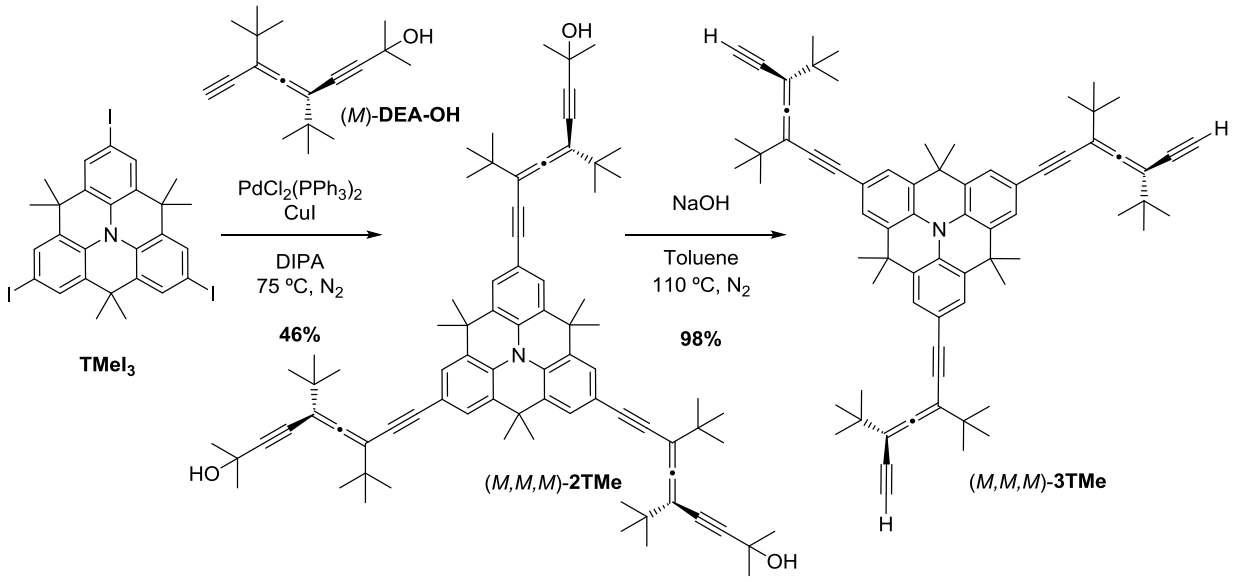

Scheme 8. Synthesis of tricoupled trisdeprotected compound (*M,M,M*)-**3TMe**.

Compound (*M,M,M*)-**2TMe** was fully characterized. ^{1}H NMR spectrum shows a singlet for the aromatic hydrogens over the triangulene core at 7.45 ppm, another one at 1.63 ppm for the methyl groups over the triangulene, and the one for acetonide methyl groups at 1.58 ppm, and 1.23 and 1.18 ppm respectively for the (*M*)-**DEA-OH** *t*Bu groups. ^{13}C NMR spectrum presents the cumulenic carbon at 211.3 ppm, the aromatic carbons of the core at 131.3, 130.2, 127.0, and 118.5 ppm, the sp^2 allenic carbons at 103.7 and 102.7 ppm, 4 carbons from alkynes at 97.2, 93.1, 82.7, and 76.2 ppm, the quaternary acetonide carbon at 65.9 ppm, the quaternary carbons of *t*Bu groups at 35.9 and 35.7 ppm, the methylene bridge of the triangulene at 35.6 ppm, the

methyls of the triangulene at 33.1 ppm, the methyl groups of the acetonide at 31.7 ppm, and finally at 29.3 and 29.1 ppm the *t*Bu of the allene.

ECD along with UV-Vis spectra of (*M,M,M*)-**2TMe** were also recorded in $CHCl_3$ at *ca.* $2 \cdot 10^{-5}$ M. This time, the dimethylmethylene-bridged *N*-heterotriangulenic core did not racemize the enantiopure allenes, as in the previous case of the carbonyl-bridged *N*-heterotriangulene. In comparison with previous benzenic derivative cores, the region of absorption is wider, reaching the 420 nm, fact which was expected, due to the higher conjugation of the triangulene core (**Figure 5**). Molar extinction coefficient ε was calculated at 378 nm for solutions of concentration between $9 \cdot 10^{-6}$ M and $3 \cdot 10^{-5}$ M, giving a value of 49101 $M^{-1} \cdot cm^{-1}$.

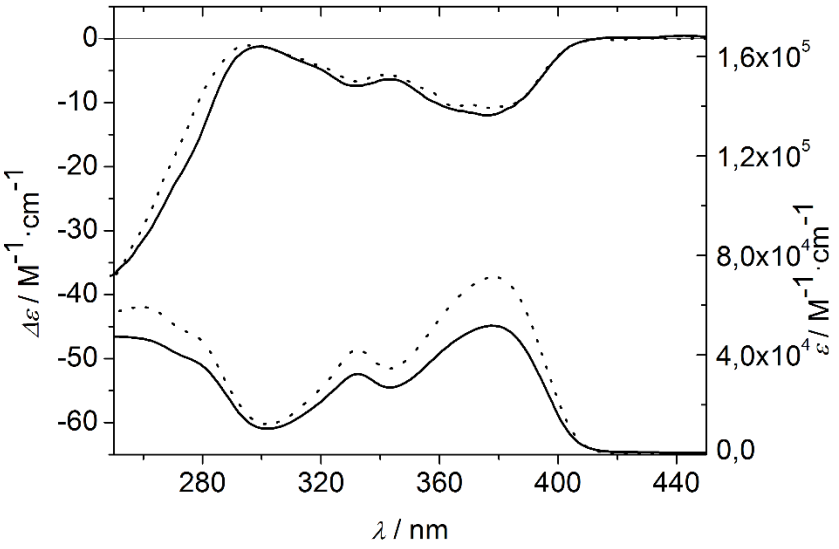

Figure 5. ECD (top) and UV-Vis (bottom) spectra of (*M,M,M*)-**2TMe** (solid line), and (*M,M,M*)-**3TMe** (dotted line).

The fact that (*M,M,M*)-**2TMe** did not loose its chirality, paves the way to continuing with the designed strategy to the chiral cage (*M,M*)$_3$-**1TMe**.

Thus, deprotection of the alkyne groups of (*M,M,M*)-**2TMe** to give the terminal acetylenes was done by treating the starting material with *ca.* 700 equiv. of flamed powdered NaOH in dry refluxing toluene for 1.5 h under N_2 (**Scheme 8**). The yield of (*M,M,M*)-**3TMe**, 98%, was calculated by integration of the ^{1}H NMR spectrum signals of the crude with an internal standard, since it was observed that after FC purification with SiO_2 as stationary phase, one half of the initial mass was lost. This could be explained due to the slight acidity of SiO_2, which could favor the formation of the radical cation of the triangulene, fact that was suggested after having noticed a bluish coloration on top of the SiO_2 phase. A possible solution could be using alumina instead of silica gel or even basifying the silica with Et_3N.

Regarding the characterization of (*M,M,M*)-**3TMe**, disappearance of the acetonide signals on both ^{1}H and ^{13}C NMR spectra, leads to the appearance of the characteristic singlet at 3.02 ppm from the terminal alkyne on ^{1}H NMR, and the upfield shift of the previous acetylenic carbon attached to the acetonide to 80.4 ppm on ^{13}C NMR.

Both **ECD** and **UV-Vis** spectra of (*M,M,M*)-**3TMe** in $CHCl_3$ are really similar to its predecessor (*M,M,M*)-**2TMe** (**Figure 5**). Molar extinction coefficient ε was calculated at 378 nm for solutions of concentration between $1 \cdot 10^{-5}$ M and $2.5 \cdot 10^{-5}$ M, giving a value of 70871 $M^{-1} \cdot cm^{-1}$.

The good results obtained on the synthesis of (*M,M,M*)-**3TMe** paved the way for the last step on the synthesis of (*M,M*)$_3$-**1TMe**, which is the Cu-catalyzed homodimerization of two trisdeprotected molecules.

5.3.3. Synthesis and characterization of (*M,M*)$_3$-1TMe

On the last step towards (*M,M*)$_3$-**1TMe**, tripodal-shaped molecule (*M,M,M*)-**3TMe** was added in dry pyridine under pseudohighdilution conditions (ϕ = 1mL·h^{-1}) over a solution of CuCl (75 eq) and $CuCl_2$ (11 eq) in dry pyridine under N_2 at r.t. for three days, affording (*M,M*)$_3$-**1TMe** in a 30% yield (**Scheme 9**). Also this time instability of the product was observed when applied on a SiO_2 TLC plate.

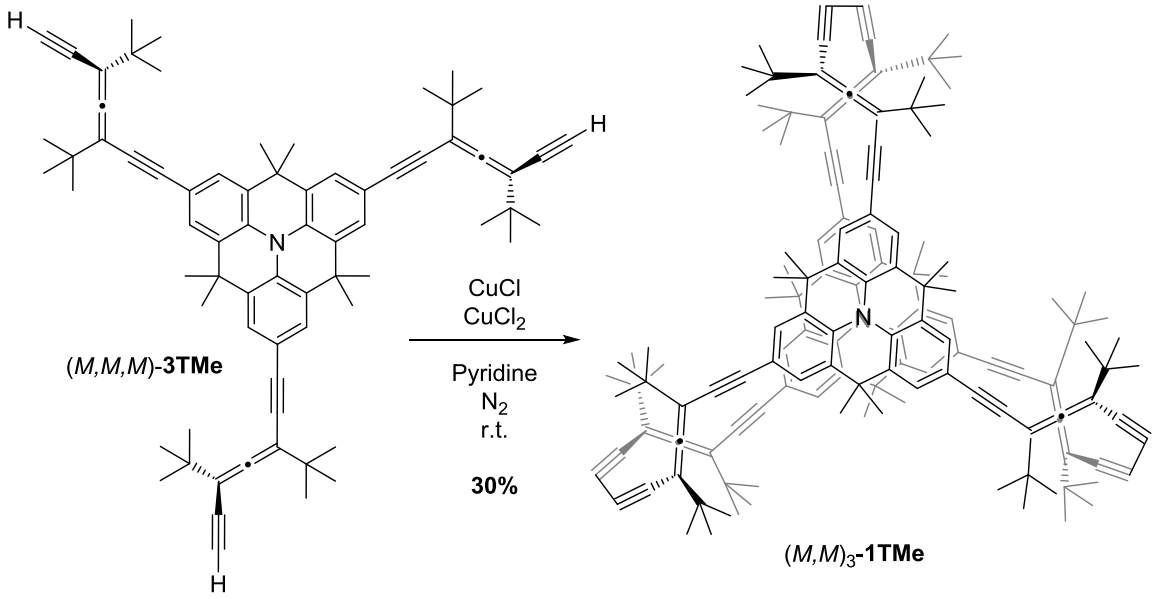

Scheme 9. Synthesis of molecular cage (*M,M*)$_3$-**1TMe**.

Cage compound (*M,M*)$_3$-**1TMe** was fully characterized by means of ^{1}H, ^{13}C, HSQC and HMBC NMR spectroscopies, as well as by UV-Vis, ECD spectroscopies, and HR-MALDI mass spectrometry.

^{1}H NMR spectrum of (*M,M*)$_3$-**1TMe** shows a characteristic feature so far not observed for the previously reported molecular cages, which is the differentiation of the diastereotopic aromatic hydrogens of the *N*-heterotriangulene core when placed on a rigid chiral environment formed by the (*M*)-**DEA** branches of the molecular cage. Thus, the two diastereotopic aromatic protons at 7.33 and 7.30 ppm coupled with each other with a typical *meta* coupling constant of 1.9 Hz. Moreover, the spectrum presents also two signals for the triangulenic diastereotopic methyl groups, one singlet at 1.66 ppm and another one at 1.37 ppm, fact which would fit with a difference between those pointing outwards and inwards the cage inner cavity. *tert*-Butyl groups remain unaltered showing singlets at 1.23 and 1.21 ppm each (**Figure 6**).

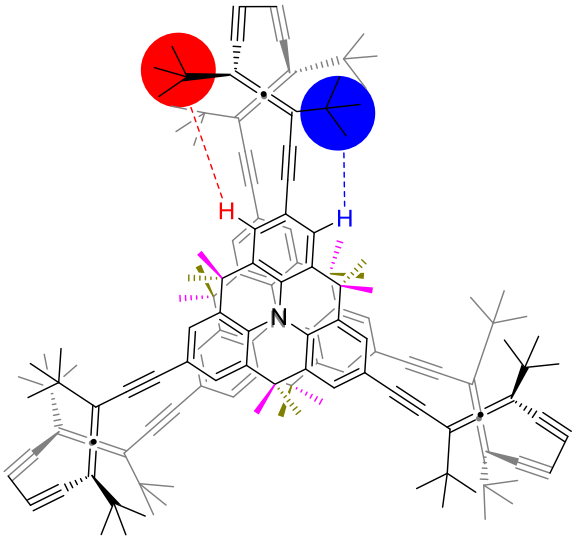

Figure 6. Diastereotopic hydrogen atoms shown on the ^{1}H NMR spectrum of $(M,M)_3$-**1TMe**. Diastereotopic aromatic hydrogen atoms on the triangulene core interacting with different chiral environments depicted in red and blue. Triangulene diastereotopic methyl groups pointing outside the cage in pink, and pointing inside de cage in khaki.

The differentiation observed on ^{1}H NMR was also observed on ^{13}C NMR spectrum of $(M,M)_3$-**1TMe**, which shows six different aromatic carbon atoms at 131.4, 130.1, 130.0, 126.8, 126.6, and 118.3 ppm, along with two triangulene methyl groups at 35.3 and 30.4 ppm, respectively.

HSQC NMR spectrum (**Figure 7**) shows correlation of the aromatic hydrogen at 7.33 ppm with the carbon atom at 126.6 ppm, the triangulenic methyl hydrogen at 1.66 ppm with the triangulenic methyl carbon at 30.4 ppm, the other triangulenic methyl hydrogen at 1.37 ppm with the other triangulenic methyl carbon at 35.3 ppm. On the other hand, HMBC NMR spectrum (**Figure 8**) shows correlation between the hydrogen at 7.33 ppm and carbons at 131.4, 126.6, and 94.4 ppm, the hydrogen at 1.66 ppm and the carbons at 130.0 and 35.3 ppm, the hydrogen at 1.37 ppm and the carbons at 130.1 and 35.3 ppm, the hydrogen at 1.23 ppm and the carbon at 104.8 ppm, and finally the hydrogen at 1.21 ppm and the carbon at 103.2 ppm.

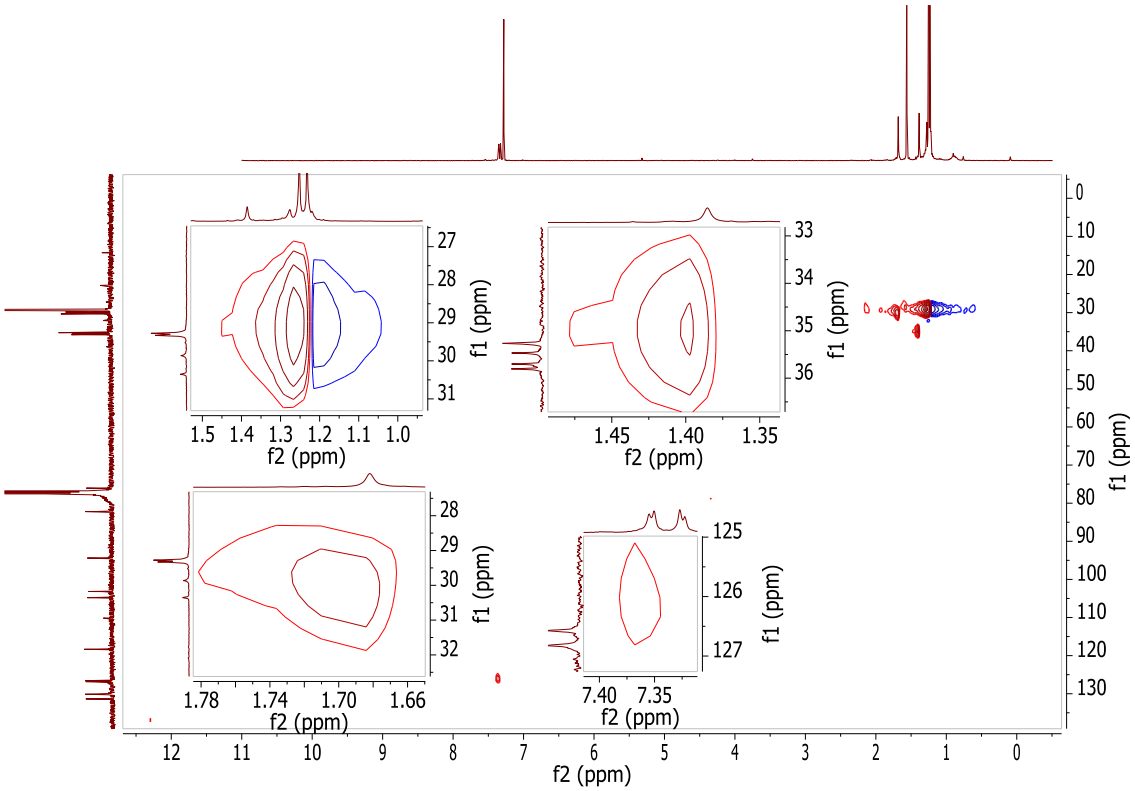

Figure 7. HSQC NMR spectrum of $(M,M)_3$-**1TMe**.

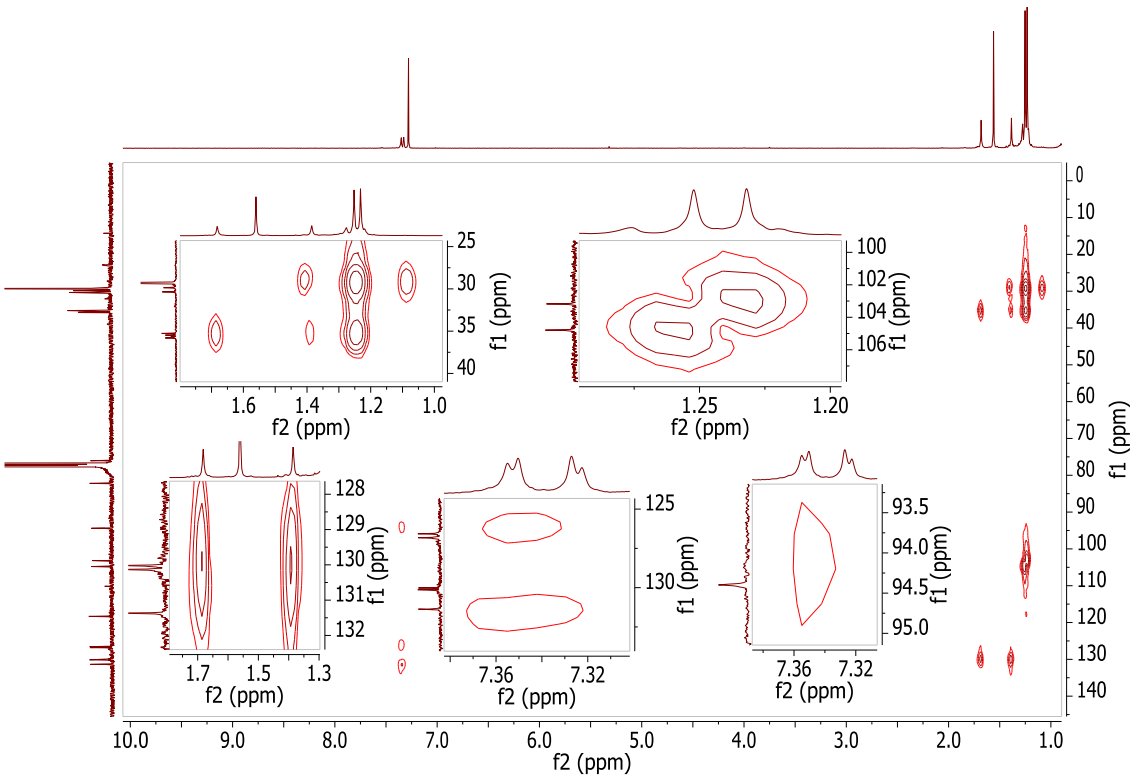

Figure 8. HMBC NMR spectrum of $(M,M)_3$-**1TMe**.

ECD spectrum of (*M,M*)$_3$-**1TMe** in $CHCl_3$ (**Figure 9**) shows a very intense positive band at *ca.* 260 nm, along with an intense negative band at *ca.* 300 nm, alternating with weaker positive and negative bands at *ca.* 270 and 400 nm respectively. Extinction coefficient ε was calculated at 378 nm in $CHCl_3$ for a batch of solution between $5 \cdot 10^{-6}$ M and $1.5 \cdot 10^{-5}$ M, giving a value of 108364 $cm^{-1} \cdot M^{-1}$. Maximum *g*-factor calculated was 0.007, which is above the values obtained for the other molecular cages presented in this thesis, giving us an idea of its stronger chiral character.

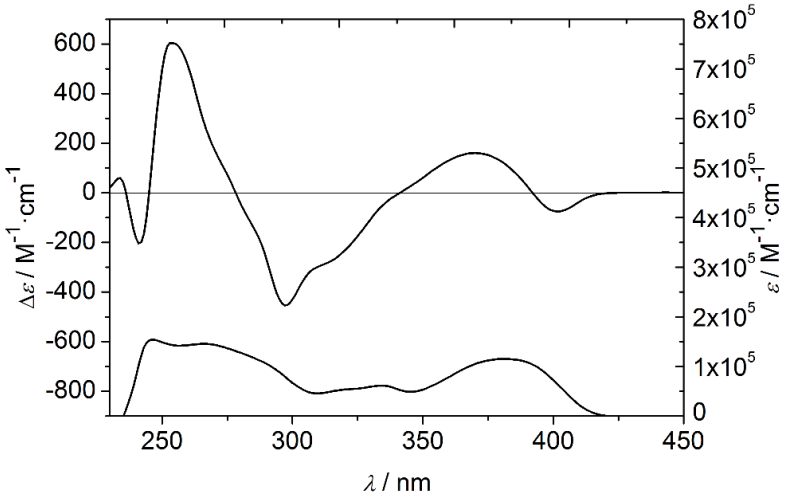

Figure 9. ECD (top) and UV-Vis (bottom) spectra of (*M,M*)$_3$-**1TMe**.

In summary, we have synthesized the covalent organic helical cage (*M,M*)$_3$-**1TMe** in an 14% overall yield after three steps where 9 new C–C bonds were formed. The whole process was achieved without an apparent loss of chirality. This cage was fully characterized and was found to have stronger chiral character and *g*-factor than the previously here reported ones.

5.3.4. Complexation scope for (*M,M*)$_3$-1TMe

The main differences between this cage, (*M,M*)$_3$-**1TMe**, and the ones synthesized on previous chapters, such as the benzenic (*P,P*)$_3$-**1H** and the methylated benzenic (*P,P*)$_3$-**1Me**, are the presence of an inner nitrogen atom bearing a lone electron pair along with a bigger size provided by the *N*-heterotriangulene core. Despite those differences, all of them are relatively electron rich molecular cages, which make them prone to act as good hosts for electron deficient or even positively charged guests. Thus, we are interested on knowing how delocalized is the lone electron pair of the nitrogen through conjugation with the three aryl rings. A simple way of testing the nitrogen basicity is doing an acid-base titration with trifluoroacetic acid (TFA), which has a pK_a of *ca.* -0.25 in water and it is less oxidizing than sulfuric acid, and check how the ECD and UV-Vis spectrum of the mixture changes. With the addition of TFA $CHCl_3$ solution over a solution of (*M,M*)$_3$-**1TMe** in $CHCl_3$ a progressive modification of the absorbance spectrum is observed in which the band at *ca.* 250 nm increases and the band at *ca.* 380 nm decreases. The last two TFA (**Figure 10**) additions, corresponding to 249 and 588 equiv. of TFA (dashed and dotted lines in the spectrum respectively) do not follow the same trend. Two inclined dotted arrows indicate the presence of two isosbestic points. This experiment suggests the existence of two processes, probably two nitrogen protonation processes. Signals tend to vanish after the addition of 492 equiv. of TFA, coinciding with turbidity observation, fact that could indicate a

precipitation of the new species formed. Moreover, when we opened the spectral window until 900 nm, a broad but weak band appears at *ca.* 640 nm, fact that concurs with the appearance of a dark bluish color in the solution. This is in good agreement with the previously postulated radical cation formation over the nitrogen atom of the triangulene core (**Figure 10**).

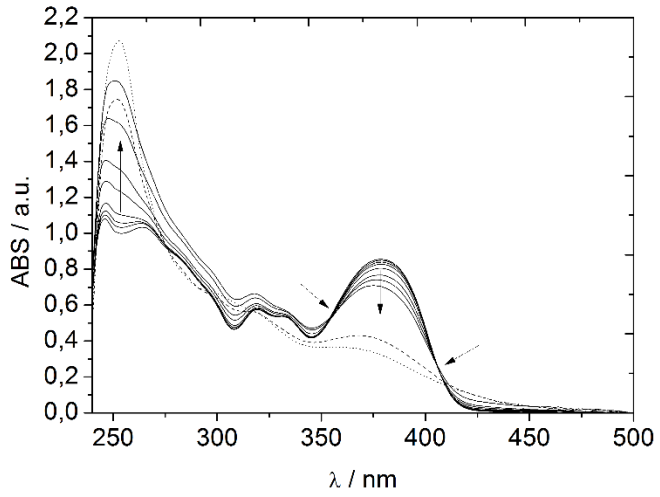

Figure 10. Absorbance titration of molecular cage (*M,M*)$_3$-**1Me** (10^{-5} M in $CHCl_3$) with increasing amount of TFA (0.339 M in $CHCl_3$ solution), from 0 to 588 equivalents of TFA.

On the other hand, what is observed after addition of TFA on the ECD is the disappearance of the CD signal. If the theory of the radical cation formation is correct, this could lead to the racemization of the allenic building blocks (**Figure 11**).

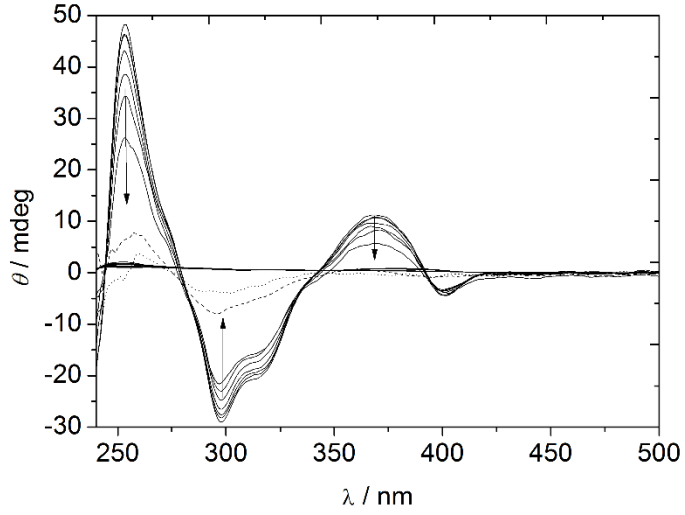

Figure 11. ECD titration of molecular cage (*M,M*)$_3$-**1Me** (10^{-5} M in $CHCl_3$) with increasing amount of TFA (0.339 M in $CHCl_3$ solution), from 0 to 588 equivalents of TFA. Arrows indicate evolution with addition of TFA.

It is know that triphenylamine, the non-bridged relative of **TMe** is considered a non-basic compound in water (pK_a of the conjugated acid < −2). Planarization through inclusion of bridges in the structure favors the delocalization of the lone pair of the nitrogen, which makes it even less basic. Previous studies from Hellwinkel et al. showed the oxidation of raw triangulene core **TMe** (10^{-3} – $5{\cdot}10^{-3}$ M) to give a bluish-violet radical cation species (λ_{max} 585 nm) by adding TFA and lead trifluoroacetate (10^{-3} M) and comparing the ESR spectra with their respective

simulations.[34] This is in good agreement with our own observations, and suggests that, even if the lone pair is delocalized through the three aryl rings, there is still some acidic character left, that can be useful on complexation with non-oxidant guests.

In conclusion, we have synthesized and fully characterized the new covalent organic helical cage (*M,M*)$_3$-**1Me**, bearing two dimethylmethylene-bridged *N*-heterotriangulenes as lids and six enantiopure (*M*)-**DEAs** as edges, which offers the interesting combination of chirality and redox properties for further host–guest applications.

5.4. References

[1] M. Kuratsu, M. Kozaki, and K. Okada, *Angew. Chem. Int. Ed.* **2005**, *44*, 4056–4058.

[2] D. Hellwinkel, and M. Melan, *Chem. Ber.* **1974**, *107*, 616–626.

[3] X. Zheng, X. Wang, Y. Qiu, Y. Li, C. Zhou, Y. Sui, Y. Li, J. Ma, and X. Wang, *J. Am. Chem. Soc.* **2013**, *135*, 14912–14915.

[4] E. Clar, and D. G. Stewart, *J. Am. Chem. Soc.* **1953**, *75*, 2667–2672.

[5] C. Adam, A. Wallabregue, H. Li, J. Gouin, R. Vanel, S. Grass, J. Bosson, L. Bouffier, J. Lacour, and N. Sojic, *Chem. Eur. J.* **2015**, *21*, 19243–19249.

[6] A. Ueda, H. Wasa, S. Nishida, Y. Kanzaki, K. Sato, D. Shiomi, T. Takui, and Y. Morita, *Chem. Eur. J.* **2012**, *18*, 16272–16276.

[7] D. Hellwinkel, and M. Melan, *Chem. Ber.* **1971**, *104*, 1001–1016.

[8] Y. Shirota, *J. Mater. Chem.* **2005**, *15*, 75–93.

[9] X. Liu, J. Liang, J. You, L. Ying, Y. Xiao, S. Wang, and X. Li, *Dye. Pigment.* **2016**, *131*, 41–48.

[10] X. Zhao, S. Wang, J. You, Y. Zhang, and X. Li, *J. Mater. Chem. C* **2015**, *3*, 11377–11384.

[11] N. Hammer, T. A. Schaub, U. Meinhardt, and M. Kivala, *Chem. Rec.* **2015**, *15*, 1119–1131.

[12] Z. Fang, R. D. Webster, M. Samoc, and Y.-H. Lai, *RSC Adv.* **2013**, *3*, 17914–17917.

[13] D. Hellwinkel, A. Wiel, G. Sattler, and B. Nuber, *Angew. Chem. Int. Ed.* **1990**, *29*, 689–692.

[14] Z. Zhou, A. Wakamiya, T. Kushida, and S. Yamaguchi, *J. Am. Chem. Soc.* **2012**, *134*, 4529–4532.

[15] F. Wu, H. Liu, L. T. L. Lee, T. Chen, M. Wang, and L. Zhu, *Chinese J. Chem.* **2015**, *33*, 925–933.

[16] F. Wu, L. T. L. Lee, J. Liu, S. Zhao, T. Chen, M. Wang, C. Zhong, and L. Zhu, *Synth. Met.* **2015**, *205*, 70–77.

[17] L. Cai, H. N. Tsao, W. Zhang, L. Wang, Z. Xue, M. Grätzel, and B. Liu, *Adv. Energy Mater.* **2013**, *3*, 200–205.

[18] J.-J. Kim, J. Yoon, E. J. Kim, B. R. Kim, Y.-J. Yoon, M. Kang, J.-J. Kim, J. Yoon, E. J. Kim, B. R. Kim, Y.-J. Yoon, and M. Kang, *Int. J. Photoenergy* **2012**, *2012*, 1–7.

[19] U. Meinhardt, F. Lodermeyer, T. A. Schaub, A. Kunzmann, P. O. Dral, A. C. Sale, F. Hampel, D. M. Guldi, R. D. Costa, and M. Kivala, *RSC Adv.* **2016**, *6*, 67372–67377.

[20] Z. Fang, V. Chellappan, R. D. Webster, L. Ke, T. Zhang, B. Liu, and Y.-H. Lai, *J. Mater. Chem.* **2012**, *22*, 15397–15404.

[21] C. Liu, Y. Li, Y. Zhang, C. Yang, H. Wu, J. Qin, and Y. Cao, *Chem. Eur. J.* **2012**, *18*, 6928–6934.

[22] K. Schmoltner, F. Schlütter, M. Kivala, M. Baumgarten, S. Winkler, R. Trattnig, N. Koch, A. Klug, E. J. W. List, and K. Müllen, *Polym. Chem.* **2013**, *4*, 5337–5344.

[23] S. Wang, M. Kivala, I. Lieberwirth, K. Kirchhoff, X. Feng, W. Pisula, and K. Müllen, *ChemPhysChem* **2011**, *12*, 1648–1651.

[24] M. Bieri, S. Blankenburg, M. Kivala, C. A. Pignedoli, P. Ruffieux, K. Müllen, and R. Fasel, *Chem. Commun.* **2011**, *47*, 10239–10241.

[25] T. Katoh, G. Imamura, S. Obata, M. Bhanuchandra, G. Copley, H. Yorimitsu, and K. Saiki, *Phys. Chem. Chem. Phys.* **2015**, *17*, 14115–14121.

[26] F. Schlütter, F. Rossel, M. Kivala, V. Enkelmann, J.-P. Gisselbrecht, P. Ruffieux, R. Fasel, and K. Müllen, *J. Am. Chem. Soc.* **2013**, *135*, 4550–4557.

[27] H. Zhang, S. Wang, Y. Li, B. Zhang, C. Du, X. Wan, and Y. Chen, *Tetrahedron* **2009**, *65*, 4455–4463.

[28] W.-W. Sy, *Synth. Commun.* **1992**, *22*, 3215–3219.

[29] M. M. Slutsky, T. V. Jones, and G. N. Tew, *J. Org. Chem.* **2007**, *72*, 342–347.

[30] J. E. Field, and D. Venkataraman, *Chem. Mater.* **2002**, *14*, 962–964.

[31] M. Kivala, W. Pisula, S. Wang, A. Mavrinskiy, J.-P. Gisselbrecht, X. Feng, and K. Müllen, *Chem. Eur. J.* **2013**, *19*, 8117–8128.

[32] Z. Fang, T.-L. Teo, L. Cai, Y.-H. Lai, A. Samoc, and M. Samoc, *Org. Lett.* **2009**, *11*, 1–4.

[33] Z. Fang, X. Zhang, Y. Hing Lai, and B. Liu, *Chem. Commun.* **2009**, *22*, 920–922.

[34] S. Bamberger, D. Hellwinkel, and F. A. Neugebauer, *Chem. Ber.* **1975**, *108*, 2416–2421.

6. Experimental Part

6.1. Materials and methods.

Reagents and solvents were purchased as reagent grade and used without further purification unless stated otherwise. THF was freshly distilled from sodium using benzophenone as a colored indicator. $(CH_2)_2Cl_2$, amines, and pyridine were freshly distilled from CaH_2. All reactions were performed in oven- or flame-dried glassware under an inert atmosphere of argon/nitrogen unless stated otherwise. Chromatography refers to flash chromatography (FC) on SiO_2 60 (0.02±0.063 mm) from Merck; ahead pressure of around 0.2 bar was applied. TLC was performed onUV_{254} SiO_2-coated plates from Merck with visualization by UV light (254 nm). HPLC: Waters 510 pump controlled by PMC pump controller, with U6K injector and UV detector. Solvents were HPLC grade and degassed with He. UV/Vis and ECD spectra were recorded with a Jasco J-815 spectropolarimeter. ^1H and ^{13}C NMR spectra were recorded with Bruker 600 MHz or 400 MHz spectrometers at 298 K with residual solvent peaks as internal reference. The chemical shifts are reported in δ (ppm) and the coupling constants *J* are given in Hz. The multiplicities are expressed as follows: s = singlet, d = doublet, t = triplet, q = quartet, m = multiplet. IR spectra were recorded with a JASCO FT/IR-4200 infrared spectrometer. Peaks are quoted in wavenumbers (cm^{-1}). EI mass spectra were recorded with a Hewlett–Packard HP5989 A or a VG-Tribid instrument operating at 70 eV. ESI mass spectra were recorded with an APEX3 instrument. MALDI mass spectra were recorded with a APEXQe FT-ICR MS (Bruker Daltonics, Billerica, MA), equipped with a 7T actively shielded magnet. Ions were generated using a Combi MALDI-electrospray ionization (ESI) source. Cyclic Voltametry (CV) measurements were carried out at room temperature in CH_2Cl_2 (0.5 mM), containing 0.1 M *n*-Bu_4NPF_6 (purchased from Acros and used without further purification) in a classical three-electrode cell (scan rate 100 mV s^{-1}). The working electrode was a glassy carbon disk electrode (3 mm in diameter). The auxiliary electrode was a Pt wire, and the reference electrode was an $Ag/AgNO_3$ electrode. All potentials are referenced to the ferrocene/ferrocenium (Fc/Fc^+) couple, used as internal standard, and are uncorrected from ohmic drop. The cell was connected to BAS CV 50 W version 2.

6.2. Synthesis of DEA-TIPS and DEA-OH.

2,2,6,6-Tetramethyl-hepta-4-yn-3-one (2)

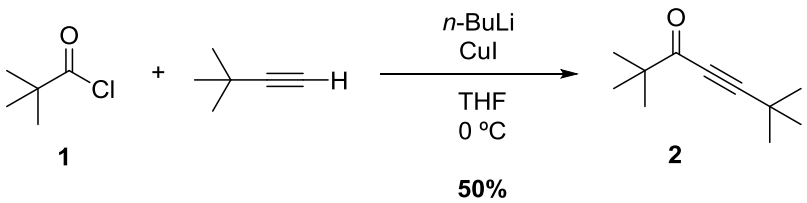

1 **2**

50%

Scheme 1. Synthesis of **2**.[1]

*n*BuLi (1.1 eq, 4.5 mmol, 1.8 mL of a 2.5 M solution in hexane) was added dropwise under Ar atmosphere at 0 °C to 3,3-dimethylbut-1-yne (1 eq, 4.0 mmol, 500 µL) in THF (4 mL). After 1 h, CuI (4.0 mmol, 764 mg) was added in small amounts over a period of 30 min (orange-red color). Then a solution of *pivaloyl chloride*, **1**, (1 eq, 4.0 mmol, 500 µL) in THF was added dropwise at 0 °C. The mixture was stirred for 1 h at 0 °C and then, warmed up to room temperature (yellow color). Sat. aq. NH_4Cl solution was added, and the mixture was extracted with Et_2O. The combined organic phases were dried with $MgSO_4$. Evaporation and FC purification (SiO_2; Cyclohexane/EtAcO 20:1) gave 2,2,6,6-tetramethyl-hepta-4-yn-3-one, **2**, (334 mg, 50%) as a clear volatile oil.

^{1}H NMR (400 MHz, $CDCl_3$) δ = 1.29 (s, 9H), 1.18 (s, 9H) ppm.

^{13}C NMR (101 MHz, $CDCl_3$) δ = 194.9, 103.2, 77.3, 44.9, 30.3, 28.0, 26.32 ppm.

(±)-**3-*tert*-Butyl-6,6-dimethyl-1-(tri*iso*propylsilyl)hepta-1,4-diyn-3-ol ((**±)-**3).**

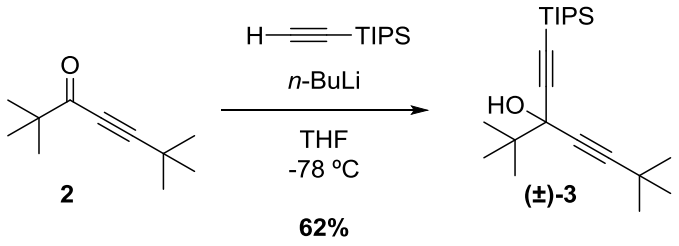

Scheme 2. Synthesis of (±)-**3**.[1]

*n*BuLi (1.5 eq, 3.25 mmol, 1.3 mL of a 2.5 M solution in hexane) was added dropwise under Ar atmosphere at –78 °C to a solution of ethynyltriisopropylsilane (1.5 eq, 3.25 mmol, 660 µL) in THF (3.6 mL). After stirring for 1 h, ynone **2** (1 eq, 2.17 mmol, 314 mg) in THF (1.5 mL) was added dropwise. After 30 min, the mixture was allowed to warm to r.t. Sat. aq. NH_4Cl solution was added, and the mixture was extracted with Et_2O. The combined organic phases were dried with $MgSO_4$. Evaporation under vacuum and FC purification (SiO_2; ciclohexane/AcOEt 20:1) gave 3-*tert*-butyl-6,6-dimethyl-1-(tri*iso*propylsilyl)hepta-1,4-diyn-3-ol (±)-**3** (563 mg, 62%) as a clear volatile oil.

^{1}H NMR (400 MHz, $CDCl_3$) δ = 1.21 (s, 9H), 1.12 (s, 9H), 1.08 (s, 21H) ppm.

^{13}C NMR (101 MHz, $CDCl_3$) δ = 108.1, 93.0, 84.8, 79.1, 71.4, 40.1, 31.1, 27.8, 25.2, 19.0, 11.7 ppm.

(±)-1-(*tert*-Butyl)-4,4-dimethyl-1-[(tri*iso*propylsilyl)ethynyl]pent-2-yn-1-ylpentafluoro benzoate. ((±)-4).

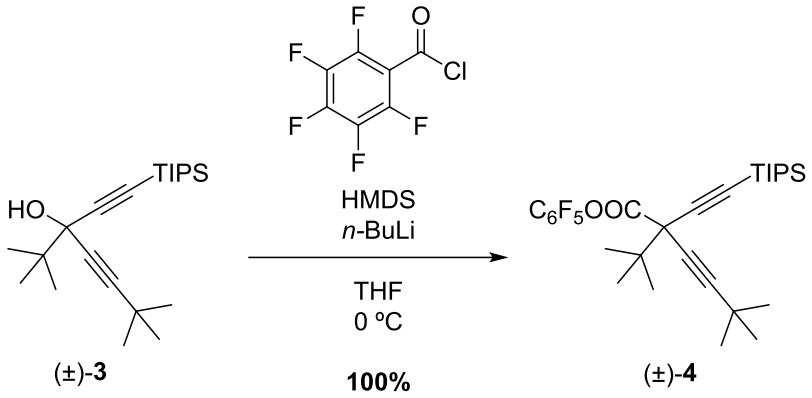

Scheme 3. Synthesis of (±)-**4**.[1]

*n*BuLi (1 eq, 5.4 mmol, 3.6 mL of a solution 1.5 M in THF) was added dropwise to a solution of bis(trimethylsilyl)amine (1.2 eq, 6.5 mmol, 1.05 g) in THF (24 mL) at 0 °C. After 1 h, this lithium hexamethyldisilazane (LHDMS) solution was added dropwise at 0 °C to the alcohol (±)-**3** (1 eq, 5.4 mmol, 1.4 g) in THF (11 mL) and stirred for 30 min at this temperature. $ClCOC_6F_5$ was added via syringe and the solution was stirred at 0 °C for 1 h. Then the mixture was warmed up to 25 °C and treated with sat. aq. NH_4Cl solution. The aq. phase was extracted with Et_2O, and the combined organic phases were dried with anh. Na_2SO_4. Evaporation under vacuum gave benzoate (±)-**4** (2.06 g, 100%) as a yellow oil, which was used without further purification.

^{1}H NMR (400 MHz, $CDCl_3$) δ = 1.22 (s, 9H), 1.18 (s, 9H), 1.08 (s, 21H) ppm.

^{13}C NMR (101 MHz, $CDCl_3$) δ = 155.9, 147.1, 144.8, 143.8, 141.4, 139.5, 136.1, 102.3, 95.8, 88.3, 78.0, 74.4, 40.5, 30.6, 27.7, 24.9, 18.7, 11.4 ppm.

^{19}F NMR (376 MHz, $CDCl_3$) δ = −139.2 (m, 2F), −150.2 (m, 1F), −161.2 (m, 2F) ppm.

(±)-5,7-Di(*tert*-butyl)-2-methyl-9-(triisopropylsilyl)nona-5,6-dien-3,8-diyn-2-ol ((±)-DEA-TIPS-OH).

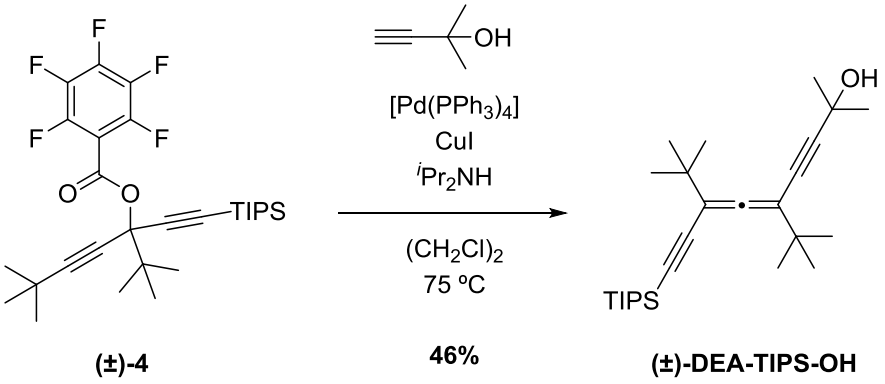

Scheme 4. Synthesis of (±)-**DEA-TIPS-OH**.[1]

Two solutions were prepared:

a: a solution of (±)-**4** (1 eq, 2.39 mmol, 1.3 g) in $(CH_2Cl)_2$ (10 mL) in a Schlenk tube;

b: a solution of $[Pd(PPh_3)_4]$ (5 mol%, 0.117 mmol, 135 mg) in $(CH_2Cl)_2$ (10 mL);

Both solutions were degassed with Ar. CuI (0.24 mmol, 45 mg) was added to solution *b* and this solution was further sparged with Ar. $^{i}Pr_2NH$ (2 eq, 5 mmol, 880 µL) and the acetonide-acetylene (4.75 mmol, 460 µL) were added to solution *a*. Solution *b* was transferred *via* cannula to *a*. After further sparging with Ar, the reaction was stirred at 60 °C for 23 h. Then the reaction mixture was treated with sat. aq. NH_4Cl solution and extracted with DCM. The combined organic phases were dried with anh. Na_2SO_4. Removal of the solvent under reduced pressure followed by FC purification (SiO_2; hexane/DCM 1:1) gave (±)-**DEA-TIPS-OH** (455 mg, 46%) as a yellow oil.

^{1}H NMR (400 MHz, $CDCl_3$) δ = 1.56 (s, 6H), 1.13 (s, 9H), 1.10 (s, 9H), 1.08 (s, 21H) ppm.

^{13}C NMR (101 MHz, $CDCl_3$) δ = 211.8, 103.8, 102.2, 100.5, 96.9, 94.1, 76.1, 65.9, 35.73 35.4, 31.7, 29.0, 18.8, 11.5 ppm.

(±)-**5,7-Di-*tert*-butyl-2-methylnona-5,6-diene-3,8-diyn-2-ol (**(±)-**DEA-OH).**

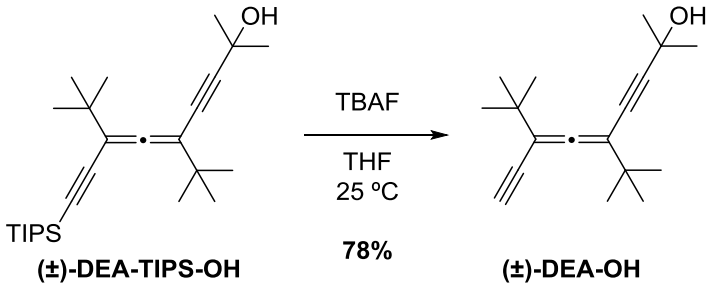

Scheme 5. Synthesis of (±)-**DEA-OH**.[1]

To a solution of (±)-**DEA-TIPS-OH** (1 eq, 0.91 mmol, 380 mg) in THF (15 mL), TBAF (1.1 eq, 1 mmol, 1 mL of a 1 M solution in THF) was added, and the mixture was stirred at 25 °C under Ar atmosphere for 5 h. Then the reaction mixture was treated with sat. aq. NH_4Cl solution and extracted with hexane. The combined organic phases were dried with anh. Na_2SO_4 and the solvent was removed under reduced pressure. FC purification (SiO_2; hexane/EtAcO 9:1) gave (±)-5,7-di-*tert*-butyl-2-methylnona-5,6-diene-3,8-diyn-2-ol, (±)-**DEA-OH**, (184 mg, 78%) as a yellow oil.

Compound (±)-**DEA-OH** was resolved by semipreparative HPLC with an *e.r.* up to 99% using a chiral stationary phase, Chiralpack IA column (particle size of 5 µm; 10 mm Ø x 250 mm). Elution was done with a mixture of hexane: *iso*propanol 99.2:0.8 at a flow rate of 2.5 mL·min^{-1}. Under these conditions a sample of (±)-**DEA-OH** (5 mg dissolved in 100 µL of *n*-hexane; injection 100 µL) can be resolved into its enantiomers with a retention time (t_R) of 17.8 and 21.1 min for (*P*)-**DEA-OH** and (*M*)-**DEA-OH** respectively.

^{1}H NMR (400 MHz, $CDCl_3$) δ = 2.98 (s, 1H), 1.54 (s, 6H), 1.12 (s, 9H), 1.11 (s, 9H) ppm.

^{13}C NMR (101 MHz, $CDCl_3$) δ = 211.7, 103.1, 102.3, 97.5, 80.4, 77.7, 75.7, 65.8, 35.6, 35.3, 31.6, 29.0, 28.9 ppm.

(±)-**(3,5-di-*tert*-butylhepta-3,4-dien-1,6-diyn-1-yl)triisopropylsilane** ((±)-**DEA-TIPS)**

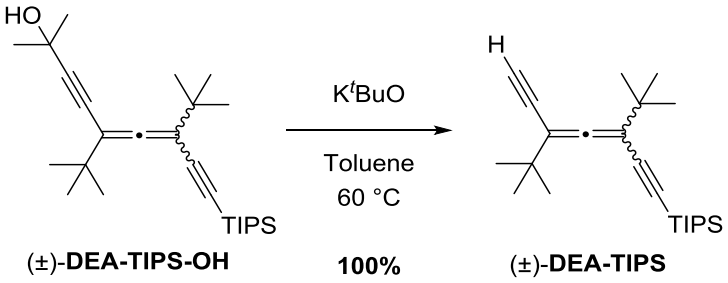

Scheme 6. Synthesis of (±)-**DEA-TIPS**.

(±)-**DEA-TIPS-OH** (1 eq, 0.5136 mmol, 213 mg) and K^{t}BuO (1 eq, 0.5136 mmol, 61 mg) were dissolved in dry toluene (60 mL) under N_2 into a round bottom flask and set at 60 °C for 30 min. The mixture was treated with distilled water, washed with sat. aq. NH_4Cl and extracted with EtOAc. The combined organic phases were dried over anh. Na_2SO_4 and the solvent was removed under reduced pressure to give (±)-**DEA-TIPS** (183 mg, quantitative yield) as an amber oil without further purification.

^{1}H NMR (400 MHz, Chloroform-*d*) δ = 2.99 (s, 1H$_{alkyne}$), 1.14 (s, 9H, ^{t}Bu), 1.13 (s, 9H, ^{t}Bu), 1.08 (s, 21H, -TIPS) ppm.

^{13}C NMR (101 MHz, Chloroform-*d*) δ = 212.7 (C$_{cumullenic}$), 104.3, 102.0, 100.2, 94.5, 80.3, 77.7 (C$_{allenes}$+C$_{alkynes}$), 35.5, 35.4 (C$_{quaternary}$ ^{t}Bu), 29.04, 28.98 (^{t}Bu), 18.8 (C$_{Me}$ -TIPS), 11.5 (C$_{quaternary}$ -TIPS) ppm.

HR-ESI-MS *m/z* (%): [M+H]$^+$ calcd. for $^{12}C_{24}{}^1H_{41}{}^{28}Si$ 357.29720, found: 357.29722 (100).

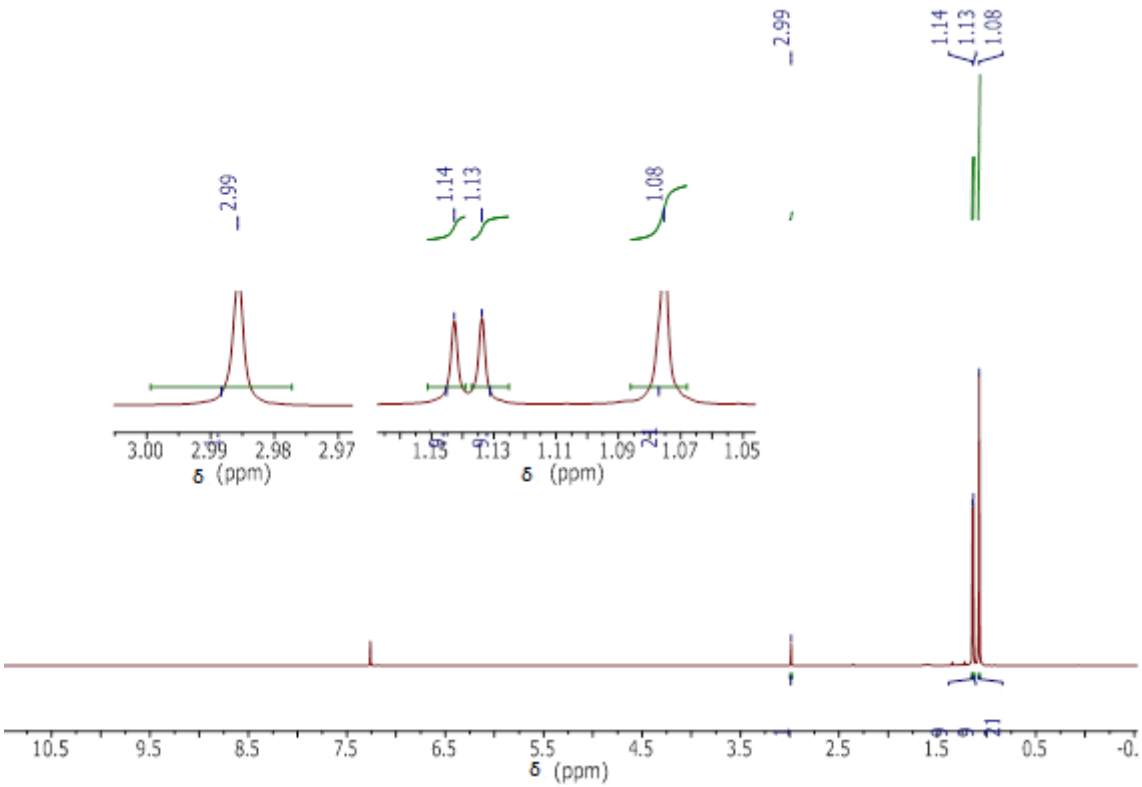

Figure 1. ^{1}H NMR spectrum of (±)-**DEA-TIPS**.

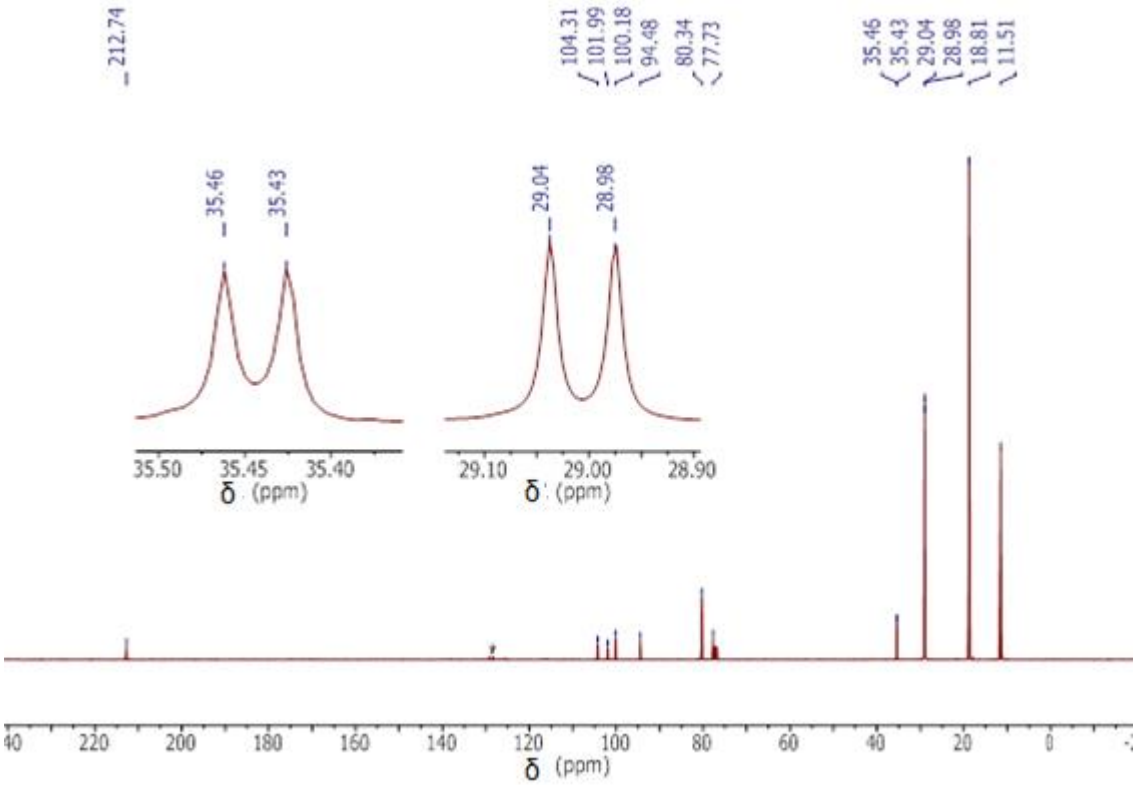

Figure 2. ^{1}H NMR spectrum of (±)-**DEA-TIPS**. * Traces of Toluene

6.3. Synthesis of molecular cage (*P,P*)$_3$-1H.

1,3,5-Triiodobenzene

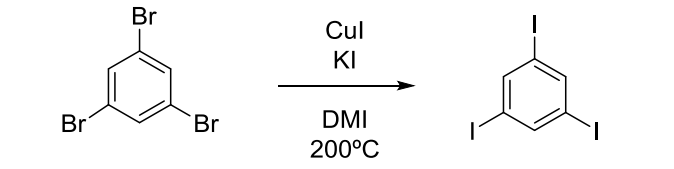

1,3,5-tribromobenzene **64%** **1,3,5-triiodobenzene**

Scheme 7. Synthesis of **1,3,5-triiodobenzene**.[10]

Flamed KI (40 eq, 20 mmol, 3.32 g), flamed CuI (12 eq, 6 mmol, 1.146 g), and 1,3,5-tribromobenzene (1 eq, 0.5 mmol, 157 mg) were dissolved in freshly distilled DMI (5 mL) under Argon in a Schlenk tube. The reaction ran at 200 °C for 5 h. The mixture was cooled into an ice bath and then filtered and washed with aq. sat. NH_4Cl and then brine. The mixture was treated with HCl 36 % (4 mL) in H_2O (50 mL), and then washed with distilled water. FC (SiO_2; hexane 100%) and crystallization from dichloromethane gave **1,3,5-triiodobenzene** (145 mg, 64% yield) as colorless needles. Spectroscopic data are in good agreement with those previously reported.[10]

^{1}H NMR (400 MHz, $CDCl_3$) δ = 8.03 (s, 3H$_{aromatic}$) ppm.

(*P,P,P*)-**2,2',2''-(benzene-1,3,5-triyltris(3,5-di-tert-butylhepta-3,4-dien-1,6-diyne-7,1-iyl))tris(propan-2-ol) (**(*P,P,P*)-**2H)**

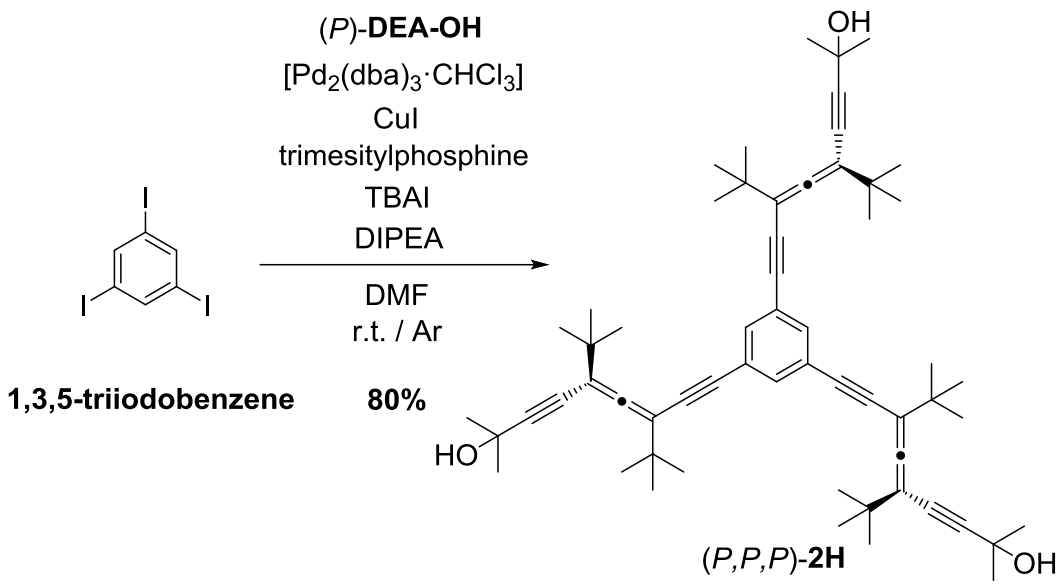

Scheme 8. Synthesis of (*P,P,P*)-**2H**.

Into a flamed Schlenk tube were placed $[Pd_2(dba)_3{\cdot}CHCl_3]$ (7.5 mol%, 0.008 mmol, 8.4 mg), purified CuI (60 mol%, 0.065 mmol, 12.4 mg), 1,3,5-triodobenzene (1 eq, 0.108 mmol, 49 mg), TBAI (6 mol%, 0.649 mmol, 240 mg), trimesitylphosphine (60 mol%, 0.065 mmol, 25 mg), diisopropylethylamine (DIPEA) (10 eq, 1.081 mmol, 188 µL), and distilled DMF (4mL). The yellow solution was bubbled with Ar and then a solution of enantiopure allene (*P*)-**DEA-OH** (3.3 eq, 0.357 mmol, 92 mg) in DMF (4mL) was added *via* cannula. The reaction ran over 22 h going from –8°C to r.t. The reaction mixture was treated with sat. aq. sat. NH_4Cl solution, then sat. KCN solution, followed by 1.5 M HCl solution and distilled water. Then, the combined aq. phases were extracted with dichloromethane (DCM), dried over anh. Na_2SO_4, and the solvent was removed under reduced pressure. Purification by FC (SiO_2, hexane:EtAcO 20%) gave the homodimer of the allene (0.049 mmol, 25.5 mg, 20%) and the tricoupled product (*P,P,P*)-**2H** (0.086 mmol, 73.5 mg, 80%).

Previous conditions employing a less reactive aryl halide such as 1,3,5-tribromobenzene and also a less reactive Pd catalyst such as $[PdCl_2(PPh_3)_2]$ in combination with CuI and Et_3N gave rise to a mixture of mono-, di-, and tricoupled products as explained in **Chapter 3**. The same results were obtained with the best conditions found (described before) but with a more hindered phosphine such as tri(o-tolyl)phosphine. The spectroscopic data of them are also included.

(*P*)-**5,7-di-tert-butyl-9-(3,5-dibromophenyl)-2-methylnona-5,6-dien-3,8-diyn-2-ol** (**(***P***)-MC-2H-Br)**

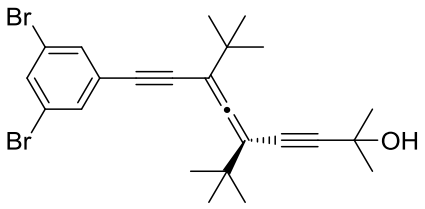

(*P*)-**MC-2H-Br**

Figure 3. Structure of (*P*)-**MC-2H-Br**.

^{1}H NMR (400 MHz, $CDCl_3$) δ = 7.59 (t, *J* = 1.8 Hz, $1H_{aromatic}$), 7.51 (d, *J* = 1.8 Hz, $2H_{aromatic}$), 1.96 (s, 1H, –OH), 1.57 (s, 6H, $2xCH_3$), 1.18 (s, 9H, ^{t}Bu), 1.14 (s, 9H, ^{t}Bu) ppm.

^{13}C NMR (101 MHz, $CDCl_3$) δ = 211.5 ($C_{cumulenic}$), 133.7, 133.0, 127.2, 122.7 ($C_{aromatic}$), 103.3, 102.9, 97.8, 89.6, 86.3, 75.6 ($C_{alkynes}$+$C_{allenes}$), 65.9 ($C_{quaternary}$, -$\underline{C}Me_2OH$), 35.79, 35.76, 31.6 (-$C\underline{Me_2}OH$), 29.2, 29.1 (Me ^{t}Bu) ppm.

IR ($CHCl_3$) ν = 3351 (br. m, str O–H), 2964 (s, str $C_{aromatic}$–H), 2868, (w, str $C_{aliphatic}$–H), 2207 (w, str C_{alkyne}ΞC_{alkyne}), 1916 (very w, C_{allene}=C_{allene}), 1709, 1580 (s, str $C_{aromatic}$=$C_{aromatic}$) cm^{-1}.

HR-EI-MS *m/z* (%): [M] = [$C_{24}H_{28}Br_2O$]; $[M–H_2O]^+$ calcd. for $^{12}C_{24}{}^{1}H_{26}{}^{79}Br_2$472.0401, found: 472.0410 (54); $[M–H_2O]^+$ calcd. for $^{12}C_{24}{}^{1}H_{26}{}^{79}Br^{81}Br$ 474.0381, found: 474.0367 (100); $[M–H_2O]^+$ calcd. for $^{12}C_{24}{}^{1}H_{26}{}^{81}Br_2$ 476.0360, found: 476.0356 (51).

UV/Vis (Hexane) λ_{max} (nm): 296, 281, 264, 225.

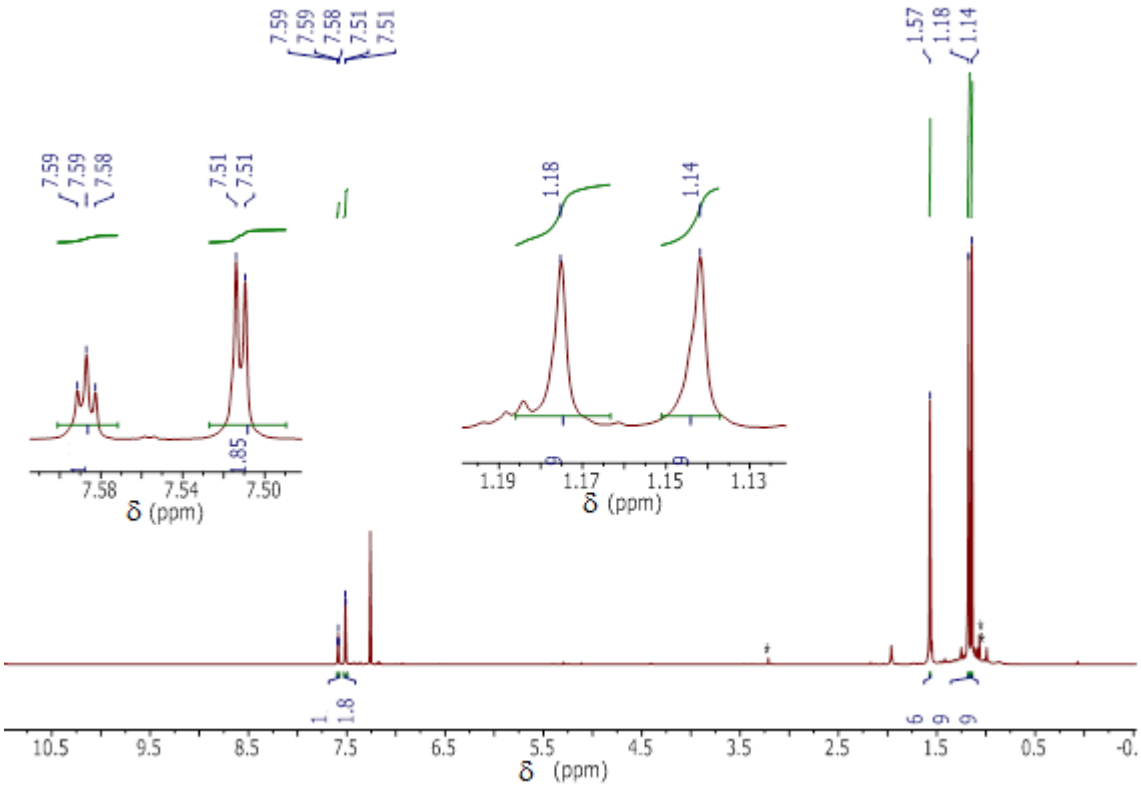

Figure 4. ^{1}H NMR of (*P*)-**MC-2H-Br**.

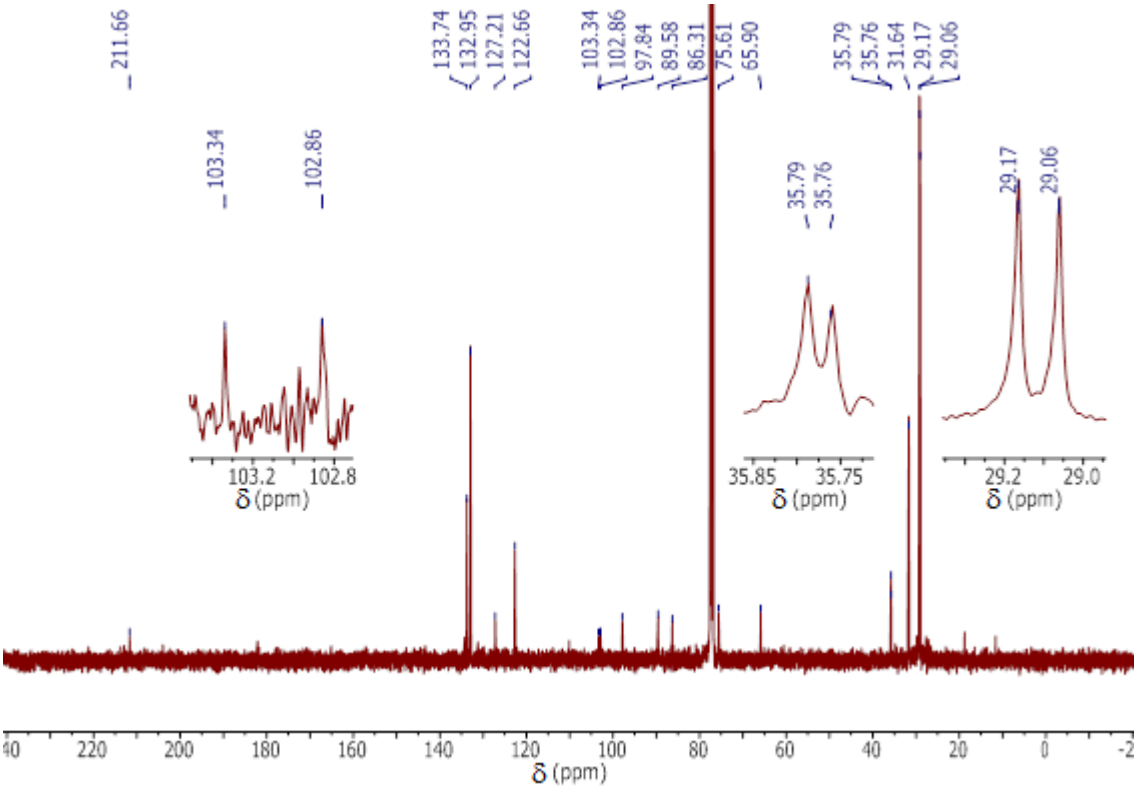

Figure 5. ^{13}C NMR of (*P*)-**MC-2H-Br**.

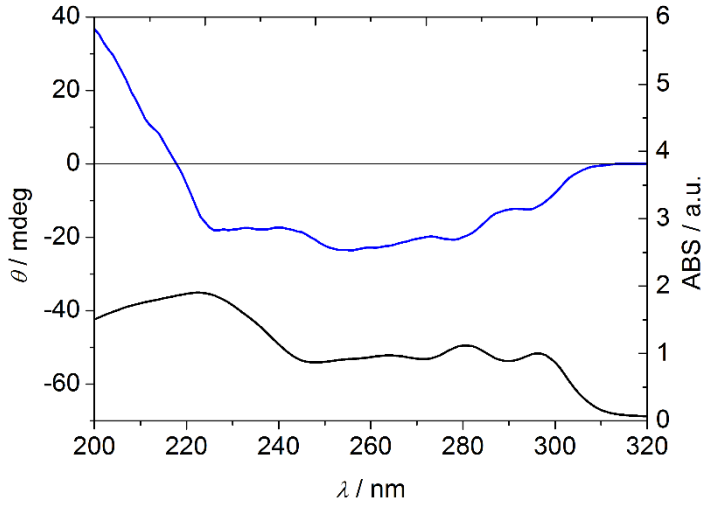

Figure 6. ECD (top) and ABS spectrum of (*M*)-**MC-2H-Br**.

(*P,P*)-**9,9'-(5-bromo-1,3-phenylene)bis(5,7-di-*tert*-butyl-2-methylnona-5,6-dien-3,8-diyn-2-ol) ((*P,P*)-DC-2H-Br)**

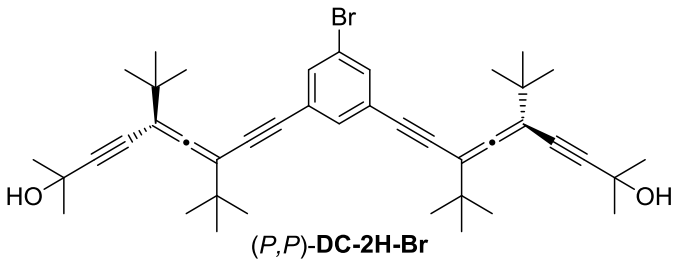

(*P,P*)-**DC-2H-Br**

Figure 7. Structure of (*P,P*)-**DC-2H-Br**.

^{1}H NMR (400 MHz, $CDCl_3$) δ = 7.50 (d, *J* = 1.8 Hz, $2H_{aromatic}$), 7.43 (t, *J* = 1.8 Hz, $1H_{aromatic}$), 2.04 (s, 2H, –OH), 1.56 (12H, -C$\underline{Me_2}$OH), 1.18 (s, 18H, ^{t}Bu), 1.14 (s, 18H, ^{t}Bu) ppm.

^{13}C NMR (101 MHz, $CDCl_3$) δ = 211.6 ($C_{cumulenic}$), 133.6, 132.8, 125.7, 121.8 ($C_{aromatic}$), 103.2, 103.0, 97.7, 90.4, 85.4, 75.7 ($C_{alkynes}$+$C_{allenes}$), 65.9 (-$\underline{C}Me_2$OH), 35.8, 35.7 ($C_{quaternary}$, -$\underline{C}Me_2$OH), 31.6 (-C$\underline{Me_2}$OH), 29.2, 29.1 (Me ^{t}Bu) ppm.

IR ($CHCl_3$) ν = 3342 (br. m, str O–H), 2964 (s, str $C_{aromatic}$–H), 2869, (w, str $C_{aliphatic}$–H), 2206 (w, str C_{alkyne}ΞC_{alkyne}), 1929 (w, C_{allene}=C_{allene}) 1583 (m, str $C_{aromatic}$=$C_{aromatic}$) cm^{-1}.

HR-ESI-MS *m/z* (%): [M] = [$C_{42}H_{53}BrO_2$]; $[M+Na]^+$ calcd. for $^{12}C_{42}{}^{1}H_{53}{}^{79}BrNaO_2$ 691.3127, found: 691.3119 (100); $[M+Na]^+$ calcd. for $^{12}C_{42}{}^{1}H_{53}{}^{81}Br^{23}Na^{16}O_2$ 693.3106, found: 693.3099 (98).

UV/Vis (Hexane) λ_{max} (nm): 295, 280, 263, 220.

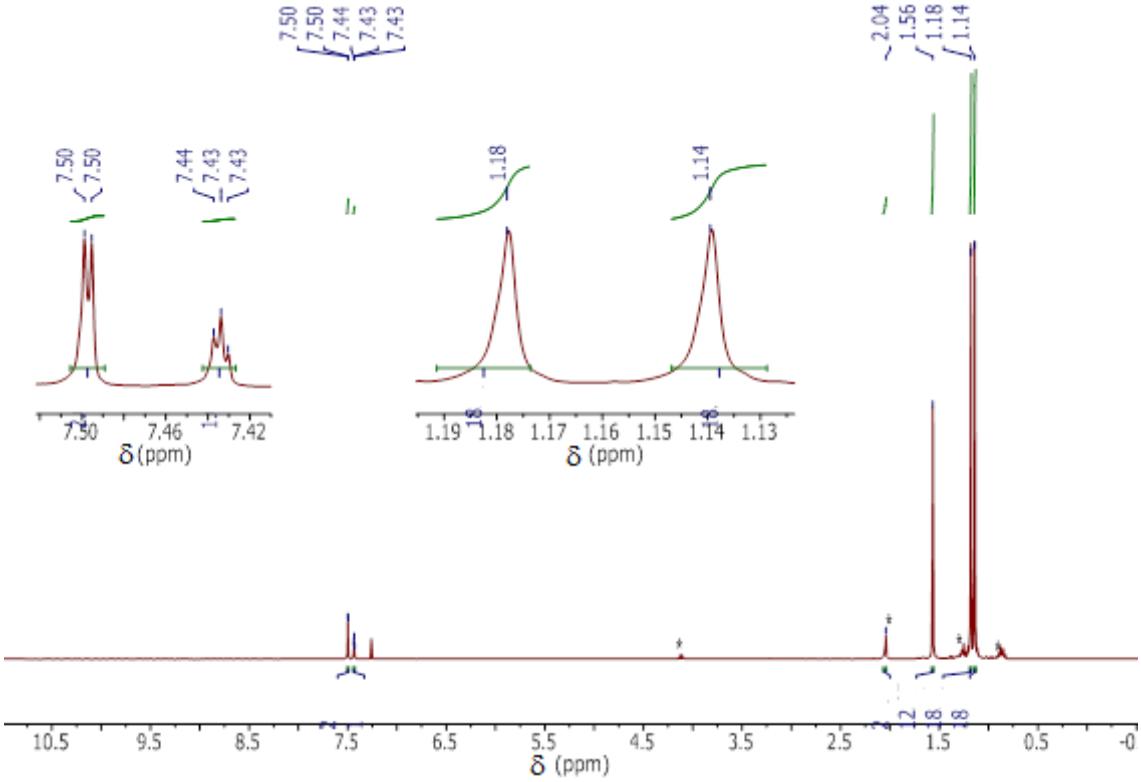

Figure 8. ^{1}H NMR of the (*P,P*)-**DC-2H-Br**.* Traces of ethyl acetate and grease.

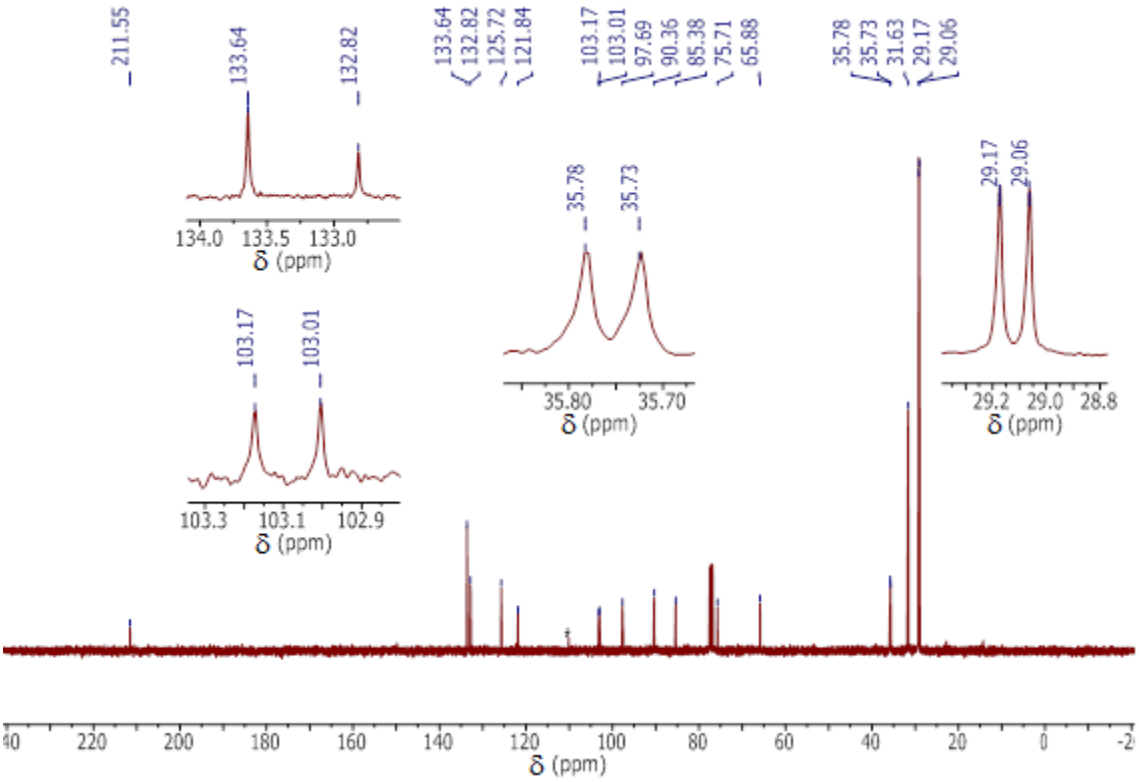

Figure 9. ^{13}C NMR of (*P,P*)-**DC-2H-Br**.

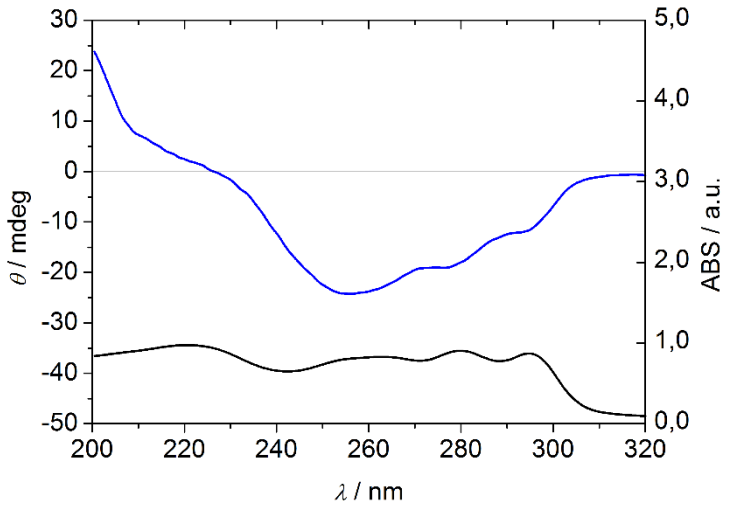

Figure 10. ECD (top) and ABS spectra of (*M,M*)-**DC-2H-Br**.

(*P*)-**5,7-Di-*tert*-butyl-9-(3,5-diiodophenyl)-2-methylnona-5,6-dien-3,8-diyn-2-ol** (**(*P*)-MC-2H-I)**

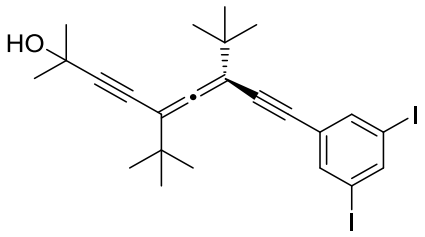

(*P*)-**MC-2H-I**

Figure 11. Structure of (*P*)-**MC-2H-I**.

^{1}H NMR (400 MHz, CD_2Cl_2) δ = 8.02 (t, *J* = 1.6 Hz, 1H), 7.77 (d, *J* = 1.6 Hz, 2H), 2.02 (s, $1H_{OH}$), 1.55 (s, $6H_{Me}$), 1.18 (s, $9H_{tBu}$), 1.14 (s, $9H_{tBu}$) ppm.

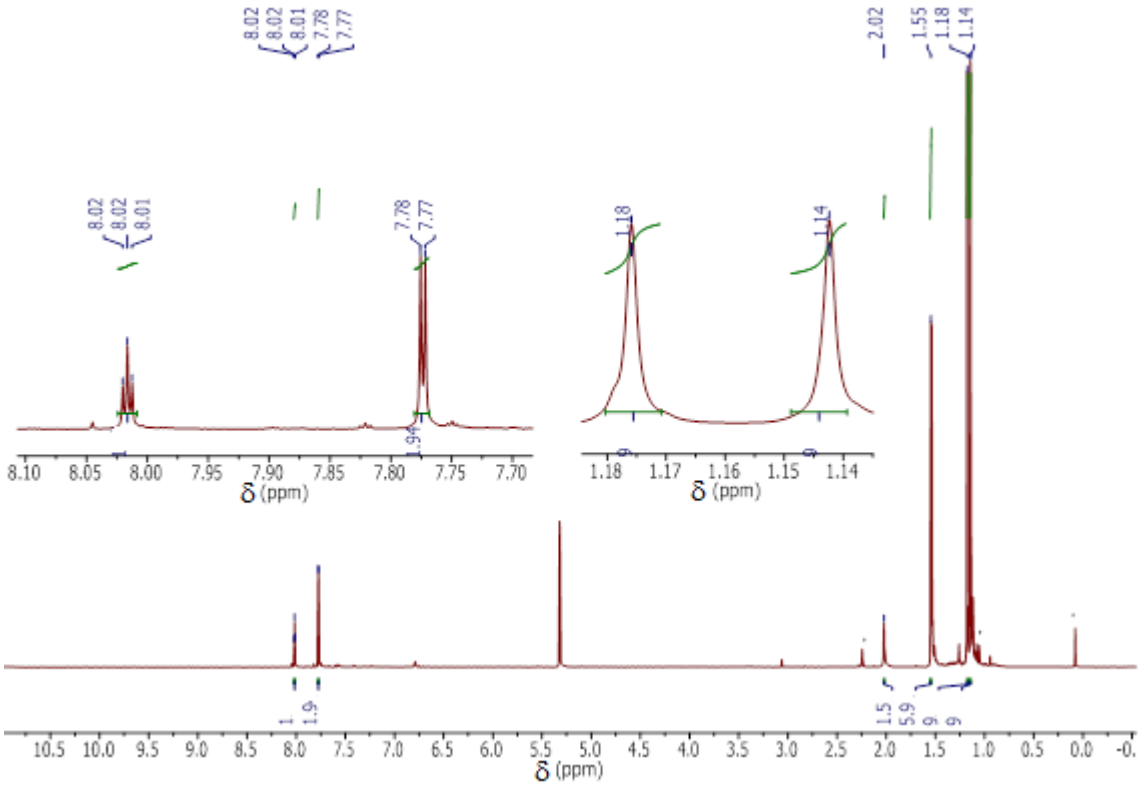

Figure 12. ^{1}H NMR spectrum of (*P*)-**MC-2H-I**.

(*P,P*)-**9,9'-(5-Iodo-1,3-phenylene)bis(5,7-di-*tert*-butyl-2-methylnona-5,6-dien-3,8-diyn-2-ol) ((*P,P*)-DC-2H-I)**

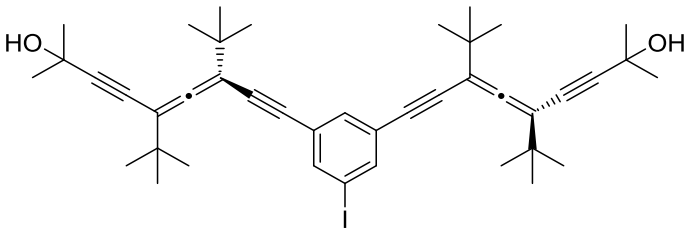

(*P,P*)-**DC-2H-I**

Figure 13. Structure of (*P,P*)-**DC-2H-I**.

^{1}H NMR (400 MHz, CD_2Cl_2) δ = 7.74 (d, *J* = 1.5 Hz, $2H_{aromatic}$), 7.50 (t, *J* = 1.5 Hz, $1H_{aromatic}$), 1.54 (s, $6H_{OH}$), 1.18 (s, $18H_{tBu}$), 1.15 (s, $18H_{tBu}$) ppm.

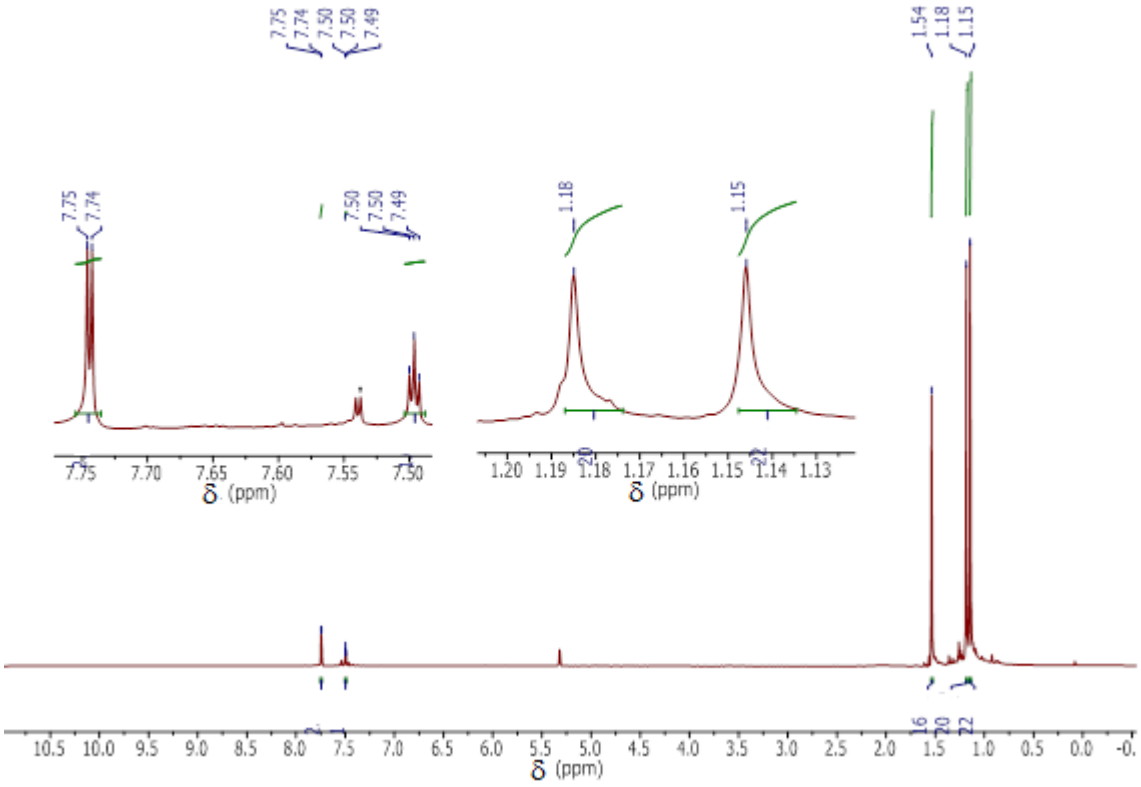

Figure 14. ^{1}H NMR spectrum of (*P,P*)-**DC-2H-I**.

Data of (*P,P,P*)-**2H**

^{1}H NMR (400 MHz, $CDCl_3$) δ = 7.44 (s, $3H_{aromatic}$), 1.57 (s, 18H, -C<u>Me$_2$</u>OH), 1.19 (s, 27H, ^{t}Bu), 1.14 (s, 27H, ^{t}Bu) ppm.

^{13}C NMR (101 MHz, $CDCl_3$) δ = 211.5 ($C_{cumulenic}$), 133.6, 124.3 ($C_{aromatic}$), 103.2, 103.0, 97.5, 91.1, 84.5, 75.9 ($C_{alkynes}$+$C_{allenes}$), 65.9 ($C_{quaternary}$, -<u>C</u>Me$_2$OH), 35.8, 35.7 ($C_{quaternary}$ ^{t}Bu), 31.6 (-C<u>Me$_2$</u>OH), 29.2, 29.1 (Me ^{t}Bu) ppm.

IR ($CHCl_3$) ν = 3358 (br. m, str O–H), 2964 (s, str $C_{aromatic}$–H), 2864, (w, str $C_{aliphatic}$–H) cm^{-1}.

HR-ESI-MS *m/z* (%): [M] = [$C_{60}H_{78}O_3$]; $[M+Na]^+$ calcd. for $^{12}C_{60}{}^{1}H_{78}{}^{23}Na^{16}O_3$ 869.5849, found: 869.5833 (100); $[M+Na]^+$ calcd. for $^{12}C_{59}{}^{13}C^{1}H_{78}{}^{23}Na^{16}O_3$ 870.5882, found: 870.5866 (65).

UV/Vis ($CHCl_3$) λ_{max} (nm): 296, 280, 267, 224.

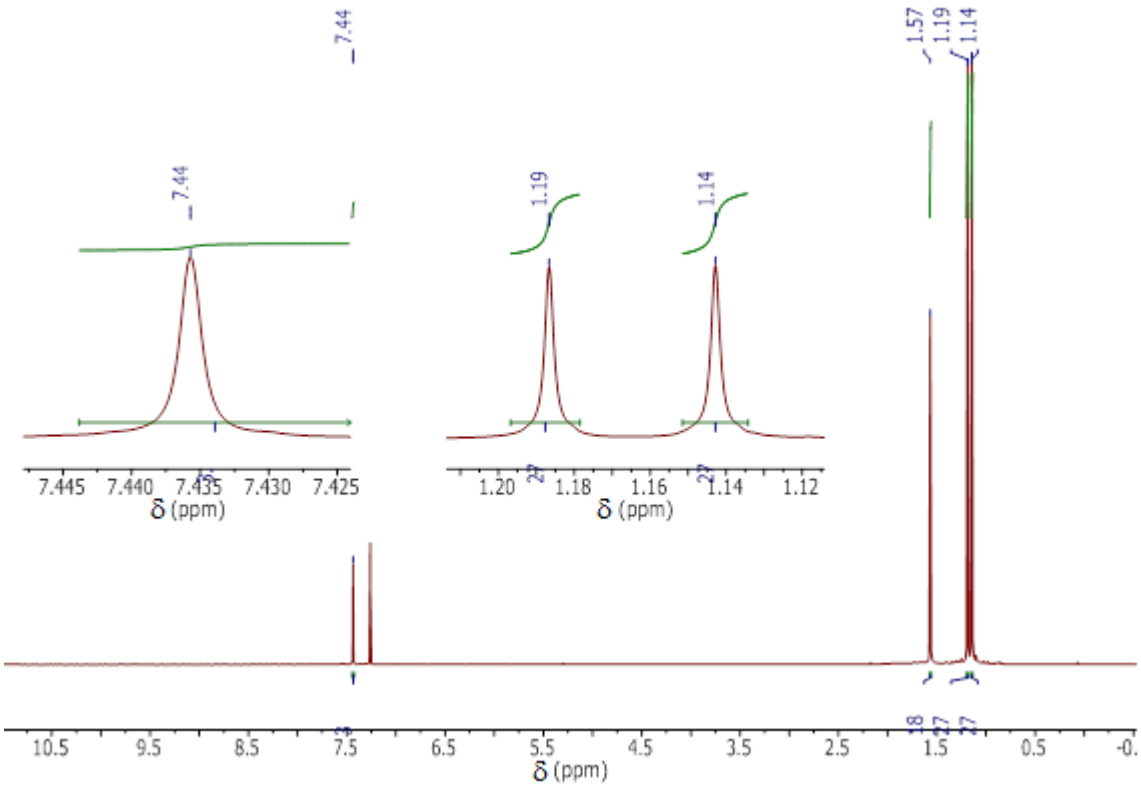

Figure 15. ^{1}H NMR of (*P,P,P*)-**2H**.

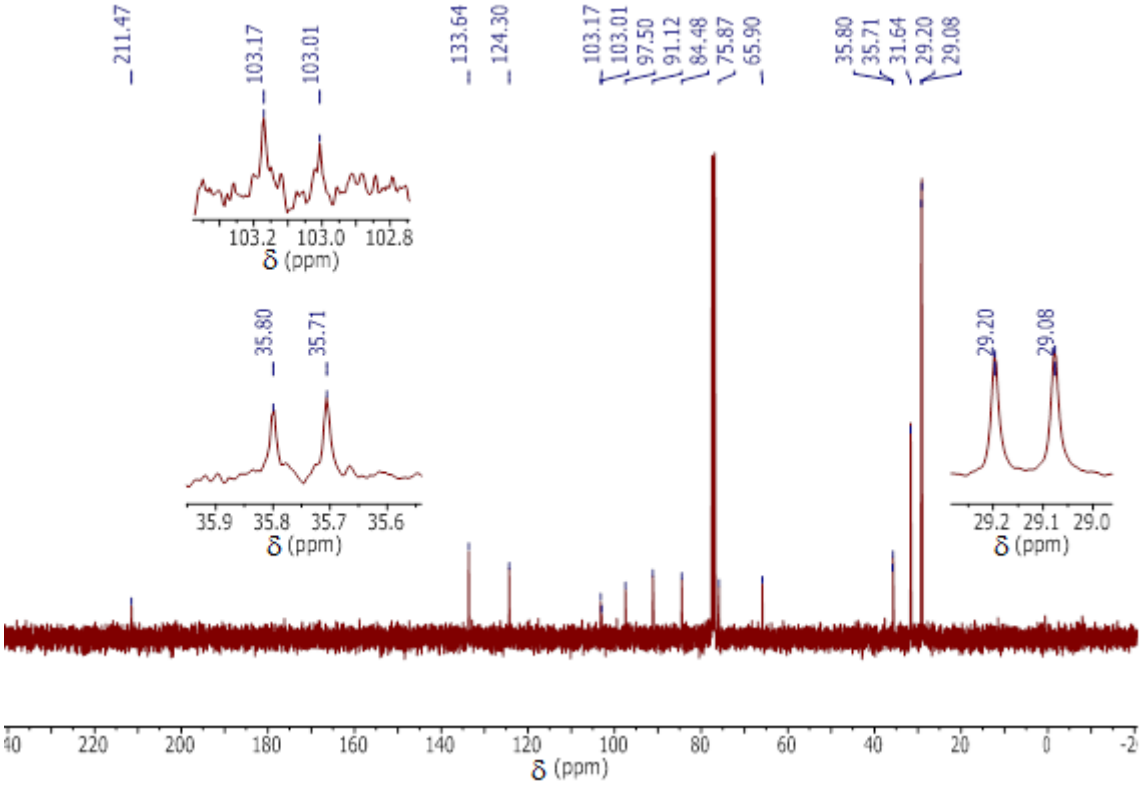

Figure 16. ^{13}C NMR of (*P,P,P*)-**2H**.

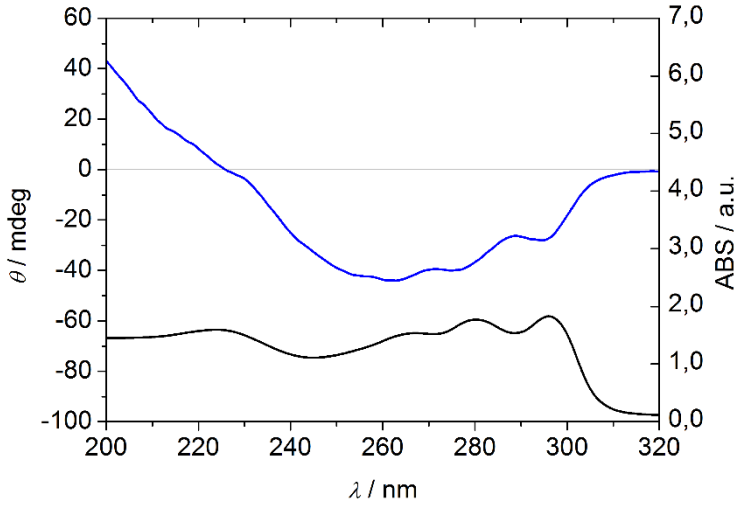

Figure 17. ECD (top) and UV/Vis (bottom) spectra of (*M,M,M*)-**2H**.

(*P,P,P*)-**1,3,5-tris(3,5-di-tert-butylhepta-3,4-dien-1,6-diyn-1-yl)benzene (**(*P,P,P*)-**3H)**

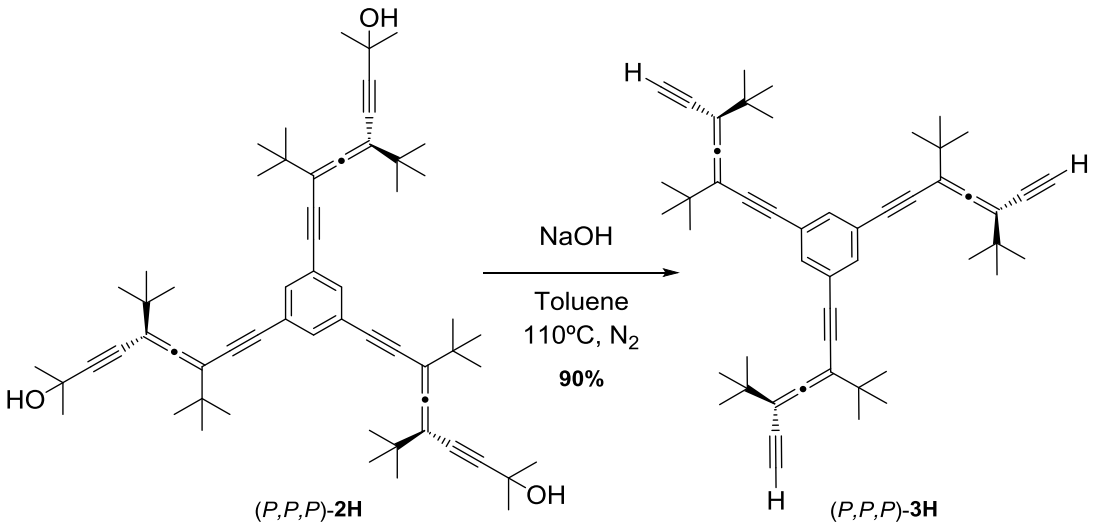

Scheme 9. Synthesis of (*P,P,P*)-**3H**.

To a suspension of powdered and flamed NaOH (300 eq, 15.76 mmol, 630 mg) in toluene (20 mL) in a round-bottom flask, a solution of (*P,P,P*)-**2H** (1 eq, 0.05 mmol, 70 mg) in dry toluene was added *via* cannula. This mixture was stirred and refluxed at 110 °C during 18 h. Toluene was removed under reduced pressure and the mixture washed with distilled water and extracted first with ethyl acetate (EtAcO) and then with DCM. The combined organic phases were dried over anh. Na_2SO_4 and then, the solvents were removed under reduced pressure, affording (*P,P,P*)-**3H** (30 mg, 90% yield) as a yellow oil that was employed without further purification.

^{1}H NMR (400 MHz, $CDCl_3$) δ = 7.43 (s, $3H_{aromatic}$), 3.02 (s, $3H_{alkyne}$) 1.20 (s, 27H ^{t}Bu), 1.17 (s, 27H ^{t}Bu) ppm.

^{13}C NMR (101 MHz, $CDCl_3$) δ = 212.3 ($C_{cumulenic}$), 133.7, 124.2 ($C_{aromatic}$), 110.1, 103.7, 102.7, 91.4, 84.1, 80.8 ($C_{alkynes}$+$C_{allenes}$), 35.9, 35.5 ($C_{quaternary}$), 29.2, 29.0 (Me ^{t}Bu) ppm.

IR ($CHCl_3$) ν = 3306 (s, str C_{alkyne}–H), 2965 (s, str $C_{aromatic}$–H), 2868, (w, str $C_{aliphatic}$–H), 2206 (w, str C_{alkyne}ΞC_{alkyne}), 1923 (w, str C_{allene}=C_{allene}), 1578 (s, str $C_{aromatic}$=$C_{aromatic}$) cm^{-1}.

HR-ESI-MS *m/z* (%): [M] = [$C_{51}H_{60}$]; $[M+H]^+$ calcd. for $^{12}C_{51}{}^{1}H_{61}$, 673.4773, found: 673.4789 (100); $[M+H]^+$ calcd. for $^{12}C_{50}{}^{13}C^{1}H_{61}$, 674.4807, found: 674.4826 (63).

UV/Vis (Hexane) λ_{max} (nm): 296, 280, 267, 220.

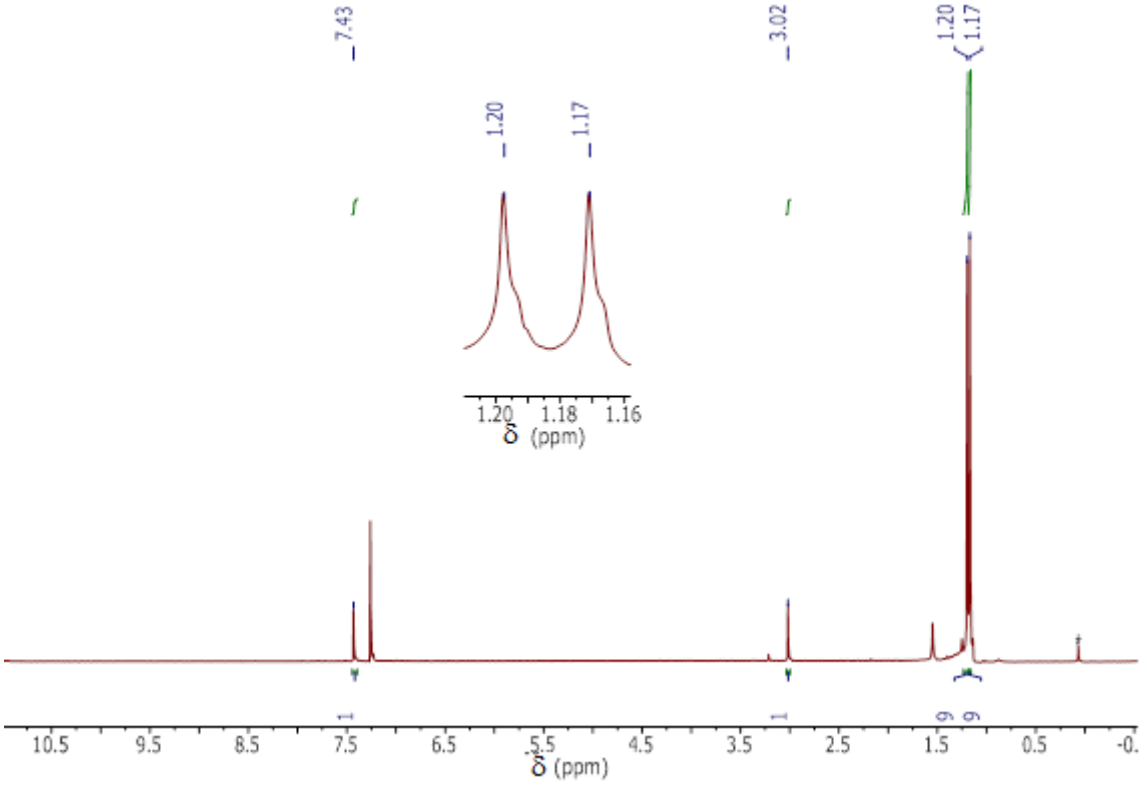

Figure 18. ^{1}H NMR of (*P,P,P*)-**3H**.

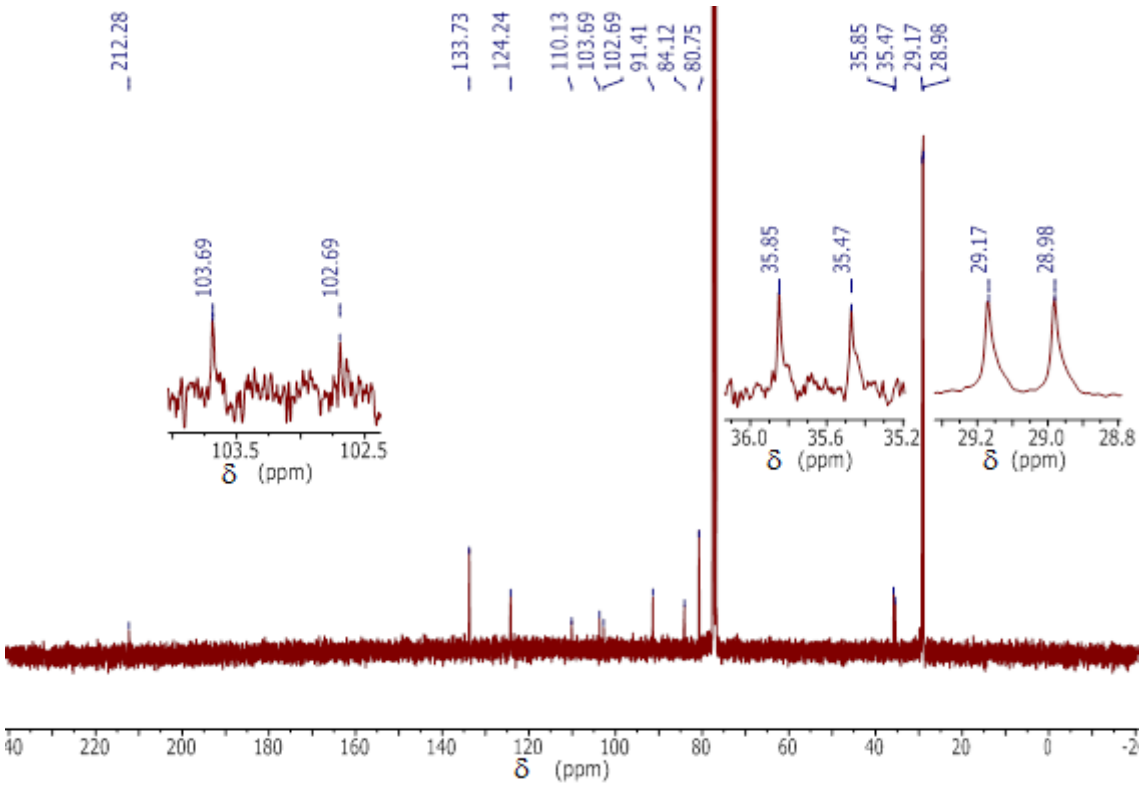

Figure 19. ^{13}C NMR of (*P,P,P*)-**3H**.

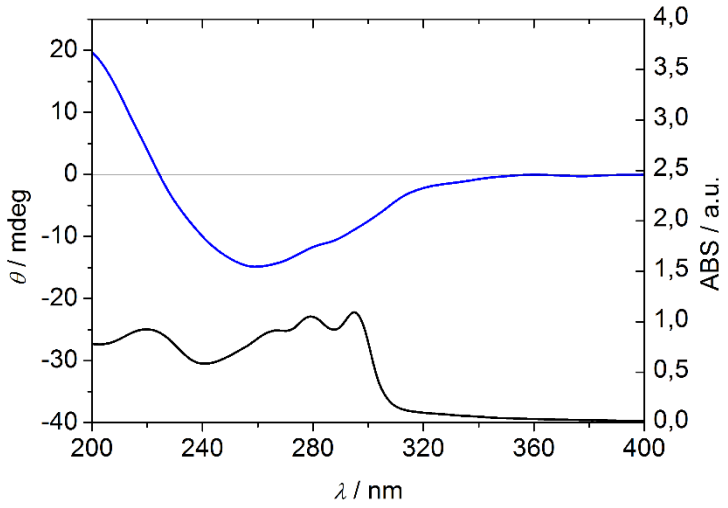

Figure 20. ECD (top) and UV/Vis (bottom) spectra of (*M,M,M*)-**3H**.

(*P,P*)$_3$-4,6,11,13,19,21,26,28,33,35,40,42-Dodeca-*tert*-butyl-1,16-(1,3,5)-benzenebicyclotetratetracontaphane-4,5,11,12,19,20,26,27,33,34,40,41-dodecaen-2,7,9,14,17,22,24,29,31,36,38,43-dodecayne ((*P,P*)$_3$-1H)

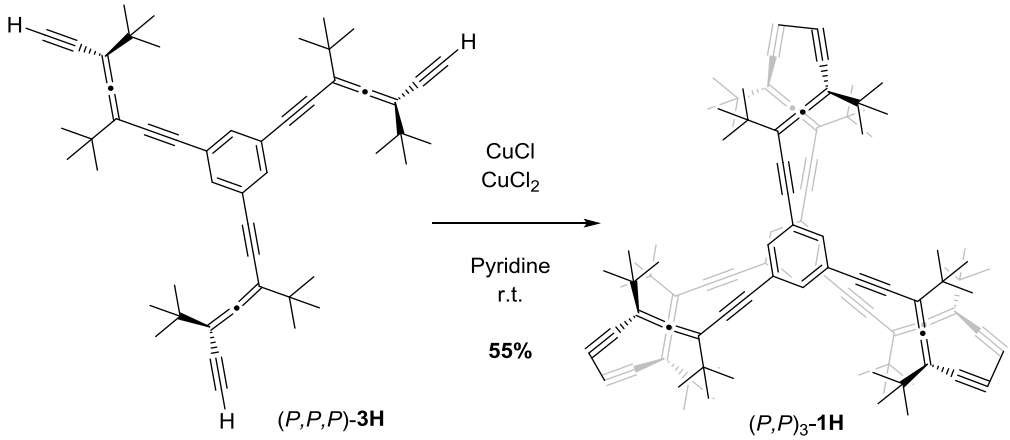

Scheme 10. Synthesis of (*P,P*)$_3$-**1H.**

Two solutions were prepared:

Solution ***a***: CuCl (75 eq, 1.67 mmol, 166 mg) and $CuCl_2$ (11 eq, 0.25 mmol, 33 mg) were placed in a round-bottom flask under N_2 atmosphere, dissolved with dry pyridine (13 mL) and bubbled with N_2 over 30 min.

Solution ***b***: Trisdeprotected product (*P,P,P*)-**3H** (1 eq, 0.02 mmol, 15 mg) was dissolved in dry pyridine (20 mL).

Both solutions were bubbled with N_2 for 1 h. Solution ***b*** was added with a flux of 1 mL·h^{-1} to solution ***a*** under N_2 at r.t. After 20 h of reaction, the solvent was removed under reduced pressure and the remaining solid was dissolved in DCM and washed first with sat. aq. NH_4Cl solution and then with sat. aq. KCN solution. The combined organic phases were dried over anh. Na_2SO_4 and evaporated to dryness. The obtained white solid was purified by FC (SiO_2; hexane:DCM 2 %) affording (*P,P*)$_3$-**1H** (9.4 mg, 55 %).

^{1}H NMR (400 MHz, CD_2Cl_2) δ = 7.38 (s, 6H$_{aromatic}$, H1), 1.19 (s, 54H ^{t}Bu, H12), 1.18 (s, 54 H ^{t}Bu, H13) ppm.

^{13}C NMR (101 MHz, CD_2Cl_2) δ = 215.6 (C$_{cumulenic}$, C8), 133.5 (C$_{aromatic}$, C1), 124.5 (C$_{aromatic}$, C2), 104.7 (C$_{allene,}$ C7), 104.0 (C$_{allene,}$ C9), 92.5 (C$_{alkyne}$, C3), 84.2 (C$_{alkyne}$, C4), 77.6 (C$_{alkyne}$, C5), 76.1 (C$_{alkyne}$, C6), 35.9 (C$_{quaternary}$, C10), 35.7 (C$_{quaternary}$, C11), 29.18 (Me ^{t}Bu, C12), 29.16 (Me ^{t}Bu, C13) ppm.

IR ($CHCl_3$) ν = 2963 (s, str C$_{aromatic}$–H); 2927 (s, str C$_{aromatic}$–H); 2864 (m, str C$_{aliphatic}$–H); 2206 (w, str C$_{alkyne}$ΞC$_{alkyne}$); 1916 (w, str C$_{allene}$=C$_{allene}$); 1734 (w); 1581 (m, str C$_{aromatic}$=C$_{aromatic}$) cm^{-1}.

HR-MALDI-MS *m/z* (%): [M] = [$C_{102}H_{114}$]; [M+H]$^+$ calcd. for $^{12}C_{102}{}^{1}H_{115}$, 1339.8999, found: 1339.8921 (97); [M+H]$^+$ calcd. for $^{12}C_{101}{}^{13}C^{1}H_{115}$, 1340.9032, found: 1340.9038 (100).

UV/Vis ($CHCl_3$) λ$_{max}$ (nm): 306, 287, 273 (sh.), 247. ***ε$_{285}$*** = 33390M^{-1}·cm^{-1} (solutions from 5·10^{-6} to 9·10^{-6} M). ***g*-factor$_{max}$** (325nm) = 0.006.

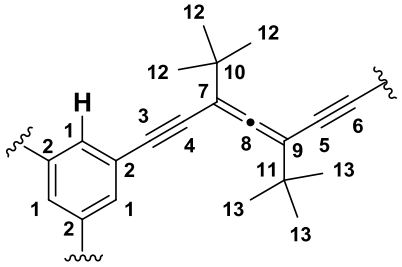

Figure 21. Reduced scheme of the **COHC** (*P,P*)$_3$-**1H** showing the labels of the different C and H atoms in the molecule.

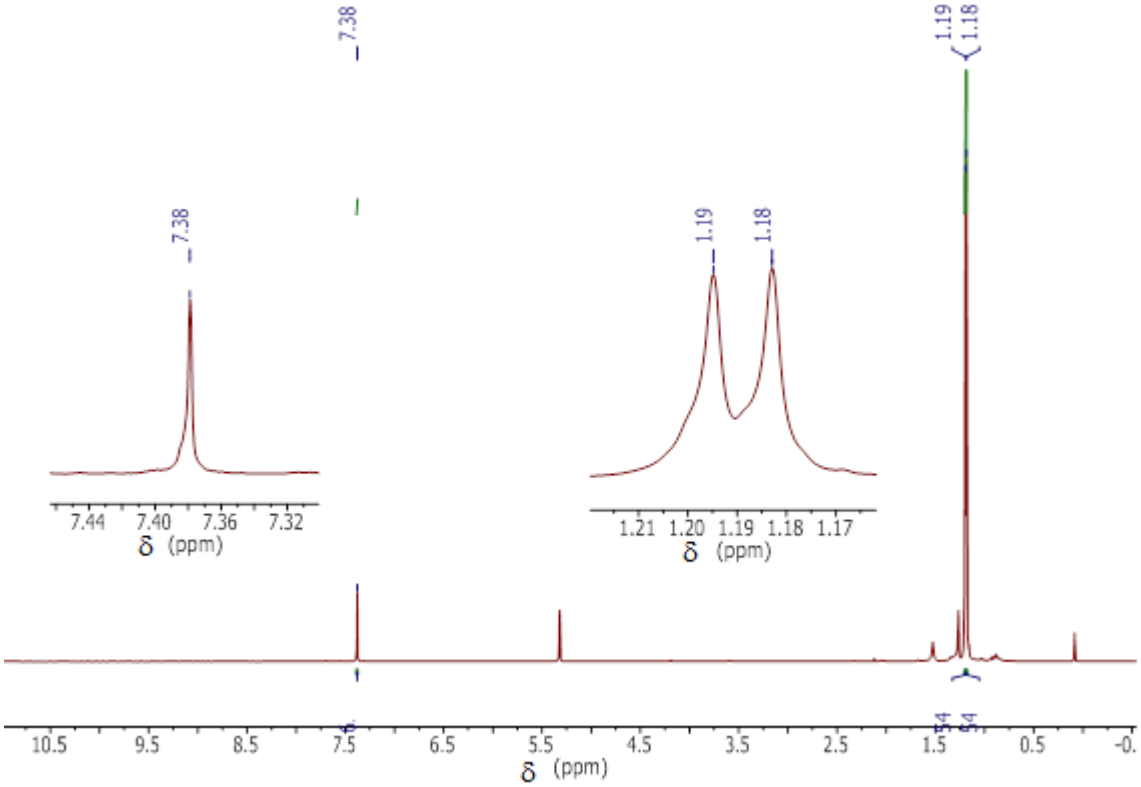

Figure 22. ^{1}H NMR spectrum of the **COHC** (*P,P*)$_3$-**1H**. ***Grease traces.

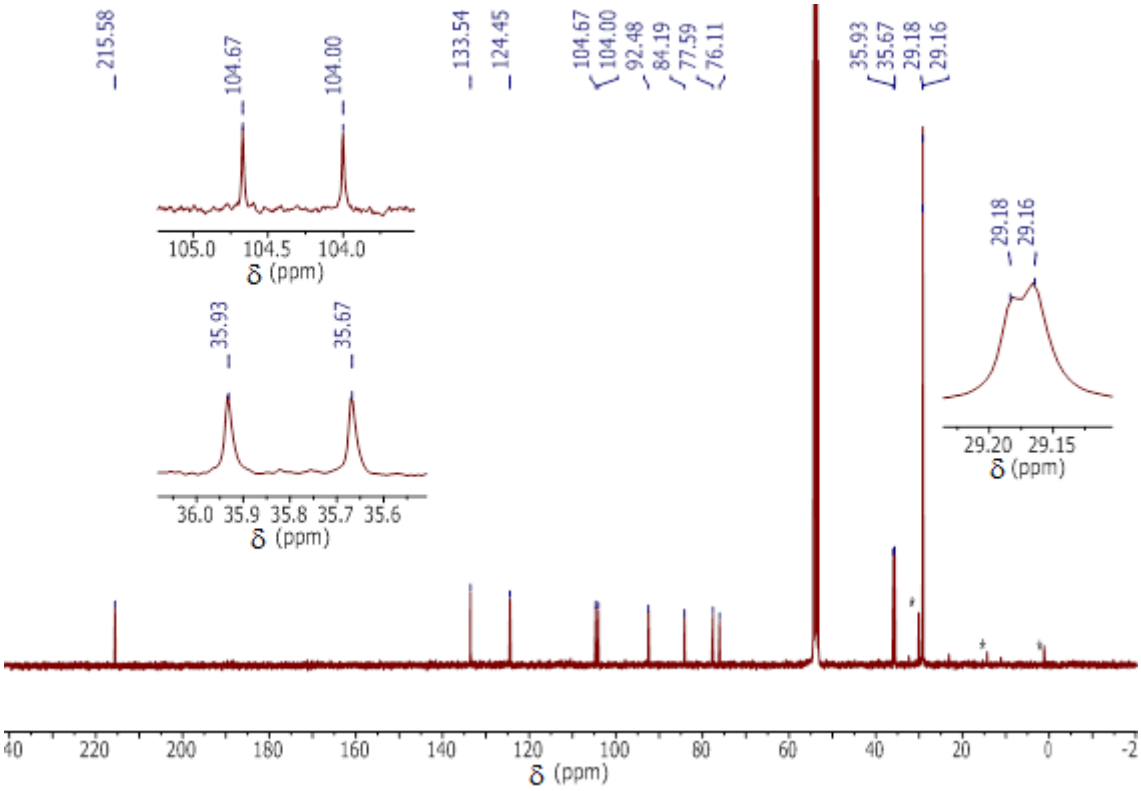

Figure 23. ^{13}C NMR spectrum of the **COHC** (*P,P*)$_3$-**1H**.

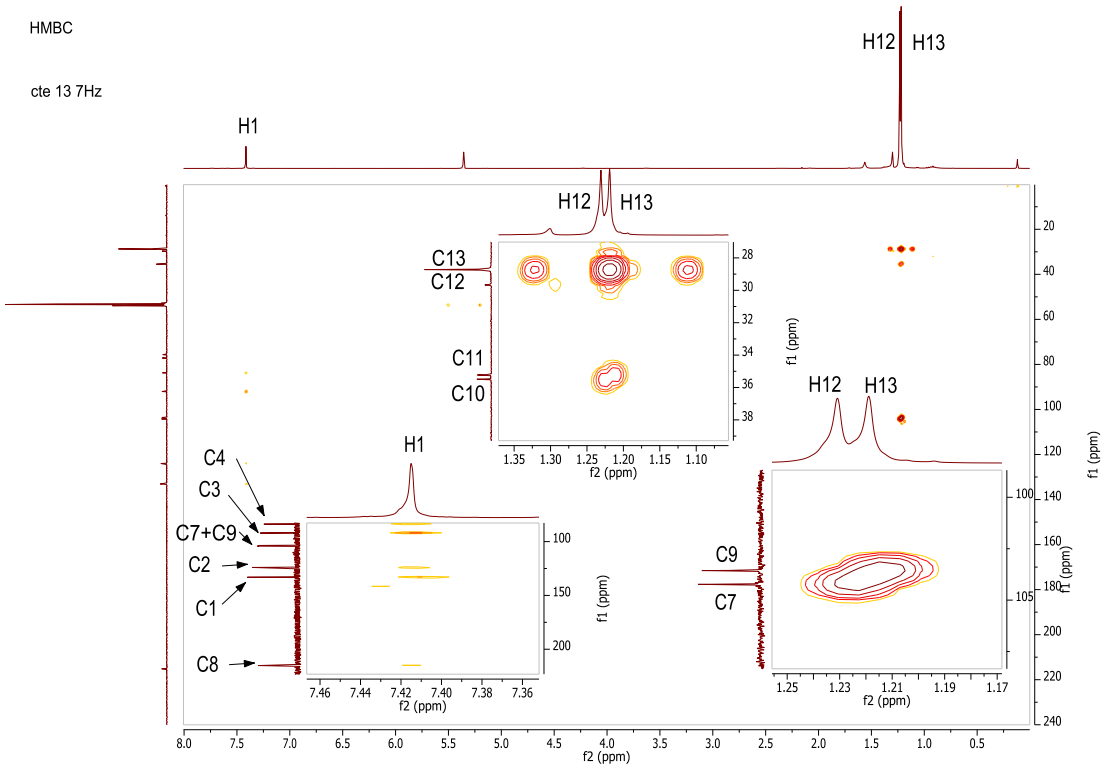

Figure 24. HMBC-NMR spectrum of the **COHC** (*P,P*)$_3$-**1H** in CD_2Cl_2.

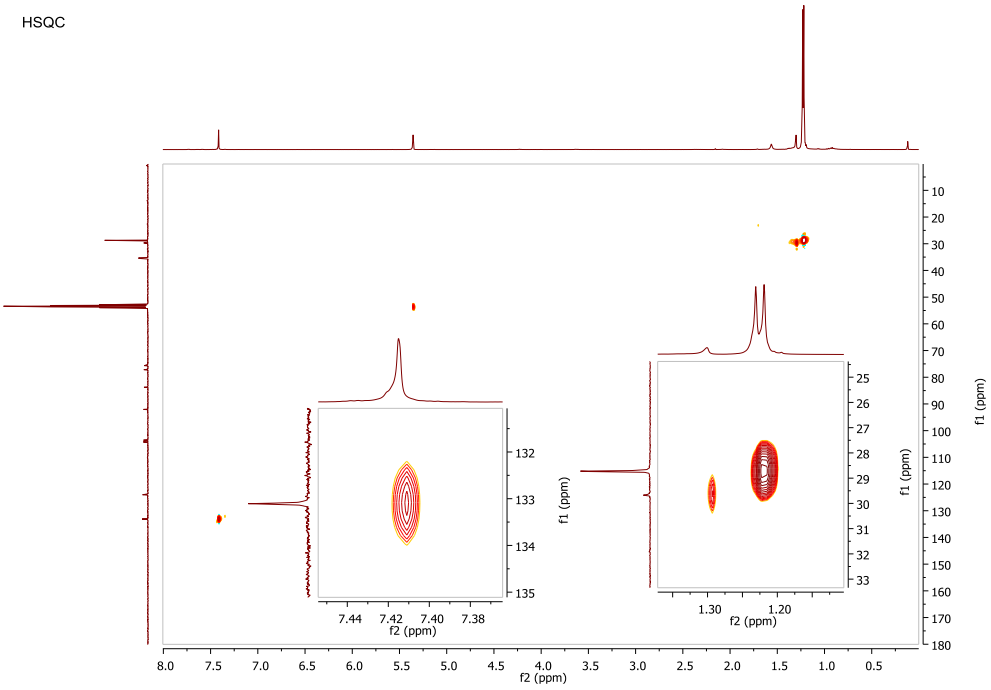

Figure 25. HSQC-NMR spectrum of the **COHC** (*P,P*)$_3$-**1H** in CD_2Cl_2.

X-ray determination of the crystal structure of (*M,M*)$_3$-**1H**

A summary of the crystallographic results is given bellow:

Crystals of (*M,M*)$_3$-**1H** for X-ray analysis were grown by slow evaporation from a mixture of MeOH/diethyl ether. A crystal was selected and mounted on a MiTeGen loop under oil and flash frozen at 100K under a cold N_2 gas stream. X-ray diffraction data were collected on a Bruker X8 kappa APEX II CCD diffractometer.

The crystal structure presents large solvent accessible voids that contained a considerable number of diffuse electron density peaks that could not be recognized and refined as solvent. The SQUEEZE[2] procedure as implemented in the PLATON[3] software suite was applied to the collected data. In this way, the disordered solvent molecules were treated as a diffuse contribution to the overall scattering of the crystal without applying specific atom positions.

One of the axial chiral connectors in molecule 1 is disordered over two positions; the coordinates for both conformations were refined together with their corresponding occupancies. The final values for the occupation parameter were 0.607(7) and the complementary of 0.393(7) respectively (See Figures S22 and S23).

X-ray crystallography data computing details

Data collection: Bruker *APEX2* software, SAINT (version 8.34A), SADABS (version 2014/5), Bruker AXS Inc, Madison, Wisconsin, USA.); cell refinement: *SAINT* V8.34A integration software; absorption correction: SADABS 2014/5 (Bruker (2014) APEX2 (Version 2014.11-0); data reduction: *SORTAV*[4];program(s) used to solve structure: *SHELXD 2013*/2[5]; program used to refine structure: *SHELXL 2014*/7[6]; molecular graphics: *ORTEP-3 for Windows*[7]; software used to prepare material for publication: *WinGX* publication routines[7].

Crystal data

$C_{102}H_{114}$
$M_r = 1339.93$
Orthorhombic, $P2_122_1$
$a = 22.1173\ (13)$ Å
$b = 23.5017\ (11)$ Å
$c = 47.927\ (3)$ Å
$V = 24912\ (2)$ Å^3
$T = 100$ K
Plate, colourless

$Z = 8$
$F(000) = 5808$
$D_x = 0.715$ Mg m^{-3}
Mo $K\alpha$ radiation, $\lambda = 0.71073$ Å
Cell parameters from 7502 reflections
$\theta = 2.2–17.5°$
$\mu = 0.04$ mm^{-1}
0.34 × 0.33 × 0.15 mm

Data collection

Bruker APEX-II diffractometer
Radiation source: sealed x-ray tube
Graphite monochromator
φ or ω oscillation scans
Absorption correction: multi-scan
SADABS2014/5 - Bruker AXS area detector scaling and absorption correction
$T_{min} = 0.828$, $T_{max} = 0.956$

80064 measured reflections
22606 independent reflections
12898 reflections with $I > 2\sigma(I)$
$R_{int} = 0.080$
$\theta_{max} = 19.8°$, $\theta_{min} = 1.0°$
$h = -20 \rightarrow 21$
$k = -22 \rightarrow 10$
$l = -45 \rightarrow 45$

Refinement

Refinement on F^2
Least-squares matrix: full
$R[F^2 > 2\sigma(F^2)] = 0.070$
$wR(F^2) = 0.202$
$S = 1.02$
22606 reflections
2081 parameters
9478 restraints
0 constraints
Primary atom site location: dual
Secondary atom site location: difference Fourier map
Hydrogen site location: inferred from neighbouring sites
H-atom parameters constrained
$w = 1/[\sigma^2(F_o^2) + (0.1062P)^2 + 1.0\sin\theta/\lambda]$ where $P = (F_o^2 + 2F_c^2)/3$
$(\Delta/\sigma)_{max} = 0.001$
$\Delta\rho_{max} = 0.19$ e Å^{-3}
$\Delta\rho_{min} = -0.15$ e Å^{-3}
Absolute structure: Flack x determined using 3984 quotients [(I+)-(I-)]/[(I+)+(I-)] (Parsons, Flack and Wagner, Acta Cryst. B69 (2013) 249-259).
Absolute structure parameter: 1.5 (10)

Special details

Geometry
All e.s.d.'s (except the e.s.d. in the dihedral angle between two l.s. planes) are estimated using the full covariance matrix. The cell e.s.d.'s are taken into account individually in the estimation of e.s.d.'s in distances, angles and torsion angles; correlations between e.s.d.'s in cell parameters are only used when they are defined by crystal symmetry. An approximate (isotropic) treatment of cell e.s.d.'s is used for estimating e.s.d.'s involving l.s. planes.

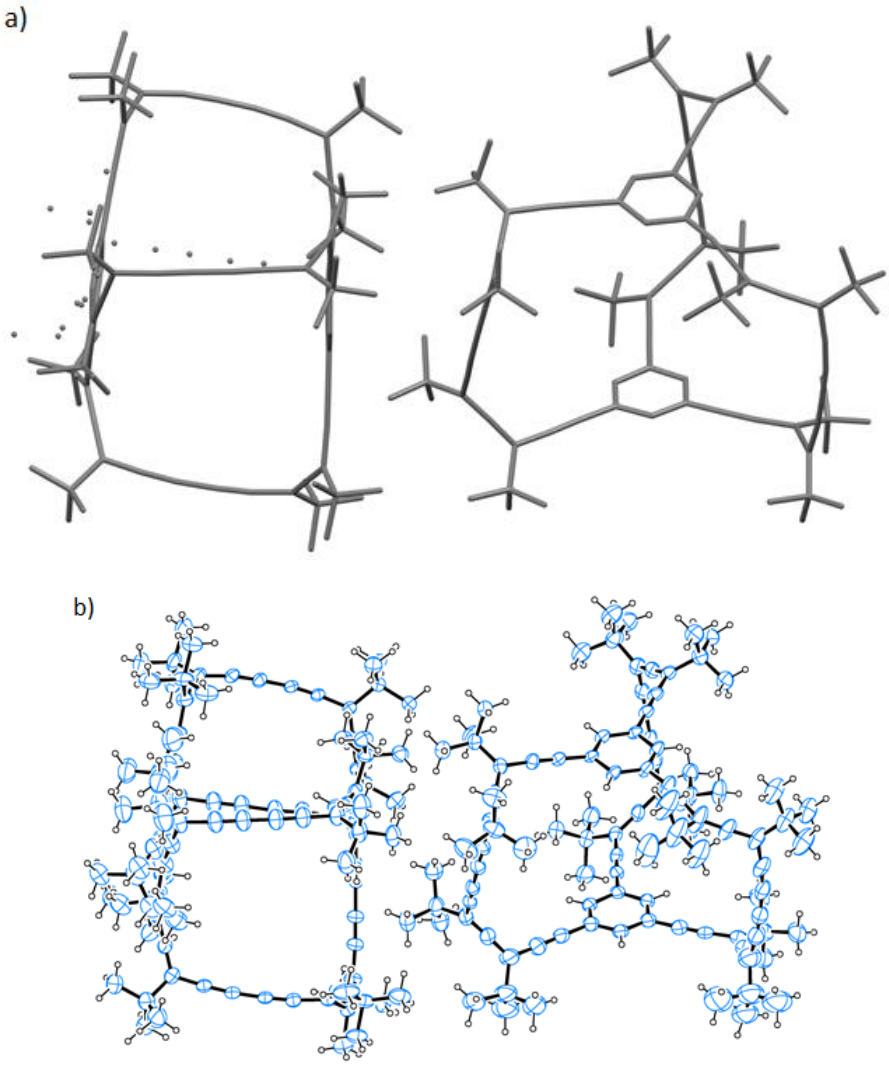

Figure 26. Schematic and ORTEP view of the Asymmetric Unit content. (a) Only C atoms are displayed. Disconnected atoms show the less populated disordered conformation. (b) ORTEP representation with ellipsoids at 30% probability. C and H atoms are displayed.

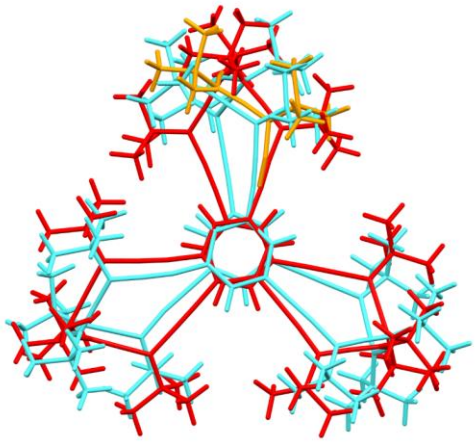

Figure 27. Overlaid representation of both crystallographically independent molecules. Molecule 1 is colored in red and molecule 2 in cyan. The less populated disordered part of molecule 1 is displayed in yellow.

Computational Data

The geometry and frequencies of a model of (*P,P*)$_3$-**1H** in which the *tert*-Bu were substituted by Me groups have also been computationally calculated employing the method CAM-B3LYP with the basis set 6-31G(d), arising a D_3 geometry as expected.[8]

6.4. Synthesis of guests.

Triphenylene-2,3,6,7,10,11-hexaamine (HATP-Sym)

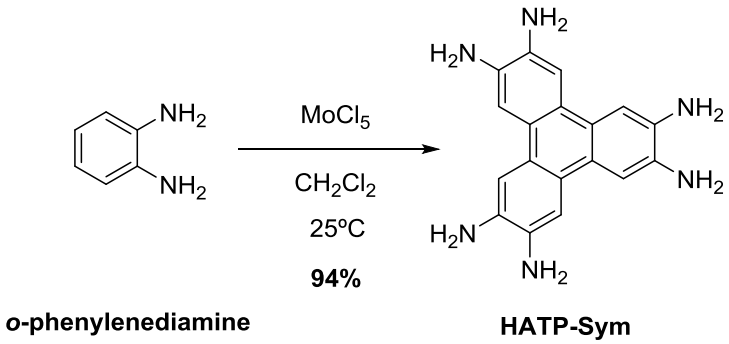

Scheme 11. Synthesis of triphenylene-2,3,6,7,10,11-hexaamine.[9]

$MoCl_5$ (1 eq, 0.9432 mmol, 258 mg,) was added to a solution of *o*-phenylenediamine (1 eq, 0.9247 mmol, 100 mg) in dry CH_2Cl_2 (10 ml). The dark reaction mixture was stirred at r.t. for 18 h under Ar atmosphere. It was then poured over cold MeOH (15 ml), diluted with water (20 ml) and extracted with hexane and then with DCM and EtOAc (20 ml). The combined extracts were dried over anh. Na_2SO_4 and the solvent was removed under vacuum. The mixture was purified by recrystallization in distilled water yielding **HATP-Sym** (257 mg, 94%) as a maroon solid.

^{1}H NMR (D_2O) δ = 7.49 (s, 6H, H_{ar}) ppm.

^{13}C NMR (D_2O) δ = 128.8, 125.9, 124.3 ppm.

LR-EI-MS *m/z* (%): $[M+Na]^+$ calcd. for $^{12}C_{18}{}^{1}H_{18}{}^{14}N_6{}^{23}Na$ 341.15, found: 341.31 (100).

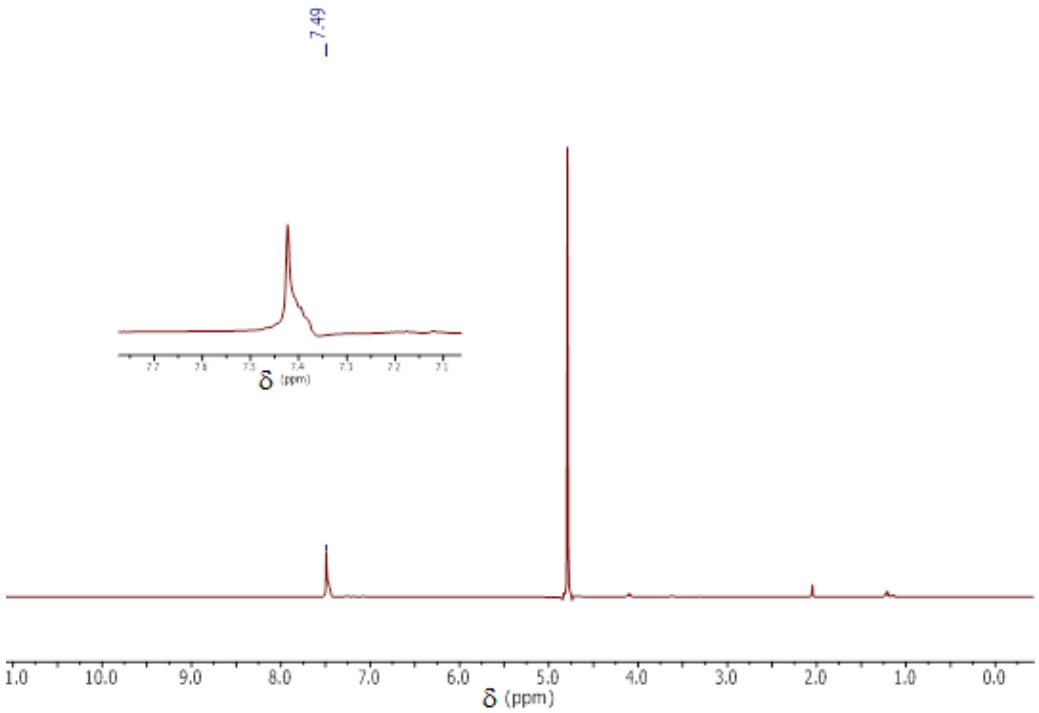

Figure 28. ^{1}H NMR spectrum of **HATP-Sym**.

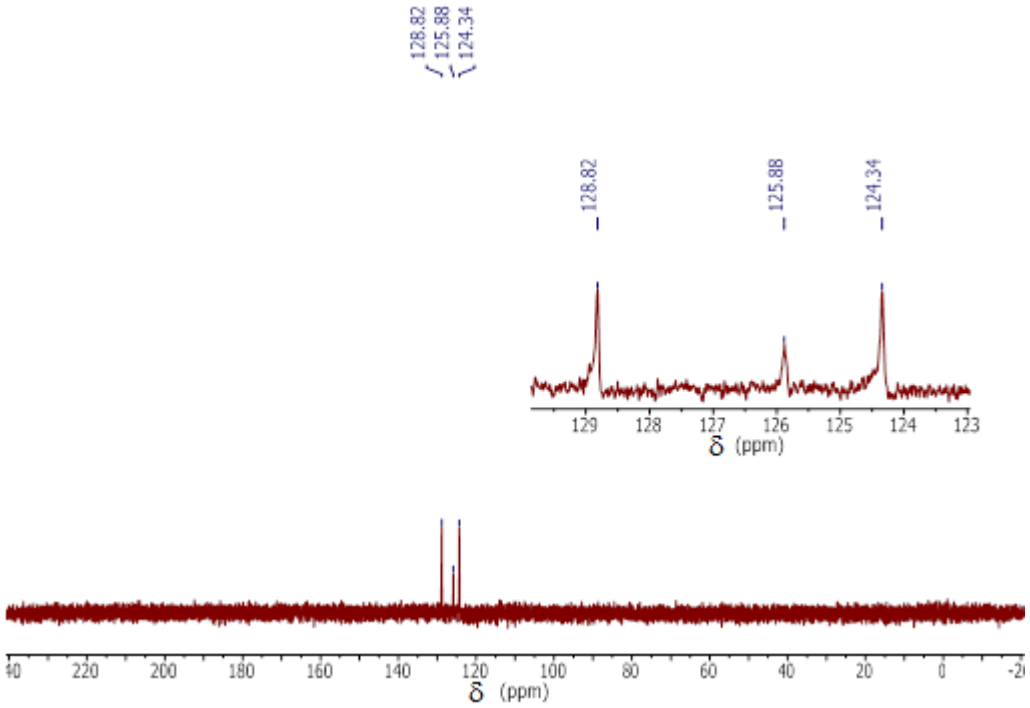

Figure 29. ^{13}C NMR spectrum of **HATP-Sym**.

2,3,6,7,10,11-Hexamethoxytriphenylene (HMeOTP).

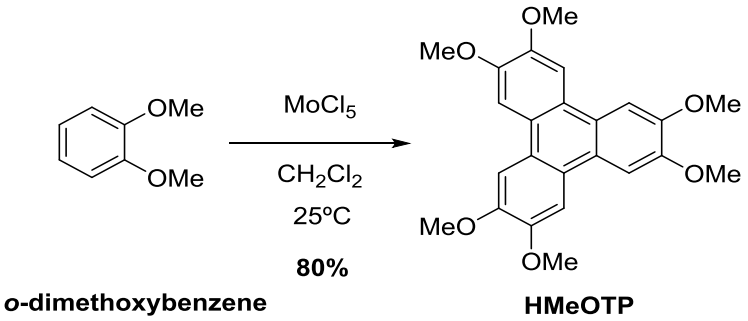

Scheme 12. Synthesis of 2,3,6,7,10,11-hexamethoxytriphenylene.[9]

$MoCl_5$ (1.02 eq, 4.208 mmol, 1.150 g) was added to a solution of 1,2-dimethoxybenzene (1 eq, 4.1257 mmol, 570 mg) in dry CH_2Cl_2 (10 ml). The reaction mixture was stirred at r.t. for 20 min under anhydrous conditions (Ar atmosphere). It was then poured over cold MeOH (15 mL), diluted with cold water (20 mL) and a white precipitate was formed. The solid was filtrated under vacuum obtaining **HMeOTP** (180 mg, 80% calculated yield for a 32% conversion of the starting material). The solution was further extracted with hexane (3x20 mL) and the combined extracts were dried with brine and then over anh. Na_2SO_4, recovering the starting material.

^{1}H NMR (400 MHz, CD_2Cl_2) δ = 7.82 (s, 6H, H_{ar}), 4.08 (s, 18H, -OMe) ppm.

^{13}C NMR (101 MHz, CD_2Cl_2) δ = 149.10, 123.12, 104.54, 55.97 ppm.

1,3,5-Tris((trimethylsilyl)ethynyl)benzene

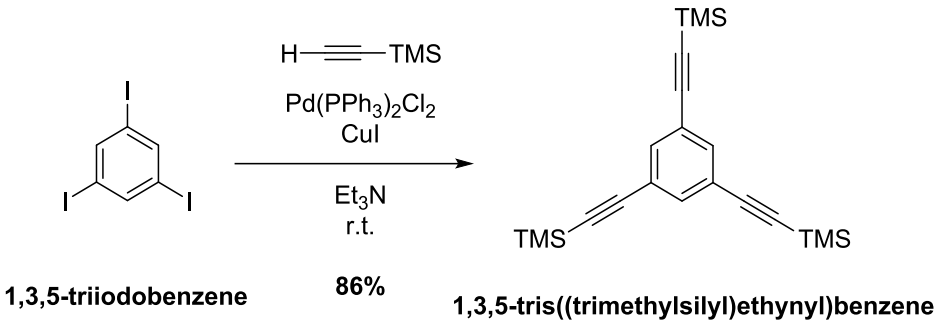

Scheme 13. Synthesis of 1,3,5-tris((trimethylsilyl)ethynyl)benzene.[11]

1,3,5-Triiodobenzene (1 eq, 0.17 mmol, 78 mg), Pd $(PPh_3)_2Cl_2$ (20 mol%, 0.03 mmol, 24 mg) and CuI (10 mol%, 0.02 mmol, 3 mg) were placed into a flamed, Argon-purged Schlenk, and dissolved in dry Et_3N (4 mL). TMS-acetylene (3.3 eq, 0.57 mmol, 81 μL) was added. After 27 h at r.t. with stirring the mixture was treated with sat. aq. NH_4Cl, washed with dichloromethane and dried with anh. Na_2SO_4. FC (SiO_2; hexane) gave 1,3,5-tris((trimethylsilyl)ethynyl)benzene (54 mg, 86% yield) as a colorless crystalline solid. Spectroscopic data are in good agreement with those previously reported.[11]

^{1}H NMR (400 MHz, $CDCl_3$) δ = 7.49 (s, $3H_{aromatic}$), 0.22 (s, $27H_{TMS}$) ppm.

^{13}C NMR (101 MHz, $CDCl_3$) δ = 135.1 ($C–H_{aromatic}$), 123.8 ($C_{aromatic}$), 103.3 (C_{alkyne}), 95.7 (C_{alkyne}), -0.02 ($C_{Me\text{-}TMS}$) ppm.

1,3,5-Triethynylbenzene (TEB)

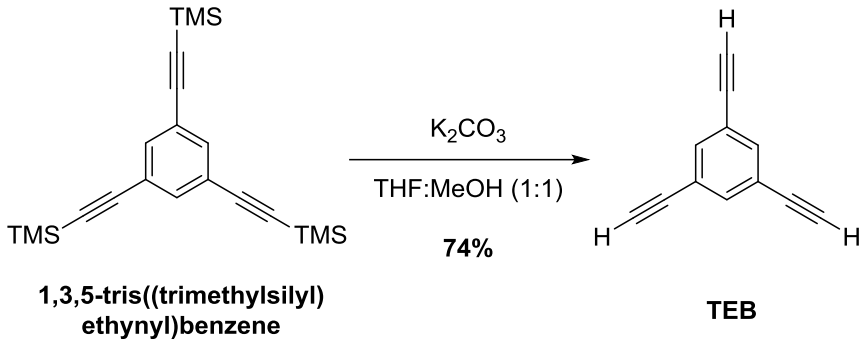

Scheme 14. Synthesis of **TEB**.

1,3,5-Tris((trimethylsilyl)ethynyl)benzene (1 eq, 0.26 mmol, 95 mg) and K_2CO_3 (21 eq, 5.41 mmol, 748 mg) were dissolved in a dry 1:1 mixture of THF:MeOH (30 mL) under Argon into a round bottom flask at r.t. After 24 h, the reaction mixture was treated with distilled water, extracted with dichloromethane and dried with anh. Na_2SO_4. FC (SiO_2; hexane) afforded the final product **TEB** (29 mg, 74% yield) as a colorless crystalline solid. Spectroscopic data found was coincident with those previously reported.[12]

^{1}H NMR (400 MHz, CD_2Cl_2) δ = 7.58 (s, 3H), 3.19 (s, 3H) ppm.

^{13}C NMR (101 MHz, CD_2Cl_2) δ = 135.9 ($C–H_{aromatic}$), 123.3 ($C_{aromatic}$), 81.8 (C_{alkyne}), 79.1 (C_{alkyne}) ppm.

Ferrocenium hexafluorophosphate (Fc^+)

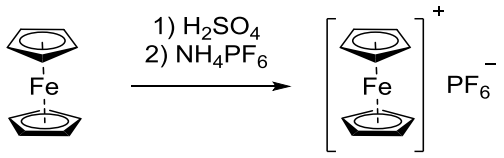

Scheme 15. Synthesis of **Fc^+**.[13]

$FeCp_2$ (1 eq, 1.61 mmol, 300 mg) was dissolved in conc. H_2SO_4 (2 mL) by stirring the mixture during 10 min into a beaker. Then the mixture was allowed to settle for 30 min. Distilled water (10 mL) was added and the solution was filtered. NH_4PF_6 (1 eq, 1.61 mmol, 263 mg) was rapidly added to the solution and a dark blue precipitate was formed. This precipitate was filtered under vacuum and then washed with distilled water (4 x 8 mL) and with diethyl ether (8 mL). After drying it overnight, **Fc^+** (500 mg, 94% yield) was obtained as a dark blue solid. Spectroscopic data as well as the elemental analysis were coincident with the ones previously reported.[13]

^{1}H NMR (400 MHz, $(CD_3)_2CO$) δ = 32.11 (s, $10H_{aromatic}$) ppm.
^{13}C NMR (101 MHz, $(CD_3)_2CO$) δ = 207.7 ($C–H_{aromatic}$) ppm.
^{19}F NMR (376 MHz, $(CD_3)_2CO$) δ = −78.7 (d, J_{F-P} = 710 Hz, PF_6) ppm.
Anal. calcd. for $C_{10}H_{10}FePF_6$: C, 36.3; H, 3.0. **Found:** C, 36.3; H, 3.1.

6.5. Synthesis of $(P,P)_3$-Me.

1,3,5-Triiodomesitylene

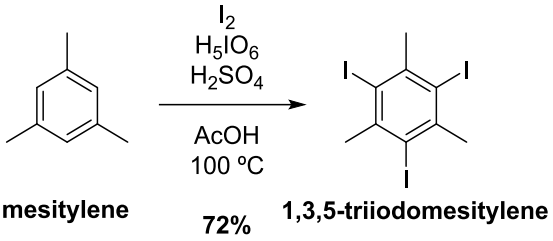

Scheme 16. Synthesis of 1,3,5-triiodomesitylene.[14]

Mesitylene (1 eq, 25 mmol, 3 g), I_2 (1.2 eq, 30 mmol, 7.6 g), periodic acid (60 mol%, 15 mmol, 3.44 g), and sulfuric acid (1 mL) were dissolved in acetic acid (25 mL) in a round bottom flask and heated at 100 °C for 7 days. The mixture was treated with distilled water and the formed brown solid was filtered off and redissolved in ethyl acetate. The solution was washed with distilled water and with sat. aq. $NaHSO_3$. Evaporation of the solvent gave a beige solid that was recrystallized from hot benzene to give the 1,3,5-triiodomesitylene (8.96 g, 72%) as a white crystalline solid. Both NMR spectroscopic data and melting point are in good agreement with the previously reported data.[14]

^{1}H NMR (400 MHz, $(CDCl_3)$ δ = 3.01 (s, $9H_{aromatic}$) ppm.
m.p. = 208 °C (Lit. 206 °C)

(*P,P,P*)-**2,2',2''-((2,4,6-Trimethylbenzene-1,3,5-triyl)tris(3,5-di-tert-butylhepta-3,4-dien-1,6-diyne-7,1-diyl))tris(propan-2-ol)** (**(***P,P,P*)-**2Me)**

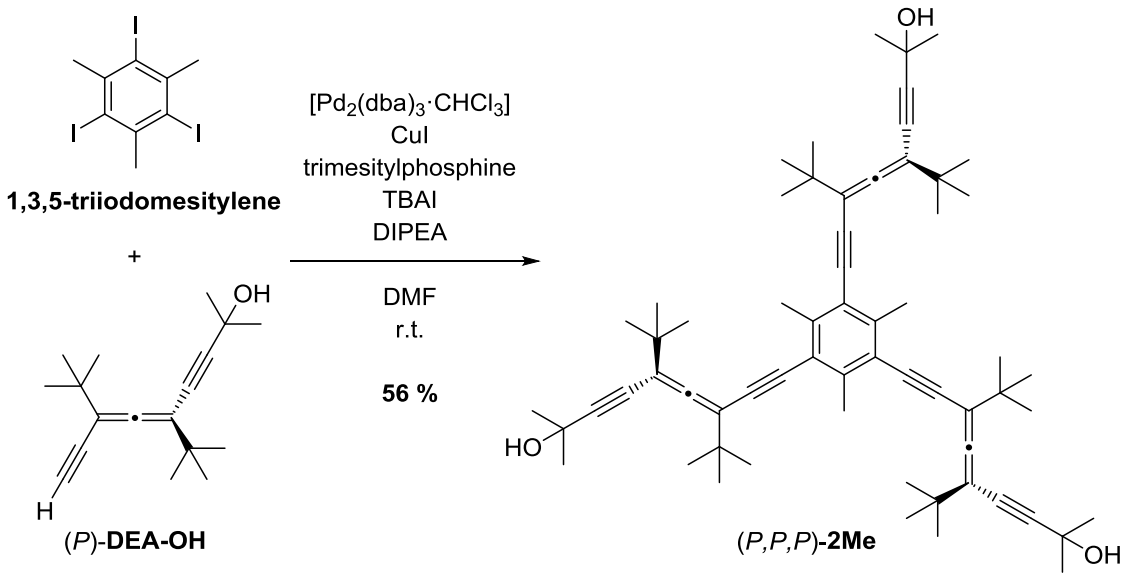

Scheme 17. Synthetic scheme to (*P,P,P*)-**2Me**.

$[Pd_2(dba)_3{\cdot}CHCl_3]$ (12 mol%, 0.0128 mmol, 13.4 mg), purified CuI (90 mol%, 0.0975 mmol, 18.6 mg), 1,3,5-triiodomesitylene (1 eq, 0.108 mmol, 49.3 mg), TBAI (9 eq, 0.9735 mmol, 359.4 mg), trimesitylphosphine (90 mol%, 0.0975 mmol, 37.8 mg), DIPEA (15 eq, 1.622 mmol, 282 µL), and distilled DMF (7 mL) were consecutively added to a flamed Schlenk flask. The yellow solution was sparged with N_2 and finally two solutions of (*P*)-**DEA-OH** (1^{st} addition: 3 eq, 0.569 mmol, 147 mg) (2^{nd} addition, after 20 h: 1 eq, 0.189 mmol, 49 mg) were added at −8 °C *via* cannula in DMF (5 mL). The reaction run for 20 h at r.t. The reaction mixture was treated with saturated aq. sat. NH_4Cl solution, then sat. aq. KCN solution, followed by 1.5 M HCl solution and last distilled water. Then, it was extracted with DCM and dried over anh. Na_2SO_4, being the solvent removed under reduced pressure. Purification by FC (SiO_2, hexane:EtOAc 20%) gave (*P,P,P*)-**2Me** (0.19 mmol, 95 mg, 56%) and allene homodimer (0.094 mmol, 48 mg, 34%).

Previous conditions employing a less reactive Pd catalyst such as $[PdCl_2(PPh_3)_2]$ in combination with CuI and Et_3N gave rise to the tricoupled product (*P,P,P*)-**2Me** (21%) together with allene homodimer and mono- and dicoupled products as discussed in **Chapter 4**. Also with a less hindered phosphine such as tri(o-tolyl)phosphine in combination with $[PdCl_2(PPh_3)_2]$, CuI, TBAI, and DIPEA in DMF, the result was the same. The spectroscopic data of the mono- and dicoupled products are also reported.

(*M*)-**5,7-Di-*tert*-butyl-9-(3,5-diiodo-2,4,6-trimethylphenyl)-2-methylnona-5,6-dien-3,8-diyn-2-ol ((*M*)-MC-2Me)**

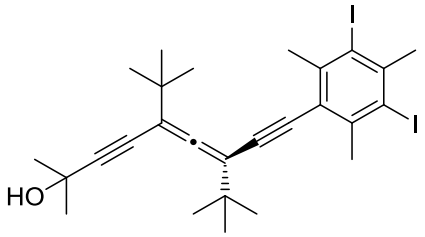

(*M*)-**MC-2Me**

Figure 30. Structure of (*M*)-**MC-2Me**.

^{1}H NMR (400 MHz, $CDCl_3$) δ = 2.96 (s, 3H, Me_{ar}), 2.68 (s, 6H, Me_{ar}), 1.98 (s, 1H, -OH), 1.57 (s, 6H, $-CMe_2OH$), 1.20 (s, 9H, ^{t}Bu), 1.14 (s, 9H, ^{t}Bu) ppm.

^{13}C NMR (101 MHz, $CDCl_3$) δ = 211.6 ($C_{cumullenic}$), 143.7, 143.4, 121.3, 103.74 ($C_{aromatic}$), 103.68, 102.8, 97.5, 91.7, 91.3, 75.8 ($C_{alkynes}$+C_{allene}), 65.9 ($C_{cuaternary}$ $-\underline{C}Me_2OH$), 39.0 (Me_{ar}), 35.8, 35.68 ($C_{cuaternary}$ ^{t}Bu), 31.65 ($-C\underline{Me}_2OH$), 29.7 (Me_{ar}), 29.3, 29.1 (Me ^{t}Bu) ppm.

IR ($CHCl_3$) ν = 3356 (m, br, str O–H), 2963 (s, str $C_{aromatic}$–H), 2929, 2902, 2865 (w, str $C_{aliphatic}$–H), 2199 (w, str C_{alkyne}ΞC_{alkyne}), 1925 (very w, C_{allene}=C_{allene}), 1716, 1508 (s, str $C_{aromatic}$=$C_{aromatic}$) cm^{-1}

HR-ESI-MS *m/z* (%): $[M+Na]^+$ calcd. for $^{12}C_{27}{}^{1}H_{34}{}^{127}I_2{}^{23}Na{}^{16}O$ 651.05912, found: 651.05986 (100).

UV/Vis ($CHCl_3$) λ_{max} (nm): 302, 287, 274 (sh.), 247.

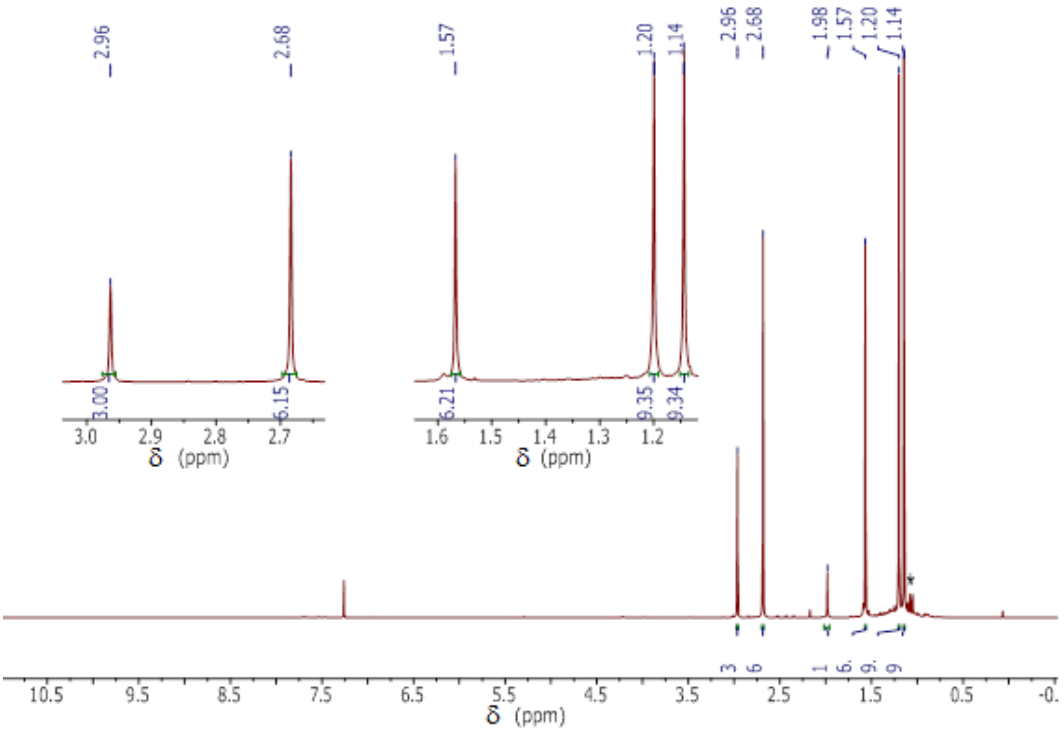

Figure 31. ^{1}H NMR spectrum of (*M*)-**MC-2Me**.

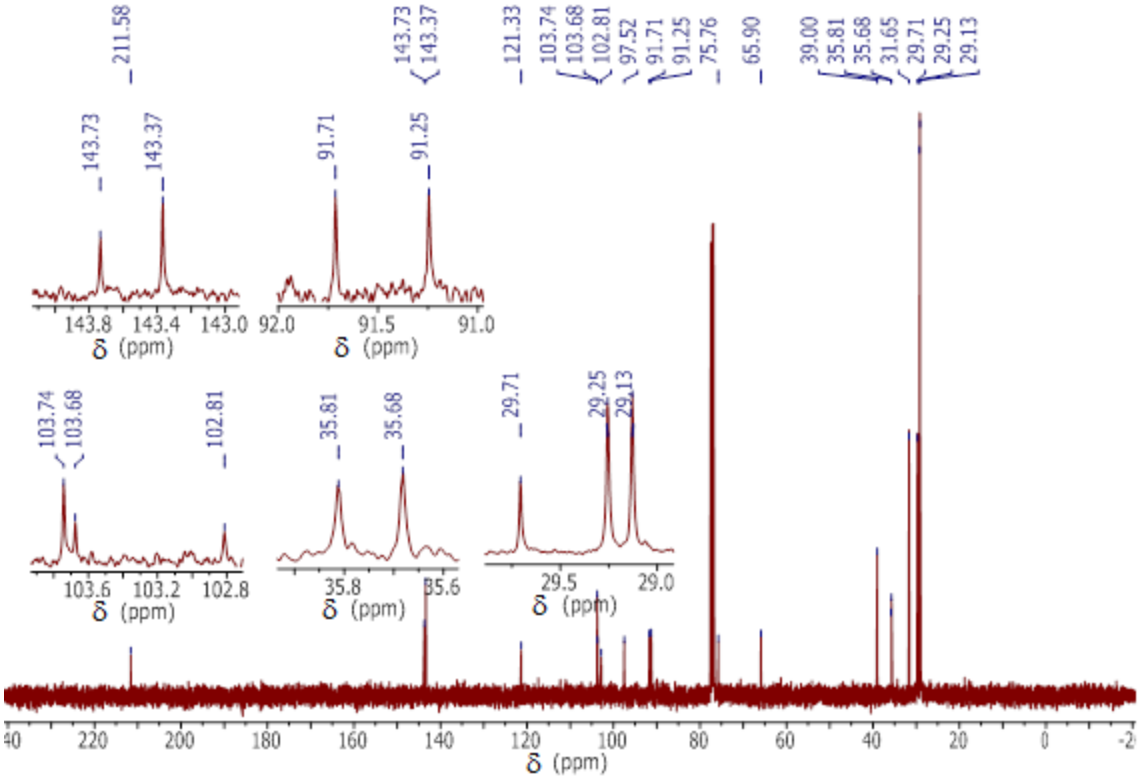

Figure 32. ^{13}C NMR spectrum of (*M*)-**MC-2Me**

.

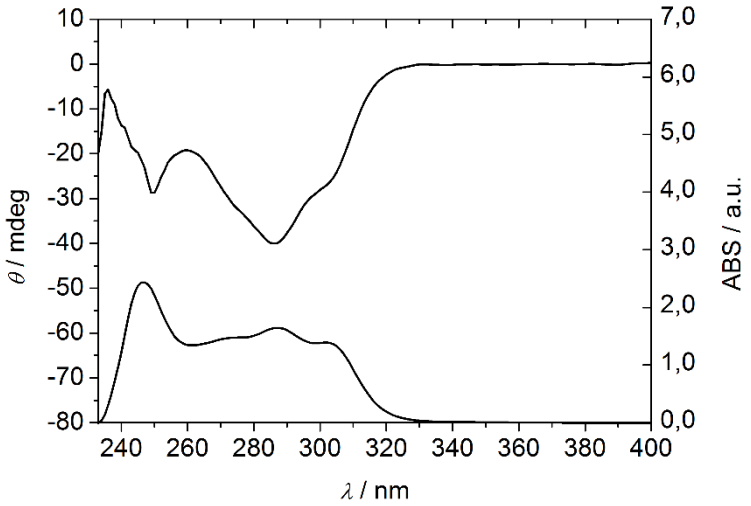

Figure 33. ECD (top) and UV/Vis (bottom) spectra of (*M*)-**MC-2Me**.

(*M,M*)-**9,9'-(5-iodo-2,4,6-trimethyl-1,3-phenylene)bis(5,7-di-tert-butyl-2-methylnona-5,6-dien-3,8-diyn-2-ol)** (**(***M,M*)-**DC-2Me)**.

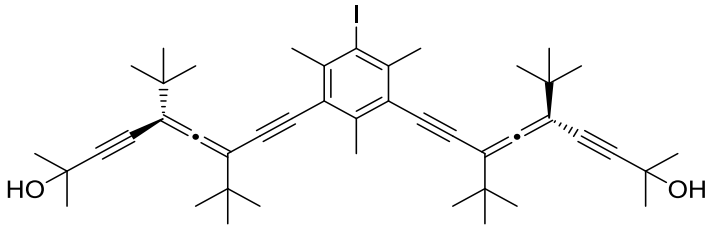

(*M,M*)-**DC-2Me**

Figure 34. Structure of (*M,M*)-**DC-2Me**.

^{1}H NMR (400 MHz, $CDCl_3$) δ = 2.69 (s, 6H, Me_{ar}), 2.54 (s, 3H, Me_{ar}), 2.02 (s, 2H, -O–H), 1.57 (s, 12H, -$\underline{Me_2}$OH), 1.20 (s, 18H, ^{t}Bu), 1.15 (s, 18H, ^{t}Bu) ppm.

^{13}C NMR (101 MHz, $CDCl_3$) δ = 211.5 ($C_{cumullenic}$), 143.0, 141.7, 121.6, 105.5 ($C_{aromatic}$), 103.8, 102.7, 97.4, 91.6, 90.7, 75.9 ($C_{alkyne+allene}$), 65.9 (-$\underline{C}Me_2OH$), 35.8, 35.7 ($C_{cuaternary}$ ^{t}Bu), 31.7 (-$\underline{Me_2}$OH), 29.4 (Me_{ar}), 29.3, 29.1 (^{t}Bu), 20.3 (Me_{ar}) ppm.

IR ($CHCl_3$) ν = 3358 (m, br, str O–H), 2964 (s, str $C_{aromatic}$–H), 2930, 2902, 2866, (w, str $C_{aliphatic}$–H), 2225 (w, str C_{alkyne}ΞC_{alkyne}), 1925 (very w, C_{allene}=C_{allene}), 1764, 1588 (s, str $C_{aromatic}$=$C_{aromatic}$) cm^{-1}

HR-ESI-MS *m/z* (%): $[M+Na]^+$ calcd. for $^{12}C_{45}{}^{1}H_{59}{}^{127}I^{23}Na^{16}O_2$ 781.34520, found: 781.34542 (100).

UV/Vis ($CHCl_3$) λ_{max} (nm): 301, 286.

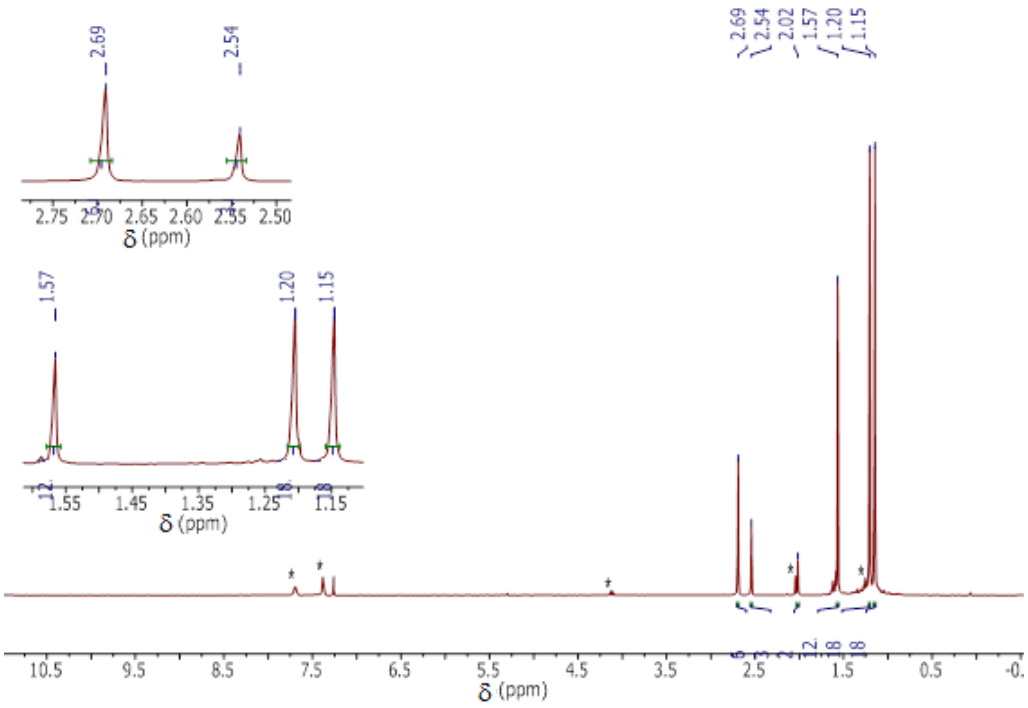

Figure 35. ^{1}H NMR spectrum of (*M,M*)-**DC-2Me**.

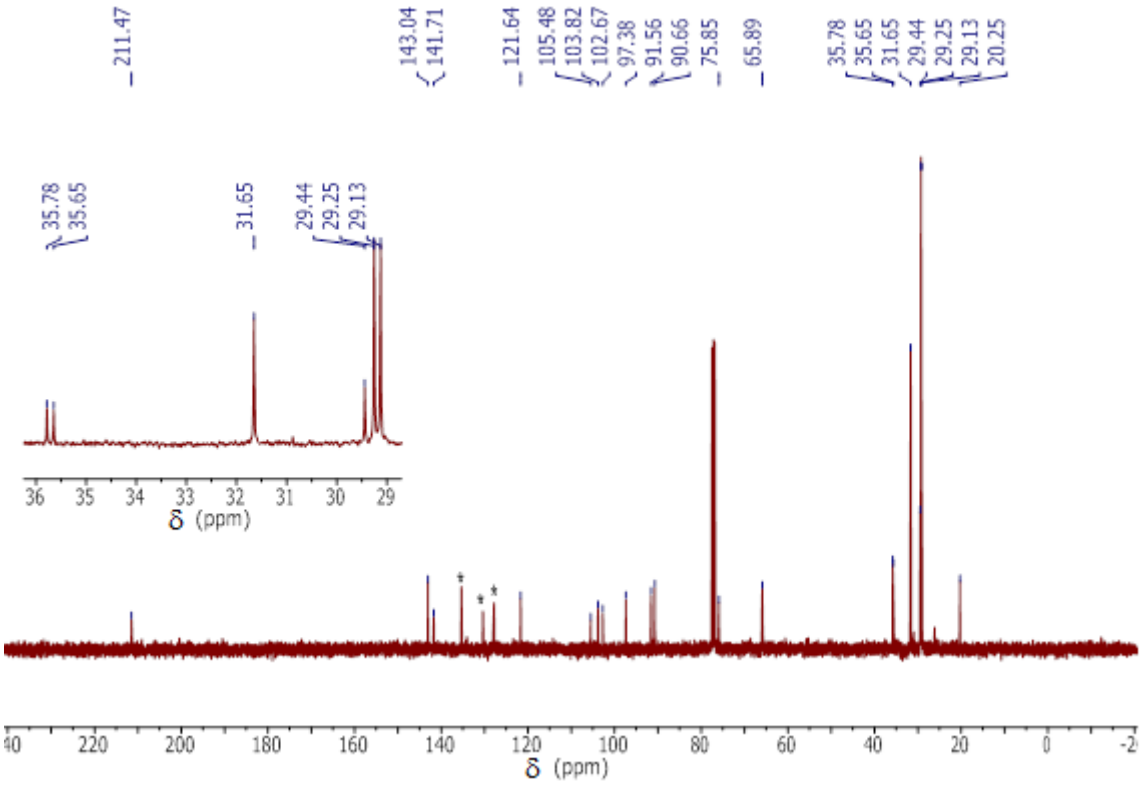

Figure 36. ^{13}C NMR spectrum of (*M,M*)-**DC-2Me**.

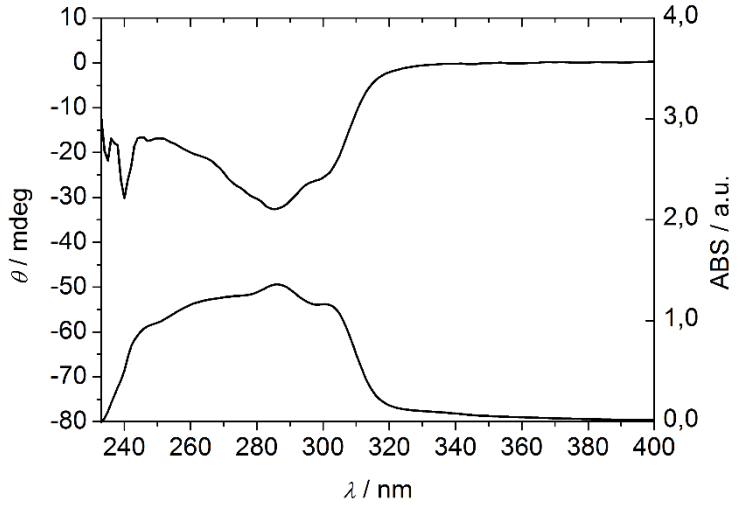

Figure 37. ECD (top) and UV/Vis (bottom) spectra of (*M,M*)-**DC-2Me**.

Data of (*P,P,P*)-**2Me**

^{1}H NMR (400 MHz, $CDCl_3$) δ = 2.57 (s, 9H, Me_{ar}), 2.03 (s, 3H, -OH), 1.56 (s, 18H, -C$\underline{Me}_2$OH), 1.21 (s, 27H, ^{t}Bu), 1.15 (s, 27H, ^{t}Bu) ppm.

^{13}C NMR (101 MHz, $CDCl_3$) δ = 211.4 ($C_{cumullenic}$), 141.6, 121.7 ($C_{aromatic}$), 104.0, 102.5, 97.2, 91.2, 90.3, 76.0 ($C_{alkyne+allene}$), 65.9 (-$\underline{C}Me_2$OH), 35.8, 35.6 ($C_{cuarternary}$ ^{t}Bu), 31.7 (-C$\underline{Me}_2$OH), 29.3, 29.1 (Me ^{t}Bu), 20.4 (Me_{ar}) ppm.

IR ($CHCl_3$) ν = 3360 (m, br, str O–H), 2964 (s, str $C_{aromatic}$–H), 2930, 2903, 2867, 2743 (w, str $C_{aliphatic}$–H), 2219 (w, str C_{alkyne}ΞC_{alkyne}), 1925 (very w, C_{allene}=C_{allene}), 1715, 1590 (s, str $C_{aromatic}$=$C_{aromatic}$) cm^{-1}.

HR-ESI-MS *m/z* (%): $[M+Na]^+$ calcd. for $^{12}C_{63}{}^{1}H_{84}{}^{23}Na^{16}O_3$ 911.63127, found: 911.63142 (100).

UV/Vis ($CHCl_3$) λ_{max} (nm): 303, 288, 274 (sh.), 249.

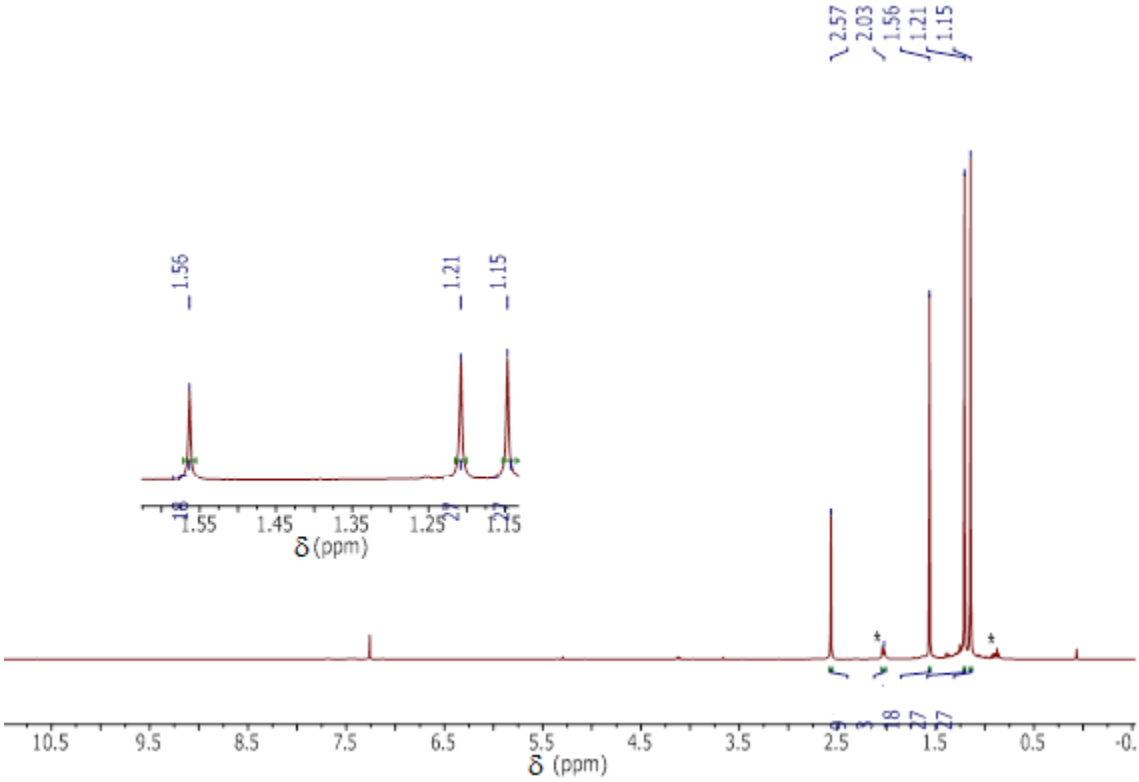

Figure 38. ^{1}H NMR spectrum of (*P,P,P*)-**2Me**.

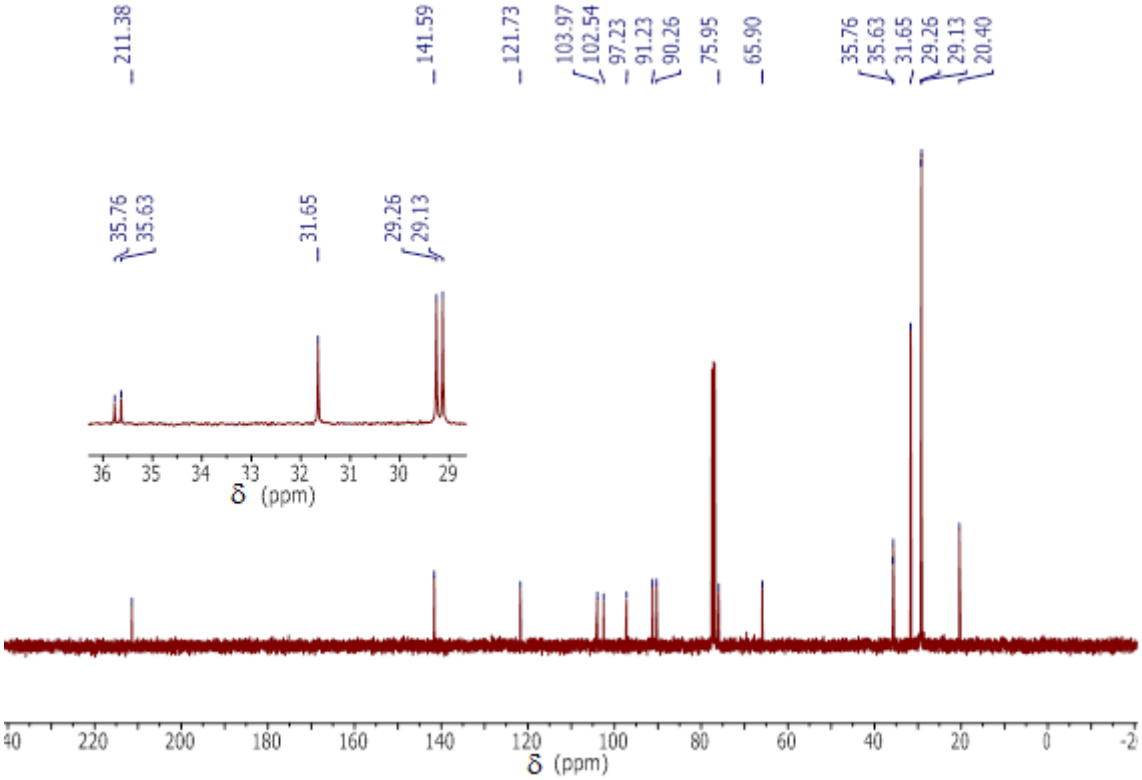

Figure 39. ^{13}C NMR spectrum of (*P,P,P*)-**2Me**.

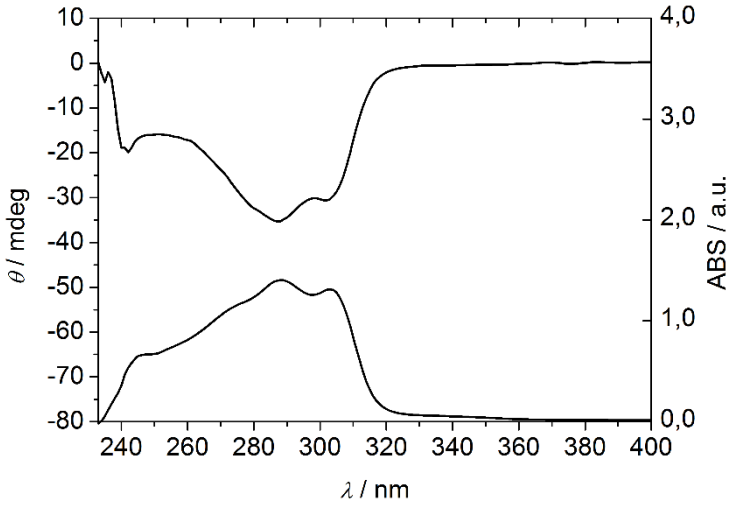

Figure 40. ECD (top) and UV/Vis (bottom) spectra of (*M,M,M*)-**2Me**.

(*P,P,P*)-**1,3,5-Tris(3,5-di-tert-butylhepta-3,4-dien-1,6-diyn-1-yl)-2,4,6-trimethylbenzene (**(*P,P,P*)-**3Me).**

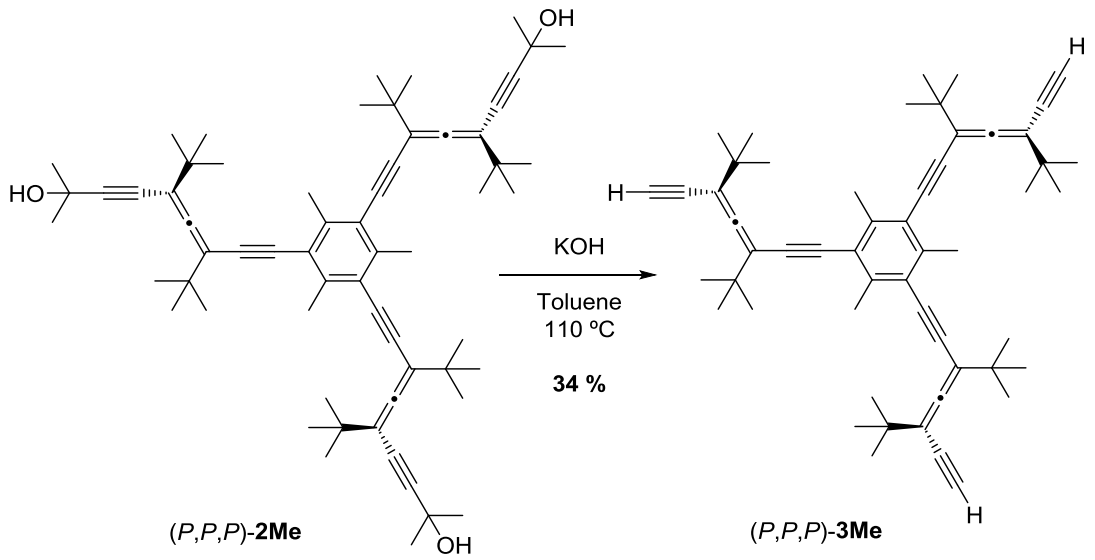

Scheme 18. Synthesis of (*P,P,P*)-**3Me**.[15]

In a round bottom flask powdered flamed KOH (114 eq, 8.91 mmol, 500 mg) was placed with dry toluene (3 mL) and over this suspension a solution of (*P,P,P*)-**2Me** (1eq, 0.05 mmol, 70 mg) in dry toluene (3 mL) was poured *via* cannula. This mixture was stirred and refluxed at 90 °C for 24 h. Toluene was removed under reduced pressure and the mixture was treated with distilled water and extracted first with hexane and then with DCM. The combined organic phases were dried over anh. Na_2SO_4 and the solvent was removed under reduced pressure. FC (SiO_2, hexane:DCM 10%) gave (*P,P,P*)-**3Me** (19 mg, 34%) as a yellow oil.

^{1}H NMR (400 MHz, $CDCl_3$) δ = 3.01 (s, 3H, H_{alkyne}), 2.56 (s, 9H, Me_{ar}), 1.22 (s, 27H, ^{t}Bu), 1.17 (s, 27H, ^{t}Bu) ppm.

^{13}C NMR (101 MHz, $CDCl_3$) δ = 212.2 ($C_{cumullenic}$), 141.7, 121.7 ($C_{aromatic}$), 104.5, 102.2, 90.9, 90.5, 80.5, 77.7 ($C_{alkyne+allene}$), 35.7, 35.5 ($C_{cuaternary}$ ^{t}Bu), 29.2, 29.0 (^{t}Bu), 20.4 (Me_{ar}) ppm.

IR ($CHCl_3$) ν = 3312 (s, str C_{alkyne}–H), 2964 (s, str $C_{aromatic}$–H), 2928, 2867 (w, str $C_{aliphatic}$–H), 2360 (w, str C_{alkyne}ΞC_{alkyne}), 1928 (w, str C_{allene}=C_{allene}), 1734 (s, str $C_{aromatic}$=$C_{aromatic}$) cm^{-1}.

HR-ESI-MS *m/z* (%): $[M+H]^+$ calcd. for $^{12}C_{54}{}^1H_{67}{}^+$ 715.52373, found: 715.52449 (100).

UV/Vis ($CHCl_3$) λ_{max} (nm): 304, 289, 274 (sh.), 247.

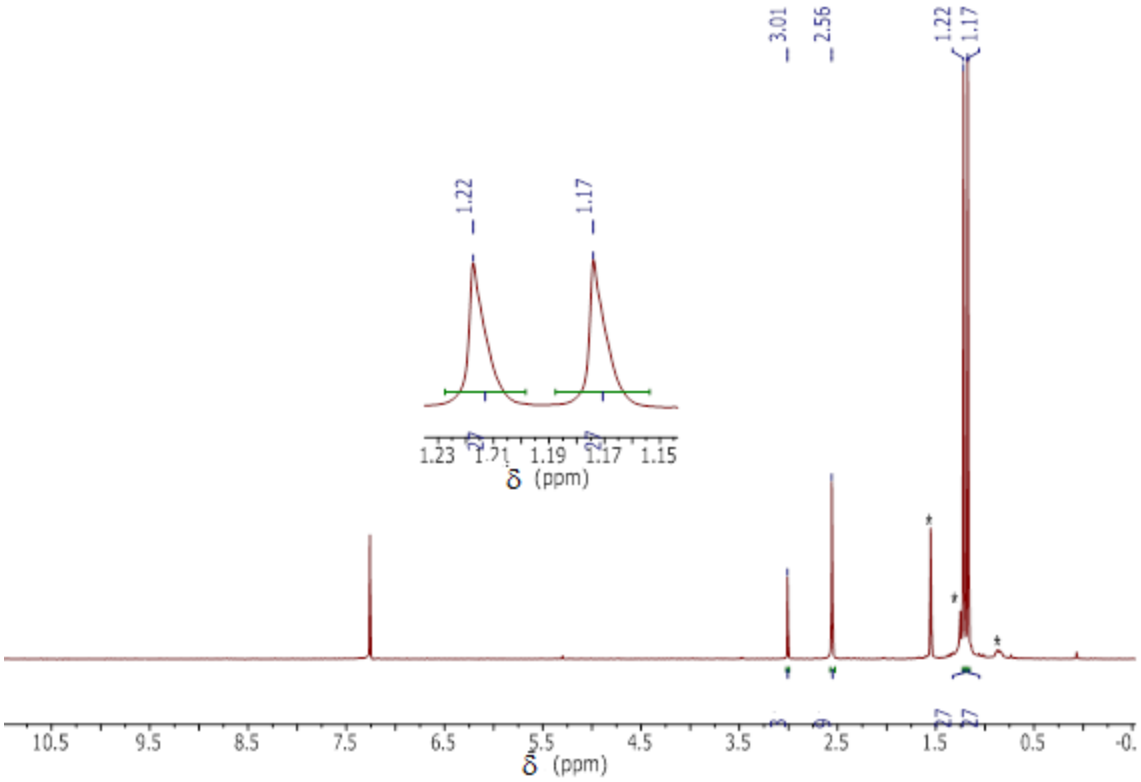

Figure 41. ^{1}H NMR spectrum of (*P,P,P*)-**3Me**.

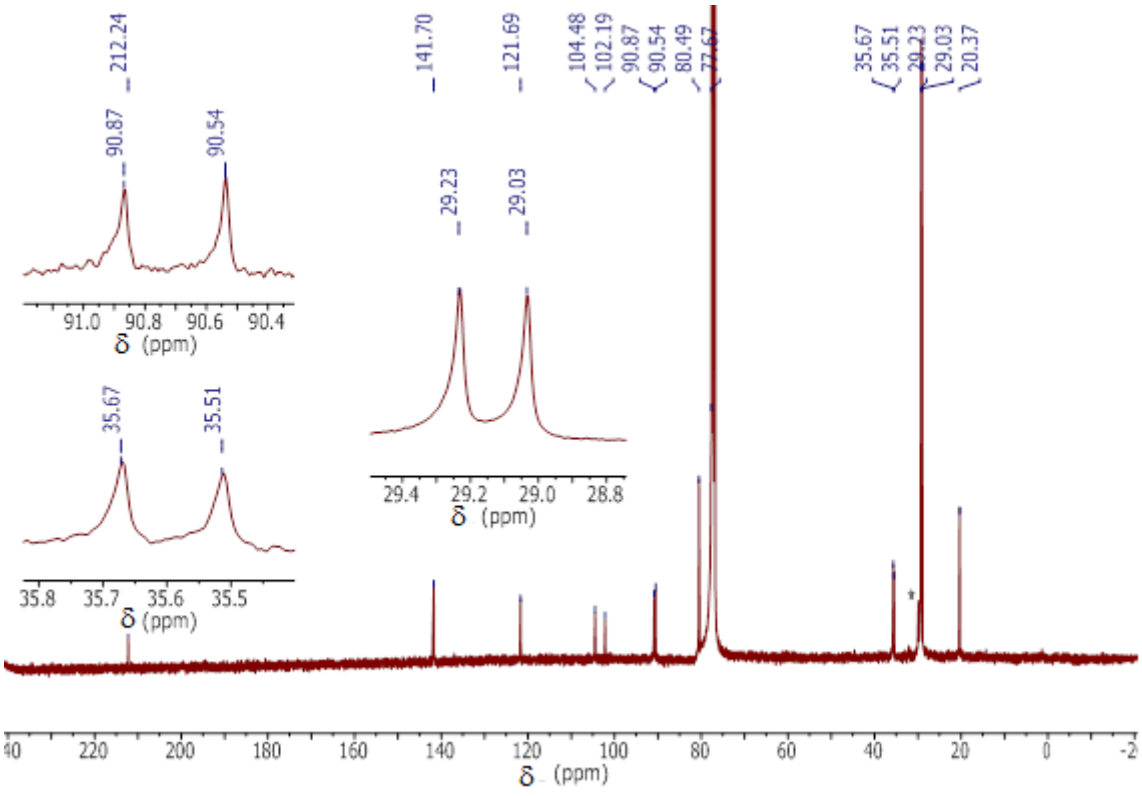

Figure 42. ^{13}C NMR spectrum of (*P,P,P*)-**3Me**.

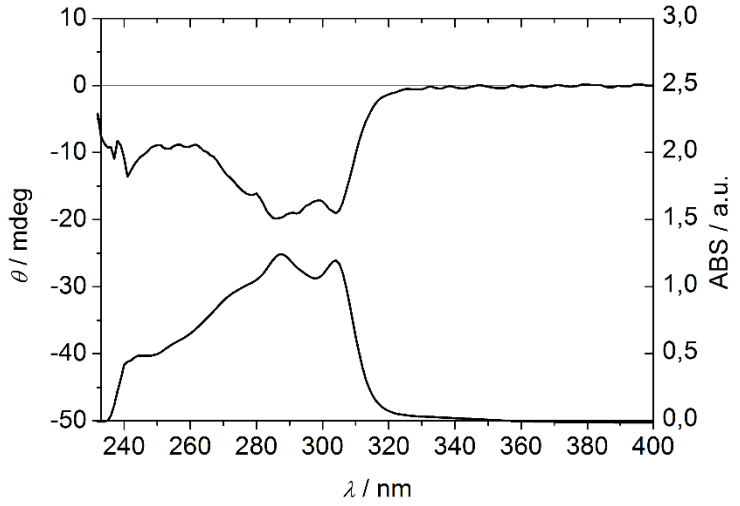

Figure 43. ECD (top) and UV/Vis (bottom) spectra of (*M,M,M*)-**3Me**.

(*P,P*)$_3$-**4,6,11,13,19,21,26,28,33,35,40,42-Dodeca-tert-butyl-1,16-(1,3,5)-2,4,6-trimethylbenzenebicyclotetratetracontaphane-4,5,11,12,19,20,26,27,33,34,40,41-dodecaen-2,7,9,14,17,22,24,29,31,36,38,43-dodecayne ((*P,P*)$_3$-1Me).**

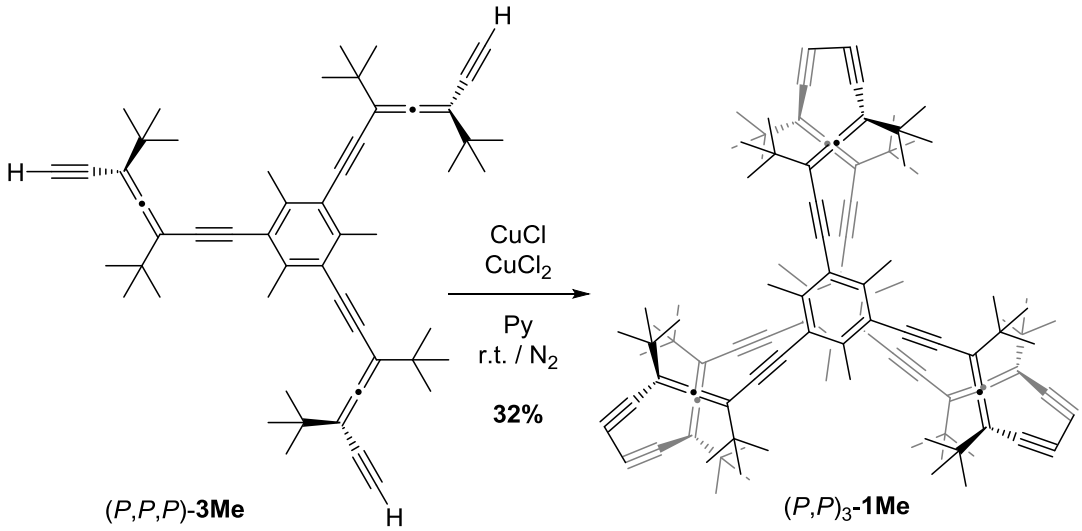

Scheme 19. Synthesis of (*P,P*)$_3$-**1Me**.

Two solutions were prepared:

Solution ***a***: CuCl (75 eq, 0.4615 mmol, 46 mg) and $CuCl_2$ (11 eq, 0.0682 mmol, 9.2 mg) were placed in a round-bottom flask under N_2 atmosphere, dissolved with dry pyridine (5 mL) and bubbled with N_2 over 30 min.

Solution ***b***: trisdeprotected product (*P,P,P*)-**3Me** (1 eq, 0.0062 mmol, 4.4 mg) was dissolved in dry pyridine (7 mL) and bubbled with N_2 over 30 min.

Solution ***b*** was dropwise added (flux = 1mL·h^{-1}) over solution ***a*** under N_2 at r.t. After 3 days, the solvent was removed under reduced pressure and the remaining solid was dissolved in DCM and washed with sat. aq. NH_4Cl solution. The combined organic phases were dried over anh. Na_2SO_4 and evaporated to dryness. The obtained white solid was purified by FC (SiO_2, hexane:DCM 2%) affording the COHC (*P,P*)$_3$-**1Me** (1.4mg, 32%) as a white solid.

^{1}H NMR (400 MHz, $CDCl_3$) δ = 2.45 (s, 18H, Me_{ar}), 1.21 (s, 54H, ^{t}Bu), 1.18 (s, 54H, ^{t}Bu) ppm.

^{13}C NMR (101 MHz, $CDCl_3$) δ = 215.2 ($C_{cumulenic}$), 141.4, 121.6 ($C_{aromatic}$), 105.1, 102.9, 91.5, 90.6, 77.4, 75.7 ($C_{alkynes+allenes}$), 35.64, 35.60 ($C_{cuaternary}$), 29.32, 29.29 (^{t}Bu), 20.2 (Me_{ar}) ppm.

IR ($CHCl_3$) ν = 2960 (s, str $C_{aromatic}$–H), 2923, 2852 (w, str $C_{aliphatic}$–H), 1918 (w, str C_{allene}=C_{allene}), 1740 (s, str $C_{aromatic}$=$C_{aromatic}$) cm^{-1}.

HR-MALDI-MS *m/z* (%): $[M+H]^+$ calcd. for $^{12}C_{108}{}^1H_{127}{}^+$ 1424.996621, found: 1424.995788 (100).

UV/Vis ($CHCl_3$) λ_{max} (nm): 309 (sh.), 289, 249. (Hexane) λ_{max} (nm): 305 (sh.) 288, 245, 200.

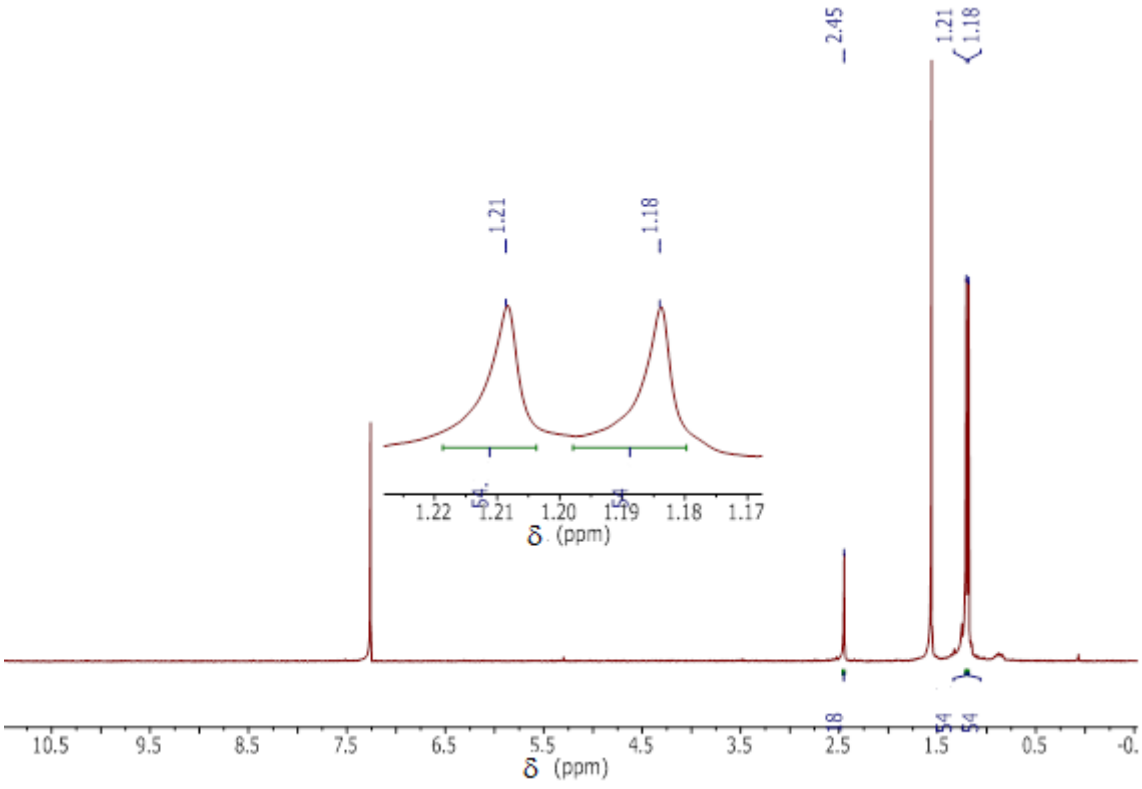

Figure 44. ^{1}H NMR spectrum of (*P,P*)$_3$-**1Me**.

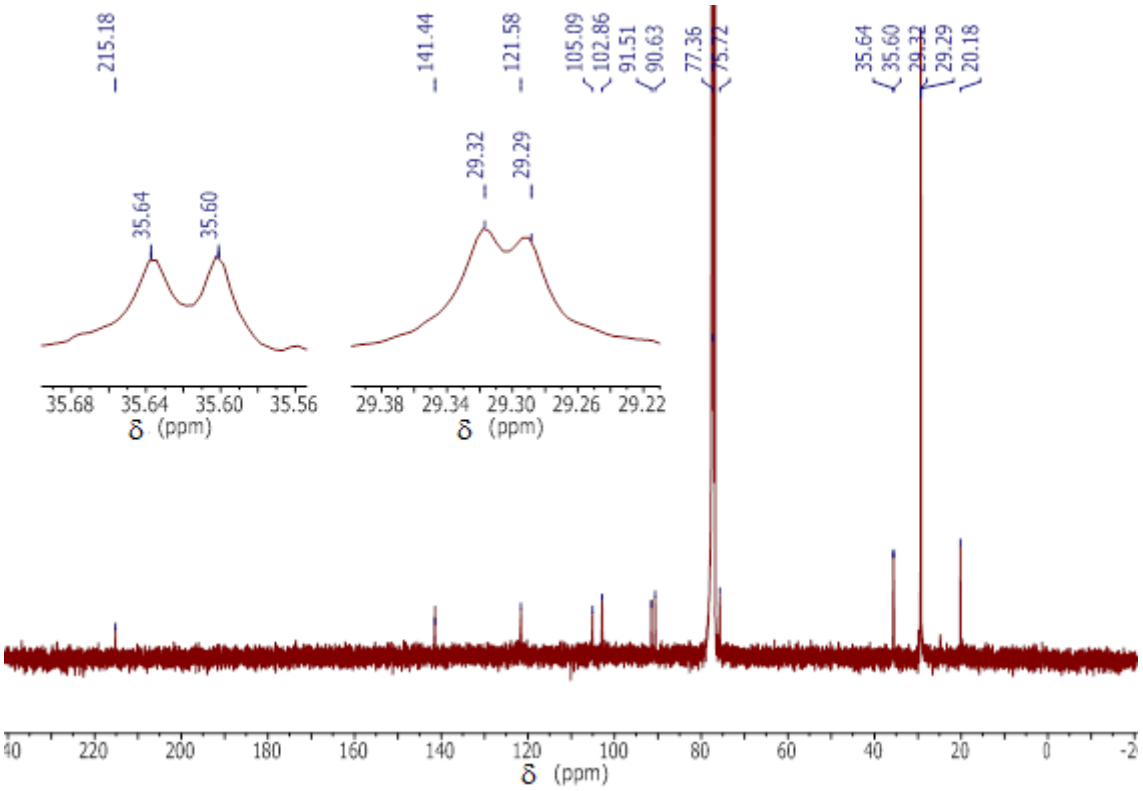

Figure 45. ^{13}C NMR spectrum of $(P,P)_3$-**1Me**.

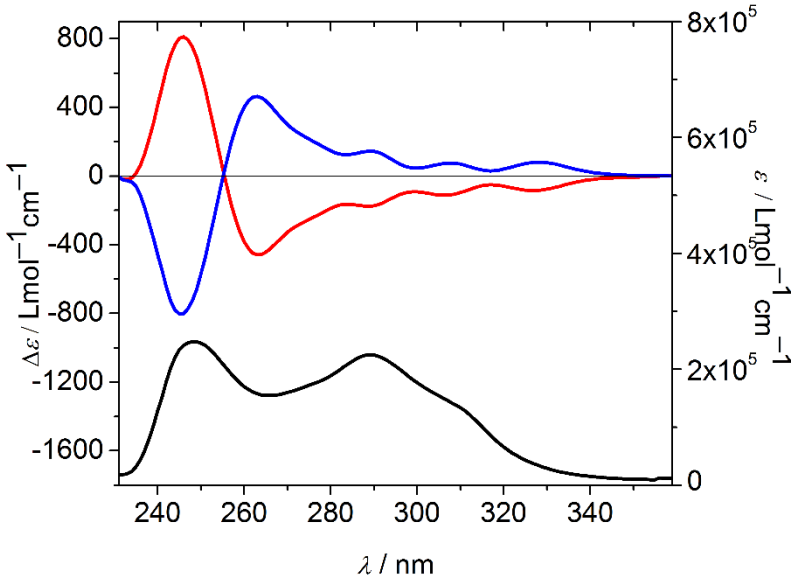

Figure 46. ECD (top) and UV/Vis (bottom) spectra of $(P,P)_3$-**1Me** (red) and $(M,M)_3$-**1Me** (blue) in hexane.

In some cases, the homocoupling reaction rendered traces of a product different to $(P,P)_3$-**1Me** $(M,M)_3$-**1Me**, derived from the coupling between two tripods, followed by the intramolecular branch closure, which gave a shackles-like structure labelled as $(P)_6$-**7**. This shackles-like molecule presented a well-defined ^{1}H NMR spectrum and was found to give the same HR-MALDI-MS as $(P,P)_3$/$(M,M)_3$-**1Me**, as expected.

^{1}H NMR (400 MHz, $CDCl_3$) δ = 2.74 (s, 6H, $Me_{aromatic}$), 2.52 (s, 12H, $Me_{aromatic}$), 1.21 (s, 18H, ^{t}Bu), 1.19 (s, 36H, ^{t}Bu), 1.18 (s, 18H, ^{t}Bu), 1.15 (s, 36H, ^{t}Bu) ppm.

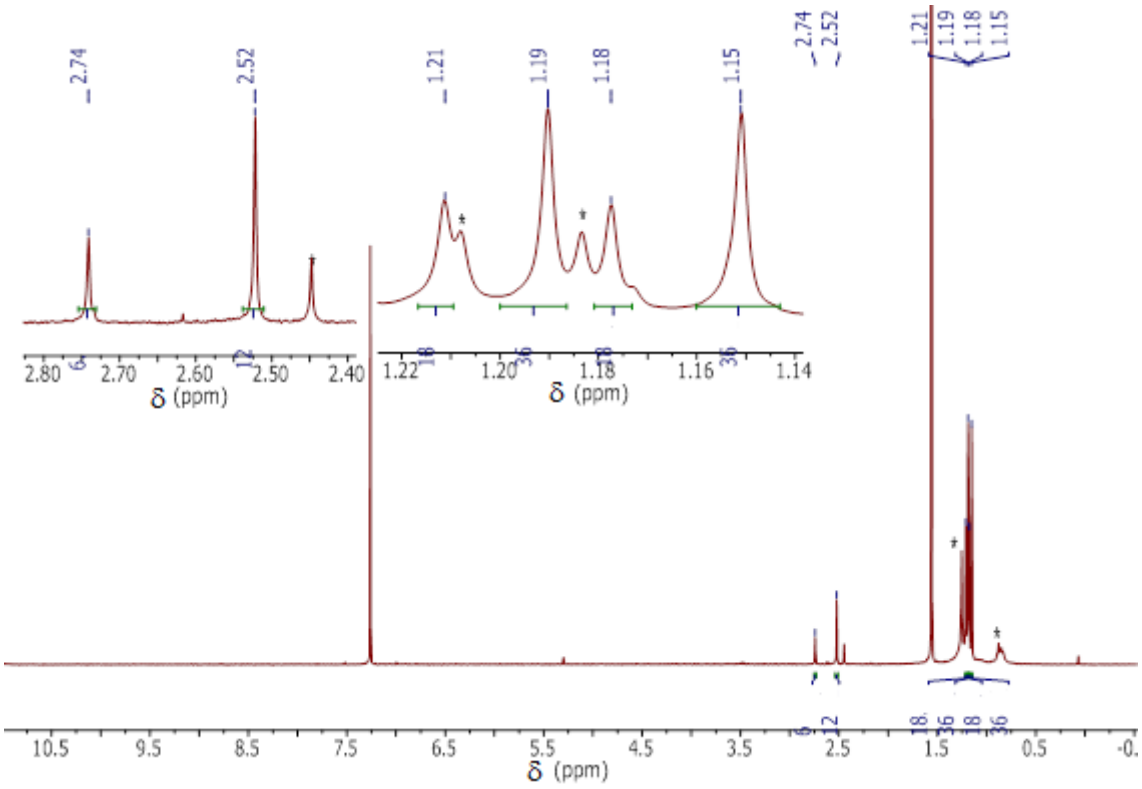

Figure 47. ^{1}H NMR spectrum of $(P)_6$-**7**. * $(P,P)_3$-**1Me** and grease traces.

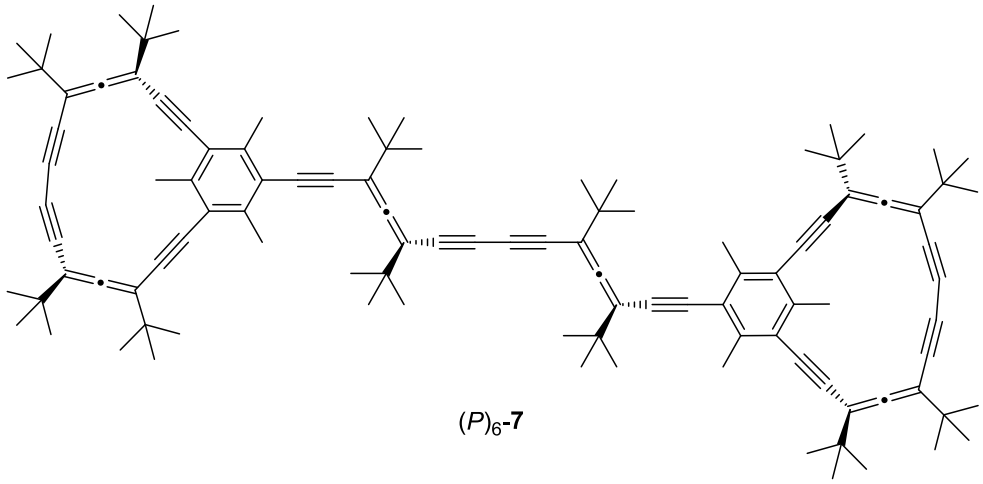

$(P)_6$-**7**

Figure 48. Structure of $(P)_6$-**7**.

6.6. Synthesis of $(P,P)_3$-1F.

((2,4,6-trifluorobenzene-1,3,5-triyl)tris(ethyne-2,1-diyl))tris(trimethylsilane) ($2F'_{TMS}$)

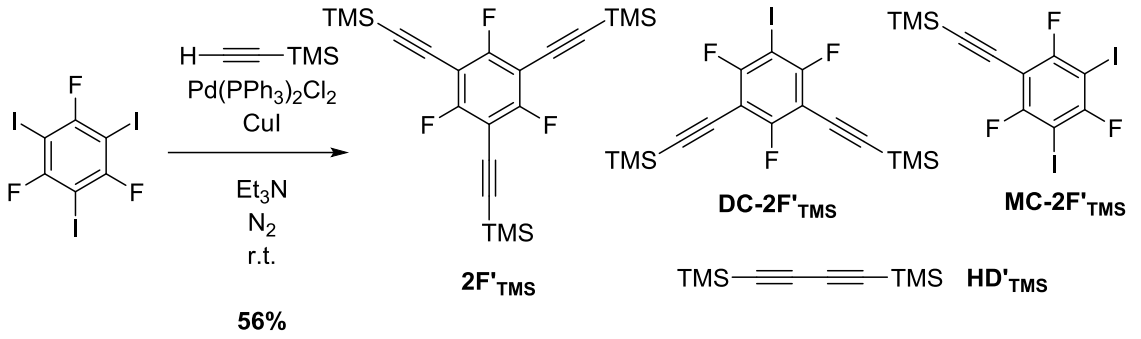

Scheme 20. Synthesis of **$2F'_{TMS}$**.[16]

$[Pd(PPH_3)_2Cl_2]$ (20 mol%, 0.0180 mmol, 13 mg), CuI (10 mol%, 0.0090 mmol, 2 mg), 1,3,5-trifluoro-2,4,6-triodobenzene (1 eq, 0.0900 mmol, 54 mg) and Et_3N (2 mL) were placed in a flamed Schlenk tube and finally TMS-acetylene (3.3 eq, 0.2971 mmol, 42 µl) was added dissolved in Et_3N (2 mL) via cannula. The reaction ran for 22 h at r.t. with stirring. The solvent was removed under reduced pressure and the crude purified by FC (SiO_2, hexane) giving **$2F'_{TMS}$** (21 mg, 56% yield).

^{1}H NMR (400 MHz, CD_2Cl_2) δ = 0.27 (s, $27H_{TMS}$) ppm.

^{19}F NMR (376 MHz, CD_2Cl_2) δ = −100.6 ppm.

^{13}C NMR (101 MHz, CD_2Cl_2) δ = 163.3 (dt, J = 261.5 Hz, J' = 7.6 Hz, $C_{aromatic}$–F), 110.4 ($C_{aromatic}$), 107.4 (C_{alkyne}), 88.7 (C_{alkyne}), -0.4 (C_{TMS}) ppm.

2,2',2''-((2,4,6-trifluorobenzene-1,3,5-triyl)tris(ethyne-2,1-diyl))tris(propan-2-ol) ($2F'_{OH}$)

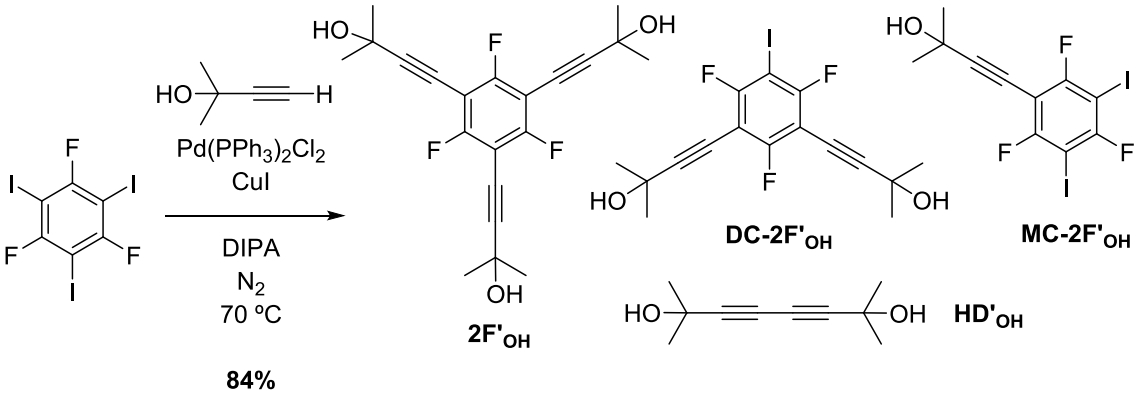

Scheme 21. Synthesis of **$2F'_{OH}$**.

$[Pd(PPH_3)_2Cl_2]$ (6 mol%, 0.0091 mmol, 7 mg), CuI (6 mol%, 0.0091 mmol, 2 mg), 1,3,5-trifluoro-2,4,6-triodobenzene (1 eq, 0.1569 mmol, 80 mg) and DIPA (1 mL) were placed in a flamed Schlenk tube and finally acetonide-acetylene (3.3 eq, 0.5179 mmol, 80 mg) was added dissolved in DIPA (1 mL) via cannula. The reaction ran for 15 h at 70 °C with stirring. The solvent was removed under reduced pressure and the crude purified by FC (SiO_2, hexane:ethylacetate (25%)) giving **2F'$_{OH}$** (50 mg, 84% yield).

^{1}H NMR (400 MHz, Methanol-d_4) δ = 1.57 (s, 18H, 3x-C$\underline{Me_2}$OH) ppm.

^{19}F NMR (376 MHz, Methanol-d_4) δ = −103.6 ppm.

^{13}C NMR (101 MHz, Methanol-d_4) δ = 163.4 (dt, ^{1}J = 259.5 Hz, ^{3}J = 7.6 Hz, $\underline{C}$-F), 106.7 ($C_{aromatic}$), 100.3 (C_{alkyne}), 67.2 (C_{alkyne}), 66.0 ($C_{quaternary}$–$\underline{C}Me_2OH$), 31.3 (-C$\underline{Me_2}$OH) ppm.

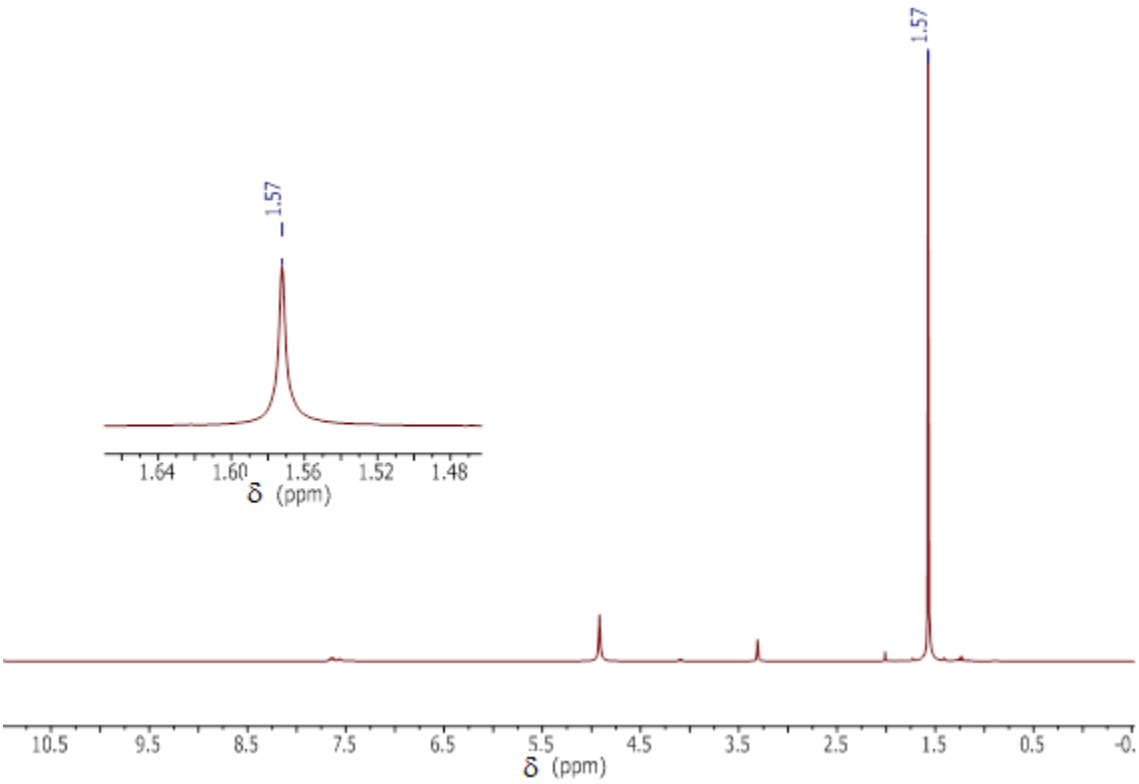

Figure 49. ^{1}H NMR spectrum of **2F'$_{OH}$**.

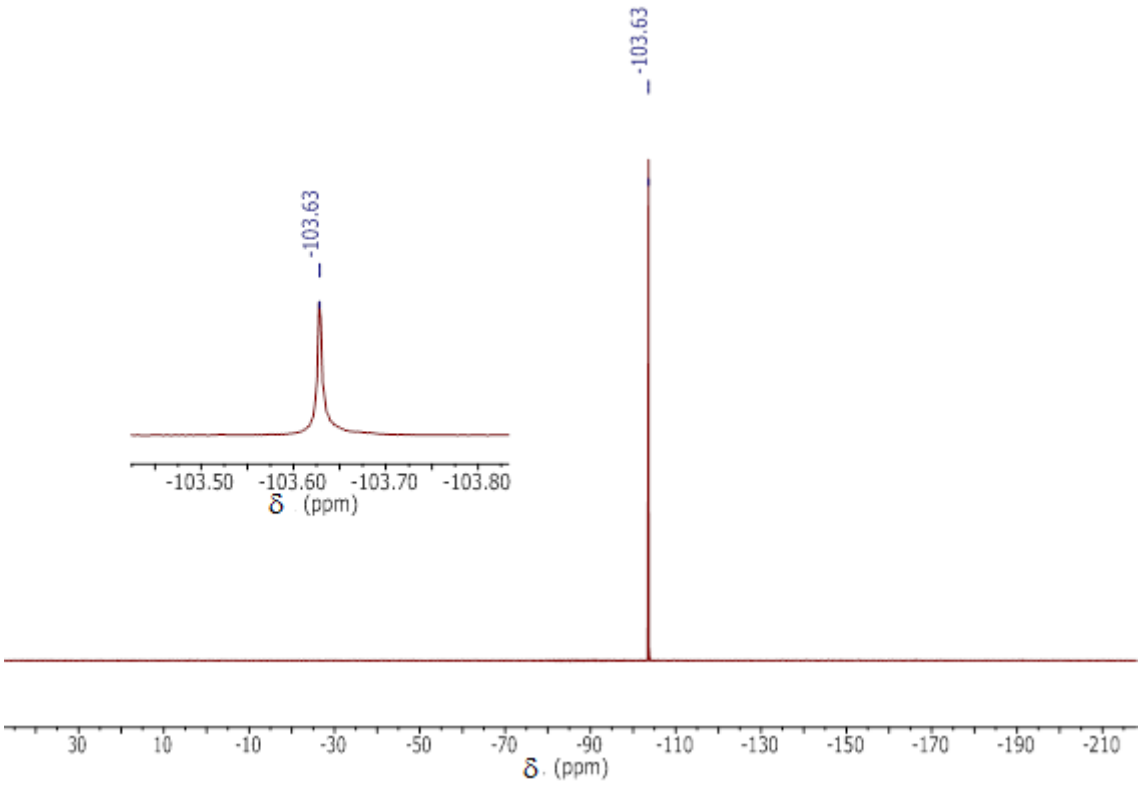

Figure 50. ^{19}F NMR spectrum of **2F'$_{OH}$**.

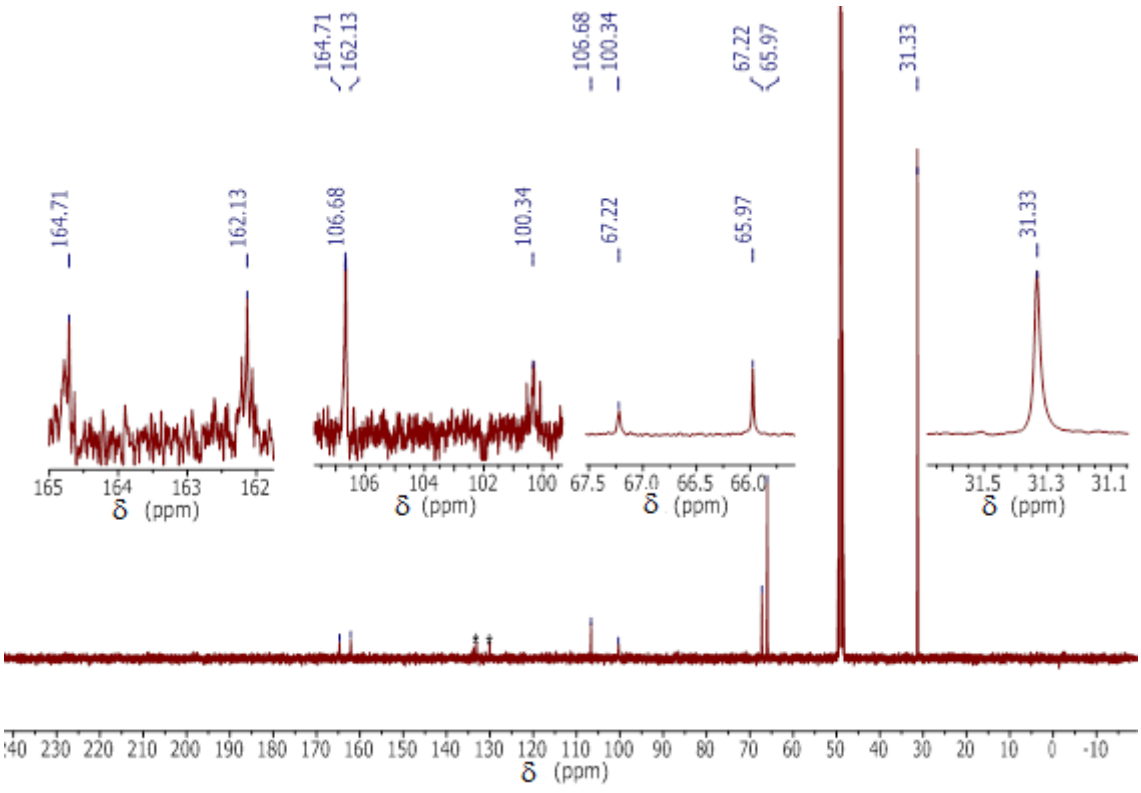

Figure 51. ^{13}C NMR spectrum of **2F'$_{OH}$**. * Traces of phosphines.

1,3,5-triethynyl-2,4,6-trifluorobenzene (3F')

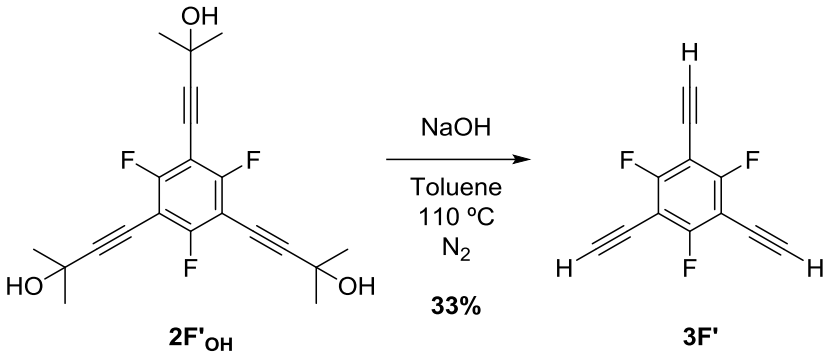

Scheme 22. Synthesis of **3F'**.[17]

Powdered flamed NaOH (4.5 eq, 0.4635 mmol, 19 mg) and **2F'$_{OH}$** (1 eq, 0.1030 mmol, 39 mg) were dissolved in refluxing dry toluene (20 mL) under N_2. The reaction ran for 26 h and it was then treated with distilled water and extracted with dichloromethane. The combined organic phases were evaporated under reduced pressure and then purified by FC (SiO_2, hexane:DCM 5%) affording **3F'** (7 mg, 33%).

^{1}H NMR (400 MHz, $CDCl_3$) δ = 3.53 (s, $3H_{alkyne}$) ppm.

^{19}F NMR (376 MHz, $CDCl_3$) δ = −98.9 (s, $3F_{aromatic}$) ppm.

^{13}C NMR (101 MHz, $CDCl_3$) δ = 164.1 (dt, ^1J = 264.0, ^3J = 7.5 Hz, -C–F), 88.6 (q, J = 3.3 Hz, $C_{aromatic}$), 77.36 (s, C_{alkyne}), 68.39 (s, C_{alkyne}) ppm.

(*P,P,P*)-**2,2',2''-((2,4,6-Trifluorobenzene-1,3,5-triyl)tris(3,5-di-*tert*-butylhepta-3,4-dien-1,6-diyne-7,1-diyl))tris(propan-2-ol) (**(*P,P,P*)-**2F$_{OH}$)**

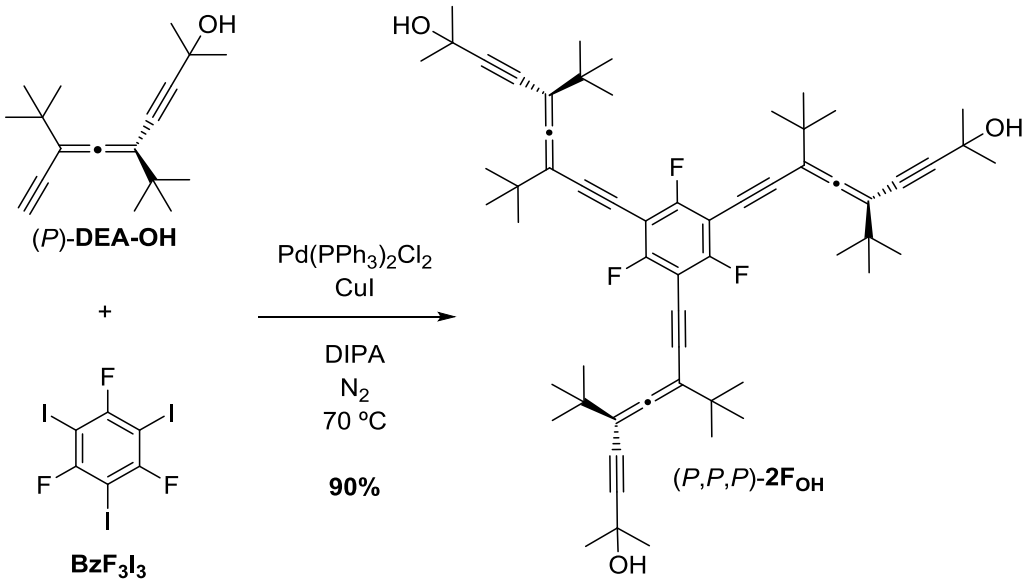

Scheme 23. Synthesis of (*P,P,P*)-**2F$_{OH}$**.

$[Pd(PPH_3)_2Cl_2]$ (6 mol%, 0.0040 mmol, 3 mg), CuI (6 mol%, 0.0040 mmol, 1 mg), 1,3,5-trifluoro-2,4,6-triodobenzene (1 eq, 0.0668 mmol, 34 mg) and DIPA (2 mL) were placed in a flamed Schlenk tube and finally (*P*)-**DEA-OH** (3.3 eq, 0.221 mmol, 57 mg) was added dissolved in DIPA (2 mL) via cannula. The reaction reacted for 21 h at 70 °C with stirring. The solvent was removed under reduced pressure and the crude purified by FC (SiO_2, DCM) giving the homodimer of the (*P*)-**DEA-OH** (6 mg, 10%) and (*P,P,P*)-**2F$_{OH}$** (54 mg, 90% yield).

^{1}H NMR (400 MHz, $CDCl_3$) δ = 2.17 (s, 3H, -OH), 1.56 (s, 18H, -C$\underline{Me_2}$OH), 1.18 (s, 27H, ^{t}Bu), 1.13 (s, 27H, ^{t}Bu) ppm.

^{19}F NMR (376 MHz, $CDCl_3$) δ = −101.0 ppm.

^{13}C NMR (101 MHz, $CDCl_3$) δ = 211.6, 161.7 (dt, *J* = 259.6 Hz, *J'* = 7.5 Hz), 103.5, 102.9, 98.0, 94.1, 77.3, 75.5 ($C_{alkynes+allenes}$), 65.8 ($C_{quaternary}$ –$\underline{C}Me_2OH$), 35.79, 35.77 ($C_{quaternary}$ ^{t}Bu), 31.6 (–C$\underline{Me_2}$OH), 29.1, 29.0 (^{t}Bu) ppm.

UV/Vis ($CHCl_3$) λ_{max} (nm): 298, 282, 269.

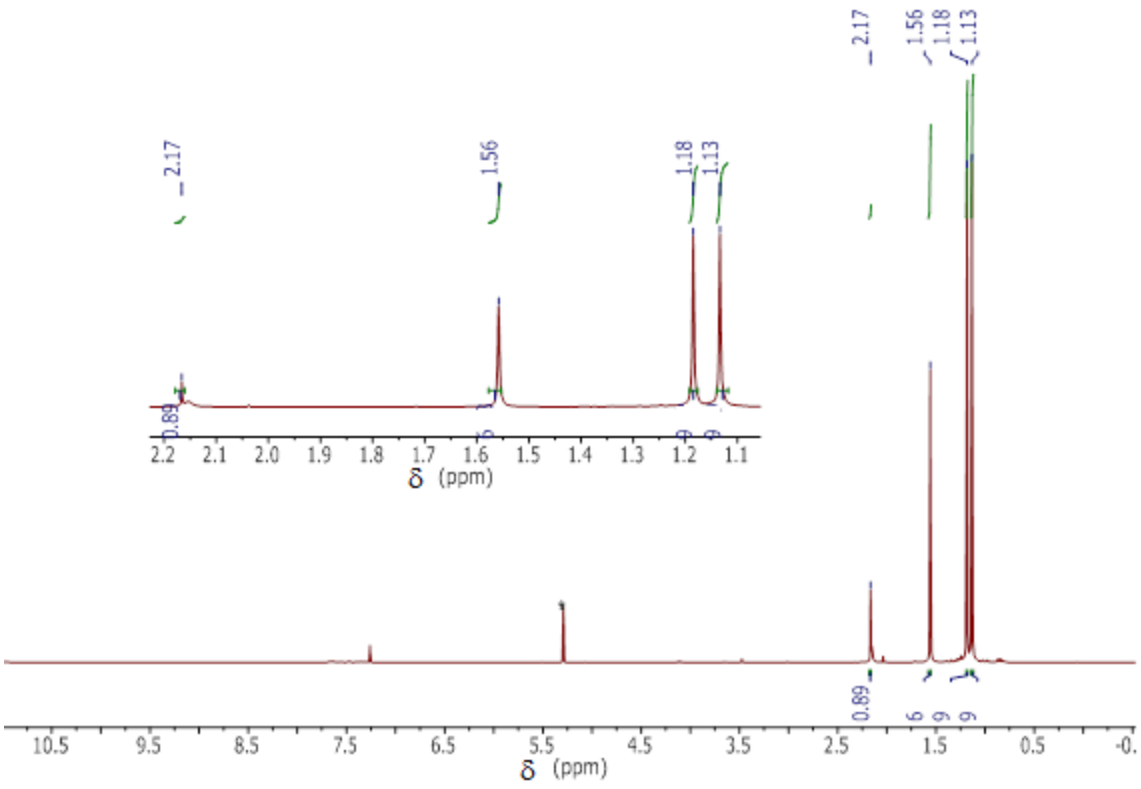

Figure 52. ^{1}H NMR spectrum of (*P,P,P*)-**2F$_{OH}$**.

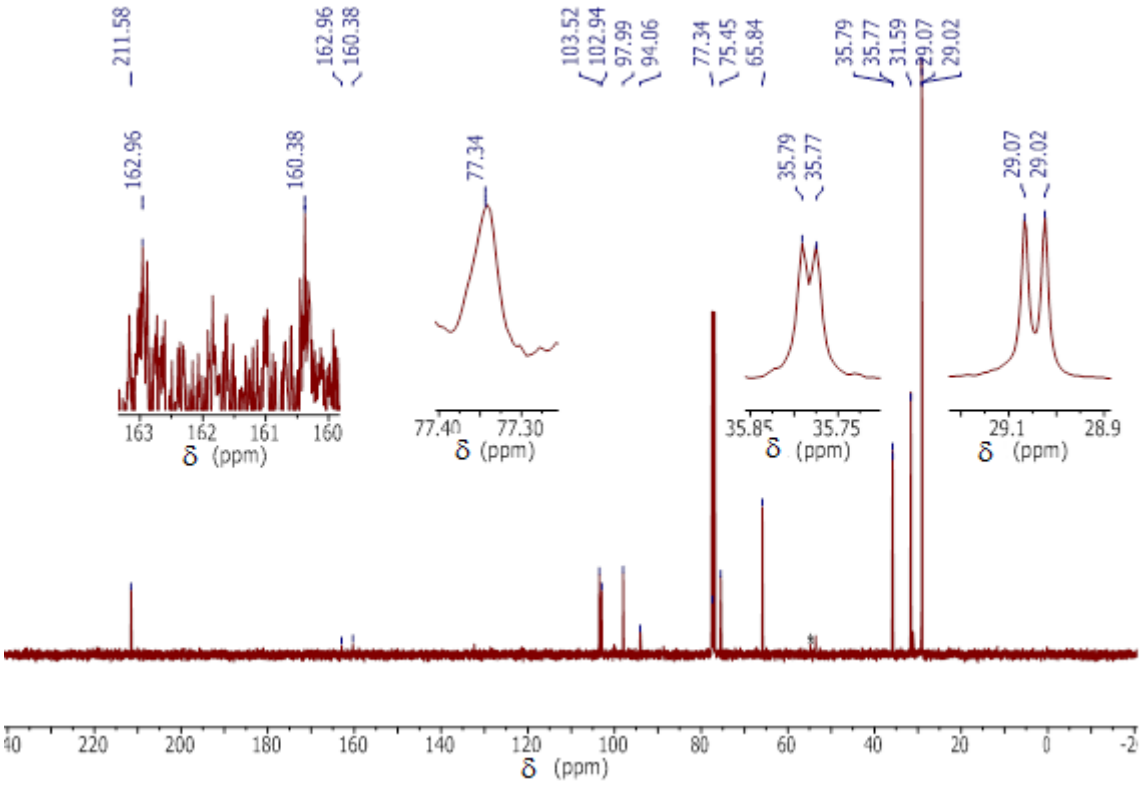

Figure 53. ^{13}C NMR spectrum of (*P,P,P*)-**2F$_{OH}$**.

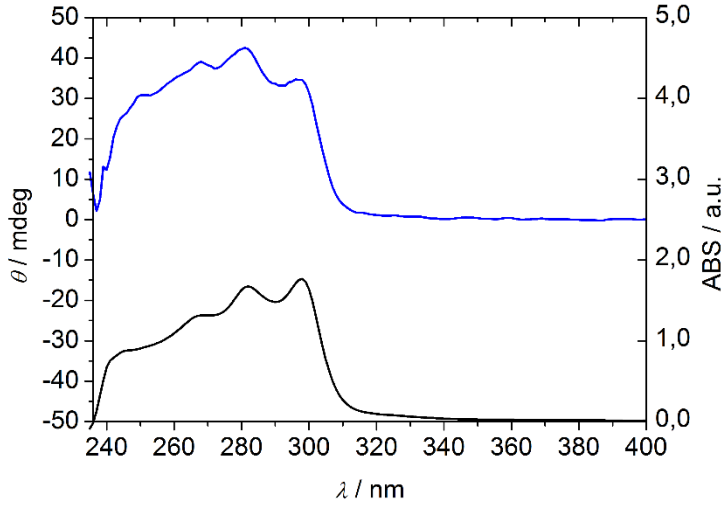

Figure 54. ECD (top) and UV/Vis (bottom) spectra of (*P,P,P*)-**2F$_{OH}$** in $CHCl_3$.

((2,4,6-trifluorobenzene-1,3,5-triyl)tris(3,5-di-tert-butylhepta-3,4-dien-1,6-diyne-7,1-diyl))tris(triisopropylsilane) ($2F_{TIPS}$)

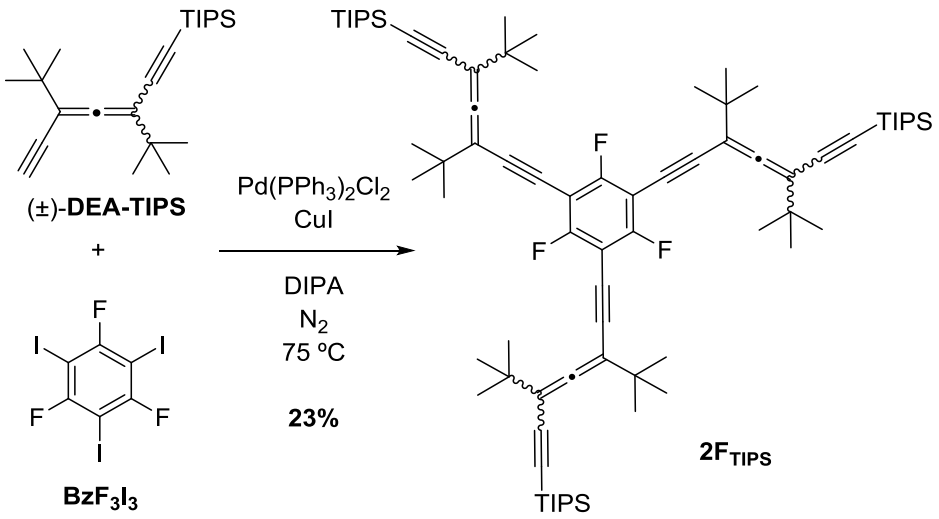

Scheme 24. Synthesis of $2F_{TIPS}$.

$[Pd(PPH_3)_2Cl_2]$ (6 mol%, 0.0077 mmol, 5 mg), CuI (6 mol%, 0.0077 mmol, 2 mg), 1,3,5-trifluoro-2,4,6-triodobenzene (1 eq, 0.129 mmol, 66 mg), DIPA (2 mL), were added to a flamed Schlenk tube followed by (±)-**DEA-TIPS** (3.3 eq, 0.4262 mmol, 152 mg) in DIPA (2 mL) via cannula. The reaction ran for 20 h at 75 °C with stirring. The solvent was removed under reduced pressure and the crude purified by FC (SiO_2, hexane) giving the $2F_{TIPS}$ (35 mg, 23% yield) along with **DEA-TIPS$_2$** (48 mg, 32% of the initial (±)-**DEA-TIPS**), **MC-$2F_{TIPS}$** (23%), and **MC-$2F_{TIPS}$** (20%).

^{1}H NMR (400 MHz, $CDCl_3$) δ = 1.19 (s, 27H, ^{t}Bu), 1.17 (s, 27H, ^{t}Bu), 1.09 (s, 63H, -TIPS) ppm.

^{19}F NMR (376 MHz, $CDCl_3$) δ = −101.0 ppm.

^{13}C NMR (101 MHz, $CDCl_3$) δ = 212.7 ($C_{cumulenic}$), 161.7 (d, *J* = 260.4 Hz, *J'* = 7.5 Hz, -C−F), 104.7, 102.6, 99.9, 95.1, 94.1, 94.0, 77.3 ($6C_{allenes+alkynes}$+$1C_{aromatic}$), 35.9, 35.6 ($C_{quaternary}$ ^{t}Bu), 29.11, 29.06 (^{t}Bu), 18.81 (Me_s TIPS), 11.49 ($C_{quaternary}$ TIPS) ppm.

HR-ESI-MS *m/z* (%): $[M+H]^+$ calcd. for $^{12}C_{78}{}^1H_{118}{}^{19}F_3{}^{28}Si_3{}^+$ 1195.84879, found: 1195.85164 (100); calcd. for 119685198, found: 1196.85380 (89); calcd. for 1197.85503, found: 1197.85774 (35).

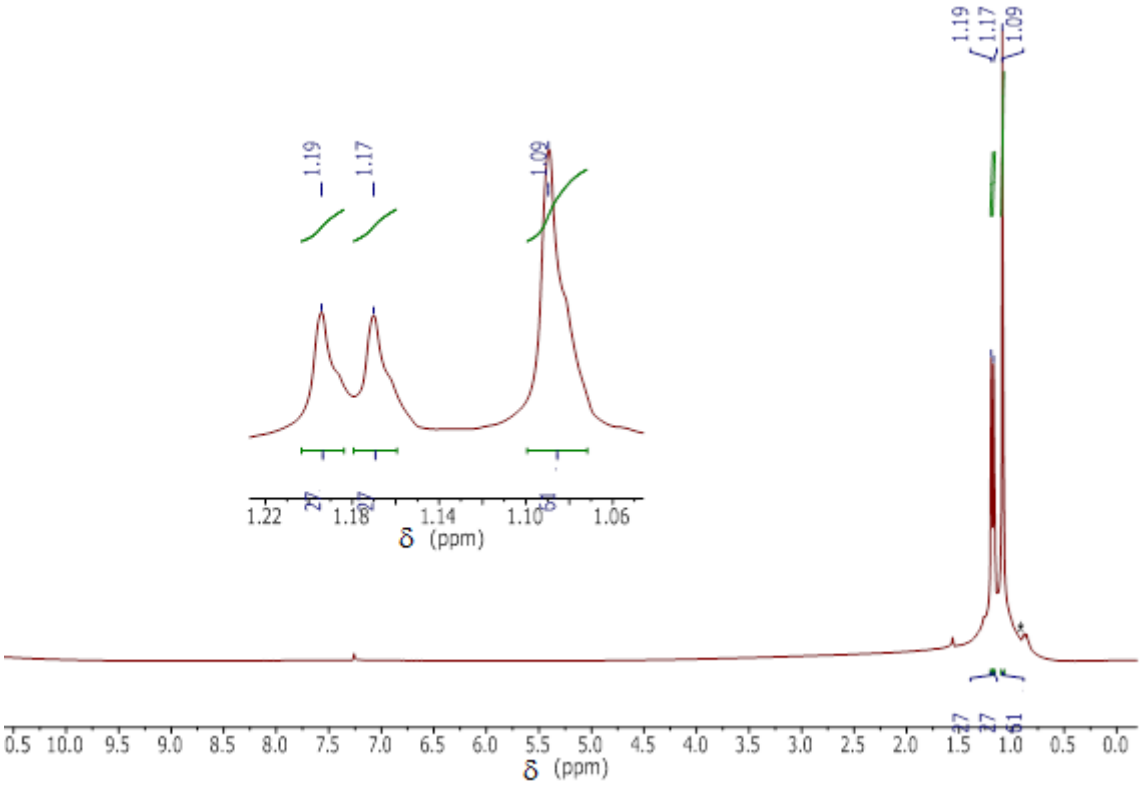

Figure 55. ^{1}H NMR spectrum of **2F$_{TIPS}$**.

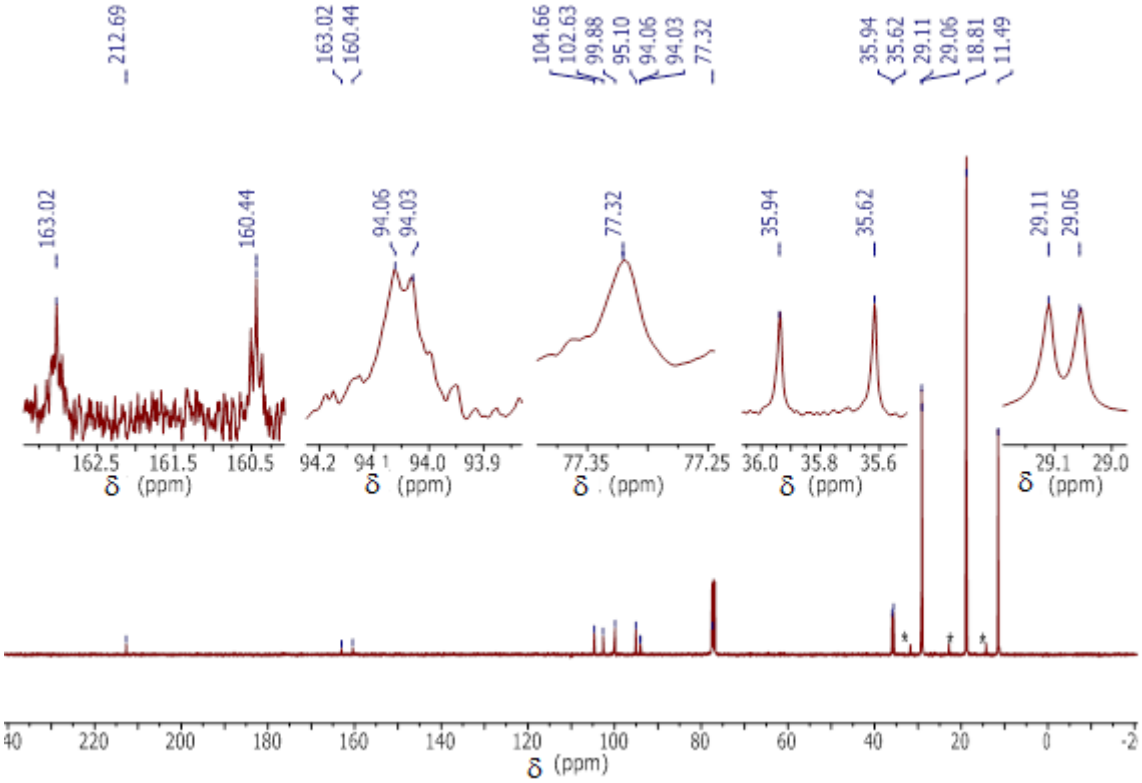

Figure 56. ^{13}C NMR spectrum of (±)-**2F$_{TIPS}$**. * Traces of Hexane.

1,3,5-Tris(3,5-di-*tert*-butylhepta-3,4-dien-1,6-diyn-1-yl)-2,4,6-trifluorobenzene (3F)

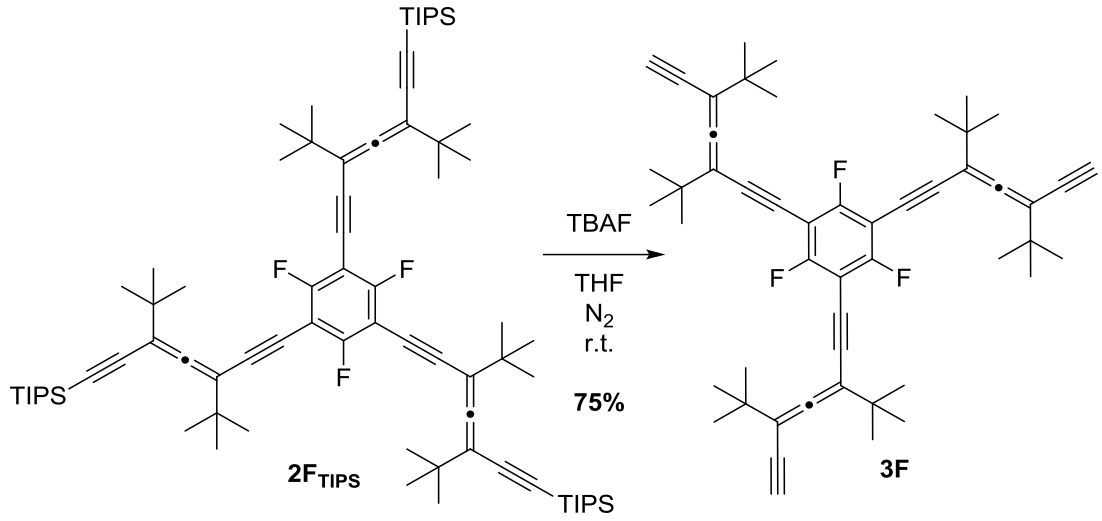

Scheme 25. Synthesis of **3F**.

Route *a*: **2F$_{TIPS}$** (1 eq, 0.0184 mmol, 22 mg) was dissolved in dry THF (5 mL) under N_2 atmosphere. TBAF (1M in THF) (3 eq, 0.0552 mmol, 55.2 μL) was added and the mixture was stirred at r.t. for 15 min. Then, the mixture was washed with aq. sat. $NaHCO_3$, extracted with DCM and dried with anh. $NaSO_4$. FC purification (SiO_2, hexane:DCM 2%) gave the diastereomeric mixture of **3F** (10 mg, 75% yield) as a yellowish oil.

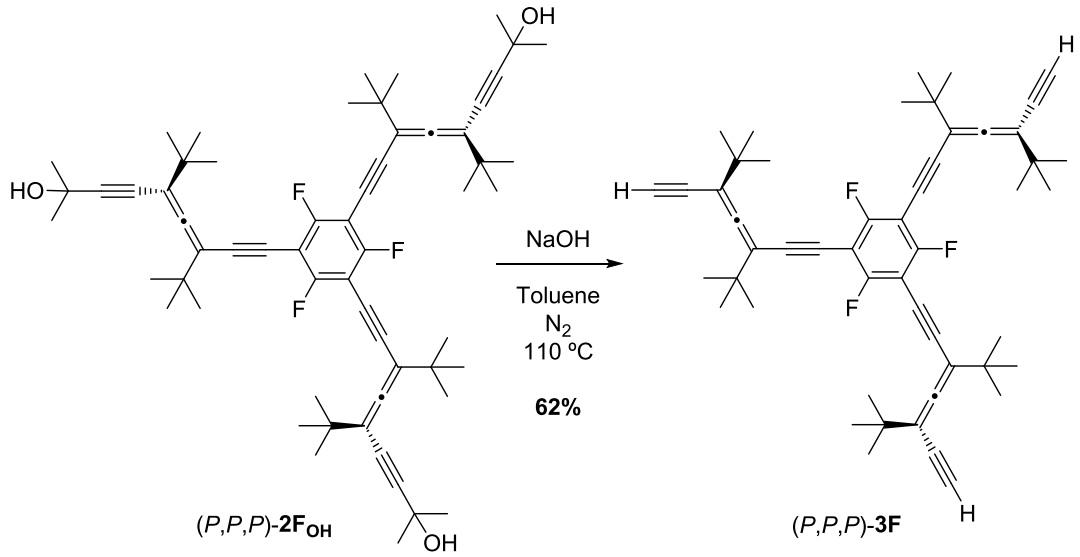

Scheme 26. Synthesis of (*P,P,P*)-**3F**.

Route *b*: (*P,P,P*)-**2F$_{OH}$** (1 eq, 0.0604 mmol, 54 mg) and powdered flamed NaOH (83 eq, 2.1730 mmol, 200 mg) were dissolved in dry toluene under N_2 and set to 110 °C for 15 h. The mixture was dried under reduced pressure, washed with distilled water, extracted with DCM and dried with anh. Na_2SO_4. The solvent was removed under reduced pressure and the crude purified by FC (SiO_2, hexane:DCM 2%) to give (*P,P,P*)-**3F** (27 mg, 62% yield) as a yellowish oil.

^{1}H NMR (400 MHz, $CDCl_3$) δ = 3.04 ($3H_{alkyne}$), 1.20 (s, 27H ^{t}Bu), 1.17 (s, 27H ^{t}Bu) ppm.
^{19}F NMR (376 MHz, $CDCl_3$) δ = −100.7 ppm.
^{13}C NMR (101 MHz, $CDCl_3$) δ = 212.4 ($C_{cumullenic}$), 161.8 (dt, ^{1}J = 260.7 Hz, ^{3}J = 7.3 Hz, $C_{aromatic}$), 103.5, 103.2, 93.7 (q, J = 3.3 Hz), 81.2, 77.7, 77.4, 77.2 ($4C_{alkyne}$+$2C_{allene}$+$C_{aromatic}$), 35.8, 35.6 ($2C_{quaternary}$ ^{t}Bu), 29.1, 28.9 (^{t}Bu) ppm.
IR ($CHCl_3$) ν = 3311 (m, str C_{alkyne}–H), 2966 (s, str $C_{aromatic}$–H), 2931, 2903, 2869 (w, str $C_{aliphatic}$–H), 2214 (w), 2098 (w), 1927 (w, str C_{allene}=C_{allene}), 1597 (s, str $C_{aromatic}$=$C_{aromatic}$), 1474, 1459 (s, str C–F) cm^{-1}.
O.R.: λ_D^{22} = +4.5 °; **S.O.R.: $[\lambda]_D^{22}$** = +332.4 °.
UV/Vis ($CHCl_3$) λ_{max} (nm): 297, 281, 269. ε_{297nm} = 78292 $M^{-1}\cdot cm^{-1}$.
HR-ESI-MS *m/z* (%): $[M]^+$, calcd. for $^{12}C_{51}{}^{1}H_{57}{}^{19}F_3{}^+$ 726.4412, found: 726.44005 (100); $[M+H]^+$ calcd. for $^{12}C_{51}{}^{1}H_{58}{}^{19}F_3{}^+$ 727.4485, found: 727.44846; $[M+K]^+$ calcd. for $^{12}C_{51}{}^{1}H_{57}{}^{19}F_3{}^{39}K^+$ 765.40410, found: 765.4044.

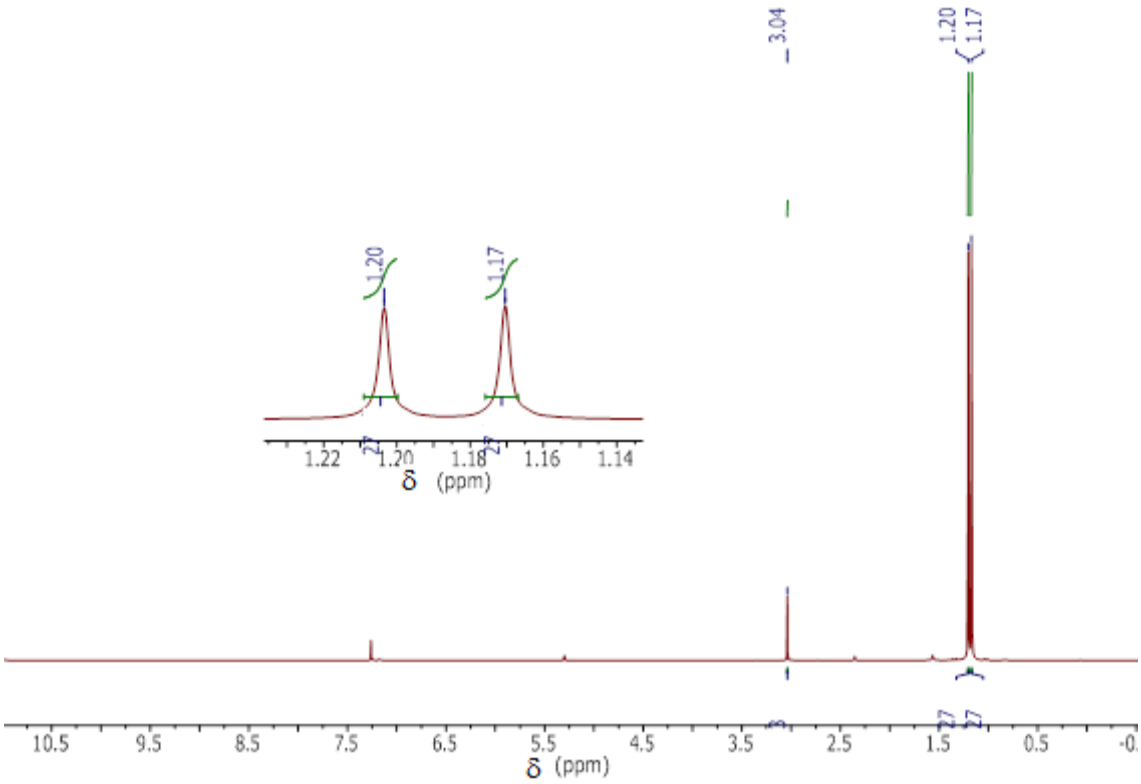

Figure 57. ^{1}H NMR spectrum of (*P,P,P*)-**3F**.

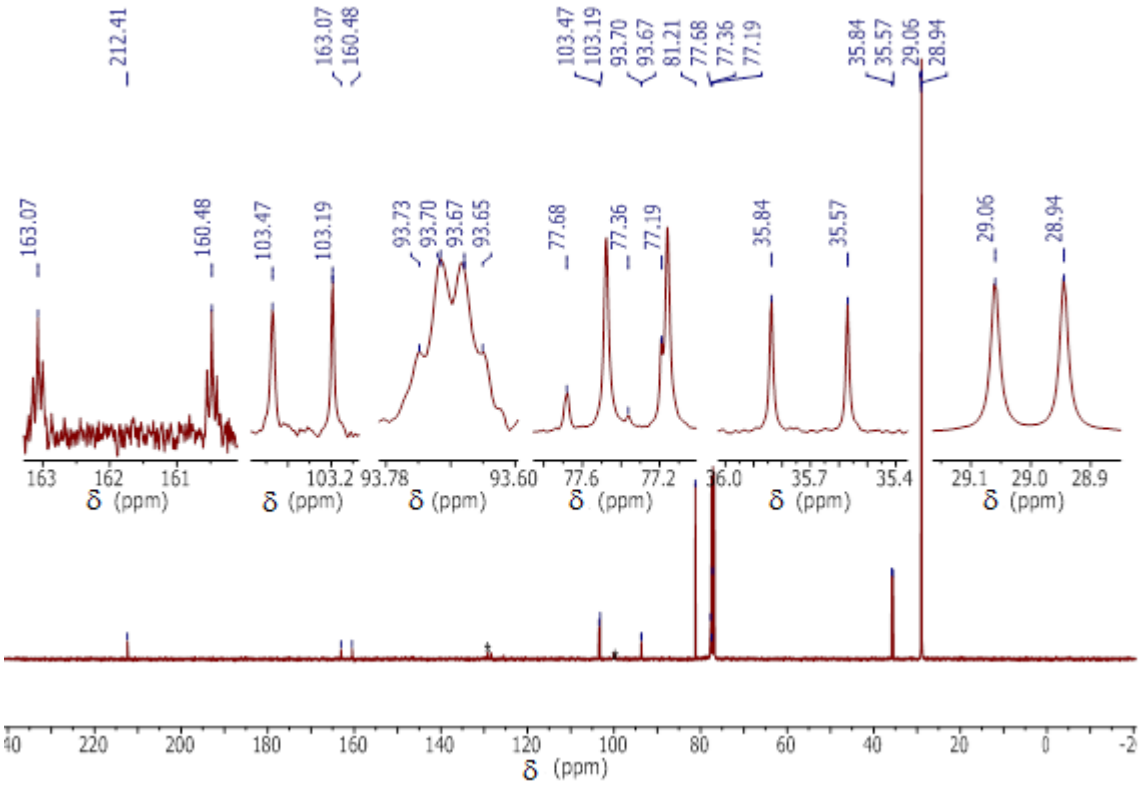

Figure 58. ^{13}C NMR spectrum of (*P,P,P*)-**3F**.

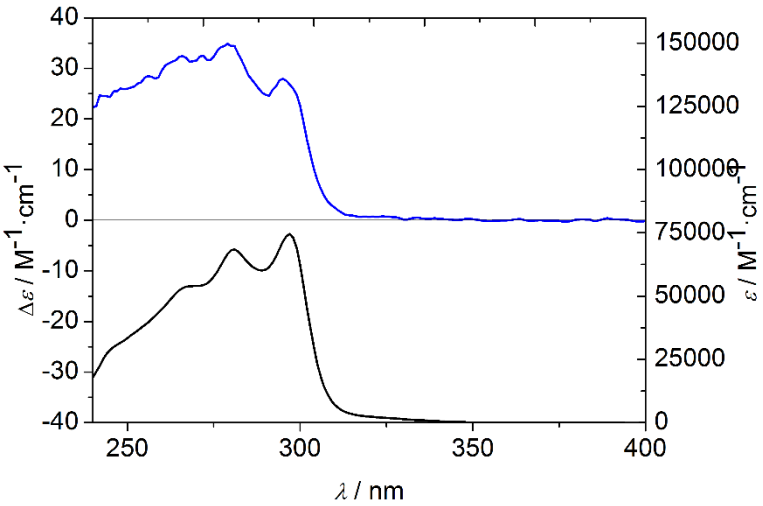

Figure 59. ECD (top) and UV/Vis (bottom) spectra of (*P,P,P*)-**3F**.

(*P,P*)$_3$-4,6,11,13,19,21,26,28,33,35,40,42-Dodeca-*tert*-butyl-1,16-(1,3,5)-2,4,6-trifluorobenzenebicyclotetratetracontaphane-4,5,11,12,19,20,26,27,33,34,40,41-dodecaen-2,7,9,14,17,22,24,29,31,36,38,43-dodecayne ((*P,P*)$_3$-**1F)**

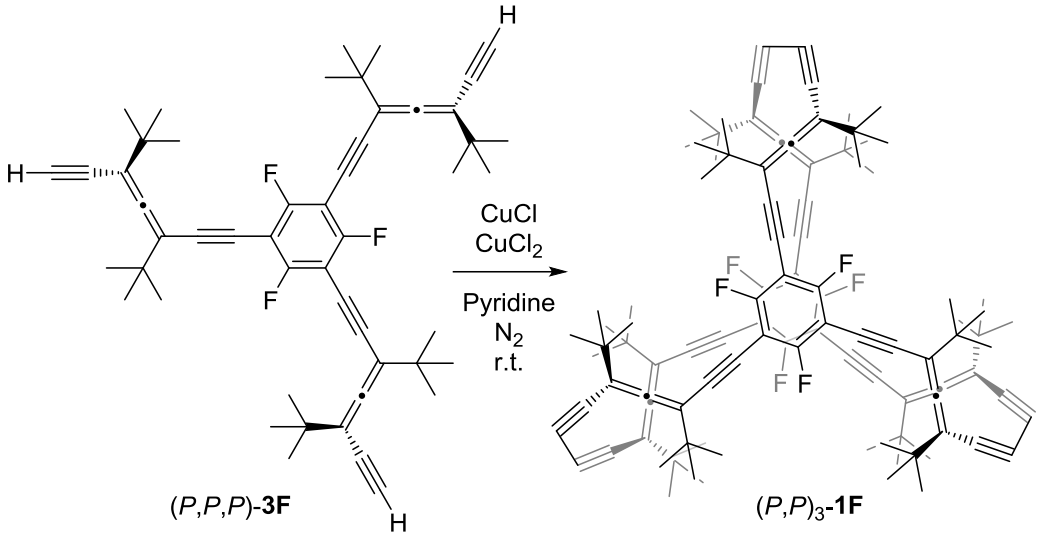

Scheme 27. Synthesis of (*P,P*)$_3$-**1F**.

Two solutions were prepared:

Solution ***a***: CuCl (75 eq, 1.9601 mmol, 194 mg) and $CuCl_2$ (11 eq, 0.2871 mmol, 39 mg) were placed in a round-bottom flask under N_2 atmosphere, dissolved in dry pyridine (16 mL).

Solution ***b***: (*P,P,P*)-**3F** (1 eq, 0.0261 mmol, 19 mg) was dissolved in dry pyridine (20 mL).

Both solutions were bubbled with N_2 for 1 h. Solution ***b*** was added with a flux of 1 mL·h^{-1} over solution ***a*** under N_2 at r.t. After 3 days of reaction, the solvent was removed under reduced pressure and the remaining solid was dissolved in DCM and washed with aq. sat. NH_4Cl solution. The combined organic phases were dried over anh. Na_2SO_4 and evaporated to dryness. The obtained residue was purified by FC (SiO_2, hexane:DCM 2%) affording the shackles-shaped molecule (*P*)$_6$-**8** (0.5 mg, 3% yield, calcd. by ^{1}H NMR with an internal standard) instead of the desired fluorinated molecular cage.

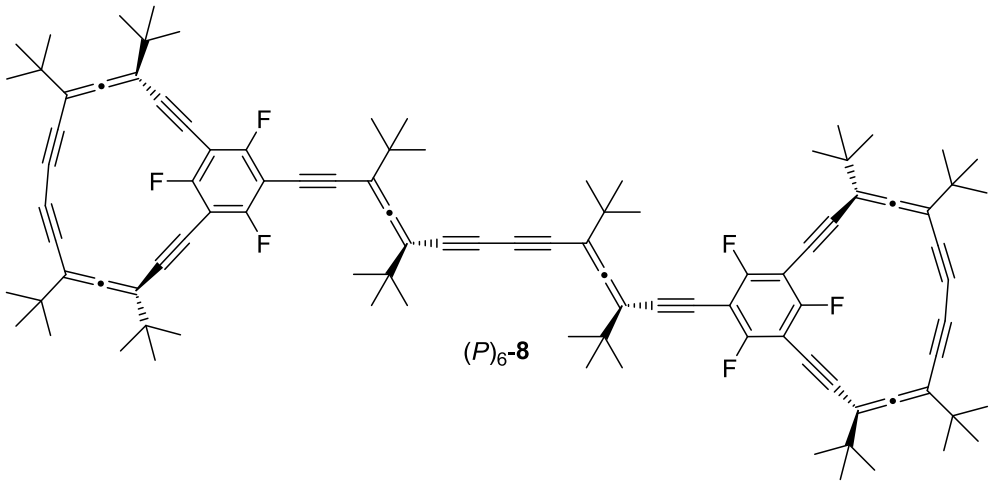

Figure 60. Structure of compound (*P*)$_6$-**8**.

^{1}H NMR (400 MHz, $CDCl_3$) δ = 1.20 (s, 18H), 1.18 (s, 36H), 1.17 (s, 18H), 1.15 (s, 36H) ppm.

^{19}F NMR (376 MHz, $CDCl_3$) δ = −101.9 ppm.

HR-MALDI-MS *m/z* (%):$[M+H]^+$ calcd. for $^{12}C_{102}{}^{1}H_{109}{}^{19}F_6{}^+$ 1448.84619, found: 1448.84617 (100); calcd. for 1447.84280, found: 1447.84240 (86); calcd. for 1449.84952, found: 1449,84875 (51); $[M+K]^+$ $^{12}C_{102}{}^{1}H_{108}{}^{19}F_6{}^{39}K^+$ calcd. for 1486.80204, found: 1486.80242 (100).

UV/Vis ($CHCl_3$) λ_{max} (nm): 317 (sh.), 303, 285.

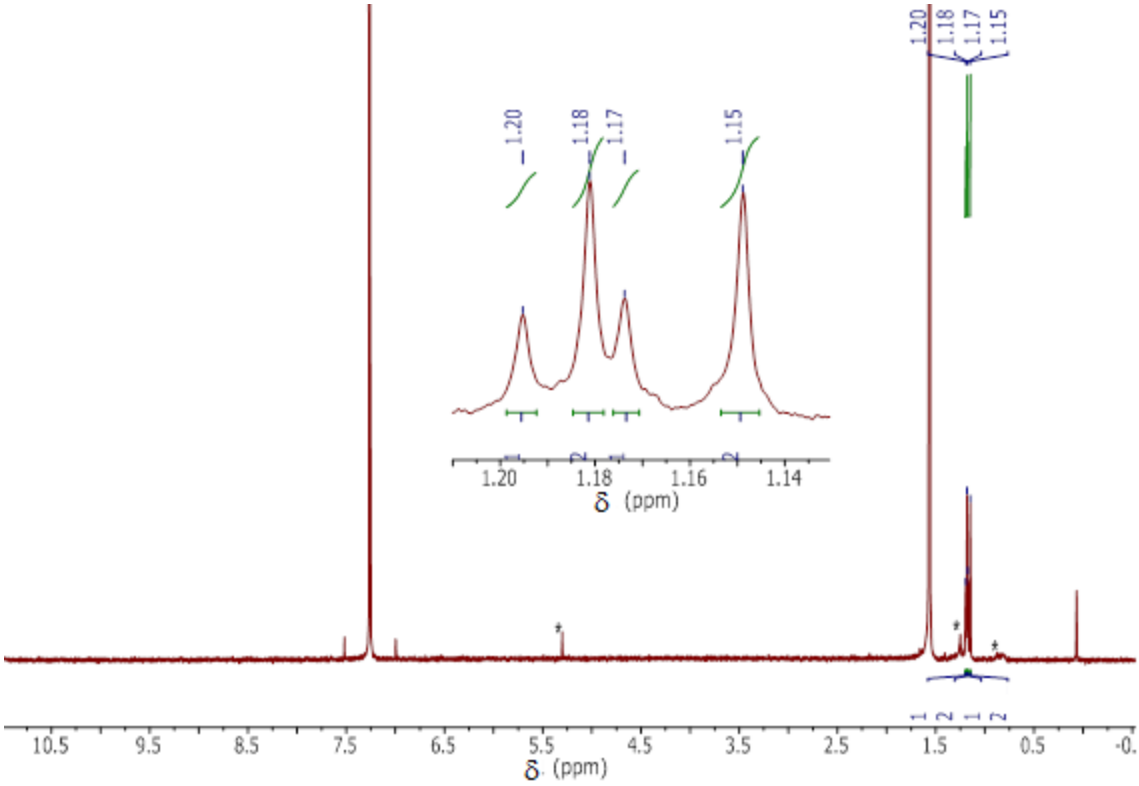

Figure 61. ^{1}H NMR spectrum of $(P)_6$-**8**.

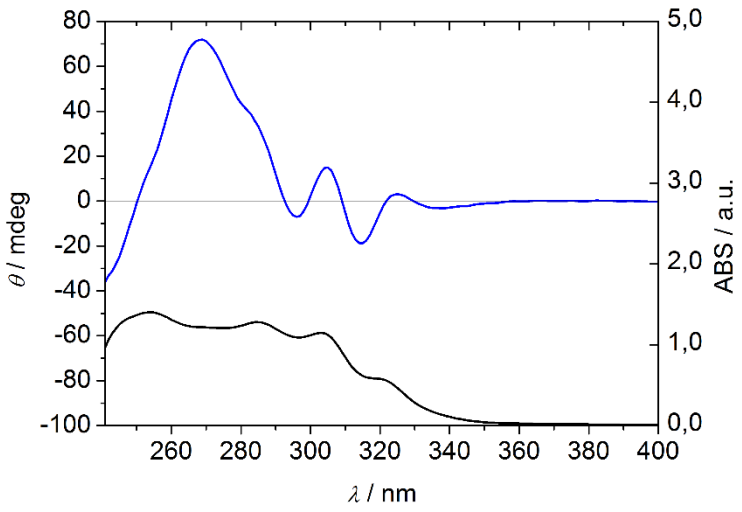

Figure 62. ECD (top) and UV/Vis (bottom) spectra of $(P)_6$-**8** in $CHCl_3$.

6.7. Synthesis of $(M,M)_3$-1TCO.

(*M,M,M*)-**2,6,10-Tris(5,7-di-*tert*-butyl-2-methylnona-5,6-dien-3,8-diyn-2-ol)-4H-benzo[9,1]quinolizino [3,4,5,6,7-defg]acridine-4,8,12-trione (**(*M,M,M*)-**2TCO)**

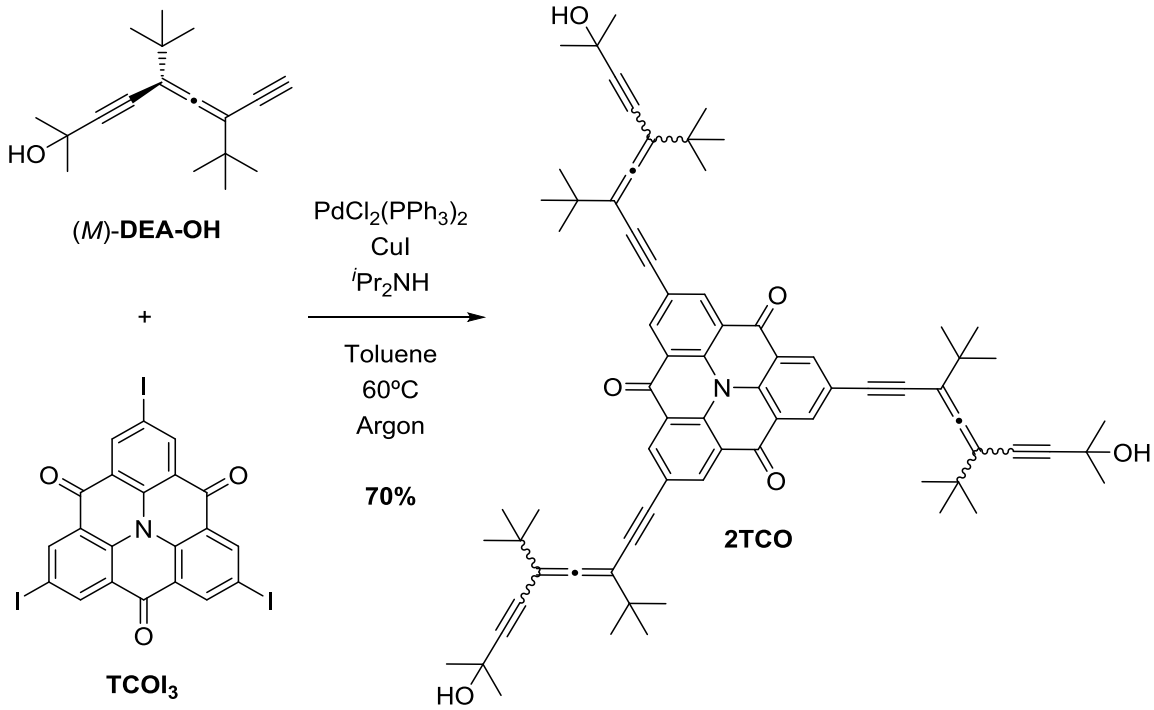

Scheme 28. Synthesis of **2TCO**.[18]

(*M*)-**DEA** (3.5 eq, 0.206 mmol, 53 mg) was dissolved in a 1:3 DIPA:Toluene mixture (5.5 mL) in a flamed and Argon-purged Schlenk. **$TCOI_3$** (1 eq, 0.06 mmol, 41 mg) was added (solid) and dissolved by bubbling the mixture for 30 min with Argon. CuI (10 mol%, 0.006 mmol, 1 mg) and $PdCl_2(PPh_3)_2$ (5% mol, 0.003 mmol, 2 mg) were added under Argon. The mixture was heated at 60 °C for 15 h, and then passed through a plug of SiO_2 with DCM. FC (SiO_2, DCM:EtOAc 1%) afforded **2TCO** (45 mg, 70% yield) as an amber oil.

^{1}H NMR (400 MHz, CD_2Cl_2) δ = 8.93 (s, $6H_{aromatic}$), 1.57 (s, $18H_{Me}$), 1.28 (s, $27H_{tBu}$), 1.21 (s, $27H_{tBu}$) ppm.

^{13}C NMR (101 MHz, CD_2Cl_2) δ = 212.1 ($C_{cumulenic}$), 175.3 ($C_{C=O}$), 137.0 ($C_{aromatic}$), 136.8 ($C_{aromatic}$), 123.8 ($C_{aromatic}$), 122.3 ($C_{aromatic}$), 103.9 (C_{alkene}), 103.3 (C_{alkene}), 98.7 (C_{alkyne}), 89.9 (C_{alkyne}), 87.0 (C_{alkyne}), 75.4 (C_{alkyne}), 65.9 ($C_{quaternary\text{-}OH}$), 36.0 ($C_{quaternary\text{-}tBu}$), 36.0 ($C_{quaternary\text{-}tBu}$), 31.7 ($C_{Me\ acetonide}$), 29.2 (C ^{t}Bu), 29.1 (C ^{t}Bu) ppm.

HR-ESI-MS *m/z* (%): [M] = $^{12}C_{75}{}^{1}H_{81}{}^{14}N^{23}Na^{16}O_6$; $[M+Na]^+$ calcd. for $^{12}C_{75}{}^{1}H_{81}N^{23}Na^{16}O_6{}^+$ 1114.59561, found: 1114.59424 (100); $[M+Na+1]^+$ 1115.5995 calcd. for $^{12}C_{75}{}^{2}H_1{}^{1}H_{80}N^{23}Na^{16}O_6{}^+$, found: 1115.59733 (81.1); $[M+Na+2]^+$ calcd. for $^{12}C_{74}{}^{13}C_1{}^{2}H_1{}^{1}H_{80}{}^{14}N^{23}Na^{16}O_6{}^+$ 1116.6029, found: 1116.60066 (32.5).

IR ($CHCl_3$) ν = 3353 (br. w, str O–H); 2965, 2930, 2902 (s, str $C_{aromatic}$–H); 2868 (s, str $C_{aliphatic}$–H); 2207 (w, str C_{alkyne}≡C_{alkyne}); 1902 (w, str C_{allene}=C_{allene}); 1662 (m, str C=O ketone); 1588 (m, str $C_{aromatic}$=$C_{aromatic}$); 1466 (m, str C–N) cm^{-1}.

CV (in DCM *vs* Fc^+/Fc): Two quasireversible reduction potentials at −1.45 and −1.52 V. Similar to those present for TIPS-ethynyl-substituted C=O-bridged triangulene.[18]

UV/Vis ($CHCl_3$, $4 \cdot 10^{-5}$ M) λ_{max} (nm): 452, 335, 323 (sh.), 287.

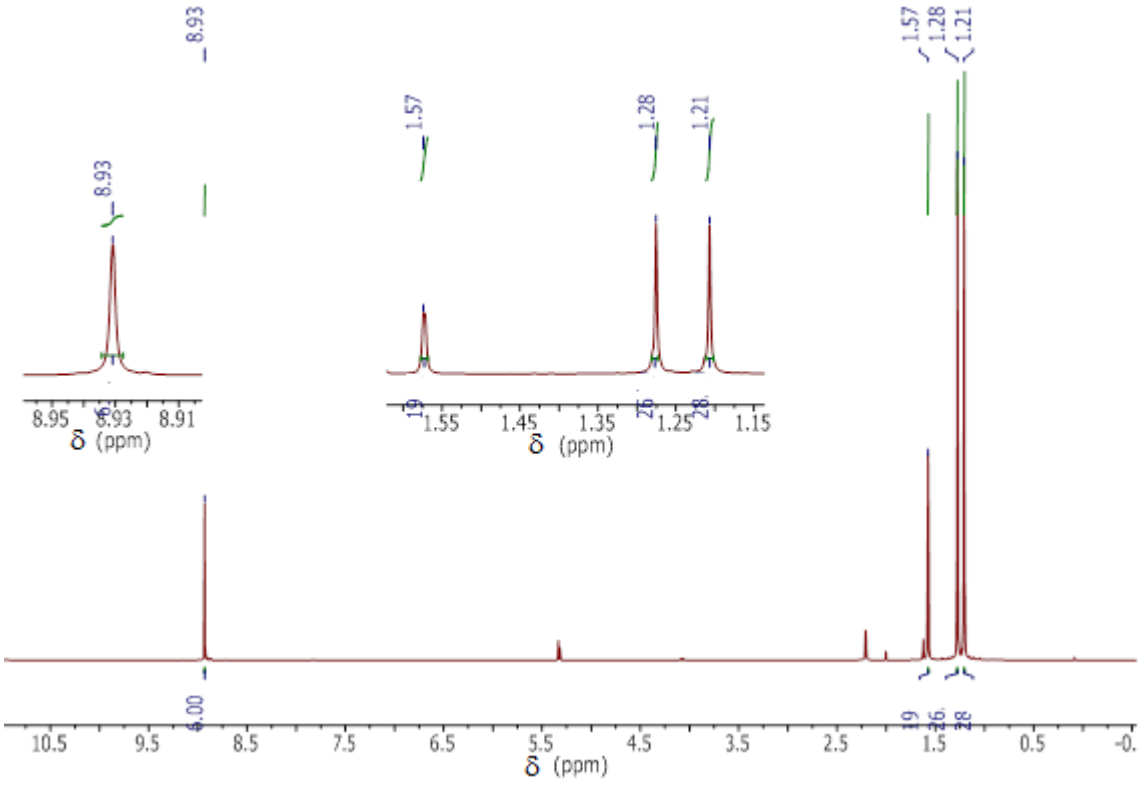

Figure 63. ^{1}H NMR spectrum of **2TCO**.

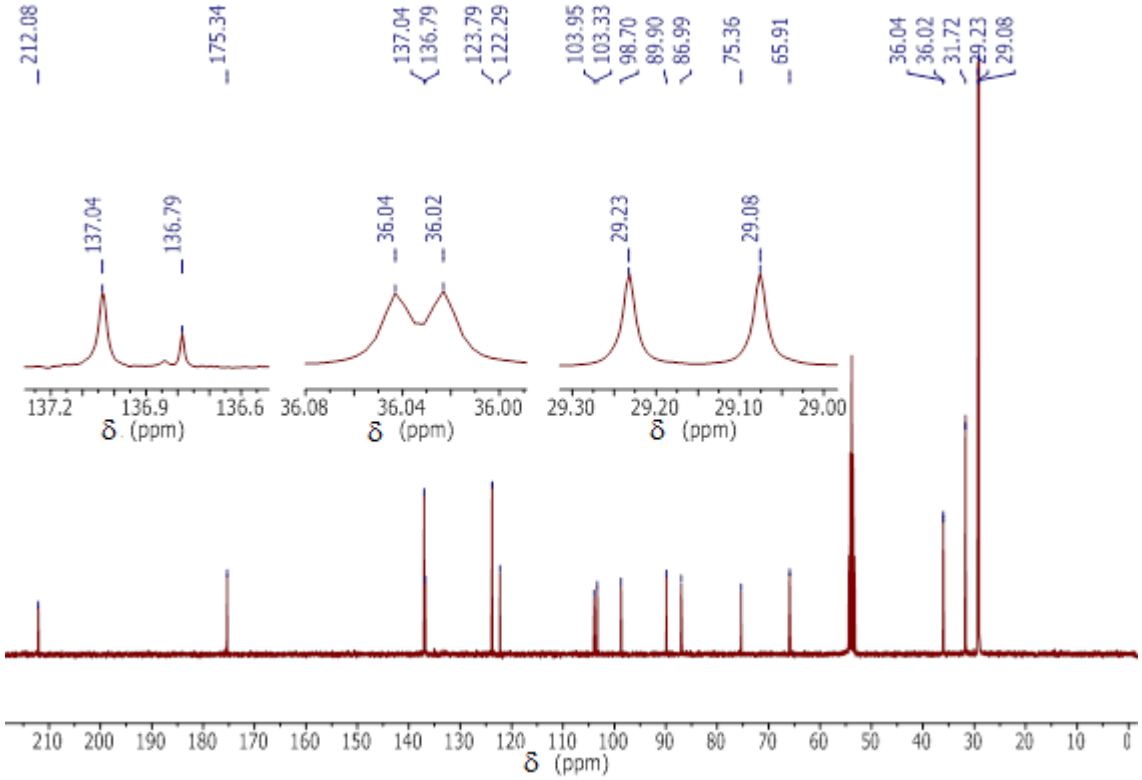

Figure 64. ^{13}C NMR spectrum of **2TCO**.

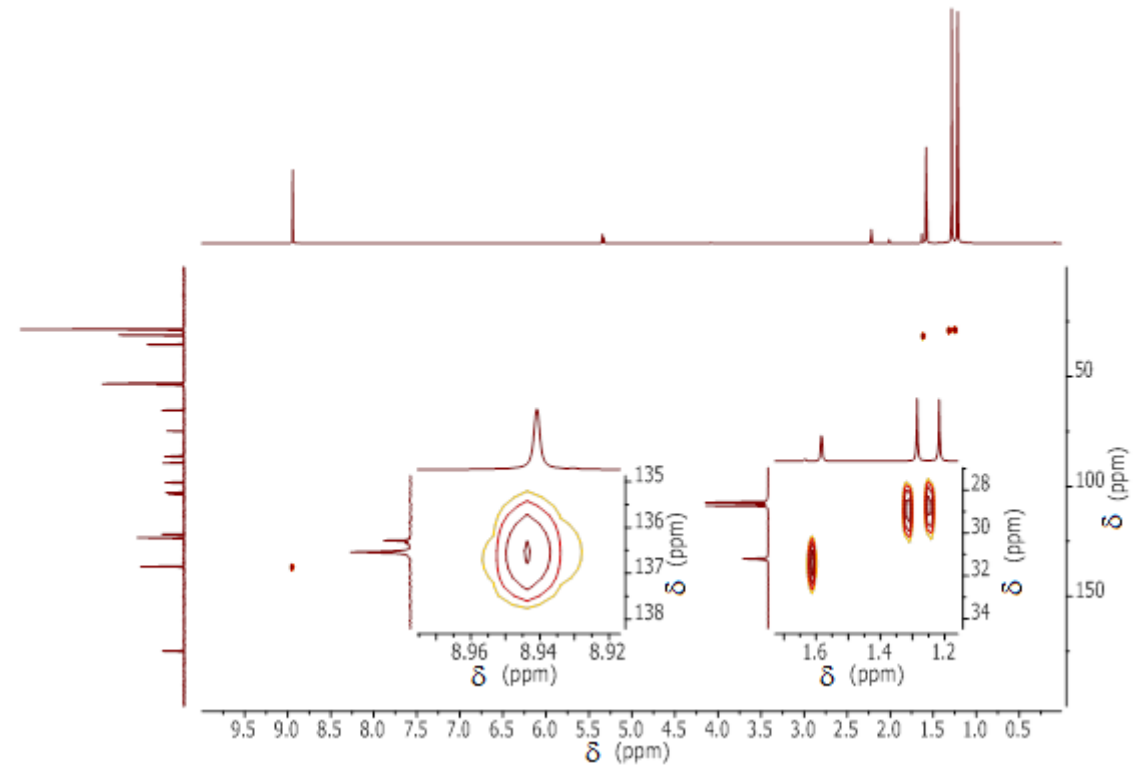

Figure 65. HSQC NMR spectrum of **2TCO**.

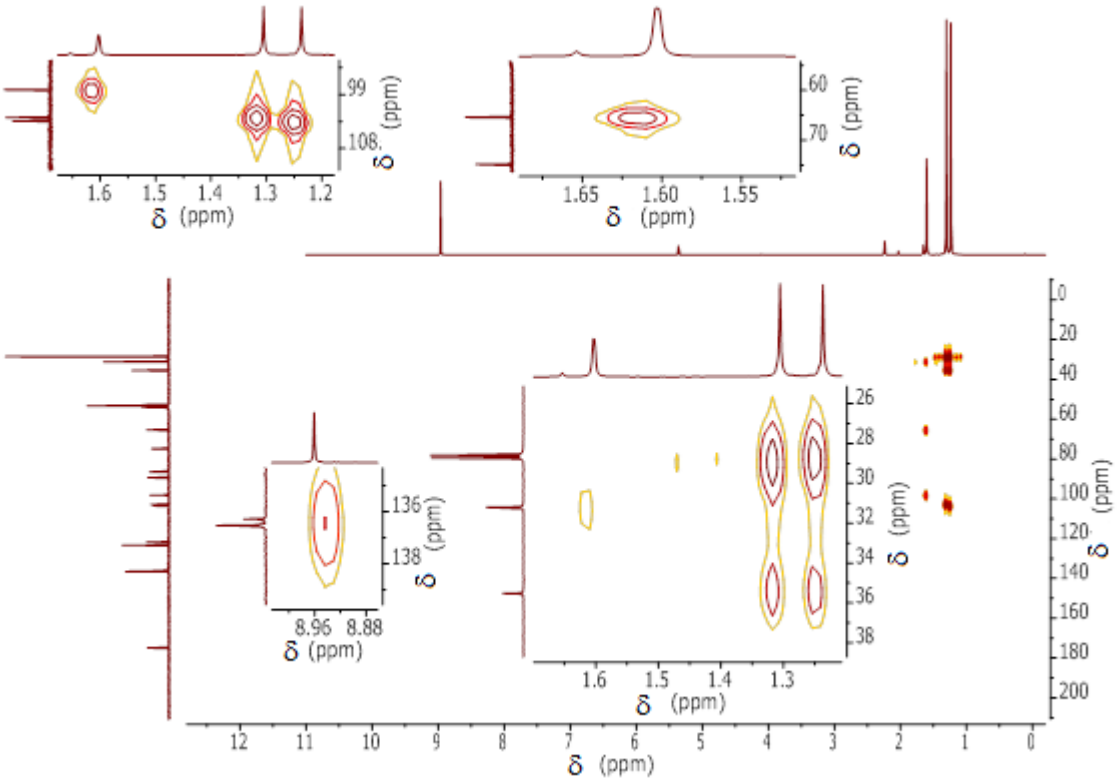

Figure 66. HMBC NMR spectrum of **2TCO**.

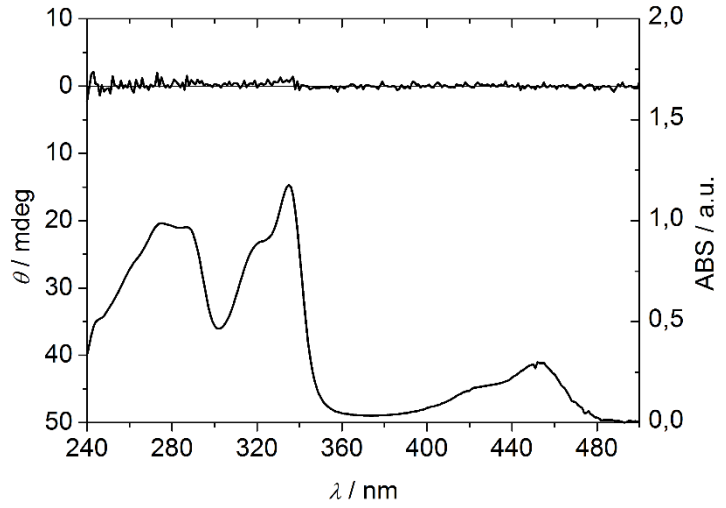

Figure 67. ECD (top) and UV/Vis spectra of **2TCO** in $CHCl_3$.

2,6,10-Tris(3,5-di-*tert*-butylhepta-3,4-dien-1,6-diyne)-4H-benzo[9,1]quinolizino[3,4,5,6,7-defg]acridine-4,8,12-trione (3TCO)

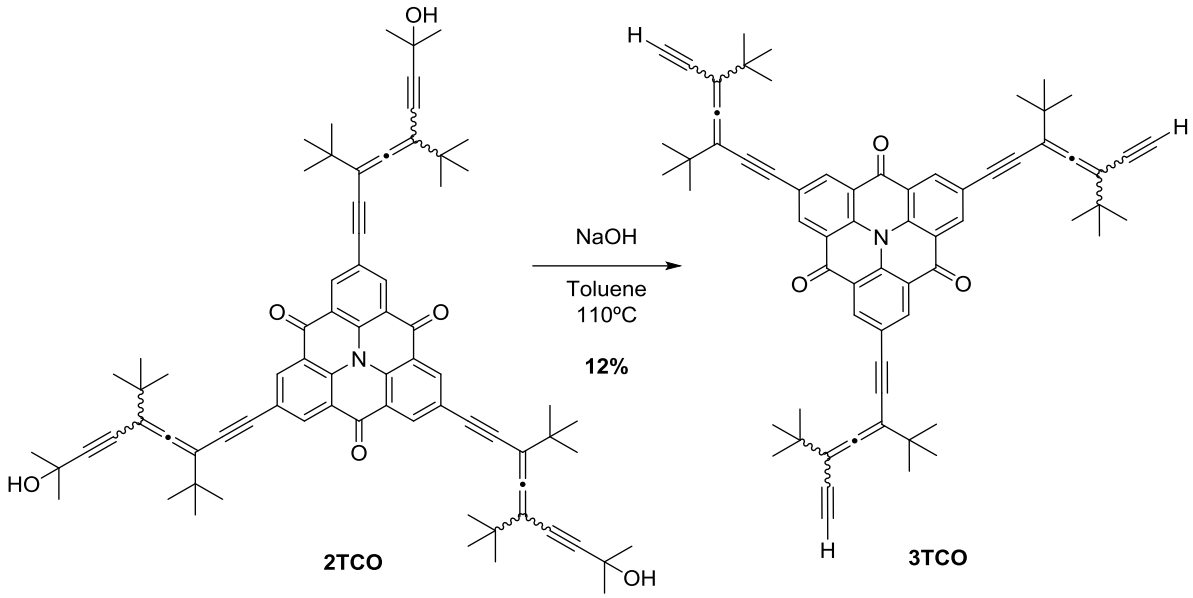

Scheme 29. Synthesis of **3TCO**.

The tricoupled triangulene (1 eq, 0.014 mmol, 15 mg) was dissolved in dry toluene (20 mL) in an amber round bottom flask. Flamed powdered NaOH (300 eq, 8.35 mmol, 334 mg) was added. The mixture was allowed to react at 120 °C for 20 h under Argon, then washed with distilled water and extracted with DCM. The solvent was evaporated under reduced pressure. FC (SiO_2, hexane) afforded **3TCO** (1.5 mg, 12% yield).

^{1}H NMR (400 MHz, CD_2Cl_2) δ = 9.00 (s, $6H_{aromatic}$), 3.14 (s, $3H_{terminal\ alkyne}$), 1.27 (s, $27H_{t\mathrm{Bu}}$), 1.21 (s, $27H_{t\mathrm{Bu}}$) ppm.

^{13}C NMR (101 MHz, CD_2Cl_2) δ = 212.9 ($C_{cumulenic}$), 175.5 ($C_{C=O}$), 137.2 ($C_{aromatic}$), 137.0 ($C_{aromatic}$), 123.9 ($C_{aromatic}$), 122.2 ($C_{aromatic}$), 103.8 (C_{alkene}), 103.5 (C_{alkene}), 90.3 ($C_{alkene/alkyne}$), 86.5 ($C_{alkene/alkyne}$), 81.51 ($C_{alkene/alkyne}$), 77.3 ($C_{alkene/alkyne}$), 36.1 ($C_{quaternary\text{-}t\mathrm{Bu}}$), 35.7 ($C_{quaternary\text{-}t\mathrm{Bu}}$), 29.2 ($C_{t\mathrm{Bu}}$), 28.9 ($C_{t\mathrm{Bu}}$) ppm.

IR ($CHCl_3$) ν = 3313, 3293 (sharp w, str C_{alkyne}–H); 2963, 2925 (s, str $C_{aromatic}$–H); 2866 (s, str $C_{aliphatic}$–H); 2202 (w, str $C_{alkyne}\Xi C_{alkyne}$); 1733 (w); 1663 (s, ketone C=O stretching); 1588 (s, str $C_{aromatic}$=$C_{aromatic}$); 1466 (s, str C–N) cm^{-1}.

UV/Vis ($CHCl_3$, $1\cdot10^{-5}$ M) λ_{max} (nm): 455, 334, 324 (sh.), 286.

HR-ESI-MS *m/z* (%): $[M]^+$ = $^{12}C_{66}{}^{1}H_{63}{}^{14}N^{16}O_3$; $[M+H]^+$, calcd. for $^{12}C_{66}{}^{1}H_{64}NO_3{}^+$ 918.4881, found: 918.48796 (100); $[M+H+1]^+$, calcd. for $^{12}C_{66}{}^{2}H_1{}^{1}H_{63}{}^{14}N^{16}O_3{}^+$: 919.4914, found: 919.49107 (70); $[M+H+2]^+$, calcd. for $^{12}C_{65}{}^{13}C_1{}^{2}H_1{}^{1}H_{63}{}^{14}N^{16}O_3{}^+$ 920.4948, found: 920.49440 (30).

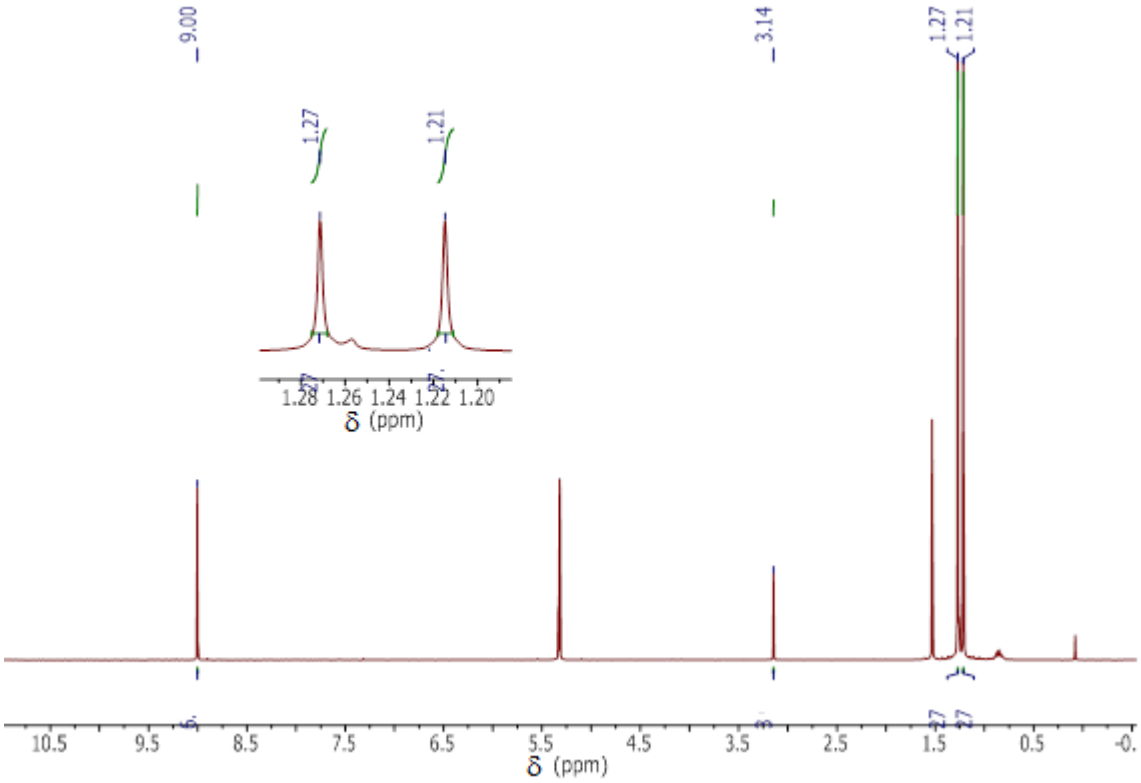

Figure 68. ^{1}H NMR spectrum of **3TCO**.

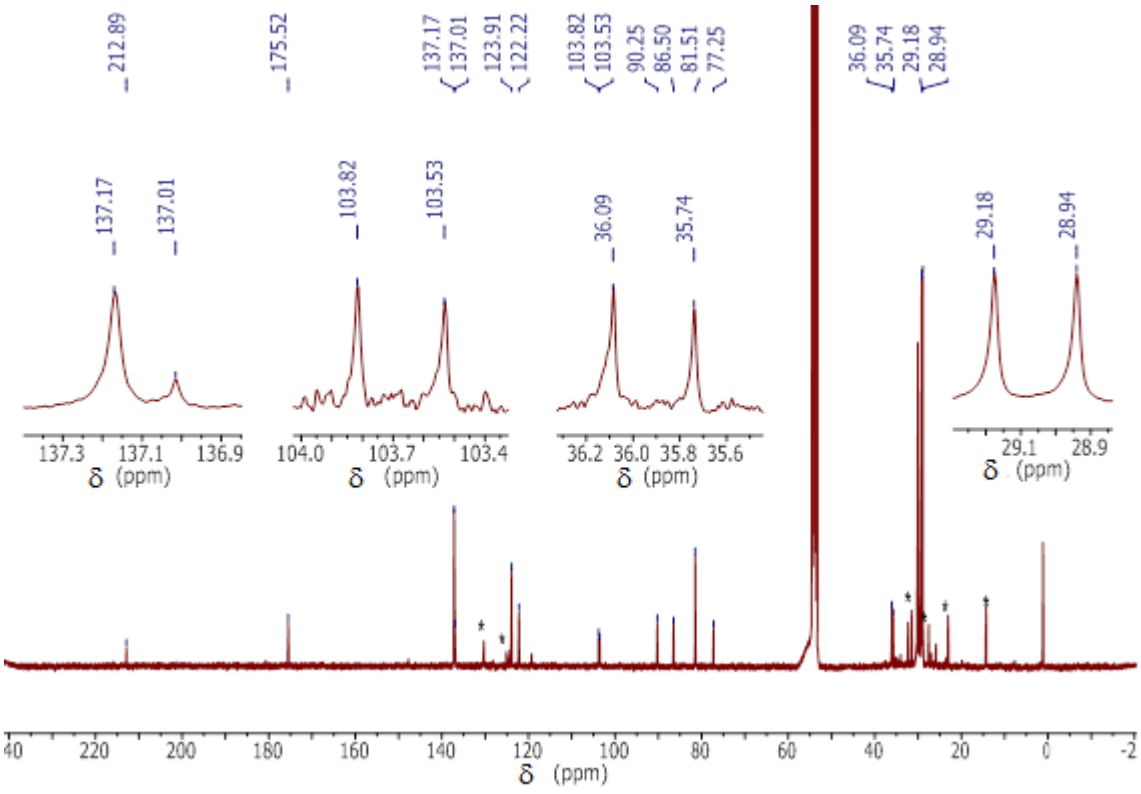

Figure 69. ^{13}C NMR spectrum of **3TCO**.

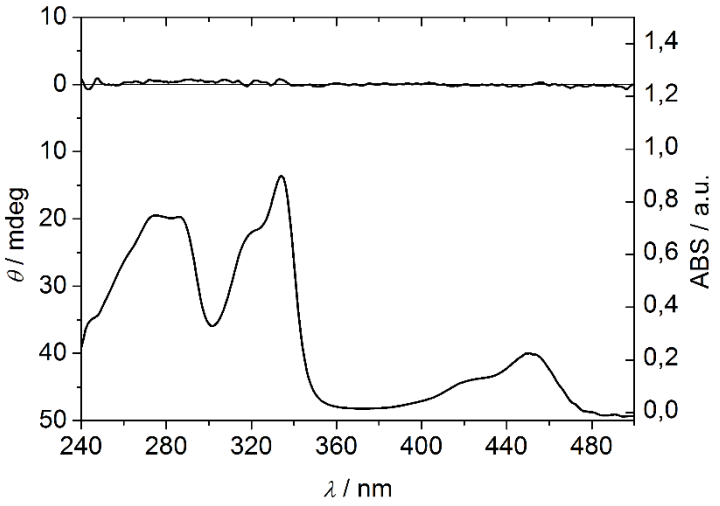

Figure 70. ECD (top) and UV/Vis (bottom) spectra of **3TCO**. **3TCO** presents no ECD spectrum between $7 \cdot 10^{-6}$ M and $2 \cdot 10^{-5}$ M.

6.8. Synthesis of (*M,M*)$_3$-1TMe.

2,6,10-Triiodo-4,4,8,8,12,12-hexamethyl-8,12-dihydro-4H-benzo[9,1]quinolizino[3,4,5,6,7-defg]acridine (TMeI$_3$)

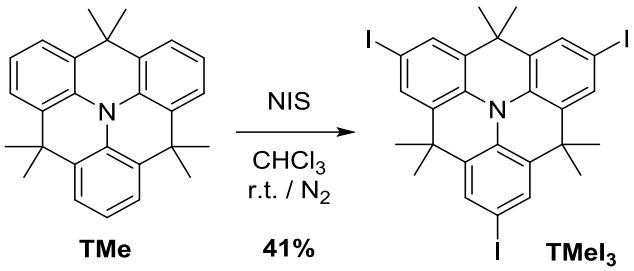

Scheme 30. Synthesis of **TMeI$_3$**.[19]

TMe (1 eq, 0.13 mmol, 48 mg) was dissolved in $CHCl_3$ (5 mL) in a round bottom flask under N_2 atmosphere. The flask was placed into an ice bath (0 °C) and NIS (3 eq, 0.39 mmol, 89 mg) was added in small portions. The mixture was allowed to react at r.t. for 2 days under N_2. FC (SiO_2, hexane) followed by recrystallization from dichloromethane afforded **TMeI$_3$** (40 mg, 41% yield).

^{1}H NMR (400 MHz, $CDCl_3$) δ = 7.60 (s, 6H$_{aromatic}$), 1.57 (s, 18H$_{Me}$) ppm.

^{13}C NMR (101 MHz, $CDCl_3$) δ = 132.5 (C$_{aromatic}$–H), 132.3 (C$_{aromatic}$–N), 131.5 (C$_{aromatic}$), 86.9 (C$_{aromatic}$–I) , 35.5 (C$_{quaternary\text{-}sp3}$), 32.9 (C$_{Me}$) ppm.

(*M,M,M*)-**2,6,10-Tris(5,7-di-*tert*-butyl-2-methylnona-5,6-dien-3,8-diyn-2-ol)-4,4,8,8,12,12-hexamethyl-8,12-dihydro-4H-benzo[9,1]quinolizino[3,4,5,6,7-defg]acridine (**(*M,M,M*)-**2TMe)**

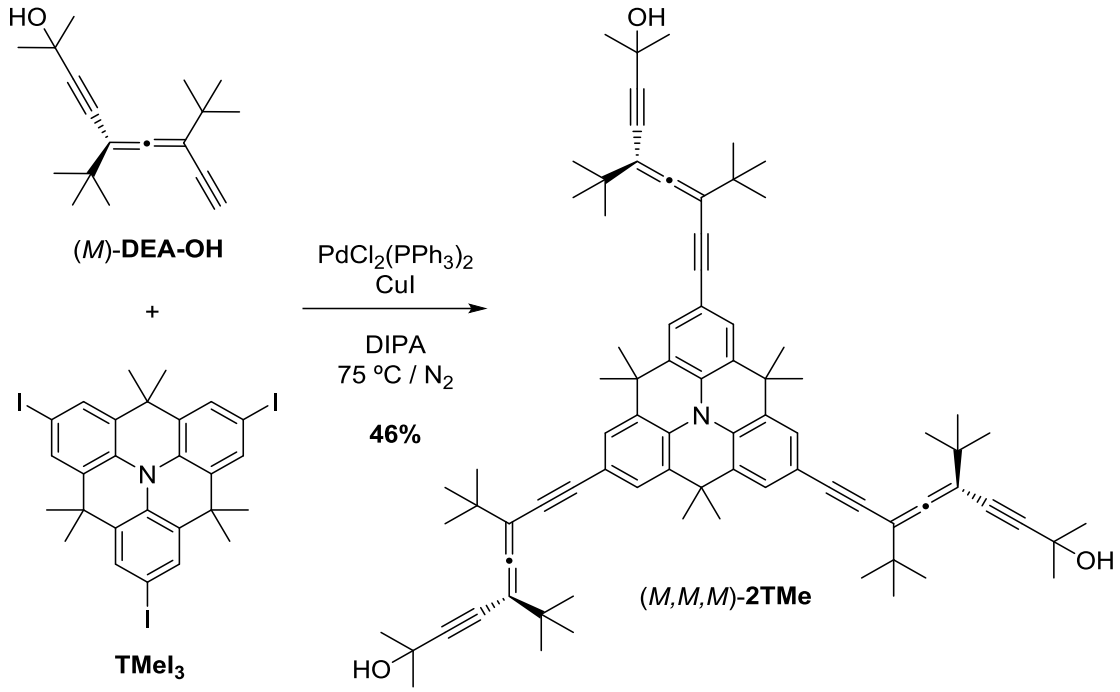

Scheme 31. Synthesis of (*M,M,M*)**-2TMe**.[20]

(*M*)-**DEA-OH** (3.3 eq, 0.1776 mmol, 46 mg) and **TMeI$_3$** (1 eq, 0.0538 mmol, 40 mg) were dissolved in dry DIPA (3 mL) in a round bottom flask and sparged with N_2 for 30 min. $PdCl_2(PPh_3)_2$ (16 mol%, 0.0086 mmol, 60 mg) and CuI (16 mol%, 0.0086 mmol, 2 mg) were dissolved in dry DIPA (3 mL) in a Schlenk tube and sparged with N_2 for 30 min. The first solution was added over the second one via cannula and the mixture was sparged with N_2 for 15 min. Then it was stirred and heated at 75 °C for 21 h. The mixture was treated with distilled water, extracted with DCM and washed with sat. aq. NH_4Cl. The combined aqueous phases were dried with anh. Na_2SO_4 and the solvent was evaporated under reduced pressure. FC purification (SiO_2, hexane:EtAcO 15 %) gave the product (*M,M,M*)-**2TMe** (28 mg, 46%) as a yellow oil.

^{1}H NMR (400 MHz, $CDCl_3$) δ = 7.45 (s, 6H$_{aromatic}$), 1.63 (s, 18H$_{Me\text{-}triangulene}$), 1.58 (s, 18H$_{Me\text{-}acetonide}$), 1.23 (s, 27H ^{t}Bu), 1.18 (s, 27H ^{t}Bu) ppm.

^{13}C NMR (101 MHz, $CDCl_3$) δ = 211.3 (C$_{cumulenic}$), 131.3 (C$_{aromatic}$), 130.2 (C$_{aromatic}$), 127.0 (C$_{aromatic}$), 118.5 (C$_{aromatic}$), 103.7 (C$_{alkene/alkyne}$), 102.7 (C$_{alkene/alkyne}$), 97.2 (C$_{alkene/alkyne}$), 93.1 (C$_{alkene/alkyne}$), 82.7 (C$_{alkene/alkyne}$), 76.2 (C$_{alkene/alkyne}$), 65.9 (C$_{quaternary\text{-}OH}$), 35.9 (C$_{quaternary\text{-}tBu}$), 35.7 (C$_{quaternary\text{-}tBu}$), 35.6 (C$_{quaternary\text{-}Me}$), 33.1 (C$_{Me\text{-}triangulene}$), 31.7 (C$_{Me\text{-}acetonide}$), 29.3 (C ^{t}Bu), 29.1 (C ^{t}Bu) ppm.

HR-ESI-MS *m/z* (%): $[M]^+$ calcd. for $^{12}C_{81}{}^{1}H_{99}{}^{14}N^{16}O_3$ 1133.762139, found: 1133.76250 (100).

IR ($CHCl_3$) ν = 3357 (br. w, str O–H), 2961 (s, str C$_{aromatic}$–H), 2863 (s, str C$_{aliphatic}$–H), 2360 (w), 2200 (w, str C$_{alkyne}$ΞC$_{alkyne}$), 1921 (w, str C$_{allene}$=C$_{allene}$), 1709 (w), 1594 (m, str C$_{aromatic}$=C$_{aromatic}$), 1439 (s, str C–N) cm^{-1}.

UV/Vis ($CHCl_3$) λ_{max} (nm): 378, 332, 279 (sh.). ε (378 nm) = 49101 $M^{-1}\cdot cm^{-1}$.

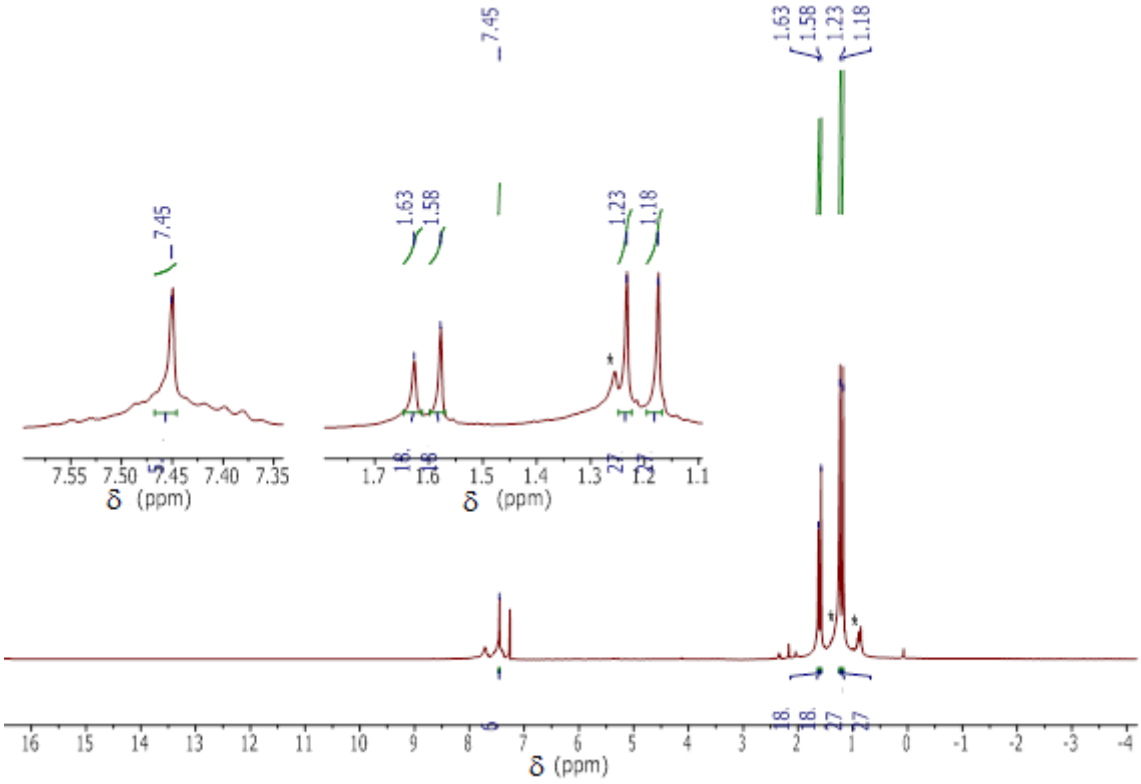

Figure 71. ^{1}H NMR spectrum of (*M,M,M*)-**2TMe**.

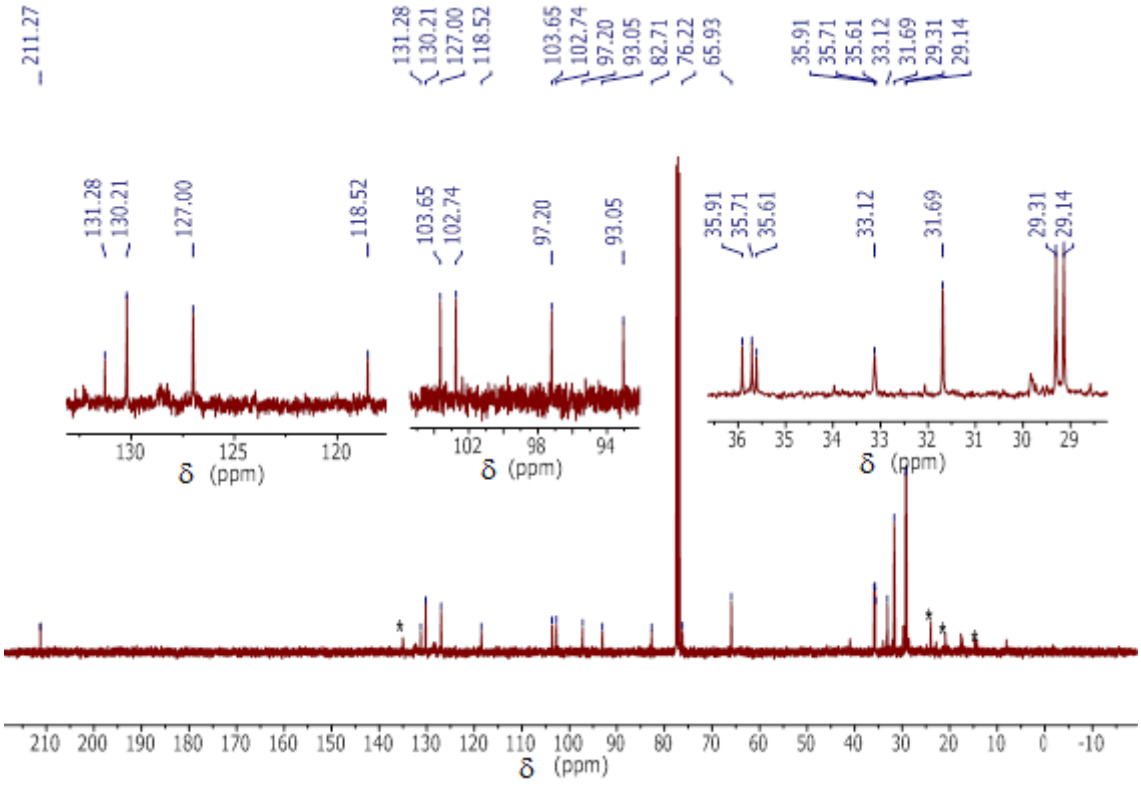

Figure 72. ^{13}C NMR spectrum of (*M,M,M*)-**2TMe**.

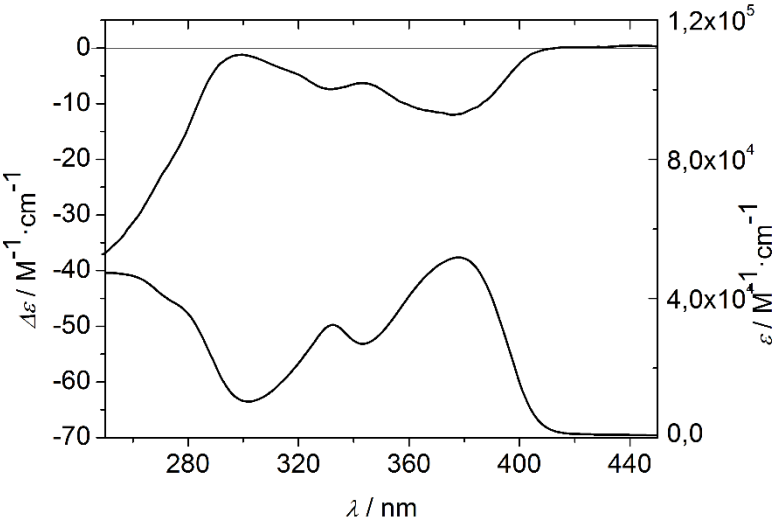

Figure 73. ECD (top) and UV/Vis (bottom) spectra of (*M,M,M*)-**2TMe** in $CHCl_3$.

(*M*)-**Monocoupled Product Data** **((*M*)-MC-2TMe)**

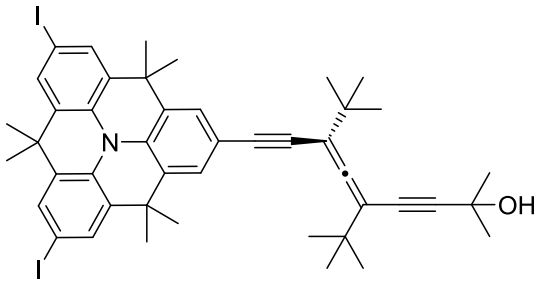

(*M*)-**MC-2TMe**

Figure 74. Structure of (*M*)-**MC-2TMe**.

^{1}H NMR (400 MHz, $CDCl_3$) δ = 7.61 (d, *J* = 2.1 Hz, $2H_{ar}$), 7.59 (d, *J* = 1.8 Hz, $2H_{ar}$), 7.43 (s, $2H_{ar}$), 1.59 (s, 12H, 4 x Me **TMe**), 1.58 (s, 6H, 2xMe -CMe_2OH + H_2O), 1.56 (s, 6H, 2 x Me **TMe**), 1.23 (s, 9H, ^{t}Bu), 1.17 (s, 9H, ^{t}Bu) ppm.

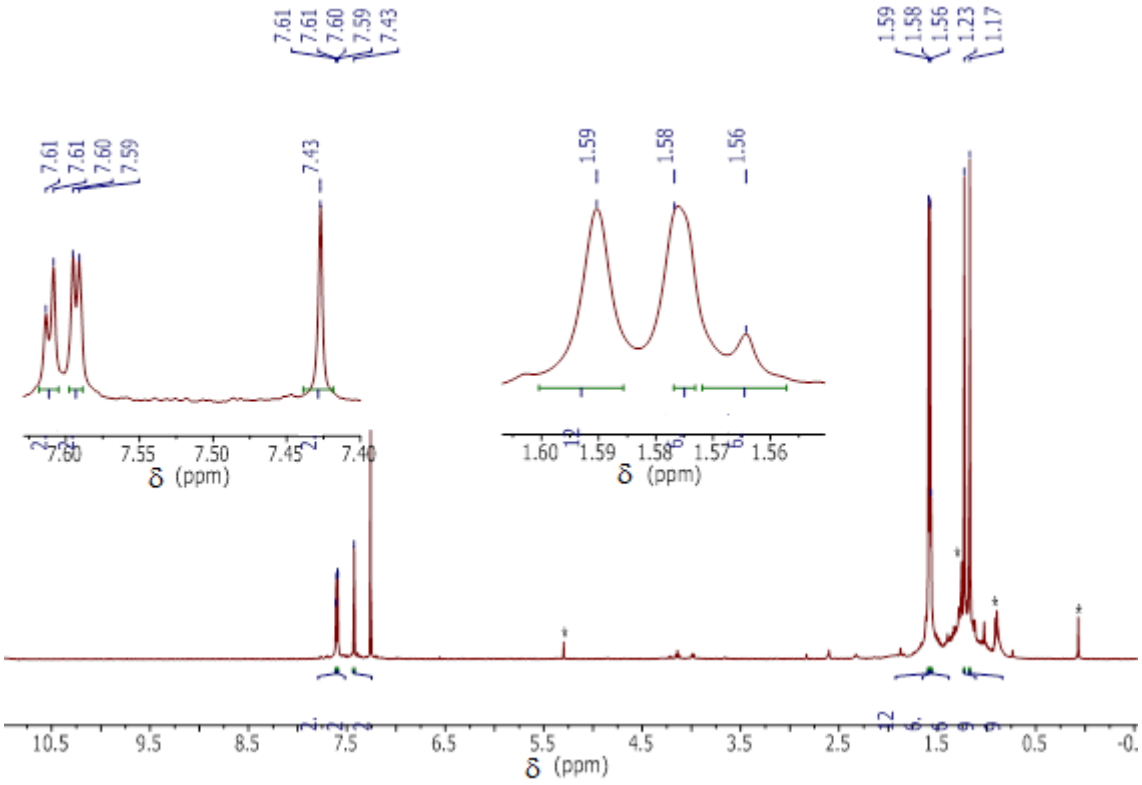

Figure 75. ^{1}H NMR of (*M*)-**MC-2TMe**.

Data of (*M,M*)-**DC-2TMe**

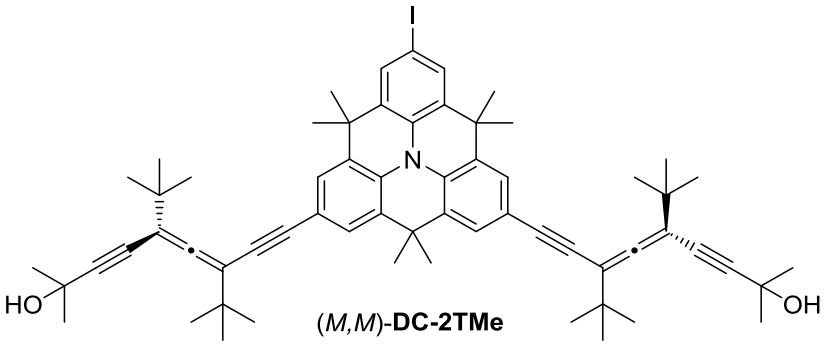

Figure 76. Structure of (*M,M*)-**DC-2TMe**.

^{1}H NMR (400 MHz, Chloroform-*d*) δ = 7.61 (s, 2H$_{ar}$), 7.45 (d, *J* = 1.8 Hz, 2H$_{ar}$), 7.43 (d, *J* = 1.8 Hz, 2H$_{ar}$), 1.62 (s, 6H, 2 x Me **TMe**), 1.60 (s, 12H, 4 x Me **TMe**), 1.58 (s, 12H, 4 x Me –CMe$_2$OH + H$_2$O), 1.23 (s, 18H, 2 x ^{t}Bu), 1.17 (s, 18H, 2 x ^{t}Bu) ppm.

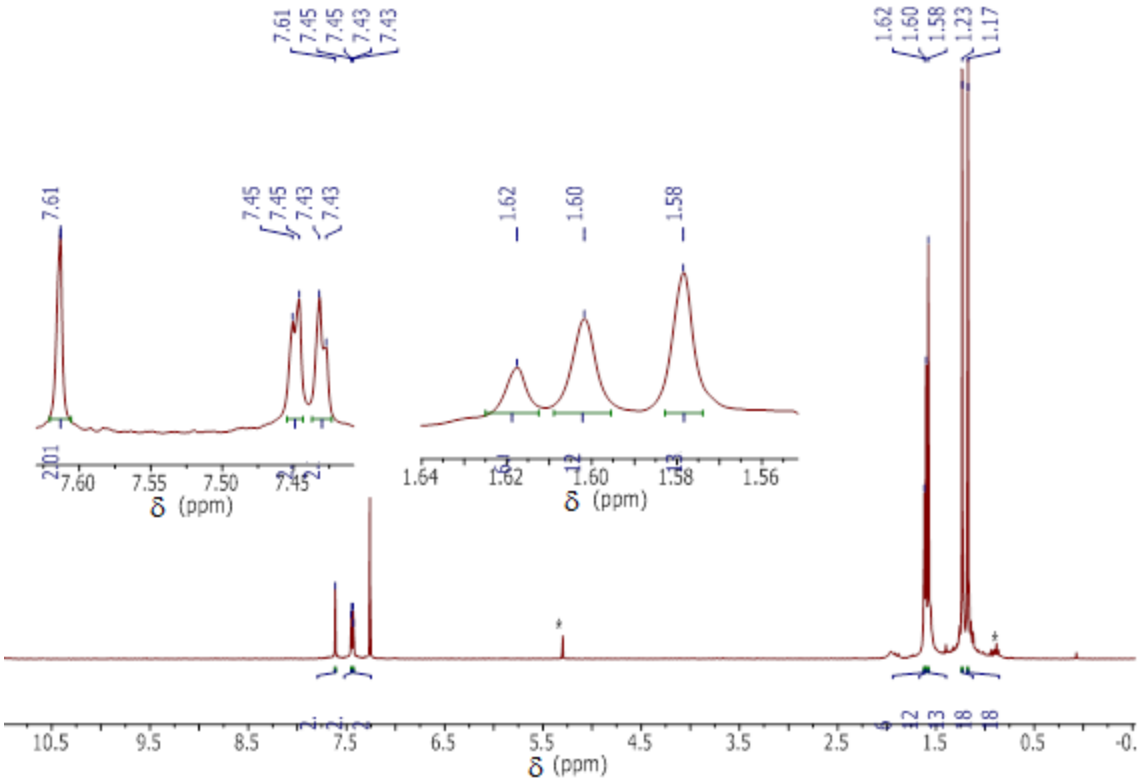

Figure 77. ^{1}H NMR of (*M,M*)-**DC-2TMe**.

(*M,M,M*)-**2,6,10-Tris(3,5-di-*tert*-butylhepta-3,4-dien-1,6-diyn-1-yl)-4,4,8,8,12,12-hexamethyl-8,12-dihydro-4H-benzo[9,1]quinolizino[3,4,5,6,7-defg]acridine (**(*M,M,M*)-**3TMe)**.

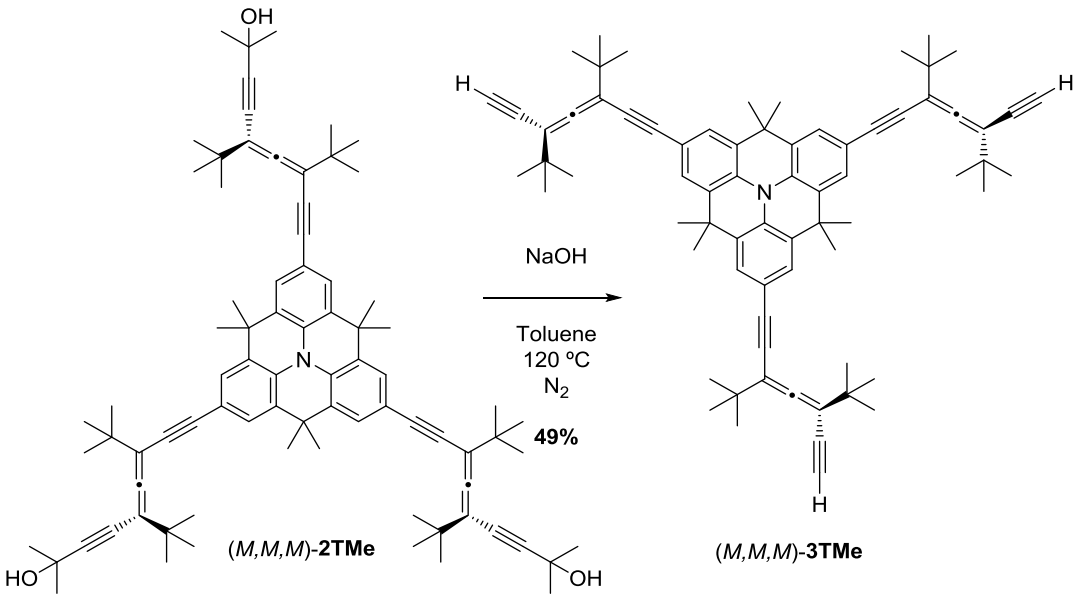

Scheme 32. Synthesis of (*M,M,M*)-**3TMe**.

(*M,M,M*)-**2TMe** (1 eq, 0.0106 mmol, 12 mg) and flamed powdered NaOH (709 eq, 7.4948 mmol, 300 mg) were placed into a round bottom flask and dissolved in dry Toluene (10 mL) under N_2. The mixture was allowed to react for 1.5 h and then treated with distilled water and extracted with EtOAc. The combined organic phases were dried with anh. Na_2SO_4 and the solvent was removed under reduced pressure. FC (SiO_2, hexane:DCM 10%) of the mixture afforded (*M,M,M*)-**3TMe** (5 mg, 49% yield).

^{1}H NMR (400 MHz, $CDCl_3$) δ = 7.45 (s, $6H_{ar}$), 3.02 (s, $3H_{alkyne}$), 1.63 (s, 18H, 6 x Me **TMe**), 1.24 (s, 27H, 3 x ^{t}Bu), 1.20 (s, 27H, 3 x ^{t}Bu) ppm.

^{13}C NMR (101 MHz, $CDCl_3$) δ = 212.1 ($C_{cumulenic}$), 131.3, 130.2, 127.0, 118.5 ($C_{aromatic}$), 104.2, 102.4 (C_{alkene}), 93.4, 82.4, 80.4, 77.9 (C_{alkyne}), 36.0, 35.6 ($C_{quaternary\text{-}tBu}$), 35.5 ($C_{quaternary\text{-}Me\ triangulene}$), 33.2 ($C_{6xMe\text{-}triangulene}$), 29.3, 29.0 (C ^{t}Bu) ppm.

IR ($CHCl_3$) 3287 (s, str C–$H_{terminal\ alkyne}$), 2961 (s, str $C_{aromatic}$–H), 2865 (s, str $C_{aliphatic}$–H), 2361 (w), 2197 (w, str C_{alkyne}ΞC_{alkyne}), 2093 (w), 1926 (w, str C_{allene}=C_{allene}), 1641 (w), 1597 (m, str $C_{aromatic}$=$C_{aromatic}$), 1438 (s, str C–N) cm^{-1}.

UV/Vis ($CHCl_3$) λ_{max} (nm): 378, 332, 277. ε (378 nm) = 70871 $M^{-1}\cdot cm^{-1}$.

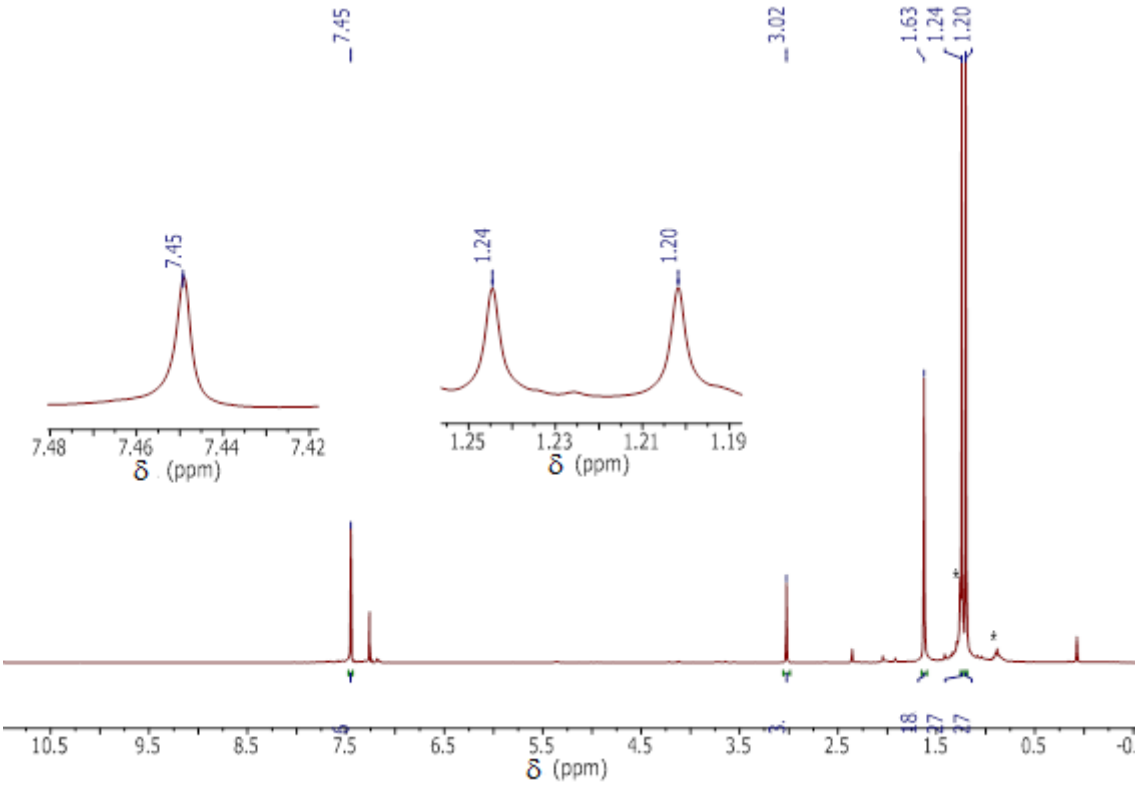

Figure 78. ^{1}H NMR spectrum of (*M,M,M*)-**3TMe**.

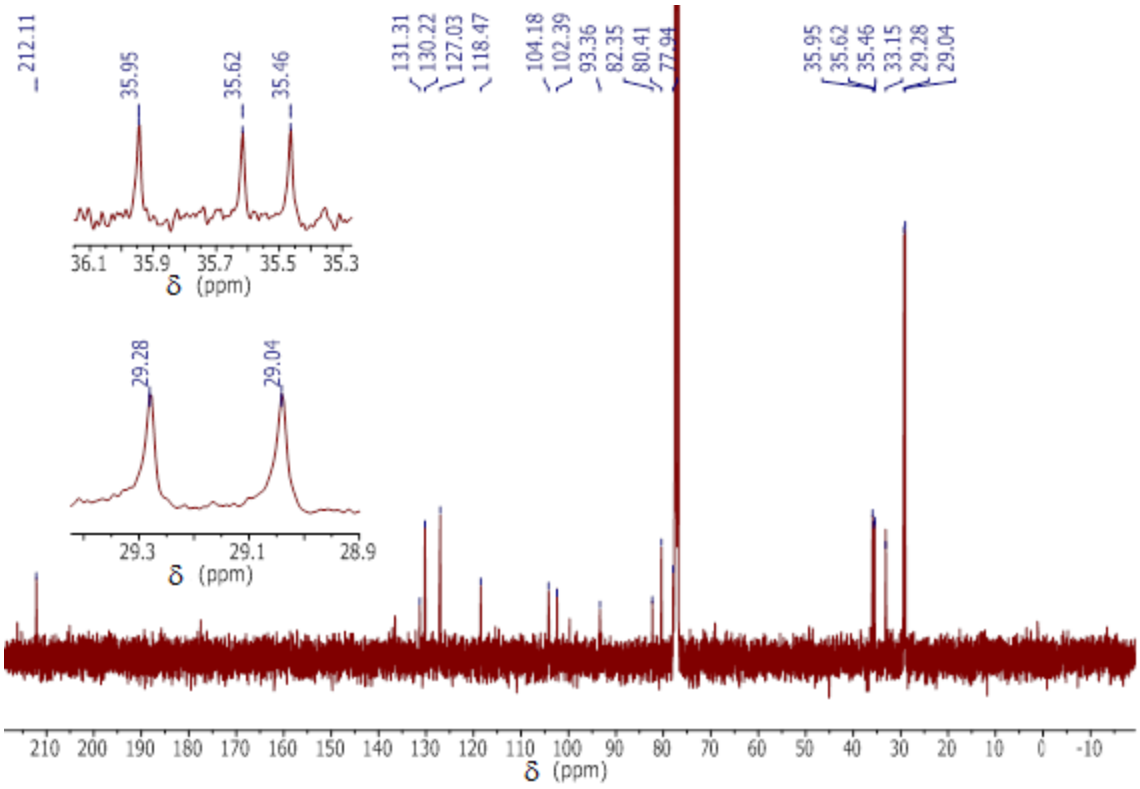

Figure 79. ^{13}C NMR spectrum of (*M,M,M*)-**3TMe**.

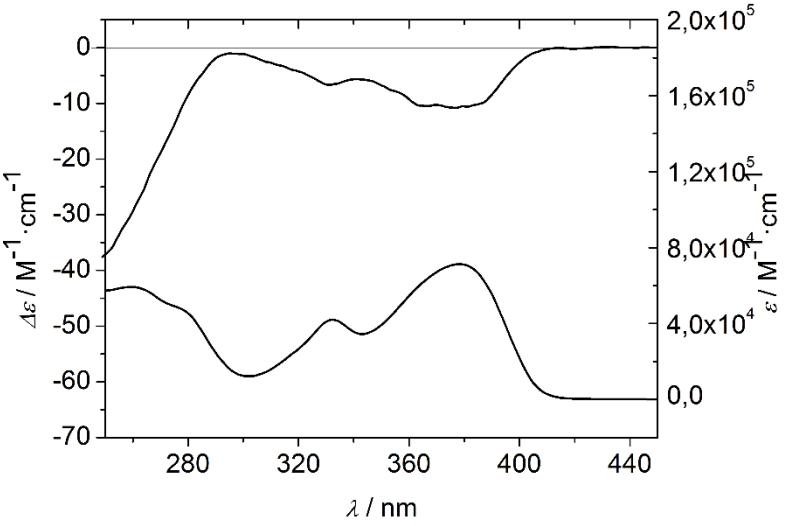

Figure 80. ECD (top) and UV/Vis (bottom) spectra of (*M,M,M*)-**3TMe** in $CHCl_3$.

(M,M)$_3$-4,6,11,13,19,21,26,28,33,35,40,42-Dodeca-*tert*-butyl-1,16-(2,6,10)- 4,4,8,8,12,12-hexamethyl-8,12-dihydro-4H-benzo[9,1]quinolizino[3,4,5,6,7-defg]acridinebicyclotetratetracontaphane-4,5,11,12,19,20,26,27,33,34,40,41-dodecaen-2,7,9,14,17,22,24,29,31,36,38,43-dodecayne ((M,M)$_3$-1TMe)

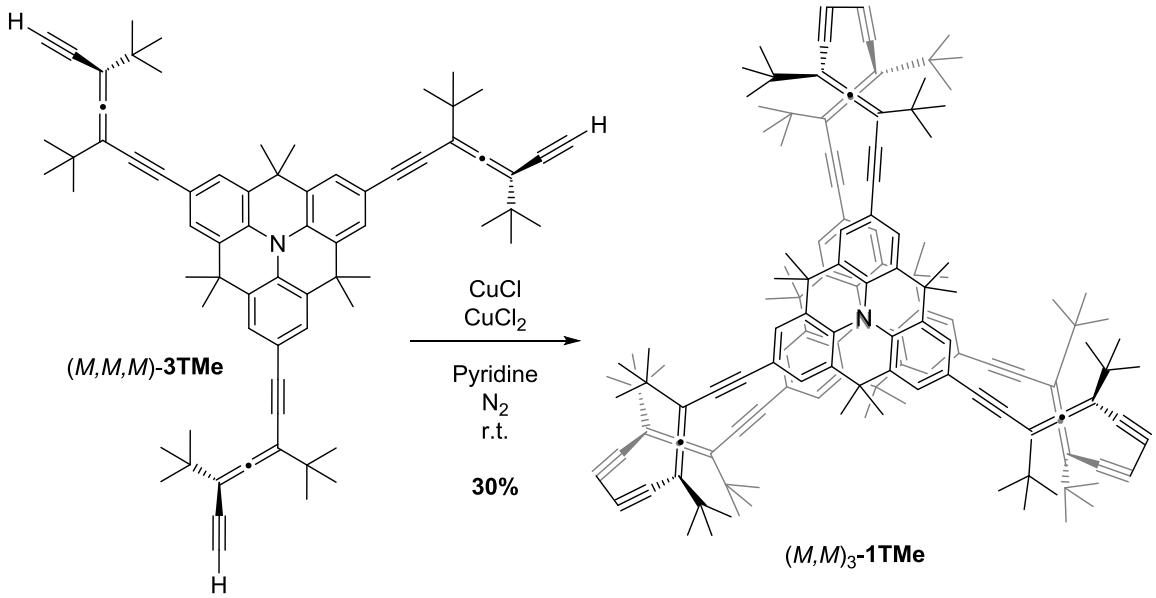

Scheme 33. Synthesis of (M,M)$_3$-**1TMe**.

Solution A: (*M,M,M*)-**3TMe** (1 eq, 0.0052 mmol, 5 mg) was dissolved in dry pyridine (10 mL) and bubbled for 1 h with N_2 into a round bottom flask.

Solution B: A mixture of CuCl (75 eq, 0.3904 mmol, 39 mg) and $CuCl_2$ (11 eq, 0.0573 mmol, 8 mg) was dissolved in dry pyridine (10 mL) and bubbled for 1 h with N_2 into a round bottom flask.

Solution A was slowly added with the help of a mechanic syringe (ϕ = 1 mL·h^{-1}) over *Solution B* under N_2. The reaction was allowed to react for 3 days. Pyridine was evaporated under reduced pressure and then the mixture was treated with aq. sat. NH_4Cl solution. The aq. phase was extracted with dichloromethane, dried with anh. Na_2SO_4, filtered and the solvent was removed under reduced pressure. FC (SiO_2, Increasing polarity from hexane to hexane:DCM 10%) gave the product (1.5 mg, 30% yield).

^{1}H NMR (400 MHz, $CDCl_3$) δ = 7.33 (d, *J* = 1.9 Hz, 6H$_{ar}$), 7.30 (d, *J* = 1.9 Hz, 6H$_{ar}$), 1.66 (s, 18H, 6xMe$_{triang}$), 1.37 (s, 18H, 6xMe$_{triang}$), 1.23 (s, 54H, 6x^{t}Bu), 1.21 (s, 54H, 6x^{t}Bu) ppm.

^{13}C NMR (101 MHz, $CDCl_3$) δ = 214.8 (C$_{cumulenic}$), 131.4, 130.1, 130.0, 126.8, 126.6, 118.3 (C$_{aromatic}$), 104.8, 103.2 (C$_{alkene}$), 94.4, 82.2, 77.4, 76.1 (C$_{alkyne}$), 35.8, 35.7, 35.5, 35.3 (2xC$_{quat.\ ^tBu}$ + C$_{quaternary\text{-}Me\ triangulene}$+C$_{Me\ triangulene}$), 30.4 (C$_{Me\ triangulene}$), 29.33, 29.28 (C ^{t}Bu) ppm.

HSQC$_{ed}$ and **HMBC** ($CHCl_3$)

UV/Vis ($CHCl_3$) λ$_{max}$ (nm): 381, 334, 266. $\varepsilon_{378\ nm}$ = 108364 M^{-1}·cm^{-1}. ***g*-factor$_{max}^{306\ nm}$** = 0.007.

HR-MALDI-MS *m/z* (%): $[M+H]^+$ calcd. for $^{12}C_{144}{}^{1}H_{157}{}^{14}N_2$ 1915.23749, found: 1915.23473 (100); $[M+H]^+$ calcd. for 1914.2341, found: 1914.22871 (64); $[M+H]^+$ calcd. for $^{13}C\ ^{12}C_{143}{}^{1}H_{157}{}^{14}N_2$ 1916.2408, found: 1916.23796 (78); $[M - Me]^+$ calcd. for $^{12}C_{143}{}^{1}H_{153}{}^{14}N_2$ 1899.2062, found: 1899.20413 (100); $[M - Me]^+$ calcd. for $^{13}C\ ^{12}C_{142}{}^{1}H_{153}{}^{14}N_2$ 1900.2101, found: 1900.20448 (58).

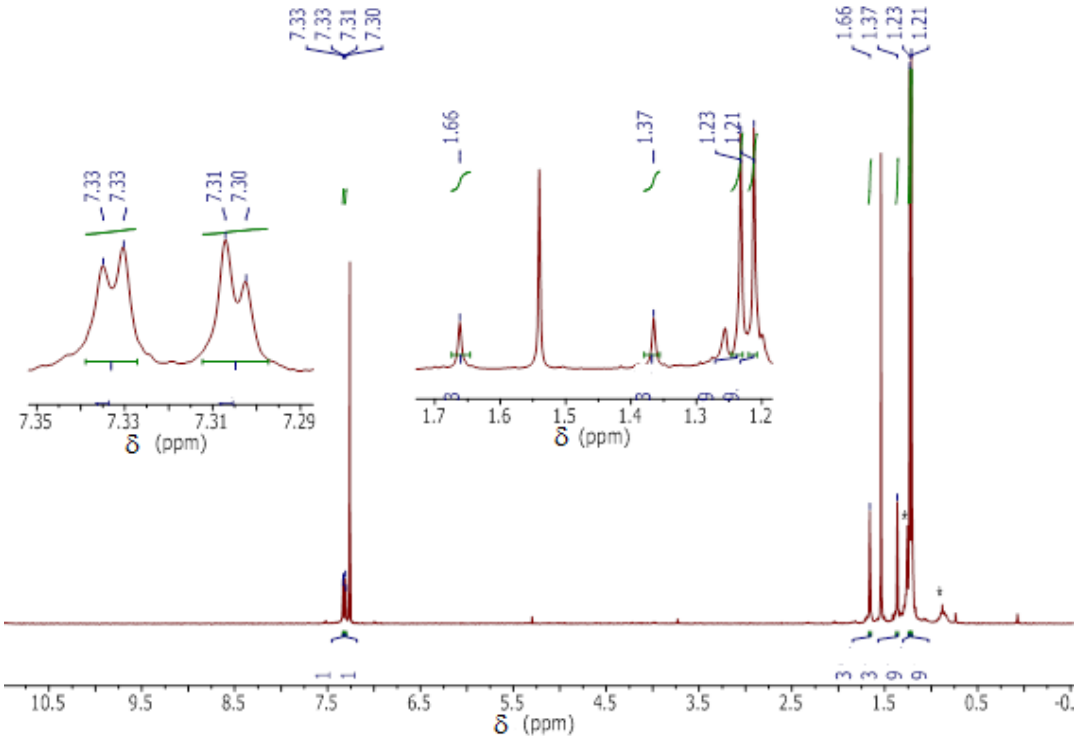

Figure 81. ^{1}H NMR spectrum of $(M,M)_3$-**1TMe**.

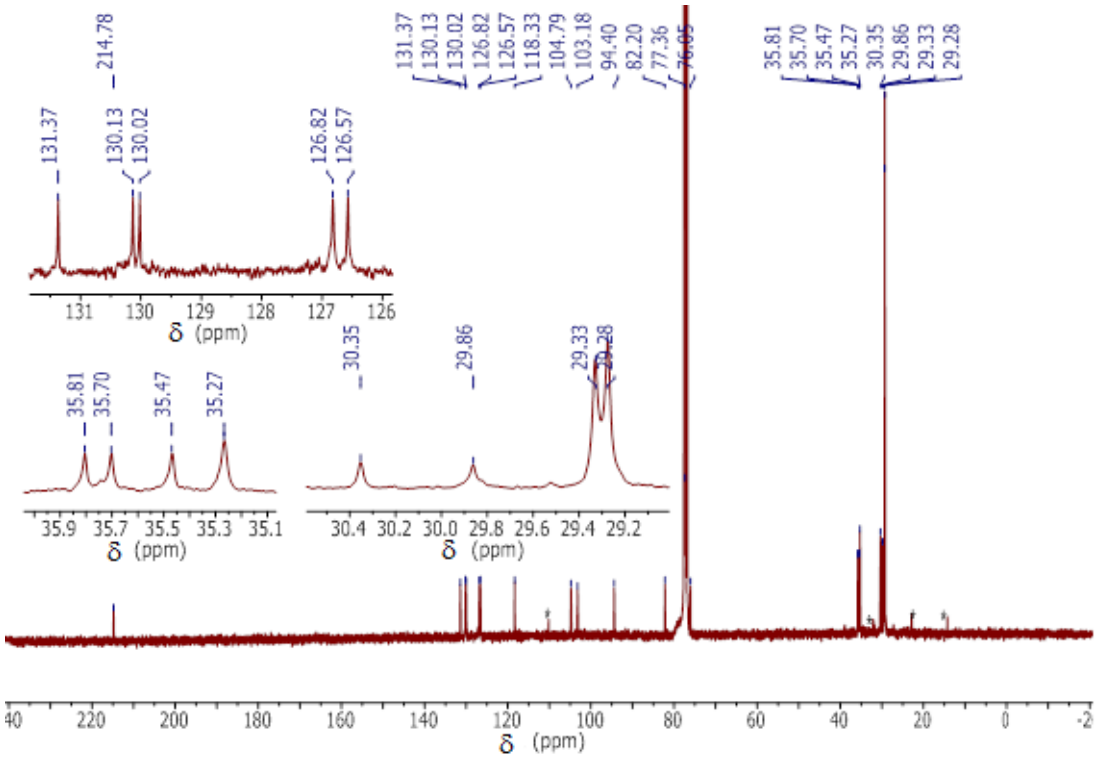

Figure 82. ^{13}C NMR spectrum of $(M,M)_3$-**1TMe**.

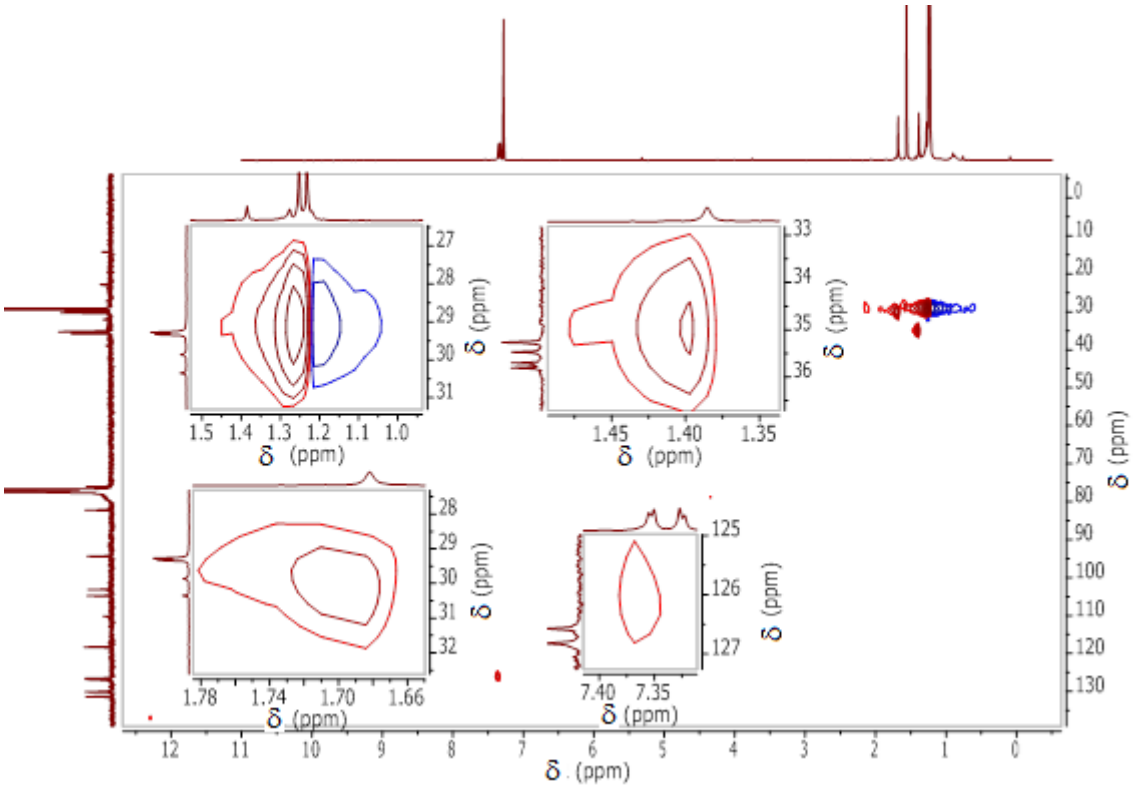

Figure 83. HSQC$_{ed}$ NMR spectrum of $(M,M)_3$-**1TMe**.

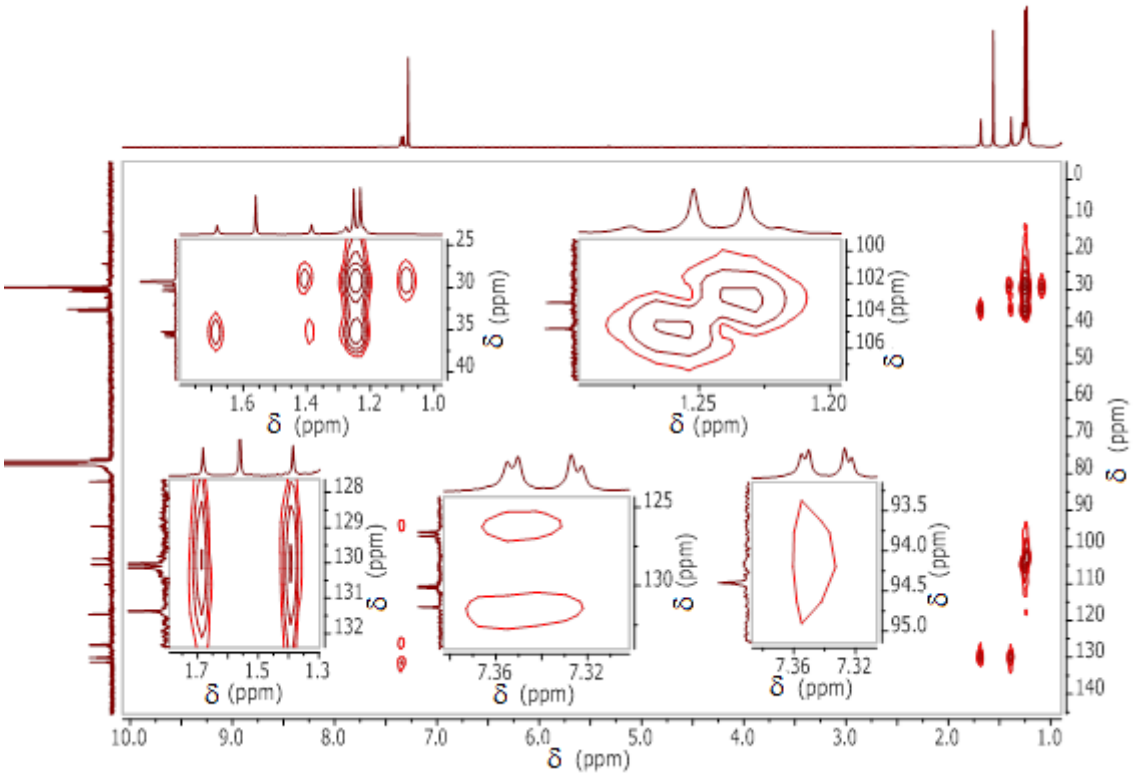

Figure 84. HMBC NMR spectrum of $(M,M)_3$-**1TMe**.

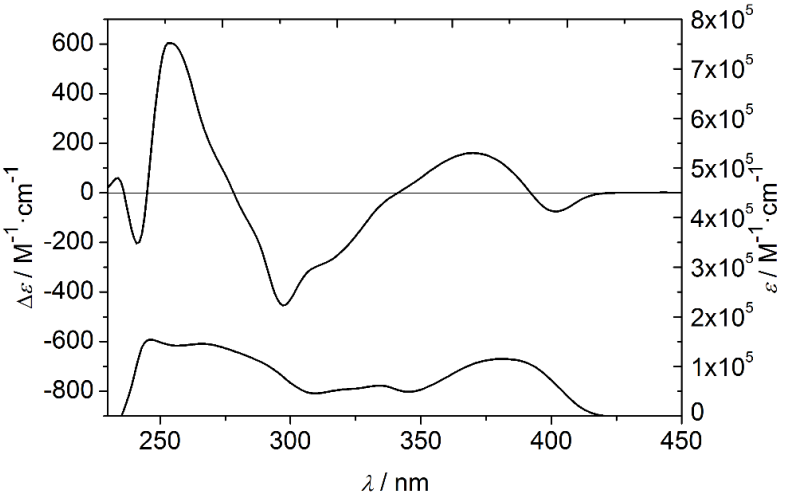

Figure 85. ECD (top) and UV/Vis (bottom) spectra of (*M,M*)$_3$-**1TMe** in $CHCl_3$.

6.9. References.

[1] J. L. Alonso-Gómez, P. Schanen, P. Rivera-Fuentes, P. Seiler, and F. Diederich, *Chem. Eur. J.* **2008**, *14*, 10564–10568.

[2] P. van der Sluis, and A. L. Spek, *Acta Crystallogr. Sect. A Found. Crystallogr.* **1990**, *46*, 194–201.

[3] A. L. Spek, *Acta Crystallogr. Sect. D Biol. Crystallogr.* **2009**, *65*, 148–155.

[4] R. H. Blessing, *Acta Crystallogr. Sect. A* **1995**, *51*, 33–38.

[5] T. R. Schneider, and G. M. Sheldrick, *Acta Crystallogr. Sect. D* **2002**, *58*, 1772–1779.

[6] G. M. Sheldrick, *Acta Crystallogr. Sect. A* **2008**, *64*, 112–122.

[7] L. J. Farrugia, *J. Appl. Crystallogr.* **2012**, *45*, 849–854.

[8] S. Míguez-Lago, A. L. Llamas-Saiz, M. Magdalena Cid, and J. L. Alonso-Gómez, *Chem. Eur. J.* **2015**, *21*, 18085–18088.

[9] S. Kumar, and M. Manickam, *Chem. Commun.* **1997**, *14*, 1615–1616.

[10] K.-I. Yamashita, M. Tsuboi, M. S. Asano, and K.-I. Sugiura, *Synth. Commun.* **2012**, *42*, 170–175.

[11] G. Hennrich, V. M. Lynch, and E. V. Anslyn, *Chem. Eur. J.* **2002**, *8*, 2274–2278.

[12] Q. Sun, L. Cai, H. Ma, C. Yuan, and W. Xu, *ACS Nano* **2016**, *10*, 7023–7030.

[13] N. G. Connelly, and W. E. Geiger, *Chem. Rev.* **1996**, *96*, 877–910.

[14] D. Trawny, V. Kunz, and H.-U. Reissig, *Eur. J. Org. Chem.* **2014**, 6295–6302.

[15] Y. Li, L. Xu, S. L.-F. Chan, Y. Li, R. Jiang, H. Liu, and C.-M. Che, *Chem. Asian J.* **2014**, *9*, 2842–2849.

[16] J. Lieffrig, O. Jeannin, and M. Fourmigué, *J. Am. Chem. Soc.* **2013**, *135*, 6200–6210.

[17] G. Hennrich, and A. M. Echavarren, *Tetrahedron Lett.* **2004**, *45*, 1147–1149.

[18] M. Kivala, W. Pisula, S. Wang, A. Mavrinskiy, J.-P. Gisselbrecht, X. Feng, and K. Müllen, *Chem. Eur. J.* **2013**, *19*, 8117–8128.

[19] Z. Fang, T.-L. Teo, L. Cai, Y.-H. Lai, A. Samoc, and M. Samoc, *Org. Lett.* **2009**, *11*, 1–4.

[20] Z. Fang, X. Zhang, Y. Hing Lai, and B. Liu, *Chem. Commun.* **2009**, *22*, 920–922.

7. Resumo

As caixas moleculares poden ser definidas como moléculas cunha cavidade permanente co tamaño, forma, e funcionalidades adecuadas para interaccionar con unha ou mais moléculas hóspede (guest), dando lugar a unha ampla variedade de aplicacións. Atendendo ás interaccións que manteñen as partes constituíntes das devanditas caixas unidas, atopámonos con diferentes tipos de caixas moleculares (**Figura 1**). As caixas supramoleculares, cuxos constituíntes se atopan unidos por enlaces febles, tales coma enlaces de hidróxeno ou halóxeno, interaccións π–π en tódalas súas modalidades, forzas de Van der Waals, interaccións dipolo–dipolo, etc, presentan a desvantaxe de non seres moi estables, feito que as favorece noutros aspectos ó mesmo tempo. Exemplos de caixas supramoleculares son as reportadas por Rebek e colaboradores. As caixas covalentes, dentro das cales nos atopamos coas metalorgánicas e as puramente orgánicas, son, con todo, mais estables, xa que os seus enlaces constitutivos son mais fortes. As metalorgánicas, entre as cales se atopan os exemplos das caixas de Fujita e colaboradores, son vastas na bibliografía, mais teñen a desvantaxe de seres lábiles, característica típica dos enlaces metal–non metal. Por outra banda, as caixas covalentes puramente orgánicas presentan grande estabilidade. A pesar disto, unha das correntes químicas nas que se reportaron un grande número de exemplos de caixas puramente orgánicas é a química dinámica covalente, na que as especies formadas se atopan en equilibrio cos produtos de partida. Dita técnica permitiu a síntese de caixas covalentes a gran escala, o que permitiu a súa aplicación en campos tan diversos coma o encapsulamento de gases de efecto invernadoiro, formación de fases estacionarias quirais para a separación de racematos, e detección de outras moléculas en sensores. Pese a abundancia de caixas orgánicas en literatura, as caixas quirais atópanse en minoría con respecto do resto debido á dificultade no manexo de compostos quirais, ben por problema de racemización, ben pola tediosa separación de diastereómeros que conleva. A súa escaseza, xunto a súa grande aplicabilidade, fanas un obxectivo moi interesante.

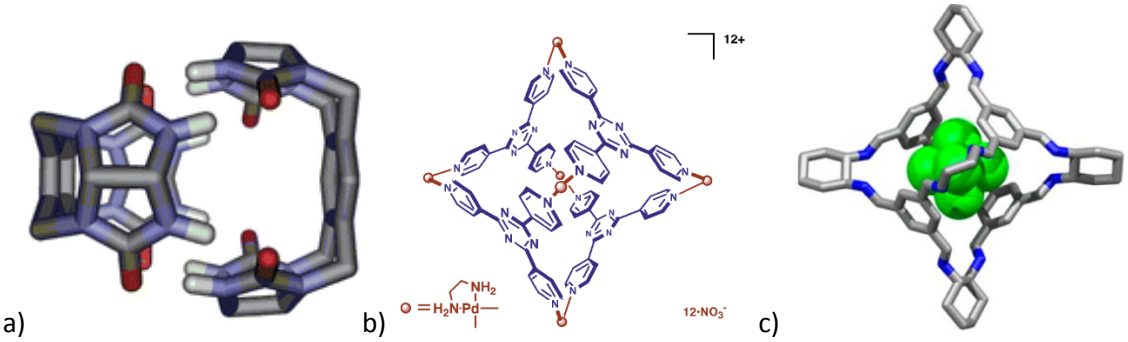

Figura 1. a) Pelota de tennis de Rebek unida por enlaces de hidróxeno. b) Caixa metalorgánica de Fujita. c) Caixa covalente de Wang con molécula de SF_6 no seu interior.

Os compostos quirais son aqueles que non son superpoñibles coa súa imaxe especular. A natureza está chea de exemplos de moléculas e macromoléculas quirais, tales coma o ADN e as proteínas, entre outras. A orixe desta homoquiralidade na natureza non é clara, mais si se sabe como introducila ou recoñecela en calquera molécula. Tradicionalmente esta ven dada pola presenza de centros quirais, mais tamén pode ser debida á presenza de eixos ou planos quirais (**Figura 2**). A quiralidade axial é aquela presente en moléculas coma os alenos, espiranos, ou diarilos adecuadamente substituídos.

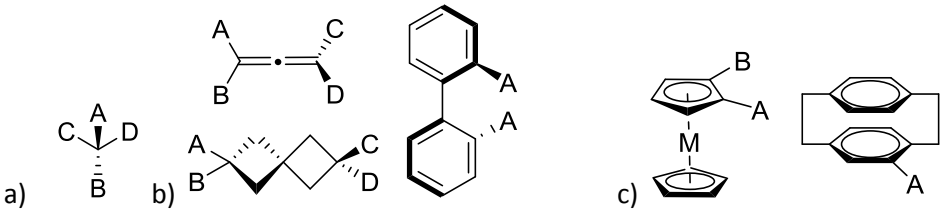

Figura 2. Representación esquemática de a) Centro quiral. b) Eixos quirais. c) Planos quirais.

Os alenos posúen dous dobres enlaces contiguos nun arranxo lineal, cun átomo de carbono central con hibridación *sp* e ámbolos dous pares de substituíntes xacendo en planos ortogonais. Os dous posibles enantiómeros denótanse cos descriptores (*P*) e (*M*) (**Figura 3**). Os alenos atópanse en produtos naturais e farmacéuticos de diversa índole, e o método de síntese mais comunmente empregado destes é a substitución de compostos proparxílicos.

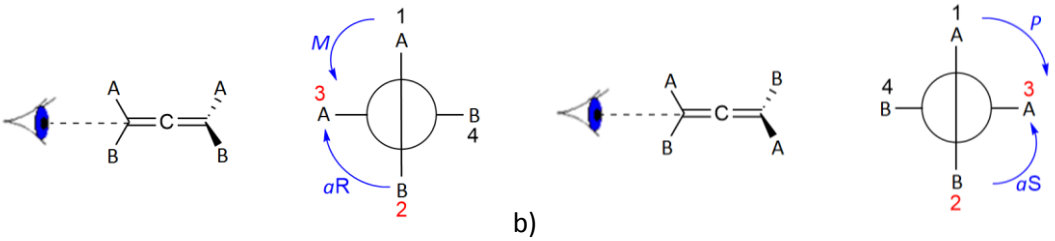

Figura 3. Exemplo de nomenclatura dun par de enantiómeros de aleno quirais. a) Configuración (*M*). b) Configuración (*P*).

Un exemplo de aleno quimicamente estable e ríxido é o di*tert*butildietinilaleno (DEA), o cal foi empregado na síntese de polímeros, macrociclos e caixas moleculares con propiedades quirópticas notorias (**Figura 4**). Ditas propiedades son comunmente medidas empregando técnicas espectroscópicas, entre as que cabe destacar o dicroismo circular electrónico (ECD), baseado na interacción dunha luz circularmente polarizada coa molécula quiral en cuestión. Aquí a luz UV circularmente polarizada á dereita e á esquerda é absorbida de xeito diferente, dando lugar a unha sinal que se converte nun espectro que representa a elipticidade fronte á lonxitude de onda. Un xeito de medir a intensidade desta resposta quiróptica é o cálculo do factor de disimetría (*g*-factor), como $\Delta\varepsilon/\varepsilon$, con valores entre 0 e 1, que está directamente relacionado coa rixidez estrutural da molécula en cuestión.

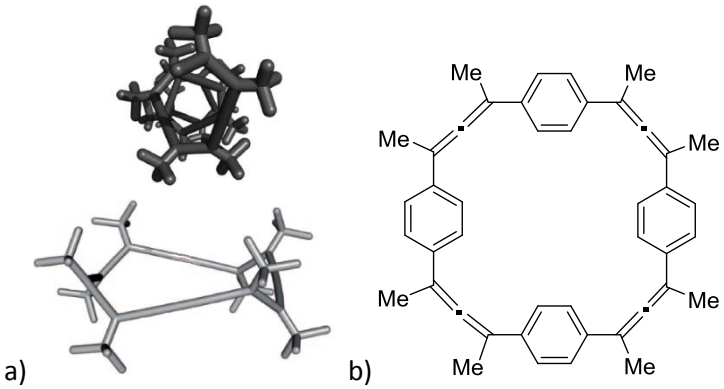

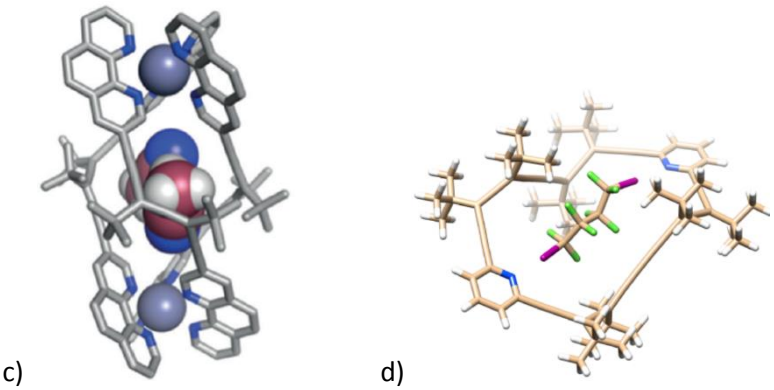

c) d)

Figura 4. a) Oligómeros de aleno cíclicos (abaixo) e acíclicos (arriba). b) Primeiro alenofano reportado por Krause e colaboradores. c) Caixa metalorgánica reportada por Diederich e colaboradores. d) Alenofano formando un complexo de inclusión cun diiodoperfluoroalcano reportado por Cid e colaboradores.

Dada a habilidade para o recoñecemento molecular que presentan as caixas moleculares así coma a abundancia de analitos quirais de interese, postúlase o desenrolo de caixas moleculares quirais para a súa aplicación en sensores coma unha meta para a comunidade científica. Para seres aplicables no mundo da sensóricas ditas caixas moleculares deben ser estruturalmente ríxidas, evitando a diminución da sinal polo promediado conformacional. Os poliedros son figuras xeométricas formadas por caras planas que definen un volume constante, dos cales atopamos exemplos coma as cápsides de virus, os paneis das abellas e a cuberta dos carboxisomas na propia natureza. Un caso particular de poliedros son os *n*-prismas, os cales se poden converter en xeometrías quirais pola introdución dun xiro entorno ó seu eixo de maior grao (**Esquema 1**).

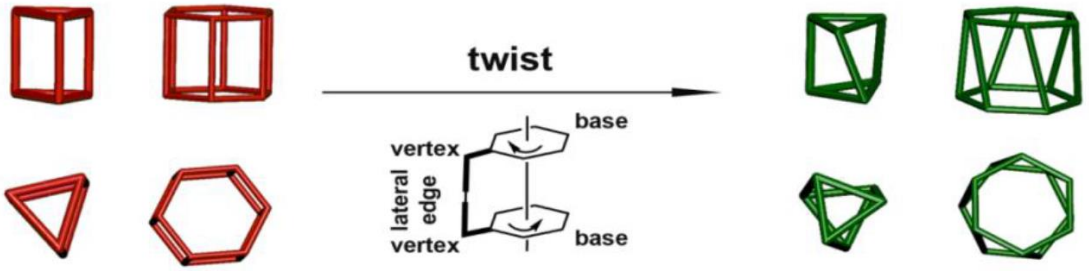

Esquema 1. De esquerda a dereita: N-prismas trigonais e hexagonais con N o número de lados. En vermello os prismas pertencentes ó grupo aquiral D_{nh} e en verde os prismas pertencentes ó grupo D_n. Vista lateral (arriba) e vista superior (abaixo).

Ademais, ó posuíren eixos C_2 poden ser construídos a través da dimerización de dúas metades idénticas. Isto lévanos a propoñer o deseño de caixas moleculares quirais ríxidas en forma de prismas torcidos, onde a súa síntese se leva a cabo empregando un proceso de dimerización, concretamente do membro mais sinxelo desta familia, o prisma de base triangular. Coma tapas do prisma empregaranse moléculas planas de simetría C_3 ás que se acoplarán tres partes axialmente quirais, que darán lugar ós vértices (**Figura 5**).

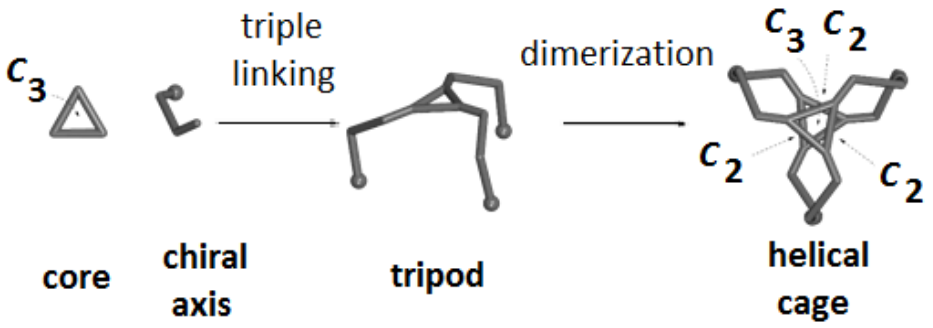

Figura 5. Representación esquemática da estratexia sintética para construír caixas moleculares quirais.

A síntese de ditas caixas moleculares en forma de prisma trigonal torcido pode levarse a cabo a partir do elemento axialmente quiral racémico, seguido da separación dos correspondentes diastereómeros ou ben empregando o enantiopuro, previa resolución quiral. Trala análise da formación dos posibles diastereómeros no caso particular de empregar DEAs como elementos axialmente quirais e un núcleo bencénico trisubstituído para dar a caixa molecular $(P,P)_3$-**1H** (**Esquema 2**), o que deu lugar á formación de 16 configuracións diferentes onde 2 son aquirais (non útiles) e 14 quirais, con poboacións relativas calculadas estatisticamente moi similares, decidiuse que o custo de separar ditos enantiómeros sería maior que empregalos de xeito enantiopuro (**Figura 6**).

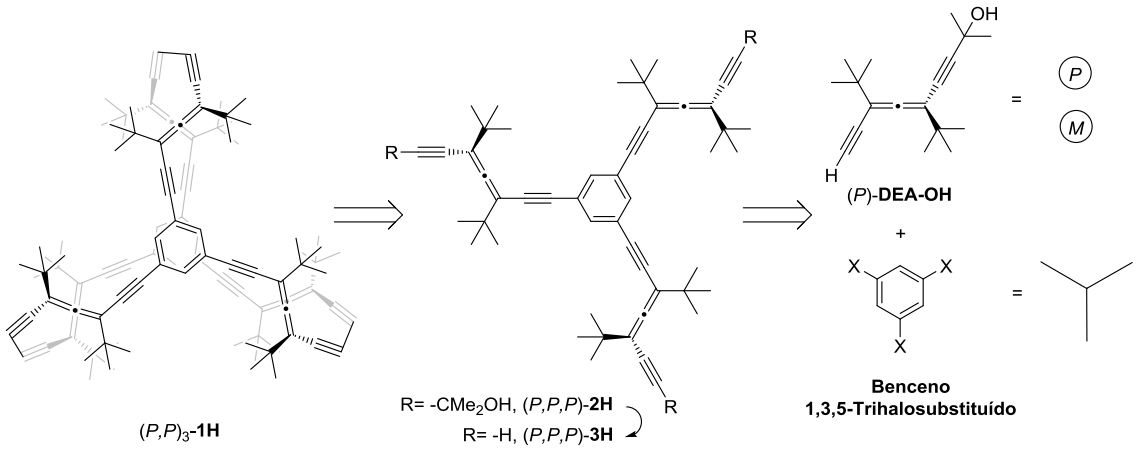

Esquema 2. Esquema retrosintético de $(P,P)_3$-**1H**.

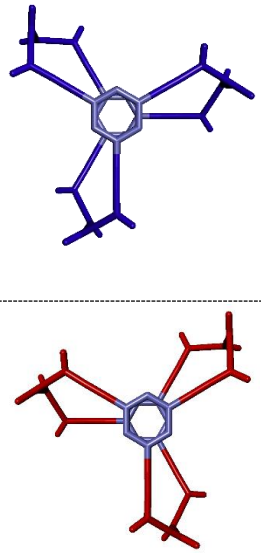

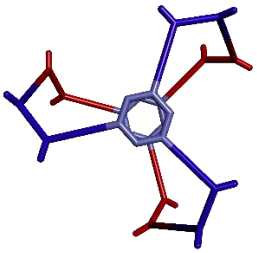

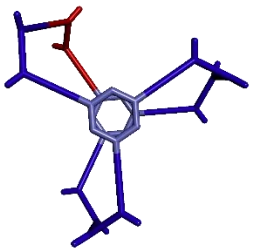

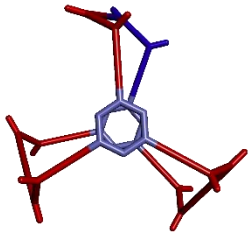

a: (*P,P,P*)$_2$-**1H** (1.56%) //
e: (*M,M,M*)$_2$-**1H** (1.56%)
D_3 chiral

b: (*P,P,P*−*M,M,M*)-**1H** (3.12%)
C_{3h} achiral

c: (*P,P,P*−*P,P,M*)-**1H** (9.38%)
// **f**: (*M,M,M*−*M,M,P*)-**1H**
(9.38%)
C_1 chiral

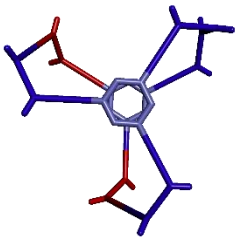

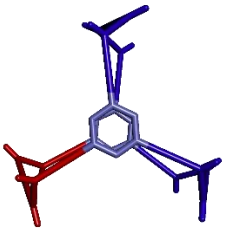

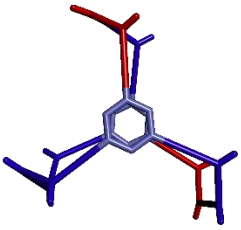

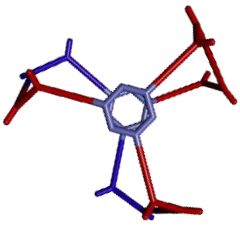

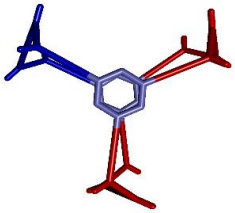

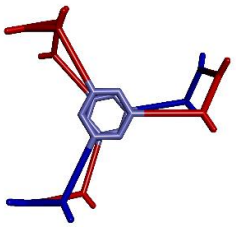

d: (*P,P,P*−*M,M,P*)-**1H** (9.38%) //
g: (*M,M,M*−*P,P,M*)-**1H** (9.38%)
C_1 chiral

h:(*P,P,M*−*P,P,M*)-**1H** (4.69%) //
n: (*M,M,P*−*M,M,P*)-**1H** (4.69%)
C_2 chiral

i: (*P,P,M*−*M,P,P*)-**1H** (4.69%)
// **o**: (*M,M,P*−*P,M,M*)-**1H**
(4.69%)
C_2 chiral

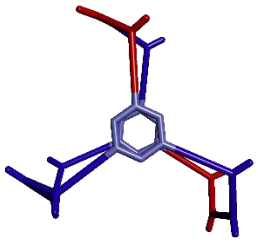

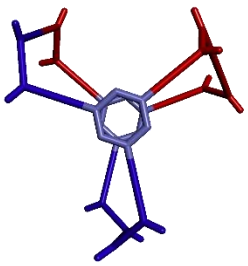

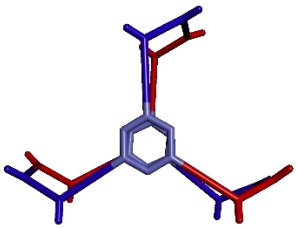

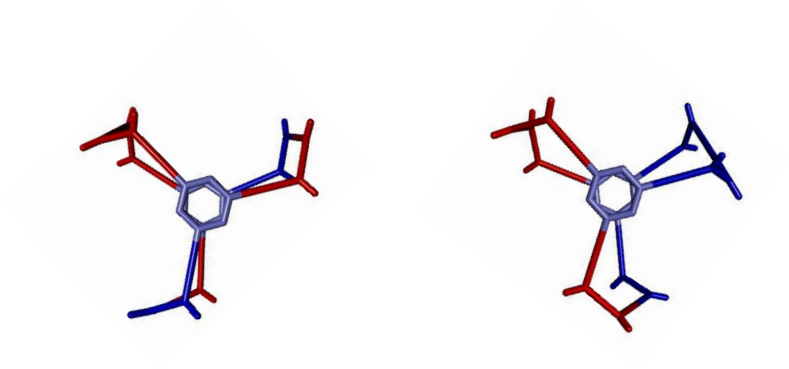

j: (*P,P,M*–*P,M,P*)-**1H** (4.69%) // **p:** (*M,M,P*–*M,P,M*)-**1H** (4.69%) C_2 Chiral	**k**: (*P,P,M*–*P,M,M*)-**1H** (9.38%) // **l**: (*M,M,P*–*M,P,P*)-**1H** (9.38%) C_1 Chiral	**m**: (*P,P,M*–*M,M,P*)-**1H** (9.38%) C_s achiral

Figura 6. Vista superior das 16 posibles configuracións xunto cos seus respectivos grupos puntuais. Núcleos bencénicos en gris, alenos (*P*) en azul e alenos (*M*) en vermello. Hidróxenos omitidos e tertbutilos reemprazados por metilos para maior claridade.

Tralo deseño de xeito teórico das caixas moleculares de interese, levouse a cabo o estudo dos guests apropiados para levar a cabo complexacións coas mesmas. Para iso fixéronse simulacións de dinámica molecular onde se medía a formación e estabilidade de diferentes complexos entre a caixa molecular proposta e diferentes guests planos de simetría C_3. Observouse que derivados de trifenileno contendo aminas daban lugar a complexos estables, e que a estabilidade melloraba a maior carga positiva do guest. Como traballo secundario estudouse a formación de redes 2D a partires de complexos contendo unha caixa e un trifenileno substituído con tres grupos amino e tres grupos amonio, onde ións cloruro actuaban coma contraións nunha rede hexagonal (**Figura 7**).

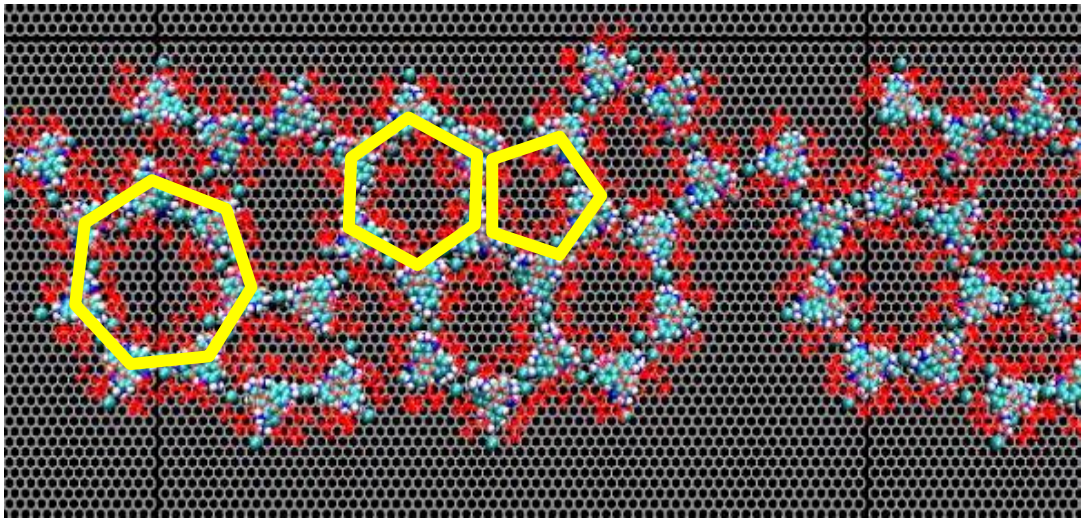

Figura 7. Captura de pantalla da simulación de dinámica molecular con agregados de 5, 6 e 7 membros salientados en amarelo. Esquelete das caixas en vermello. Guests e linkers: C en azul claro, N en azul escuro, H en branco e Cl en verde.

Para constatar a validez da metodoloxía proposta na síntese de caixas moleculares helicoidais, proponse como primeiro obxectivo a síntese da caixa molecular $(P,P)_3$-**1H**, composta por dous núcleos de benceno trihalosubstituídos e seis unidades enantiopuras alénicas. Para isto lévase a cabo en primeira instancia unha reacción de acoplamento cruzado de Sonogashira das citadas

partes constitutivas en presenza dun catalizador de Pd, un cocatalizador de Cu e unha amina, para dar lugar ó produto triacoplado (*P,P,P*)-**2H** nun 80% de rendemento no mellor dos casos. Obsérvase mellora do rendemento no paso de Br a I como halóxeno sobre o núcleo bencénico, así coma no incremento da voluminosidade da amina e a reactividade do catalizador de Pd. O seguinte paso consiste na desprotección en medio básico dos grupos 2-hidroxipropilo protexendo os alquinos, para dar o composto tridesprotexido (*P,P,P*)-**3H** nun 90% de rendemento. Por último, o homoacoplamento catalizado por Cu de dúas moléculas de (*P,P,P*)-**3H** en condicións de Breslow en réxime de pseudoalta dilución conseguida cunha adición lenta do reactivo dá lugar á caixa molecular (*P,P*)$_3$-**1H** nun 55% de rendemento no mellor dos casos. Obsérvase que a velocidade de adición é un factor clave na formación do produto en bo rendemento.

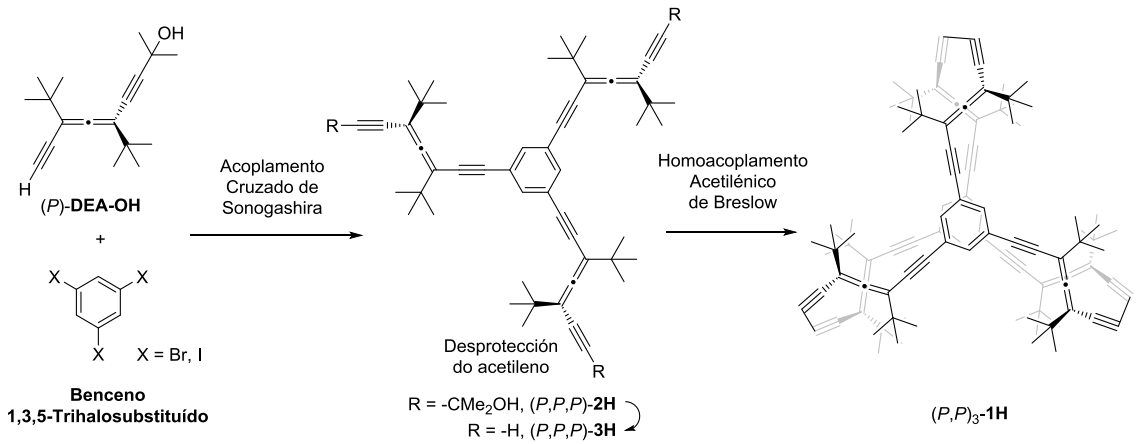

Esquema 3. Esquema sintético de (*P,P*)$_3$-**1H**.

(*P,P*)$_3$-**1H**, así coma o seu enantiómero (*M,M*)$_3$-**1H**, foron totalmente caracterizados por RMN de ^{1}H, ^{13}C, HSQC e HMBC, asignando todas e cada unha das sinais do espectro. Tamén por espectroscopías IR, UV-Vis, ECD, onde se observou unha resposta quiróptica notoria presentando grande amplificación quiral con respecto á suma de seis unidades de aleno, cun *g*-factor de 0.006. Ademais empregouse na caracterización espectroscopía de masas HR-MALDI-MS, e obtívose un cristal apropiado para a súa medida por Raios-X, onde se observou unha estrutura sen poros nin canles accesible cunha cela unidade formada por dúas moléculas de caixa (**Figura 8**).

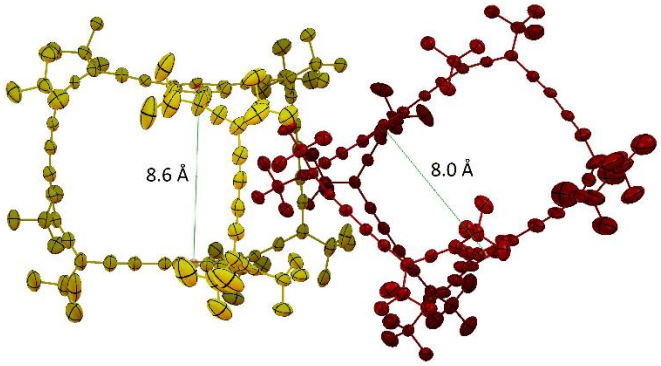

Figura 8. Representación elipsoidal da cela unidade da estrutura cristalina de (*M,M*)$_3$-**1H**.

Acto seguido sintetizáronse e probáronse as complexacións con (*P,P*)$_3$-**1H** por medio de valoracións por RMN ^{1}H sumado ó tratamento de datos de Benesi-Hildebrand algúns dos guests derivados dos estudos de dinámica molecular, con cores bencénicos e trifenilénicos, entre os cales destacan o trietinilbenceno (**TEB**), trifluorotriiodobenceno (**BzF$_3$I$_3$**), trifenileno (**TP**), hexaaminotrifenileno asimétrico (**HATP-Asym**) e simétrico (**HATP-Sym**), hexahidroxitrifenileno (**HHTP**), e hexametoxitrifenileno (**HMeOTP**). So **BzF$_3$I$_3$** deu resultados positivos, cunha constante de asociación (K_a) de 9 M^{-1}. Dito resultado racionalizouse en función dos coeficientes de empaquetamento do guest dentro do volume calculado da cavidade da caixa, atendendo á súa adecuación á regra do 55% de Rebek, así coma atendendo ó seu carácter electrónico calculado e representado cun mapa de potencial electrostático mapeado sobre a densidade electrónica (**Figura 9**). Desta análise desprendeuse a conclusión de que a apetencia de dita caixa molecular é maior por guests electronicamente deficientes coma o **BzF$_3$I$_3$**. O seguinte paso sería a busca de guests con capacidade de interaccionar con ambalasdúas caras internas da caixa a través de interaccións π–π.

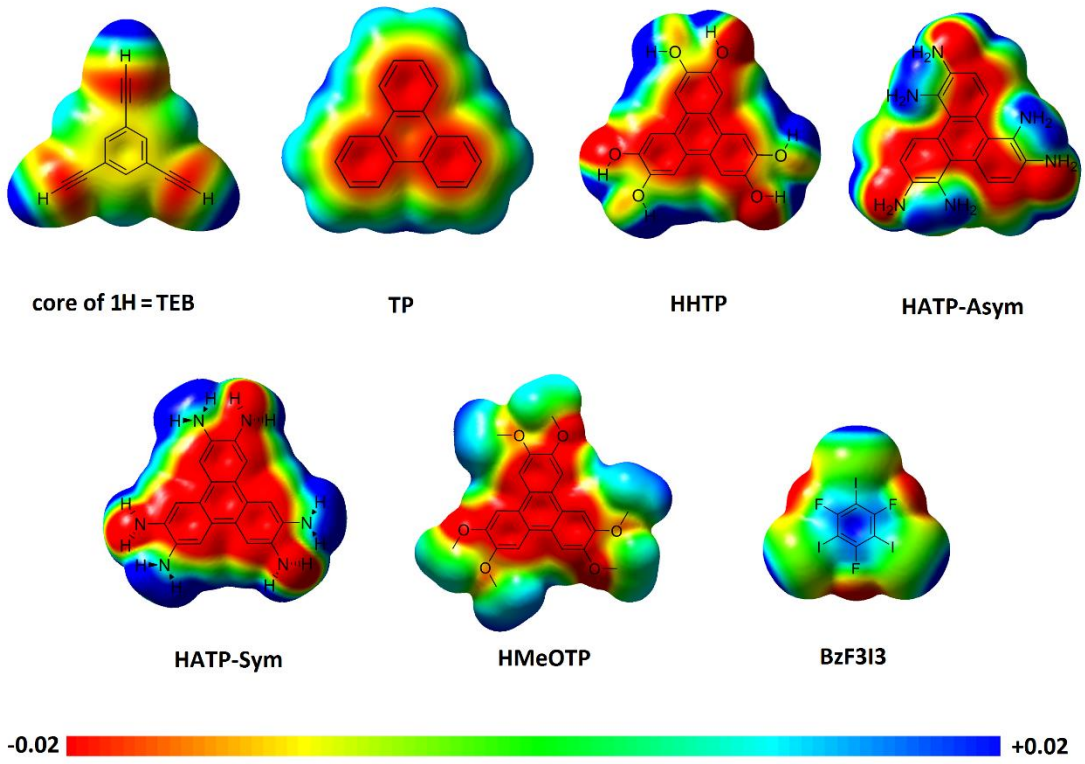

Figura 9. Representación do mapa de potencial electrostático (MEP) mapeado sobre a superficie de densidade electrónica do núcleo de (*P,P*)$_3$-**1H** e dos guests testados con *Gaussian 09* ó nivel de teoría B3LYP/6-31G(d), excepto para **BzF$_3$I$_3$** que se empregou B3LYP/LanL2DZ (isovalor = 0.020, densidade = 0.00040). Escala de cor: vermello indica riqueza electrónica e azul indica pobreza electrónica.

Outro xeito de mellorar a complexación cos guests é variar o carácter electrónico dos núcleos aromáticos da caixa. Por iso se propón a síntese de caixas que posúan como núcleos bencenos triplemente metilados (mais rica en electróns, (*P,P*)$_3$-**1Me**), triplemente fluorados (mais pobre en electróns, (*P,P*)$_3$-**1F**), e un núcleo de triazina (moi pobre en electróns, (*P,P*)$_3$-**1N**) (**Figura 10**).

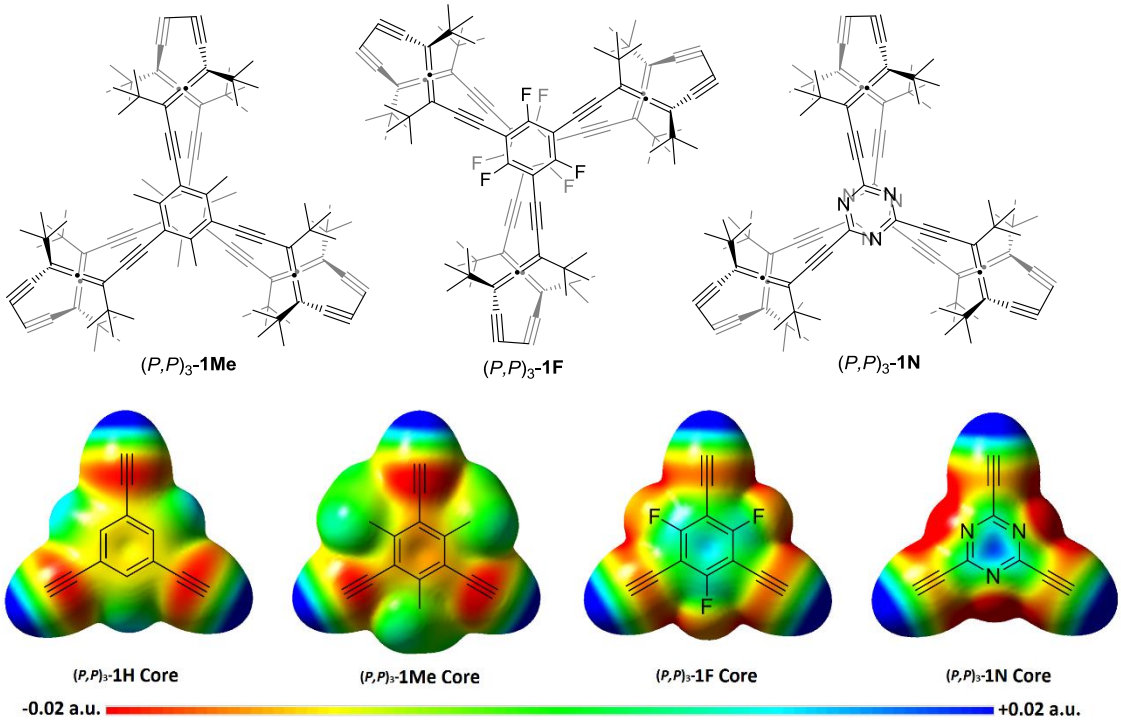

Figura 10. Estrutura das caixas moleculares (*P,P*)$_3$-**1Me**, (*P,P*)$_3$-**1F**, e (*P,P*)$_3$-**1N** (arriba). MEP dos núcleos das citadas caixas moleculares (abaixo). Vermello indica riqueza electrónica e azul pobreza electrónica.

A síntese de (*P,P*)$_3$-**1Me** comeza coa triple iodación do mesitileno nun 72%, seguido do triple acoplamento de Sonogashira do DEA co 1,3,5-triidomesitileno para dar o produto triacoplado (*P,P,P*)-**2Me** nun 56%. Dita diminución no rendemento do acoplamento explícase pola riqueza do núcleo bencénico, que desfavorece a adición oxidante na primeira etapa da Sonogashira. O seguinte paso é a desprotección de (*P,P,P*)-**2Me** en medio básico para dar (*P,P,P*)-**3Me** nun 34% de rendemento, seguido do seu homoacoplamento baixo condicións de Breslow para dar (*P,P*)$_3$-**1Me** nun 32%. Esta caixa amosa unhas propiedades quirópticas da orde das da anterior, cun *g*-factor de 0.004 (**Figura 11**).

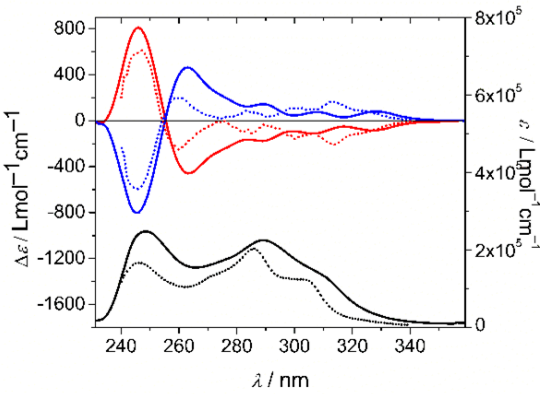

Figura 11. Espectro de absorción (panel inferior) o de(*P,P*)$_3$-**1Me** (liña negra sólida) e (*P,P*)$_3$-**1H** (liña negra punteada), e espectro de ECD (panel superior) de (*P,P*)$_3$-**1Me** (liña vermella sólida),

(*P,P*)$_3$-**1H** (liña vermella punteada), (*M,M*)$_3$-**1Me** (liña azul sólida), e (*M,M*)$_3$-**1H** (liña azul punteada) en $CHCl_3$ a aproximadamente 10^{-5} M.

En base ós resultados de complexación obtidos para (*P,P*)$_3$-**1H** cos guests planos decidiuse probar a cambiar os guests por compostos sándwich ou paraciclofanos na complexación con (*P,P*)$_3$-**1H** e (*P,P*)$_3$-**1Me**. Entre os guests atópanse o ferroceno (**Fc**), o ferrocenio (**Fc$^+$**), o cobaltocenio (**Cob$^+$**), o rutenocenio (**Rut$^+$**), o [2.2]paraciclofano (**PCP**) e o 4,5,7,8,12,13,15,16-octafluoro [2.2]paraciclofano (**PCP-F$_8$**), onde os catiónicos se atopan balanceados polo contraión PF_6^-. Os valores de K_a atópanse reflectidos na **Táboa 1**.

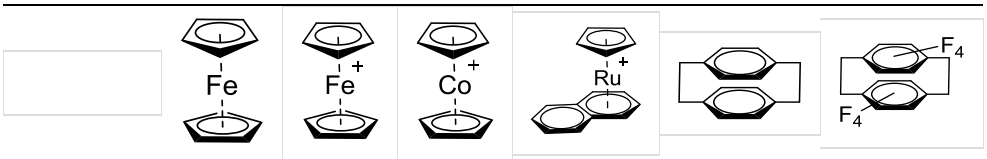

	Fc	**Fc$^+$**	**Cob$^+$**	**Rut$^+$**	**PCP**	**PCP-F$_8$**
(*P,P*)$_3$-**1H**	n/c[c,d]	22[c]	16[c]	29,[c] 50[d]	n/c[c]	n/a
(*P,P*)$_3$-**1Me**	n/a	n/a	296[d]	905[d]	n/a	43[d]

Táboa 1. Constantes de asociación (K_a) e estructura dos guests probados nos estudos de complexación. Ferroceno (**Fc**), ferrocenio hexafluorofosfato (**Fc$^+$**), cobaltocenio hexafluorofosfato (**Cob$^+$**), η^5-ciclopentadienil-η^6-naftalenorutenio (III) hexafluorofosfato (**Rut$^+$**), [2.2]paraciclofano (**PCP**), e 4,5,7,8,12,13,15,16-octafluoro [2.2]paraciclofano (**PCP-F$_8$**). A táboa de K_a (M^{-1}) amósase para ambos [(*P,P*)$_3$-**1H**@guest] e [(*P,P*)$_3$-**1Me**@guest]. [c] Disolvente = acetona-d_6. [d] Disolvente = diclorometano-d_2. n/c = non se observa formación do complexo. n/a = dato non dispoñible.

Tendo en conta factores puramente estéricos, presuponse que os guests **PCP**, **Rut$^+$**, e **PCP-F$_8$** serían os mais apropiados para a complexación coas caixas (*P,P*)$_3$-**1H** e (*P,P*)$_3$-**1Me**. Pola contra, **Rut$^+$** é o único dos tres que dá unha constante de asociación elevada, preto de 500 M^{-1}, o que deixa ver a prevalencia do carácter electrónico fronte á compoñente estérica (**Figura 12**).

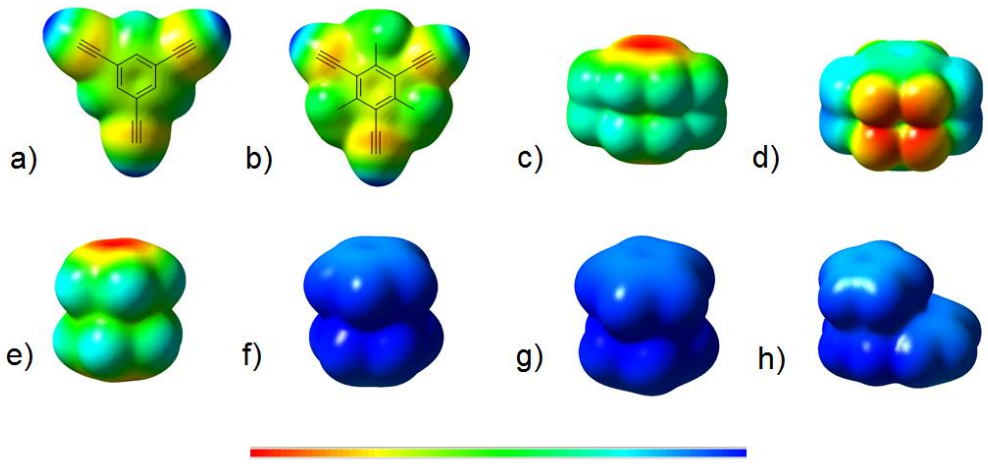

Figura 12. MEP de: a) núcleo de (*P,P*)$_3$-**1H**; b) núcleo de (*P,P*)$_3$-**1Me;** c) **PCP**; d) **PCP-F$_8$**; e) **Fc**; f) **Fc$^+$**; g) **Cob$^+$**; h) **Rut$^+$**. Escala de cor: vermello indicando rexións ricas en electróns e azul pobres. *GaussView 5.0.8* (Isovalor = 0.0100, densidade = 0.00400).

A elevada constante de asociación para (*P,P*)$_3$-**1Me@Rut$^+$** permitiu que este complexo fose detectado por medio dunha valoración por ECD (**Figura 13**).

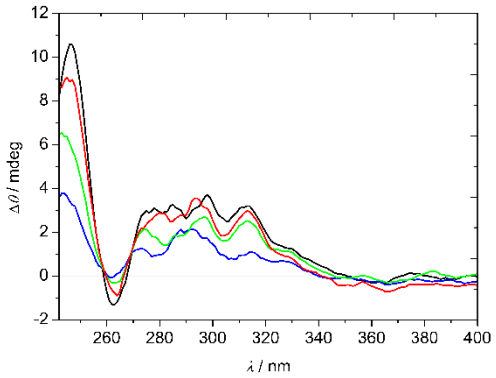

Figura 13. ECD inducido para a complexación [(*P,P*)$_3$-**1Me@Rut$^+$**] con 30 eq (liña negra), 25 eq (vermella), 17 eq (verde) e 8 eq (azul) de **Rut$^+$** en DCE, obtido pola resta de ECD de [(*P,P*)$_3$-**1Me@Rut$^+$**] ó de (*P,P*)$_3$-**1Me**. Esta diferencia é atribuída á formación de [(*P,P*)$_3$-**1Me@Rut$^+$**].

Tanto no caso de (*P,P*)$_3$-**1F** coma no de (*P,P*)$_3$-**1N**, previa á síntese con aleno, empregouse no seu canto acetileno protexido co acetónido (grupo 2-hidroxipropilo) ou acetileno protexido con trimetilsililo (TMS) noutros casos.

No caso da caixa molecular fluorada (*P,P*)$_3$-**1F**, a súa síntese tentouse por dúas vías, empregando o aleno anteriormente citado, así coma outro racémico protexido cun grupo triisopropilsililo (TIPS) no canto do 2-hidroxipropilo. No mellor dos casos, co aleno protexido con 2-hidroxipropilo, obtívose o produto triacoplado (*P,P,P*)-**2F** nun 90% de rendemento, seguida da desprotección para dar o produto tridesprotexido (*P,P,P*)-**3F** nun 62%. O homoacoplamento de dúas moléculas de (*P,P,P*)-**3F** en condicións de Breslow para dar (*P,P*)$_3$-**1F** non tivo lugar en ningún dos casos, observándose trazas de produtos correspondentes ó peche intramolecular de dúas ramas de (*P,P,P*)-**3F**.

No relativo á caixa con núcleo de triazina (*P,P*)$_3$-**1N**, no primeiro paso foron empregadas condicións de Negishi, dada a incompatibilidade do cloruro cianúrico cos reactivos tipicamente empregados nas condicións de Sonogashira. Tamén se empregou o aleno racémico protexido con TIPS, para evitar posible reacción do cloruro cianúrico co alcol terciario do grupo protector 2-hidroxipropilo. Neste caso nin o acoplamento de Negishi deu bos resultados, polo que se propoñen condicións de Stille como alternativa en traballos futuros.

Á vista dos resultados obtidos nas complexacións de (*P,P*)$_3$-**1Me** cos compostos sándwich, dos que se coñece a súa actividade redox, pensouse no deseño de caixas moleculares que combinaran propiedades quirópticas e redox ó mesmo tempo, que permitiran oxidar e reverter ó seu estado de oxidación inicial xogando coa aplicación dun potencial dado.

Os triangulenos, moléculas triangulares altamente conxugadas formadas pola fusión de seis aneis bencenoides, son especies redox−activas. Especificamente, aquelas que conteñen un átomo interno de nitróxeno, coñecidos como N-heterotriangulenos, foron amplamente investigados. Deles sábese que son facilmente oxidados á súa forma catión−radical. Ditos compostos son derivados planos da trifenilamina, moi empregado polas súas propiedades de absorción e emisión. Os seus análogos ponteados son empregados como transportadores de ocos, debido á mellor comunicación entre aneis aromáticos, e deron lugar a aplicacións tales como celas solares sensibilizadas por colorantes (DSSCs), diodos orgánicos emisores de luz

(OLEDs), transistores orgánicos de efecto campo (OFETs), formación de fibras e superficies 2D mímicas do grafeno dopado, e formación de macrociclos útiles como interruptores moleculares.

Ditas plataformas xa tiñan sido estudadas en reaccións de acoplamento cruzado con éxito, o que nos permitiu empregalas coa metodoloxía proposta na síntese de caixas moleculares. Concretamente, na síntese das caixas moleculares (*M,M*)$_3$-**1TCO** e (*M,M*)$_3$-**1TMe** (**Esquema 4**), contendo triangulenos ponteados con grupos carbonilo (deficiente en electróns) e dimetilmetileno (rico en electróns) respectivamente (**Figura 14**).

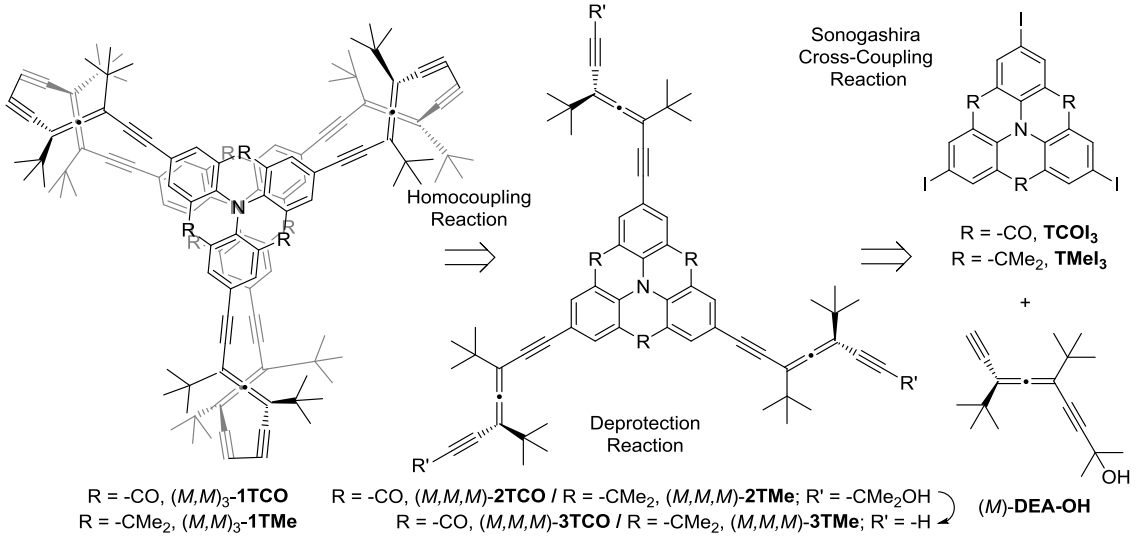

Esquema 4. Esquema retrosintético das caixas de trianguleno (*M,M*)$_3$-**1TCO** e (*M,M*)$_3$-**1TMe**.

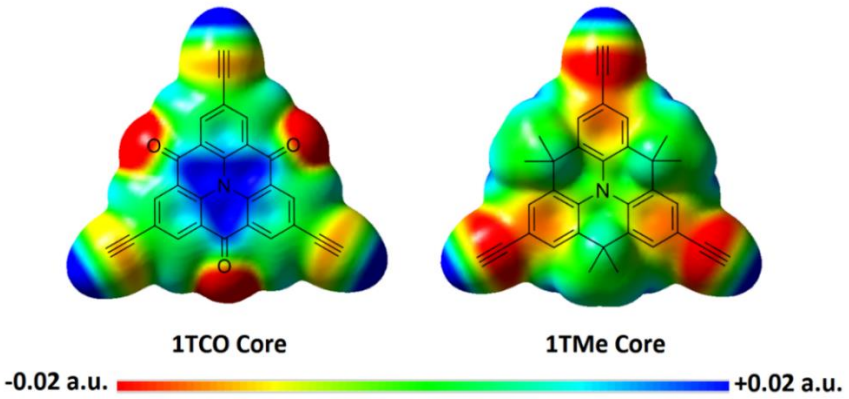

Figura 14. MEP dos cores de (*M,M*)$_3$-**1TCO** e (*M,M*)$_3$-**1TMe** á nivel de cálculo B3LYP/6-31Gd.

A reacción de acoplamento cruzado de Sonogashira entre (*M*)-**DEA-OH** e o N-heterotrianguleno carbonilado triiodado **TCOI$_3$** deu lugar ó produto triacoplado (*M,M,M*)-**2TCO** nun 70%. Durante a súa caracterización fixéronse medidas de voltametría cíclica, amosando dous potenciais cuase reversibles a −1.45 e −1.52 V en diclorometano fronte ó par Fc/Fc$^+$. Desafortunadamente, o composto presenta un espectro de ECD totalmente plano, co que se supón que o core deficiente en electróns racemizou os alenos enantiopuros.

A pesar diso levouse tamén a cabo a desprotección en medio básico de (*M,M,M*)-**2TCO** para dar (*M,M,M*)-**3TCO** nun 12%. O homoacoplamento en condicións de Breslow de dúas moléculas de (*M,M,M*)-**3TCO** para dar a caixa molecular non tivo lugar.

No caso da caixa molecular (*M,M*)$_3$-**1TMe**, a síntese comezou co acoplamento cruzado en condicións de Sonogashira de (*M*)-**DEA-OH** co núcleo de N-heterotrianguleno ponteado con dimetilmetilenos e triiodado para dar (*M,M,M*)-**2TMe** nun 46%, seguido de desprotección en medio básico para dar (*M,M,M*)-**3TMe** nun 98%, e o homoacoplamento en condicións de Breslow para dar (*M,M*)$_3$-**1TMe** nun 30%.

Cabe salientar da caracterización de (*M,M*)$_3$-**1TMe** a diferenciación observada dos metilos ponte do trianguleno apuntando cara o interior e o exterior da caixa molecular, así como a diferenciación dos hidróxenos aromáticos pola presenza dun ambiente quiral próximo, denotada polo desdobramento de sinais de RMN de ^{1}H e ^{13}C. Ademais, neste caso a quiralidade consérvase, presentando a caixa unha resposta quiróptica notable medida por ECD, cun *g*-factor de 0.007, o maior das caixas presentadas neste manuscrito.

Para comprobar a dispoñibilidade do par electrónico solitario sobre o nitróxeno da caixa fíxose unha valoración ácido-base con ácido trifluoroacético (TFA), observándose un aumento progresivo na intensidade do espectro de absorción coa adición sucesiva de TFA, ata os 492 equivalentes, tralo cal se observa unha caída repentina das bandas e se apreza unha coloración azulada na disolución e turbidez. Por outra banda o ECD da mestura vai perdendo intensidade ata desaparecer, co que se supón que se racemizan os alenos. O ECD non se recupera trala adición dunha base indicando un proceso irreversible.

Como conclusión, diremos que no presente manuscrito se desenrolou o deseño de caixas moleculares covalentes orgánicas helicoidais con forma de prisma triangular torcido baseadas no acoplamento entre núcleos aromáticos planos de simetría C_3 e ditertbutildietinilalenos (DEAs). A metodoloxía sintética está baseada nun triple acoplamento cruzado entre o núcleo e os DEAs, seguido dunha posterior desprotección, e homoacoplamento catalizado por Cu. Leváronse a cabo ademais estudos de dinámica molecular (MD) para elucidar os guests plausibles na complexación coas caixas moleculares propostas, xunto co desenrolo dunha estratexia para a formación de redes 2D a partires da ensamblaxe de caixas moleculares helicoidais. Acadouse con éxito a síntese das caixas moleculares contendo seis DEAs e como núcleos o benceno trisubstituído ((*P,P*)$_3$-**1H**), mesitileno ((*P,P*)$_3$-**1Me**), e un N-heterotrianguleno con pontes dimetilmetileno ((*M,M*)$_3$-**1TMe**). (*P,P*)$_3$-**1H** amosou unha grande amplificación quiral con respecto á suma de seis unidades alénicas. (*P,P*)$_3$-**1Me** deu lugar á complexación de diferentes compostos sándwich, entre os cales cabe destacar o **Rut$^+$**, que foi detectado por medio de espectroscopía ECD. Finalmente a caixa molecular (*M,M*)$_3$-**1TMe** ofrece a posibilidade de combinar as súas propiedades quirópticas coas súas propiedades redox. Todos estes avances no mundo do recoñecemento molecular abren as portas á mellora dos sensores empregando a quiralidade como motivo director do recoñecemento.